Multiscale modelling of thermo-electro-mechanically coupled material behaviour

von der Fakultät Maschinenbau
der Technischen Universität Dortmund
zur Erlangung des akademischen Grades

Doktor-Ingenieur (Dr.-Ing.)

genehmigte Dissertation

von

Dilek Güzel

aus Istanbul

Vorsitz:	PD Dr.-Ing. T. Kaiser
Referent:	Prof. Dr.-Ing. habil. A. Menzel
Korreferenten:	Prof. Dr. A. Pandolfi
	Prof. Dr.-Ing. habil. Ralf Jänicke
Tag der Einreichung:	16.06.2025
Tag der mündlichen Prüfung:	20.11.2025

Bibliografische Information Der Deutschen Bibliothek
Die Deutsche Bibliothek verzeichnet diese Publikation in der Deutschen Nationalbibliografie; detaillierte bibliografische Daten sind im Internet über **http://dnb.d-nb.de/** abrufbar.

Bibliographic information published by Die Deutsche Bibliothek
Die Deutsche Bibliothek lists this publication in the Deutsche Nationalbibliografie; detailed bibliographic data is available in the Internet at **http://dnb.d-nb.de/**.

Schriftenreihe des Instituts für Mechanik

Herausgeber: Institut für Mechanik
Fakultät Maschinenbau
Technische Universität Dortmund
Leonhard-Euler-Str. 5
D-44227 Dortmund

Druck: Koffler DruckManagement GmbH

Als Manuskript gedruckt. Printed in Germany.

ISSN 0000-0000
ISBN 000-000-000-000

"Would it save you a lot of time if I just gave up and went mad now?"

Douglas Adams - The Hitchhiker's Guide to the Galaxy

Acknowledgements

The work presented in this thesis is the result of my research conducted at the Institute of Mechanics at TU Dortmund University during my time as a research assistant from July 2021 to June 2025. The financial support provided by the Deutsche Forschungsgemeinschaft (DFG), Project-ID 278868966 – TRR188, is gratefully acknowledged.

First and foremost, I express my deepest appreciation to Prof. Andreas Menzel for welcoming me into his research group and for his continuous support throughout my doctoral studies. His scientific expertise and insightful feedback were essential in shaping this research. Together with Prof. Jörn Mosler, he provided the opportunity to work within an exceptional research team.

I am also very grateful to the members of my examination committee: Prof. Anna Pandolfi for agreeing to serve as co-referee, and Prof. Ralf Jänicke for serving as third referee. In addition, I thank PD Dr. Tobias Kaiser for serving as chair of the committee and, beyond this formal role, for his guidance, patience, and countless discussions on homogenisation over the past four years.

I would also like to thank Prof. Ercan Gürses for introducing me to Applied Elasticity in Ankara in 2017 and for sharing his enthusiasm and knowledge of solid mechanics, which played an important role in shaping my academic path and continues to encourage me to this day.

My sincere gratitude goes to my colleagues for their continuous support, fruitful discussions, and the collegial atmosphere that made this time both scientifically productive and personally enjoyable. I especially thank Kerstin Walter and Christina McDonagh for their extraordinary support in administrative matters and the organisation of numerous social events, as well as Matthias Weiß for providing the necessary hardware and software resources. Special thanks go to my office partner, Merlin Böddecker, for the many discussions and shared moments throughout the years, often extending well beyond standard working hours. I am also grateful to all colleagues with whom I shared many conversations over countless coffees: Dr. Thorsten Bartel, Samuel Brabender, Klas Feike, Volker Fohrmeister, Tim Furlan, Gian-Luca Geuken, Dr. Fabian Guhr, Marius Harnisch, PD Dr. Patrick Kurzeja, Dr. Henning Lammen, Dr. Kai Langenfeld, Laurenz Mätzig, Dr. Marzena Mucha, Alexander Niehüser, Dr. Isabelle Noll, Justice Olatunbosun, Felix Rörentrop, Dr. Lars Rose, Dr. Markus Schewe, Dr. Robin Schulte, Lennart Sobisch, Dr. Leon Sprave, Dr. Tillmann Wiegold, Hendrik Wilbuer, Dr. David Wiedemann, and Dr. Carina Witt.

Lastly, and most importantly, my heartfelt thanks go to my friends Arin, Can, Gül, Melih and Ozan and, above all, to my family–especially my parents, Nuran and Beşler, and my siblings, Metincan and Deniz, and my brother-in-law, Bilal. I also thank the Meier family for their warmth and kindness. Finally, I thank my boyfriend, Lukas, for

his love, patience, and unwavering support throughout every step of this journey, even when convergence was slow and the solution far from obvious.

Dortmund, December 2025 Dilek Güzel

Zusammenfassung

Die vorliegende Arbeit befasst sich mit der multiskalen Modellierung des thermo-elektro-mechanisch gekoppelten Materialverhaltens, wobei der Schwerpunkt auf dem Einfluss mikrostruktureller Merkmale wie Einschlüssen, Poren und Materialgrenzflächen liegt. Im ersten Teil wird ein thermodynamisch konsistentes Kohäsionszonenmodell für elektrische Leiter entwickelt, die einer gekoppelten thermo-elektro-mechanischen Belastung ausgesetzt sind. Im Fokus stehen verformungsinduzierte Schädigungsprozesse an Grenzflächen, deren Einfluss auf die thermische und elektrische Leitfähigkeit untersucht wird. Die Formulierung wird anhand eines analytischen Beispiels validiert und durch eine numerische Fallstudie eines Drahtbondproblems demonstriert. Der zweite Teil der Arbeit befasst sich mit der zerstörungsfreien Prüfung von Metallen mittels Widerstandsmessungen. Es wird eine thermo-elektro-mechanisch gekoppelte Multiskalenformulierung für elektrische Leiter bei infinitesimalen Deformationen entwickelt, die anschließend erweitert wird, um Materialgrenzflächen auf Mikroskalenebene explizit zu berücksichtigen. Der vorgeschlagene Rahmen wird anhand einer Reihe von numerischen Beispielen veranschaulicht, die wichtige Merkmale wie Größeneffekte und die Auswirkungen deformationsinduzierter Grenzflächenschädigung abbilden. Darüber hinaus werden die Vorhersagefähigkeiten des Multiskalenmodells hervorgehoben, insbesondere im Hinblick auf elektrisch leitfähige Materialien mit resistiven Korngrenzen. Um langjährige Diskrepanzen bei der Messung des spezifischen Widerstands von Korngrenzen zu beheben, greift die Arbeit die Andrews-Methode wieder auf und interpretiert sie im Rahmen des vorgeschlagenen multiskalen Modellierungsansatzes mithilfe der Homogenisierungstheorie neu. Diese Neuinterpretation stellt einen klaren Zusammenhang zwischen dem messbaren makroskopischen Widerstand und dem mikroskopischen Grenzflächenverhalten her. Der abschließende Teil der Arbeit liefert eine mathematische Grundlage für den multiskalen Ansatz zur thermoelektrischen Homogenisierung. Unter Verwendung der Hill–Mandel-Homogenisierung, asymptotischer Erweiterungen und einer Zwei-Skalen-Konvergenztechnik wird gezeigt, dass die makroskopischen Gleichungen, die das gekoppelte thermo-elektrische Verhalten beschreiben, die zuvor aus physikalischen Argumenten abgeleitet wurden, auch durch die mathematische Homogenisierungstheorie rigoros erhalten werden können. Insgesamt bieten die in dieser Arbeit entwickelten Konzepte eine mathematisch und physikalisch konsistente Grundlage für die multiskalen Analyse von thermo-elektro-mechanisch gekoppelten Feldern in elektrischen Leitern.

Abstract

This work addresses the multiscale modelling of thermo-electro-mechanically coupled material behaviour, with particular emphasis on the influence of microstructural features such as inclusions, pores and material interfaces. In the first part, a thermodynamically consistent cohesive zone model is developed for electrical conductors subjected to coupled thermo-electro-mechanical loading. Special attention is given to the deformation-induced interface damage processes on the thermal and electrical conductivity. The formulation is validated through an analytical example and demonstrated via a numerical case study involving a wire bonding problem. The second part of the thesis is motivated by non-destructive testing of metals using resistivity measurements. A thermo-electro-mechanically coupled multiscale formulation for electrical conductors in small-strain settings is presented and later extended to explicitly account for material interfaces at the microscale. The proposed framework is illustrated through a series of numerical examples, capturing key features such as size effects and the impact of mechanically induced interfacial degradation. Furthermore, the predictive capabilities of the multiscale model are highlighted, particularly in relation to electrically conductive materials with resistive grain boundaries. In response to long-standing discrepancies in grain boundary resistivity measurements, the thesis revisits the Andrews method and reinterprets it within the proposed multiscale modelling framework using homogenisation theory. This reinterpretation establishes a clear link between measurable macroscopic resistance and microscopic interface behaviour. The final part of the thesis provides a mathematical foundation for the multiscale approach to thermo-electrical homogenisation. Using Hill–Mandel-type homogenisation, asymptotic expansions, and two-scale convergence technique, it is shown that the macroscopic equations governing coupled thermo-electrical behaviour – previously derived from physical arguments – can also be rigorously obtained through mathematical homogenisation theory. Overall, the developments in this thesis provide a mathematically and physically consistent basis for the multiscale analysis of thermo-electro-mechanically coupled fields in electrical conductors.

Publications

This thesis is based on the following peer-reviewed journal articles which were either published or submitted during the progress of this thesis. Alterations of the original articles were made whenever considered relevant to, e.g. prevent repetitions, strengthen the understanding and improve the reading flow of this work.

1. D. Güzel, T. Kaiser, A. Menzel: *A thermo-electro-mechanically coupled cohesive zone formulation for predicting interfacial damage*, European Journal of Mechanics - A/Solids, 99:104935, 2023, [74]

2. D. Güzel, T. Kaiser, A. Menzel: *A computational multiscale approach towards the modelling of microstructures with material interfaces in electrical conductors*, Mathematics and Mechanics of Solids, 30(2):247–266, 2025, [76]

3. D. Güzel, T. Kaiser, H. Bishara, G. Dehm, A. Menzel: *Revisiting Andrews method and grain boundary resistivity from a computational multiscale perspective*, Mechanics of Materials, 198:105115, 2024, [71]

4. D. Güzel, T. Furlan, T. Kaiser, A. Menzel: *Neper-Mosaic: Seamless Generation of periodic representative volume elements on unit domains*, SoftwareX, 28:101912, 2024, [75]

5. D. Güzel, D. Wiedemann, T. Kaiser, A. Menzel: *On dissipative effects in thermo–electrically coupled systems: Hill–Mandel-type homogenisation, asymptotic expansions and two-scale convergence*, Journal of the Mechanics and Physics of Solids, 208:106427, 2026, [72]

For journal articles 1–4, the author of this thesis was responsible for developing the theoretical framework, performing all numerical implementations, conducting simulation studies, and preparing the manuscripts. An open-source code associated with journal article 4 has also been published as part of that work. The first and the second author of journal article 4 equally contributed to the development of this open-source code. For journal article 5, the author of this thesis contributed to the theoretical development – particularly the formulation of the Hill–Mandel-type homogenisation framework and the asymptotic expansion method – and was responsible for the numerical implementation, simulation, analysis, and manuscript preparation. The existence proof established in journal article 5, see Section 7.2.3, has been elaborated particularly by the second author of journal article 5.
Special markers are used throughout this thesis to indicate sections of text that have been pre-published in the aforementioned journal articles. The notation $\overset{\text{qtd.}}{\underset{[74]}{}}\{$marks text

reproduced from journal article 1, extending up to the corresponding closing marker $\}^{\text{qtd.}}_{[74]}$. The quoted block may span up to the end of the respective numbered section and is repeated in the following section if continuation is necessary. The quoted text is reproduced verbatim, except for minor editorial adjustments. Similarly, the markers $^{\text{qtd.}}_{[76]}\{$and $^{\text{qtd.}}_{[71]}\{$, $^{\text{qtd.}}_{[75]}\{$, $^{\text{qtd.}}_{[72]}\{$indicate text originating from journal articles 2 and 3, 4 and 5 respectively.

In addition, the following contribution was published during and alongside the preparation of the thesis, which is not directly covered in this thesis.

6. D. Güzel, T. Kaiser, L. Lücker, N. Baak, F. Walther, A. Menzel: *Characterisation of damage by means of electrical measurements: Numerical predictions*, Proceedings in Applied Mathematics and Mechanics, 23:e202300013, 2023, [73]

For the proceeding article 6, the author of this thesis developed the theoretical framework, carried out the numerical implementations and simulations and prepared the manuscript.

Contents

1 Introduction

1.1 Motivation and state of the art

The research presented in this thesis has been conducted within the framework of TRR188 (Collaborative Research Centre, CRC188), which focuses on understanding and optimising damage mechanisms during forming processes. Damage is an inherent aspect of these processes and can never be fully avoided. However, under the guiding principle that damage is not a failure, TRR188 aims to fundamentally understand the damage mechanisms and the effects on product properties. Bridging the fields of forming technology, materials science, material testing, and mechanics, TRR188 pursues two key paradigm shifts: first, shifting the focus in forming technology from formability to usability by considering the actual properties of a formed product rather than its nominal properties; and second, integrating damage quantification and control throughout the entire process chain. By achieving these objectives, TRR188 lays the foundation for a new generation of tailor-made, high-performance lightweight products that maintain their reliability throughout their service life.

Within this framework, this thesis focuses on characterising damage through electrical resistivity measurements by developing a thermo-electro-mechanically coupled multiscale framework. The fundamental relationship that describes a material's opposition to electron flow was first derived in 1826 by Georg Ohm, namely

$$V = I \cdot R \tag{1.1}$$

where V, I denote the voltage applied to the material and the electric current flowing through the material, respectively. R is the electrical resistance of the material specimen and is influenced by both the material's geometric structure and its intrinsic properties—commonly referred to as specific resistivity,

$$R = \rho \frac{L}{A} \quad \text{and} \quad \rho = \frac{1}{\kappa} \tag{1.2}$$

where L is the the macroscopic length and A is the cross-sectional area of the conductor, which contribute to the geometrical factors affecting resistance. The specific resistivity ρ is defined as inverse of conductivity, κ. Furthermore, the specific resistivity of materials is influenced by multiple factors, including grain boundaries, cracks, and pores, making

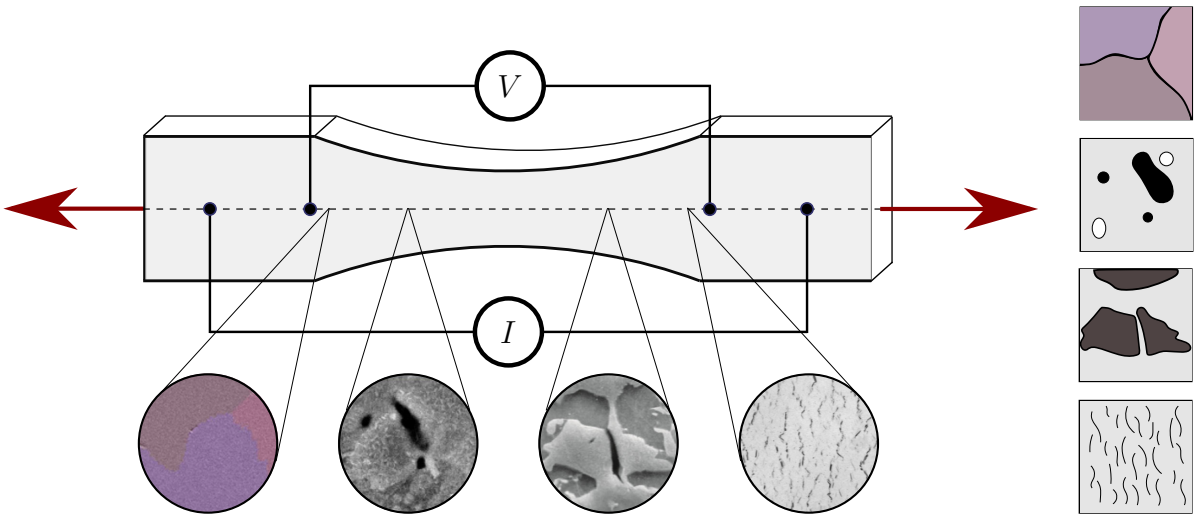

Figure 1.1: Schematic of a resistivity measurement on a mechanically loaded specimen, showing how local microstructural features –grain boundaries, pores, phase heterogeneities (martensite and ferrite) and microcracks– alter current paths and contribute to the total electrical resistance. Such mechanisms make resistivity a sensitive, non-destructive indicator of internal damage and microstructural evolution during deformation or fatigue. Insets depict typical metallic microstructural features: grain boundaries, courtesy Hanna Bishara, Max Planck Institute for Sustainable Materials; pores reproduced from [39]; martensite-ferrite islands reprinted from [116], under the terms of the Creative Commons Attribution License (CC BY); and microcracks reprinted from [99], under the terms of the Creative Commons Attribution License (CC BY).

it challenging to directly quantify their individual contributions through experiments. To address this, numerical simulations are employed to analyse the different contributions to resistivity, enabling a deeper understanding of how damage affects electrical performance.

The remainder of this chapter is structured as follows. Section 1.1.1 presents key experimental techniques for measuring electrical resistivity in conductive materials, with particular attention to their relevance in damage characterisation and non-destructive evaluation. Section 1.1.2 provides an overview of homogenisation approaches– from mathematical theory to computational schemes –that form the theoretical backbone of this thesis. Section 1.1.3 introduces the concept of material interfaces, highlighting their role in microstructural degradation and their significance in multiscale modelling. In Section 1.1.4, various methods of analysis of damage phenomena are presented. Finally, the outline and objective of the thesis are given in Section 1.2.

1.1.1 Electrical resistivity measurements

In material characterisation, particularly for assessing damage and degradation, non-destructive techniques are essential to avoid altering or compromising the sample. This is especially critical in microelectronics, thin-film systems, and structural health monitoring, where changes in electrical resistivity can serve as sensitive indicators of internal material states and potential failure mechanisms.

The two-probe measurement technique is the simplest method for determining electrical resistivity. In this method, the current is passed through the sample and the resulting voltage drop is measured using the same pair of contacts. The resistivity is then calculated based on the measured resistance and the sample geometry. While straightforward, this technique includes the effects of contact resistance and wire resistance, which can significantly affect accuracy –particularly in low-resistivity materials such as metals.

To overcome these limitations, electrical resistivity measurements often employ a four-probe configuration, where separate pairs of electrodes are used for current injection and voltage measurement, see Figure 1.1. Unlike the simpler two-probe method –where voltage and current are applied through the same contacts– the four-probe configuration uses four probes, a current is applied through the outer two probes, while the voltage drop is measured across the inner two. Within this general approach, the four-point probe (4PP) method refers to a specific and widely adopted configuration in which four equally spaced probes are arranged linearly on the sample surface. This geometry allows for straightforward analytical treatment and is commonly used in thin-film and bulk material characterisation [129].

There are several ways to extend standard four-point probe (4PP) methods beyond traditional DC measurements. Techniques such as the alternating current potential drop (ACPD) method enable frequency-dependent impedance characterisation, allowing for the extraction of additional parameters such as permeability and effective thickness in layered materials [29]. For small-scale applications, modified 4PP approaches have been adapted to measure patterned films and nanostructures by incorporating current-flow simulations [68]. At the nanoscale, integration with atomic force microscopy (AFM) enables simultaneous topographic and electrical measurements, offering high spatial resolution and improved accuracy in systems where contact resistance is otherwise dominant [97].

In addition to these techniques, hybrid systems that integrate Hall effect measurements with four-wire resistivity techniques have been developed to achieve a comprehensive characterisation of semiconductor materials. These combined systems often employ the van der Pauw method alongside Hall voltage measurements to extract key parameters including carrier concentration, mobility, and conductivity type. The van der Pauw approach is particularly advantageous for samples of arbitrary shape, such as flat circular pellets, as it enables accurate resistivity measurements without requiring knowledge of the current distribution within the material [142]. However, the method demands the formation of high-quality ohmic contacts and precise control of contact placement [105].

While the four-point probe remains one of the most trusted techniques for measuring electrical conductivity, various contactless methods have been developed that offer complementary advantages, particularly where physical contact is impractical or undesirable. Optical techniques based on free-carrier absorption in the infrared range enable high-resolution mapping of sheet resistance–down to scales of 10 µm–across large areas without probe alignment errors [87]. However, they typically require meticulous calibration and may struggle with accuracy in heavily doped materials due to nonlinear absorption characteristics. Similarly, electromagnetic approaches such as magnetic induction tomography induce eddy currents via external coils and infer conductivity

distributions from the resulting magnetic fields. These techniques have proven useful in biomedical and soft-matter contexts where non-invasive imaging is essential. Though generally less precise than four-point measurements, recent advances in eddy current methods, such as multi-frequency and pulsed variants, have improved spatial resolution and enabled additional characterisation of conductivity and permeability [124].

1.1.2 Homogenisation theory

Accurately predicting the macroscopic behaviour of heterogeneous materials, while accounting for their complex microstructures, remains a significant challenge in materials science and engineering. Homogenisation techniques offer an elaborate framework to address this challenge by bridging the gap between different scales. By determining effective properties that represent the overall response of materials, homogenisation enables efficient simulations and analyses at the engineering scale as illustrated in Figure 1.2. Today, this approach is well-established in diverse fields, including the design of composite materials [30, 103], the analysis of polycrystalline aggregates [17, 126], and the modelling of biological tissues [59, 70], to name but a few.

Mathematical homogenisation: Analytical homogenisation is a rigorous mathematical approach to derive the effective properties or, rather, governing multiscale equations of heterogeneous materials through closed-form solutions. Grounded in the framework of two-scale convergence [3, 139], which rigorously describes the behaviour of functions oscillating at two distinct scales, this method involves solving microscopic boundary value problems, often referred to as cell problems, to determine effective macroscopic relations. By considering the behaviour of the solution to the cell problem, two-scale convergence allows for the passage from the microscopic scale, characterised by rapid oscillations, to the macroscopic scale, where the effective properties manifest themselves. While the two-scale convergence method is a well-established approach due to its explicit nature, it is limited to periodic settings, or to be more precisely, to a setting with strict separation of scales. For non-periodic structures, different notions of convergence need to be introduced. For second-order symmetric elliptic operators, Spagnolo proposed the concept of $G-$convergence [35, 164]. A key result of $G-$convergence is a compactness theorem. It states that for any bounded and uniformly coercive sequence of coefficients of a symmetric second-order elliptic equation, there exists a subsequence such that the solutions of the corresponding equations $G-$converge to the solution of the homogenised equation. To overcome the restriction to symmetric operators, $H-$convergence was defined by Murat and Tartar [137]. In essence, $H-$convergence provides a way to find a homogenised set of coefficients that not only captures the macroscopic behaviour of the solutions, but also ensures that the associated fluxes converge. In the broader context of variational methods and homogenisation, $\Gamma-$convergence as introduced by De Giorgi [36] is a key concept. It is a rather abstract notion of convergence for functionals, providing a framework for studying the behaviour of minimising sequences of variational problems. For a more

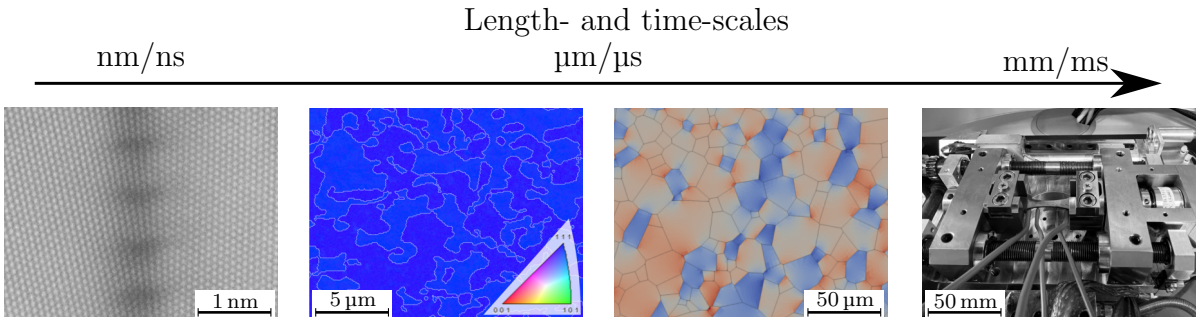

Figure 1.2: Multiscale representation of material characterisation and modelling across length and time scales. At the nanoscale, atomic-resolution imaging captures lattice structure and dislocation behaviour. At the microscale, grain boundary networks emerge as critical features, where individual grains can serve as representative volume elements for mesoscale modelling. Further up the scale, grain interactions inform continuum-level behaviour relevant to component performance and device-scale electrical measurements. Atomic-resolution image and grain boundary networks image are reprinted from "Understanding grain boundary electrical resistivity in Cu: the effect of boundary structure" by Bishara et al., 2021, *ACS Nano 15*, 16607–16615 [23]. Representative volume element image is reprinted from [75] under the terms of the Creative Commons Attribution License (CC BY). Experimental setup image is reprinted from [73] under the terms of the Creative Commons Attribution License (CC BY).

comprehensive introduction to analytical homogenisation methods, see, e.g., [170].

Asymptotic expansion method: In contrast to analytical homogenisation, the method of two-scale asymptotic expansions offers a more heuristic approach to homogenisation, enabling the formal analysis of a broad range of problems in periodic domains. In this method, the solution fields are assumed to be formally representable by a regular expansion in power series of length-scale ratio ε. Substituting this ansatz into the governing equations and collecting terms of the same order yields an hierarchical set of equations. These equations can be solved successively to determine the unknown micro- and macroscale fields. The leading-order term (zeroth-order), typically represents the homogenised solution, whereas higher-order terms capture the local fluctuations induced by the microstructure. However, convergence of the sequence of solutions in the limit $\varepsilon \to 0$ is not guaranteed. Moreover, the applicability of this method relies on the assumption of a distinct scale separation between the micro- and macroscale, $\ell \ll L$, see Figure 1.3. In recent years, a combination of asymptotic expansion- with finite element-based approaches has been investigated for mechanical [5, 40, 49, 147, 150, 185] and multifield problems [19, 27, 37, 48, 64, 115, 163, 178, 186]. Moreover, a comprehensive review of asymptotic expansion approaches is provided in [18].

Hill–Mandel-type computational homogenisation: Complementing analytical homogenisation and asymptotic expansion approaches from a physics point of view, Hill–Mandel-type multiscale schemes make use of the concept of energy equivalence between scales [80]. To this end, detailed information about the underlying microstructure is collected in unit cells and highly accurate material models that have been developed

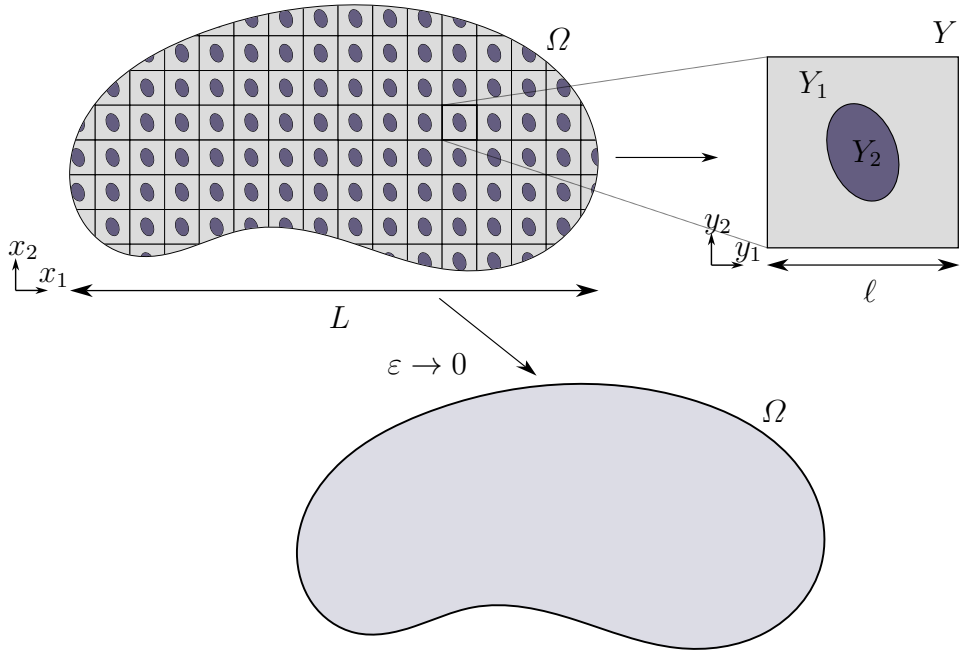

Figure 1.3: Macroscopic Ω and microscopic domains Y with a distinct separation of the corresponding length scales L and ℓ. The periodic representative cell Y is composed of two constituent domains Y_1 and Y_2, representing different materials. Scale separation occurs for $\ell \ll L$.

at the level of individual phases are used. In doing so, purely constitutive macroscale relations are substituted by additional microscale boundary value problems and the predictive capability of the models is significantly increased. These methods have, amongst others, successfully been applied over the past decades to study purely mechanical [56, 60, 106, 107, 130, 133], thermo-mechanical [21, 160, 162, 175, 189], electro-mechanical [100, 102] as well as magneto-mechanical problems [89, 101]. For further reading, see [60, 158].

1.1.3 Material interfaces

Material interfaces can occur at different material length scales. Understanding the properties and the behaviour of interfaces is of utmost importance because interfaces can significantly influence the effective constitutive response of the material under consideration. Experimental findings show that grain boundaries may significantly affect the electrical properties [23, 123], as illustrated in Figure 1.4. To this end material interfaces at the microscale need to be accounted for in simulations in order to model the macroscopic behaviour realistically. Moreover, predicting the evolution of interfacial damage is essential in order to optimise the material's performance and reliability.

The term interface typically refers to an idealised, zero-thickness model that approximates the finite-thickness interphase separating distinct bulk phases. The interface is thus modelled as a two-dimensional manifold embedded in three-dimensional space [93]. Interface models can be categorised into distinct classes based on the continuity or discontinuity of certain variables. In the context of mechanical problems, the primary

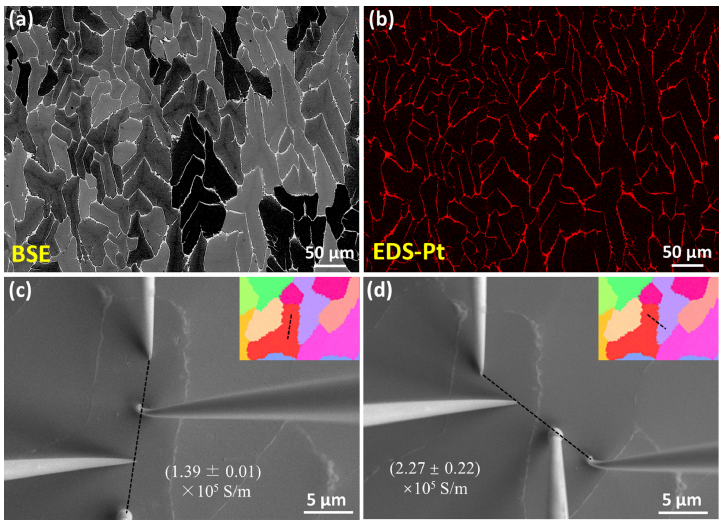

Figure 1.4: (a) Backscattered electron (BSE) image of a pre-BM NbCo(Pt)Sn sample. (b) Corresponding energy-dispersive X-ray spectroscopy (EDX) map of Pt. Position layout of the four needles used for the local electrical measurements – (c) within the grain interior and (d) crossing a high angle grain boundary. Reprinted from "Dopant-segregation to grain boundaries controls electrical conductivity of n-type NbCo(Pt)Sn half-Heusler alloy mediating thermoelectric performance" by Luo et al., 2021, *Acta Materialia 217*, 117147 [123].

quantities used for classification are displacement and traction. Figure 1.5 schematically summarises the main types of interface models relevant to mechanical applications, which are briefly reviewed in the following sections.

Classic cohesive interface models date back to the seminal works of Barenblatt [11] and Dugdale [38]. In these classic models, traction continuity is assumed, whereas the displacement field may exhibit a jump-discontinuity across the interfaces. Moreover, the cohesive interface has been proven to be an essential tool when coupled with the finite element method to model debonding and delamination processes of different materials since established in [81]. An extensive amount of literature has been devoted to the development of this particular type of interface with various contributions focusing on purely mechanical problems [135, 138, 144, 154, 177] as well as on coupled multiphysics problems. In particular, thermo-mechanical coupling has been addressed in [47, 77, 169, 182, 190] and electro-mechanical coupling has been studied in [8, 98, 109, 176, 179]. Another type of interface is the elastic interface which dates back to the developments on surface elasticity by Gurtin and Murdoch [69]. Unlike the cohesive interface model, the elastic interface model allows traction jumps across the interface while a continuous displacement field is assumed [166, 167]. More recently, it was shown in [92] that cohesive and elastic interfaces are two extremes of generalised imperfect interfaces that account for discontinuities in both the displacement and traction field [90, 91].

In the context of cohesive and generalised imperfect interfaces, an important modelling consideration arises from the definition of interface displacement relative to the separating bulk phases. Most formulations implicitly assume that the interface is located at the mid-surface between the two bodies, such that the interface displacement

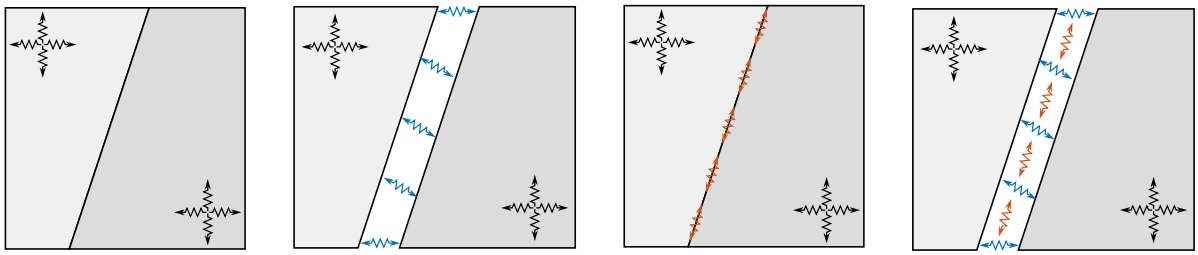

Figure 1.5: Classification of interface models.

is identified with the average displacement across the discontinuity. Although this assumption simplifies the mathematical treatment and is widely adopted in the literature, it is not strictly necessary. In fact, it can be relaxed to allow for more general interface representations. This more flexible approach forms the basis of what is referred to as the extended general interface model [52]. Very recently, a fundamentally new formulation, the canonical interface model, has been introduced, in which the interface displacement is treated as an independent field variable [94]. This variationally consistent model generalises all previous interface formulations, enabling them to be recovered as special cases by tuning a unified set of thermodynamically motivated parameters.

In addition to sharp interface models discussed above, another prominent class of interface modelling techniques is based on phase-field formulations. These models represent interfaces as smoothly varying fields rather than sharp discontinuities. Originally developed to regularise crack surfaces in brittle fracture, the phase-field approach introduces a scalar-valued damage variable that diffuses the sharp crack topology over a finite width. Grounded in the variational fracture framework introduced by Francfort and Marigo [55] and further developed by Bourdin et al. [28], phase-field method have been widely applied in fracture mechanics, microstructure evolution [26, 134]. While phase-field models offer clear advantages in terms of flexibility and regularised energy minimisation, they differ fundamentally from the sharp interface formulations considered in this work.

Since material interfaces significantly influence the effective behaviour of heterogeneous materials –particularly in the presence of debonding, grain boundaries– it is essential to incorporate interface effects into multiscale modelling frameworks. To this end, various approaches have been developed to predict the macroscopic response of materials with embedded interfaces. These include both mean-field analytical methods and computational multiscale formulations, each offering different advantages depending on the complexity and resolution required.

Classic mean field analysis techniques have been extended to cohesive interfaces in order to predict the macroscopic response in the case of debonding or dewetting of particles [30, 61, 86, 165, 172]. Other than analytical approaches, computational homogenisation methods have been employed in the presence of cohesive interfaces [82, 127, 141, 179]. In these methods, multiscale formulations provide the traction-separation relations that

are governed by the evolution of microscopic cracks. More recently, the work [93] established a computational multiscale formulation for continua with generalised imperfect interfaces at the microscale and different aspects, such as damage evolution, are discussed [50, 51, 156, 157]. Alternatively, phase-field formulations have been extended to computational homogenisation settings to model fracture evolution in heterogeneous microstructures. Recent contributions [22, 118, 120] have proposed variationally consistent two-scale frameworks, where the phase-field variable may be interpreted as a microstructural quantity only –treated as an internal variable at the macroscale via volume averaging. In addition to finite element-based multiscale approaches, the boundary element method (BEM) has emerged as a valuable tool for representing microstructures with material interfaces in computational homogenisation studies [2, 16, 17, 183]. Due to its ability to accurately capture the geometry and associated physics of interfaces, BEM provides an alternative or, rather, complementary approach to the finite element method employed in this thesis.

1.1.4 Modelling of damage

Understanding damage mechanisms and quantifying damage are important in order to optimise structures and to increase their reliability. To achieve this goal, experimental- and simulation-based techniques are to be combined. Different methods exist for the analysis of damage phenomena such as fracture mechanics, phase field models, cohesive zone formulations and continuum damage modelling.

Continuum damage mechanics denotes a collection of approaches and models focusing on the simulation of degradation phenomena in continua. In these approaches, specific microstructural features and their evolution are not explicitly resolved; instead, their cumulative effects on the material response are modelled through internal variables. Damage mechanisms such as microcracks, grain boundary decohesion, void growth, rupture, and delamination are thus implicitly captured. To model ductile damage, two principal modelling philosophies have been developed over the past four decades: micromechanically motivated models and phenomenological models.

Micromechanically motivated models account for the underlying microstructure and specific damage mechanisms, whereas phenomenological models describe material degradation based on macroscopic observations, without directly modelling microscale processes. In both approaches, damage is typically represented using a scalar-valued variable d or a tensorial counterpart $\boldsymbol{d}$. In Lemaitre-type models –often referred to as $[1-d]$ formulations– damage leads to a degradation of elasticity and plasticity-related material parameters. However, the resulting material softening gives rise to ill-posedness in the governing equations, manifested by spurious mesh dependency in finite element simulations. To address this, regularisation techniques have been proposed, including non-local damage models [14, 44], gradient-enhanced (micromorphic) formulations [1, 54, 146, 168], and rate-dependent evolution laws [41, 113].

While continuum damage mechanics provides a powerful tool for modelling diffuse damage in the bulk, many failure mechanisms are highly localised – particularly at material interfaces such as grain and phase boundaries. In such cases, sharp-interface

approaches offer a more appropriate modelling paradigm. Two principal methods are commonly employed: linear elastic fracture mechanics and cohesive zone models. Linear elastic fracture mechanics describes crack propagation in brittle materials by quantifying singular fields near a crack tip using stress intensity factors and energy release rates, under the assumption of a pre-existing sharp crack. In contrast, cohesive zone formulations model progressive failure by prescribing a traction–separation relationship across an interface. This approach enables the simulation of crack initiation and propagation without prior knowledge of the crack path and is particularly effective in representing interfacial degradation.

1.2 Objective of this work

This thesis develops a computational multiscale framework for the analysis of coupled electro-mechanical behaviour in heterogeneous materials containing microstructural features such as inclusions, pores, and grain or phase boundaries. The framework aims to capture how these microstructural features influence macroscopic responses, particularly in the context of non-destructive evaluation through resistance-based measurements.

The objective of **Chapter 2** is to establish a rigorous and thermodynamically consistent framework for modelling coupled thermo-electro-mechanical behaviour in electrically conductive solids, serving as the theoretical foundation for the multiscale methods developed in later chapters. To this end, the chapter derives the governing equations for thermo-electro-mechanically coupled conductors. While these balance laws date back to classical continuum theories [45, 85], the focus here is to recapitulate the essential components required for the subsequent derivation of the weak form and its finite element implementation. The chapter concludes with representative boundary value problems and a validation of the proposed finite element framework using analytical solutions. A similar approach to [153] is employed for the derivation, although in contrast to the dynamic formulation presented there, only static analytical solutions are considered in this work.

Within **Chapter 3**, a cohesive zone model is developed for predicting damage in electrically conductive solids subjected to coupled thermo-electro-mechanical loading. The chapter builds on earlier electro-mechanically coupled cohesive interface model [98], and extends it to account for thermal effects, with a focus on interfacial failure phenomena. This includes, in particular, the explicit treatment of interface temperature – an aspect not addressed in [98] but essential for modelling thermally coupled interface degradation [110]. This formulation is particularly relevant in materials with interfaces such as grain or phase boundaries, where degradation influences electrical and thermal conductivity–making the model applicable for non-destructive evaluation scenarios. To achieve this, the chapter derives a thermodynamically consistent interface model, including all relevant balance laws, dissipation inequalities, and constitutive relations. The chapter addresses both bulk and interface behaviour and incorporates damage evolution driven by mechanical opening, which in turn affects electrical and thermal response. The model is validated against analytical solutions for a one-dimensional bar with a cohesive inter-

face, and its predictive capability is demonstrated through a detailed simulation of wire bonding failure. The numerical examples presented in this chapter demonstrate how interfacial degradation influences the coupled thermal and electrical response, and set the stage for multiscale methods that resolve such interfacial effects in **Chapter 5**.

Starting with **Chapter 4**, the focus shifts to the computational multiscale framework of electrically conductive materials under coupled thermo-electro-mechanical loading. This formulation extends the framework introduced in [100] for small-strain electro-mechanical problems. The key distinction in the present work is the inclusion of thermal fields, enabling the consistent treatment of heat conduction alongside electrical and mechanical effects. While Hill–Mandel-type computational homogenisation has been widely applied to multiphysics problems, a consistent thermo-electro-mechanical homogenisation framework for electrically conductive materials has only recently begun to emerge [33, 34]. Notably, these recent contributions primarily focus on thermoplastic polymers, whereas the present work targets metallic conductors, where thermo-electro-mechanical interactions are tightly coupled and relevant to resistance-based diagnostics.

Motivated by the influence of material interfaces on the effective electro-mechanical behaviour of conductors, **Chapter 5** extends the first-order computational homogenisation framework developed in **Chapter 4** to materials featuring cohesive-type interfaces at the microscale. The aim is to capture displacement and potential jumps across grain or phase boundaries and to investigate their impact on the macroscopic electrical and mechanical response. It is shown that, in the presence of such interfaces, the scale-bridging formulation presented here recovers the classical first-order homogenisation results –consistent with previous findings for mechanical problems [93, 157]. In addition, the presence of interfaces endows the material with an internal length scale, thereby enabling the prediction of size effects within a first-order framework. This contrasts with classical multiscale approaches, where such effects typically require higher-order formulations [107]. Through numerical examples, the chapter investigates interface-induced size effects, anisotropic conductivity in microstructures, and deformation-driven interfacial degradation. The results demonstrate that incorporating interface behaviour at the microscale enables the prediction of phenomena that lie beyond the reach of classical first-order homogenisation schemes, setting the stage for more realistic simulations of polycrystalline conductors in **Chapter 6**.

Chapter 6 explores the predictive capabilities of the proposed computational multiscale framework for electrically conductive materials with resistive grain boundaries. Motivated by long-standing discrepancies in grain boundary resistivity measurements, the chapter revisits the Andrews method [6] and reinterprets it through the lens of homogenisation theory. This allows the problem to be addressed from a multiscale modelling perspective, linking measurable macroscopic resistance to grain-level interface behaviour. Analytical benchmarks and finite element simulations are conducted across various microstructures, ranging from idealised to statistically representative polycrystalline geometries. The results reveal limitations of classical additive models and highlight the importance of anisotropy, grain alignment, and interface resistance. A central conclusion is that the proposed multiscale formulation not only recovers the expected isotropic behaviour in the quasi-homogeneous limit but also provides accurate

predictions in anisotropic settings. The chapter also introduces the open-source NeperMosaic tool for generating periodic microstructures, enabling efficient representative volume element studies with realistic grain morphologies.

Chapter 7 approaches the thermo-electrical homogenisation problem from a mathematical perspective, providing theoretical justification for the multiscale framework used throughout the thesis. While earlier chapters adopt an energy-equivalence-based homogenisation approach, this formulation inherently relies on modelling assumptions, such as scale separation, periodicity, and the use of macroscopic quantities as inputs to microscale constitutive relations, without offering a formal justification. This chapter rigorously re-examines the same problem using analytical techniques. The objective of **Chapter 7** is to show that the macroscopic equations governing thermo-electrical behaviour, previously derived from computational and physical reasoning, can also be obtained through classical mathematical homogenisation methods. Two complementary approaches are considered: asymptotic expansion [18] and two-scale convergence [3, 139]. The former introduces a formal ansatz to separate microscale and macroscale contributions and leads to a system of nested cell problems. The latter provides a rigorous functional framework for proving that the microscale solutions converge, in the appropriate sense, to an effective macroscopic solution. A key conclusion of this chapter is that all three formulations, Hill-Mandel-type homogenisation, asymptotic expansion, and two-scale convergence, lead to the same homogenised system of equations. This consistency not only validates the assumptions employed in **Chapter 4** but also ensures that the proposed framework is mathematically well-posed. By unifying engineering practice with mathematical theory, **Chapter 7** establishes a solid analytical foundation for the multiscale modelling of thermo-electro-mechanical processes in heterogeneous materials.

2 Continuum thermo-electrodynamics

Modern engineering applications, ranging from advanced microelectronics to high-performance energy systems, increasingly rely on materials operating under complex thermal, electrical, and mechanical loads. The intricate interplay between these physical fields necessitates a comprehensive understanding of their coupled behaviour, as traditional uncoupled analyses often fail to capture the full range of material responses and underlying failure mechanisms. Within the context of a thermo-electro-mechanically coupled formulation for electrical conductors, the scope of the present chapter is twofold:

- *To provide a rigorous and thermodynamically consistent framework for describing thermo-electro-mechanical interactions in electrical conductors, serving as the theoretical basis for the analyses carried out in subsequent chapters.*
- *To demonstrate the validity and reliability of the proposed modelling approach through comparison with analytical benchmark solutions, thereby justifying its use throughout the remainder of the thesis.*

To set the stage, the notation and essential concepts from functional analysis used throughout this thesis are briefly reviewed in Section 2.1. The chapter begins with a discussion of the thermodynamic principles governing coupled phenomena, followed by the formulation of the relevant balance laws in Section 2.2. These include the conservation of mass, balances of linear and angular momentum, the continuity equation of electric charge, and the first and second laws of thermodynamics – all within the small-strain framework. Building upon these balance laws, a variational (weak) form of the governing equations is derived, and a corresponding finite element implementation is introduced in Section 2.3. To validate the implementation, a set of analytical solutions is presented in Section 2.4. The chapter concludes with microchip simulations in Section 2.5, which illustrate the capabilities and practical relevance of the proposed framework.

2.1 Notation

Before delving into the physical principles, we first introduce the mathematical notation and functional analysis framework employed throughout this thesis. For the reader's convenience, the following essential relations and definitions used throughout the thesis

are presented in a consolidated form. Section 2.1.1 outlines the tensor notation adopted herein; for a comprehensive overview of tensor calculus, the interested reader is referred to the textbook [88]. Section 2.1.2 presents selected elements of functional analysis relevant to the discussions in this work. A more detailed treatment of functional analysis may be found in standard references such as [4, 151].

2.1.1 Index notation and tensor calculus fundamentals

Definition 1 (**Einstein's summation convention**). Whenever an index appears twice in a term, summation over that index is implied. Such repeated indices are called dummy indices, while those that appear only once are referred to as free indices.

Definition 2. **(Tensors)** Let $\mathbf{e}_i$, with $i \in 1, \ldots, d$, represent the Cartesian basis vectors spanning the d-dimensional Euclidean vector space $\mathbb{R}^d$. First-order tensors (vectors) are expressed as

$$\boldsymbol{u} = \sum_{i=1}^{d} u_i \,, \qquad \mathbf{e}_i = u_i \, \mathbf{e}_i, \tag{2.1a}$$

making use of Einstein's summation convention. Higher order tensors follow analogous forms:

$$\text{Second-order:} \quad \boldsymbol{T} = T_{ij} \, \mathbf{e}_i \otimes \mathbf{e}_j, \tag{2.1b}$$

$$\text{Fourth-order:} \quad \mathsf{T} = \mathsf{T}_{ijkl} \, \mathbf{e}_i \otimes \mathbf{e}_j \otimes \mathbf{e}_k \otimes \mathbf{e}_l. \tag{2.1c}$$

In this thesis, scalars typically are denoted by non-bold lowercase letters, first-order tensors by bold lowercase letters, second-order tensors by bold uppercase letters, and fourth-order tensors by bold sans-serif uppercase letters.

Definition 3. **(Inner tensor products)** Let $\boldsymbol{\mathcal{S}}$ and $\boldsymbol{\mathcal{T}}$ be tensors of arbitrary order. Inner tensor products are denoted by dots, with the number of dots indicating the number of contractions

$$\begin{aligned} \boldsymbol{\mathcal{S}} \cdot \boldsymbol{\mathcal{T}} &= [\mathcal{S}_{ij\ldots kl} \, \mathbf{e}_i \otimes \mathbf{e}_j \ldots \otimes \mathbf{e}_k \otimes \mathbf{e}_l] \cdot [\mathcal{T}_{mn\ldots op} \, \mathbf{e}_m \otimes \mathbf{e}_n \ldots \otimes \mathbf{e}_o \otimes \mathbf{e}_p] \\ &= \mathcal{S}_{ij\ldots kl} \, \mathcal{T}_{ln\ldots op} \, \mathbf{e}_i \otimes \mathbf{e}_j \ldots \otimes \mathbf{e}_k \otimes \mathbf{e}_n \ldots \otimes \mathbf{e}_o \otimes \mathbf{e}_p \,, \end{aligned} \tag{2.2a}$$

$$\begin{aligned} \boldsymbol{\mathcal{S}} : \boldsymbol{\mathcal{T}} &= [\mathcal{S}_{ij\ldots kl} \, \mathbf{e}_i \otimes \mathbf{e}_j \ldots \otimes \mathbf{e}_k \otimes \mathbf{e}_l] : [\mathcal{T}_{mn\ldots op} \, \mathbf{e}_m \otimes \mathbf{e}_n \ldots \otimes \mathbf{e}_o \otimes \mathbf{e}_p] \\ &= \mathcal{S}_{ij\ldots kl} \, \mathcal{T}_{kl\ldots op} \, \mathbf{e}_i \otimes \mathbf{e}_j \ldots \otimes \mathbf{e}_o \otimes \mathbf{e}_p \,. \end{aligned} \tag{2.2b}$$

Definition 4. **(Outer tensor products)** Given arbitrary tensors $\boldsymbol{\mathcal{S}}$ and $\boldsymbol{\mathcal{T}}$, their standard outer product (dyadic product) is defined as

$$\begin{aligned} \boldsymbol{\mathcal{S}} \otimes \boldsymbol{\mathcal{T}} &= [\mathcal{S}_{ij\ldots kl} \, \mathbf{e}_i \otimes \mathbf{e}_j \ldots \otimes \mathbf{e}_k \otimes \mathbf{e}_l] \otimes [\mathcal{T}_{mn\ldots op} \, \mathbf{e}_m \otimes \mathbf{e}_n \ldots \otimes \mathbf{e}_o \otimes \mathbf{e}_p] \\ &= \mathcal{S}_{ij\ldots kl} \, \mathcal{T}_{mn\ldots op} \, \mathbf{e}_i \otimes \mathbf{e}_j \ldots \otimes \mathbf{e}_k \otimes \mathbf{e}_l \otimes \mathbf{e}_m \otimes \mathbf{e}_n \ldots \otimes \mathbf{e}_o \otimes \mathbf{e}_p \,, \end{aligned} \tag{2.3a}$$

Additionally, two non-standard dyadic products are employed

$$\begin{aligned}\boldsymbol{\mathcal{S}}\overline{\otimes}\boldsymbol{\mathcal{T}} &= [\mathcal{S}_{ij\ldots kl}\,\mathbf{e}_i\otimes\mathbf{e}_j\ldots\otimes\mathbf{e}_k\otimes\mathbf{e}_l]\,\overline{\otimes}\,[\mathcal{T}_{mn\ldots op}\,\mathbf{e}_m\otimes\mathbf{e}_n\ldots\otimes\mathbf{e}_o\otimes\mathbf{e}_p]\\ &= \mathcal{S}_{ij\ldots km}\,\mathcal{T}_{ln\ldots op}\,\mathbf{e}_i\otimes\mathbf{e}_j\ldots\otimes\mathbf{e}_k\otimes\mathbf{e}_l\otimes\mathbf{e}_m\otimes\mathbf{e}_n\ldots\otimes\mathbf{e}_o\otimes\mathbf{e}_p\,, \qquad (2.3b)\\ \boldsymbol{\mathcal{S}}\underline{\otimes}\boldsymbol{\mathcal{T}} &= [\mathcal{S}_{ij\ldots kl}\,\mathbf{e}_i\otimes\mathbf{e}_j\ldots\otimes\mathbf{e}_k\otimes\mathbf{e}_l]\,\underline{\otimes}\,[\mathcal{T}_{mn\ldots op}\,\mathbf{e}_m\otimes\mathbf{e}_n\ldots\otimes\mathbf{e}_o\otimes\mathbf{e}_p]\\ &= \mathcal{S}_{ij\ldots kn}\,\mathcal{T}_{lm\ldots op}\,\mathbf{e}_i\otimes\mathbf{e}_j\ldots\otimes\mathbf{e}_k\otimes\mathbf{e}_l\otimes\mathbf{e}_m\otimes\mathbf{e}_n\ldots\otimes\mathbf{e}_o\otimes\mathbf{e}_p\,. \qquad (2.3c)\end{aligned}$$

Definition 5 (**Tensor transposition**). The transpose of a second-order tensor $\boldsymbol{T}$ is defined such that, for all vectors $\boldsymbol{a},\boldsymbol{b}\in\mathbb{R}^d$,

$$\boldsymbol{a}\cdot\boldsymbol{T}\cdot\boldsymbol{b}=\boldsymbol{b}\cdot\boldsymbol{T}^{\mathrm{t}}\cdot\boldsymbol{a}\,. \qquad (2.4a)$$

Accordingly, the transpose of $\boldsymbol{T}$ has the Cartesian representation

$$\boldsymbol{T}^{\mathrm{t}}=T_{ji}\,\mathbf{e}_i\otimes\mathbf{e}_j=T_{ij}\,\mathbf{e}_j\otimes\mathbf{e}_i\,. \qquad (2.4b)$$

For a fourth-order tensor T, major transposition and minor transposition read, respectively

$$\begin{aligned}\boldsymbol{S}:\mathsf{T}:\boldsymbol{T} &= \boldsymbol{T}:\mathsf{T}^{\mathrm{T}}:\boldsymbol{S}\,, \qquad (2.4c)\\ \boldsymbol{S}:\mathsf{T}:\boldsymbol{T} &= \boldsymbol{S}:\mathsf{T}^{\mathrm{t}}:\boldsymbol{T}^{\mathrm{t}}\,, \qquad (2.4d)\end{aligned}$$

for all second-order tensors $\boldsymbol{T},\boldsymbol{S}\in\mathbb{R}^{d\times d}$. Moreover, Cartesian representations of the symmetric fourth-order tensors are expressed as

$$\begin{aligned}\mathsf{T}^{\mathrm{T}} &= T_{klij}\,\mathbf{e}_i\otimes\mathbf{e}_j\otimes\mathbf{e}_k\otimes\mathbf{e}_l\,, \qquad (2.4e)\\ \mathsf{T}^{\mathrm{t}} &= T_{ijlk}\,\mathbf{e}_i\otimes\mathbf{e}_j\otimes\mathbf{e}_k\otimes\mathbf{e}_l\,. \qquad (2.4f)\end{aligned}$$

Definition 6. **(Symmetric tensors)** With the definition of tensor transpositions at hand, a second-order symmetric tensor $\boldsymbol{T}$ accordingly reads

$$\boldsymbol{T}=\boldsymbol{T}^{\mathrm{t}}=\boldsymbol{T}^{\mathrm{sym}}\,. \qquad (2.5a)$$

A symmetric fourth-order tensor that has major symmetries and minor symmetries are defined as

$$\begin{aligned}\mathsf{T} &= \mathsf{T}^{\mathrm{T}}=\mathsf{T}^{\mathrm{SYM}}\,, \qquad (2.5b)\\ \mathsf{T} &= \mathsf{T}^{\mathrm{t}}=\mathsf{T}^{\mathrm{sym}}\,. \qquad (2.5c)\end{aligned}$$

In this work, a symmetric fourth-order tensor $\mathsf{T}^{\mathrm{Sym}}$ is defined as a fourth-order tensor that possesses both major and minor symmetries.

Definition 7. **(Identity tensors)** The second-order identity tensor is defined via the Kronecker delta symbol, namely

$$\boldsymbol{I}=\delta_{ij}\,\mathbf{e}_i\otimes\mathbf{e}_j\,,\qquad \delta_{ij}=\begin{cases}1\,, & \text{if } i=j\\ 0\,, & \text{if } i\neq j\end{cases}\,. \qquad (2.6a)$$

The fourth-order identity tensor follows as

$$\mathsf{I} = \boldsymbol{I} \,\overline{\otimes}\, \boldsymbol{I} \,. \tag{2.6b}$$

The deviatoric projection of the fourth-order identity tensor reads

$$\mathsf{I}^{\mathrm{dev}} = \boldsymbol{I} \,\overline{\otimes}\, \boldsymbol{I} - \frac{1}{3}\, \boldsymbol{I} \otimes \boldsymbol{I} \,. \tag{2.6c}$$

Definition 8. **(Permutation tensor)** The third-order permutation tensor (Levi–Civita symbol), is given by

$$\boldsymbol{\epsilon} = \epsilon_{ijk}\, \mathbf{e}_i \otimes \mathbf{e}_j \otimes \mathbf{e}_k \,,\ \epsilon_{ijk} = \begin{cases} +1\,, & \text{for even permutations of } i,j,k;\ \text{i.e. } (123, 231, 312) \\ -1\,, & \text{for odd permutations of } i,j,k;\ \text{i.e. } (132, 213, 321) \\ 0\,, & \text{if there is a repeated index} \end{cases} \tag{2.7}$$

with the properties $\epsilon_{ijk} = \epsilon_{jki} = \epsilon_{kij}$, $\epsilon_{ijk} = -\epsilon_{ikj}$ and $\epsilon_{ijk} = -\epsilon_{jik}$.

Definition 9. **(Vector (cross) product)** With the definition of permutation tensor at hand, the vector (cross) product of $\boldsymbol{u}$ and $\boldsymbol{v}$ is defined as

$$\boldsymbol{u} \times \boldsymbol{v} = \boldsymbol{\epsilon} : [\boldsymbol{u} \otimes \boldsymbol{v}] \,. \tag{2.8}$$

The vector product of two vectors produces a vector. Note that the vector product is not commutative.

Definition 10. **(Gradient operator)** The gradient operator, denoted by $\nabla_x \bullet$, operates with respect to the variable $\boldsymbol{x}$

$$\nabla_{\boldsymbol{x}} \boldsymbol{\mathcal{T}} = \frac{\partial\, \mathcal{T}_{ij\ldots kl}}{\partial\, x_m}\, \mathbf{e}_i \otimes \mathbf{e}_j \ldots \otimes \mathbf{e}_k \otimes \mathbf{e}_l \otimes \mathbf{e}_m \,. \tag{2.9}$$

Definition 11. **(Divergence operator)** The divergence operator is defined via the gradient

$$\nabla_x \cdot \boldsymbol{\mathcal{T}} = \nabla_x \boldsymbol{\mathcal{T}} : \boldsymbol{I} = \frac{\partial\, \mathcal{T}_{ij\ldots kl}}{\partial\, x_l}\, \mathbf{e}_i \otimes \mathbf{e}_j \ldots \mathbf{e}_k \,. \tag{2.10}$$

Definition 12. **(Curl operator)** The curl of a vector field is introduced as

$$\nabla_x \times \boldsymbol{u} = \boldsymbol{\epsilon} : \nabla_x \boldsymbol{u} = \epsilon_{ijk}\, \frac{\partial\, u_k}{\partial\, x_j}\, \mathbf{e}_i \,. \tag{2.11}$$

2.1.2 Elements of functional analysis

Definition 13. **(Normed vector space)** A normed vector space X is a vector space equipped with a norm $\|\bullet\| : X \to \mathbb{R}$ satisfying the following properties for all $\boldsymbol{u}, \boldsymbol{v} \in X$ and $\alpha \in \mathbb{R}$

1. $\|\boldsymbol{u}\| \geq 0$ with $\|\boldsymbol{u}\| = 0 \iff \boldsymbol{u} = \boldsymbol{0}$,
2. $\|\alpha\, \boldsymbol{u}\| = |\alpha| \|\boldsymbol{u}\|$,
3. $\|\boldsymbol{u} + \boldsymbol{v}\| \leq \|\boldsymbol{u}\| + \|\boldsymbol{v}\|$.

Definition 14. **(Banach space)** A Banach space is a complete normed vector space. The $d-$dimensional Euclidean space $\mathbb{R}^d$ equipped with the one-norm $\|\bullet\|_1$, the 2-norm $\|\bullet\|_2$, the supremum norm $\|\bullet\|_\infty$ are, for instance, Banach spaces.

Definition 15. **(Inner product space)** An inner product space X is a vector space equipped with an inner product $(\bullet, \bullet) : X \times X \to \mathbb{R}$ that satisfies the following properties for all $\boldsymbol{u}, \boldsymbol{v}, \boldsymbol{w} \in X$ and scalars $\alpha, \beta \in \mathbb{R}$:

1. $(\boldsymbol{u}, \boldsymbol{v}) = (\boldsymbol{v}, \boldsymbol{u})$,
2. $(\alpha\, \boldsymbol{u} + \beta\, \boldsymbol{v}, \boldsymbol{w}) = \alpha\, (\boldsymbol{u}, \boldsymbol{w}) + \beta\, (\boldsymbol{v}, \boldsymbol{w})$,
3. $(\boldsymbol{u}, \boldsymbol{u}) \geq 0$ with $(\boldsymbol{u}, \boldsymbol{u}) = 0 \iff \boldsymbol{u} = \boldsymbol{0}$.

An inner product induces a norm, $\|\boldsymbol{u}\| = \sqrt{(\boldsymbol{u}, \boldsymbol{u})}$, and hence a metric.

Definition 16. **(Hilbert space)** A Hilbert space X is a complete inner product space. For example, the space of square-integrable functions on domain $L^2\,(\Omega)$ with the associated norm

$$(\boldsymbol{u}, \boldsymbol{v})_{L^2(\Omega)} = \int_\Omega \boldsymbol{u} \cdot \boldsymbol{v}\, \mathrm{d}x\,, \tag{2.12}$$

is a Hilbert space with an inner product. Similarly, the space $H_0^1\,(\Omega)$ of square-integrable functions that has compact support and have square integrable derivatives

$$(\boldsymbol{u}, \boldsymbol{v})_{H_0^1(\Omega)} = \int_\Omega \boldsymbol{u} \cdot \boldsymbol{v} + \nabla_x \boldsymbol{u} \cdot \nabla_x \boldsymbol{v}\, \mathrm{d}x\,, \tag{2.13}$$

is a Hilbert space with an inner product.

Definition 17. **(Bounded linear functional)** Let X be a Hilbert space. A linear functional j on X is a function $j : X \to \mathbb{R}$ satisfying

$$j\,(\alpha\, \boldsymbol{u} + \beta\, \boldsymbol{v}) = \alpha\, j\,(\boldsymbol{u}) + \beta\, j\,(\boldsymbol{v})\ , \quad \text{for all } \boldsymbol{u}, \boldsymbol{v} \in X \text{ and } \alpha, \beta \in \mathbb{R}\,. \tag{2.14}$$

Furthermore, a linear functional j is said to be bounded if there exists a constant $L \in [0, \infty)$ such that

$$|j\,(\boldsymbol{u})| \leq L \|\boldsymbol{u}\|_X \quad \text{for all } \boldsymbol{u} \in X\,. \tag{2.15}$$

Definition 18. **(Dual of Hilbert space)** The dual X^* of a Hilbert space X is the space of all bounded linear functionals on X.

Definition 19. **(Lebesgue space)** For $p \in [1, \infty)$, the Lebesgue space L^p is defined by

$$L^p(\Omega) = \{\boldsymbol{u} : \Omega \to \mathbb{R} : \|\boldsymbol{u}\|_{L^p(\Omega)} < \infty\} \tag{2.16}$$

with the norm

$$\|\boldsymbol{u}\|_{L^p(\Omega)} = \left[\int_\Omega |\boldsymbol{u}|^p \, \mathrm{d}x\right]^{1/p} . \tag{2.17}$$

Definition 20. **(Multi-index)** A multi-index $\boldsymbol{\alpha}$ is a tuple of k non-negative integers, i.e. $\boldsymbol{\alpha} = (\alpha_1, \ldots, \alpha_k)$.

Definition 21. **(Weak derivative)** Let $\Omega \subset \mathbb{R}^d$. A function $f \in L^1_{\mathrm{loc}}(\Omega)$ has a weak derivative $D^\alpha f$, if there exists a function $g \in L^1_{\mathrm{loc}}$ such that

$$\int_\Omega F\, g \, \mathrm{d}x = [-1]^{|\alpha|} \int_\Omega f\, D^\alpha F \, \mathrm{d}x \quad \text{for all } F \in C_0^\infty(\Omega) . \tag{2.18}$$

Definition 22. **(Sobolev space)** Let k be a non-negative integer and $p \in [1, \infty)$. Suppose that weak derivatives $D^{\boldsymbol{\alpha}}_k f$ exist for all $|\boldsymbol{\alpha}| \leq k$. The Sobolev space $W^k_p(\Omega)$ is defined by

$$W^k_p(\Omega) = \{f \in L^p(\Omega) : \|f\|_{W^p_k(\Omega)} < \infty\} \tag{2.19}$$

which is equipped with the norm

$$\|\boldsymbol{u}\|_{W^k_p(\Omega)} = \left[\sum_{|\boldsymbol{\alpha}| \leq k} \|D^{\boldsymbol{\alpha}} \boldsymbol{u}\|^p_{L^p(\Omega)}\right]^{1/p} . \tag{2.20}$$

Definition 23. **(Periodic function spaces)** Let $\Omega \subset \mathbb{R}^d$ be a fixed periodic cell (or lattice fundamental domain) and denote by

$$\Lambda = \{\, z \in \mathbb{R}^d : z = k_1 e_1 + \cdots + k_d e_d,\ k_i \in \mathbb{Z} \,\}$$

the lattice of period-shifts. A measurable function $u : \mathbb{R}^d \to \mathbb{R}$ is called Ω–periodic if

$$u(x + z) = u(x) \quad \text{for a.e. } x \in \mathbb{R}^d \quad \text{and every } z \in \Lambda.$$

We then define

$$L^2_\#(\Omega) = \{\, u \in L^2_{\mathrm{loc}}(\mathbb{R}^d) \colon u \text{ is } \Omega\text{–periodic}\},$$

and

$$H^1_\#(\Omega) = \{\, u \in H^1_{\mathrm{loc}}(\mathbb{R}^d) \colon u \text{ is } \Omega\text{–periodic}\},$$

both equipped with the associated norms.

Remark 1. For all $p \in [1, \infty)$ and all k, $W^k_p(\Omega)$ is a Banach space. For the special case of $p = 2$, $H^k(\Omega) \coloneqq W^k_2(\Omega)$ is a Hilbert space.

2.2 Balance equations and related kinematics

With the fundamentals of tensor notation and elements of functional analysis established, we now turn to the physical laws that govern coupled thermo-electro-mechanical systems. In this section, the balance equations governing thermo-electro-mechanically coupled systems are presented within the framework of small-strain theory. In the context of continuum thermo-electrodynamics, these balance laws emerge from the combination of fundamental electromagnetic field equations and classical thermomechanical principles. The electromagnetic component is described by Maxwell's equations, while the thermomechanical part is governed by the following fundamental laws

1. Conservation of mass
2. Balance of linear momentum
3. Balance of angular (moment of) momentum
4. Balance of energy
5. Entropy inequality

For a comprehensive overview and further details beyond those presented here, the reader is referred to the classical texts [45, 46, 85].

The derivation of the balance equations is carried out for a continuum as sketched in Figure 2.1. Let $\Omega \subset \mathbb{R}^d$ be a bounded Lipschitz domain with boundary $\partial\Omega$. We consider the family of admissible control volumes

$$\mathcal{V} =: \{\, \omega \subseteq \Omega \;\mid\; \omega \text{ open, bounded, Lipschitz} \,\}. \tag{2.21}$$

For a bounded domain Ω representing a closed system, mass is a conserved quantity. Consequently conservation of mass reads in the integral form,

$$\frac{\mathrm{d}}{\mathrm{d}t} \int_\Omega \rho\,(\boldsymbol{x})\; \mathrm{d}x = \int_\Omega \frac{\mathrm{d}\rho\,(\boldsymbol{x})}{\mathrm{d}t}\, \mathrm{d}x + \int_{\partial\Omega} \boldsymbol{n}\,(\boldsymbol{x}) \cdot \dot{\boldsymbol{u}}\,(\boldsymbol{x})\, \rho\,(\boldsymbol{x})\; \mathrm{d}x = 0 \tag{2.22}$$

where $\rho : \Omega \to \mathbb{R}$ is the mass density per unit volume, $\boldsymbol{n} : \Omega \to \mathbb{R}^d$ is the outward unit surface normal to domain Ω and $\boldsymbol{u} : \Omega \to \mathbb{R}^d$ is the displacement vector. The integral statement (2.22) is an instance of the global conservation laws and is understood to hold not only for Ω, but equally for any $\omega \in \mathcal{V}$. Localising these balance equations for arbitrary $\omega \in \mathcal{V}$ by using the divergence theorem results in the pointwise form

$$\dot{\rho}\,(\boldsymbol{x}) + \rho\,(\boldsymbol{x})\, \nabla_x \cdot \dot{\boldsymbol{u}}\,(\boldsymbol{x}) = 0 \quad \text{in } \Omega \tag{2.23}$$

with $\dot{\bullet}$ representing the time derivative of a quantity.

Remark 2. Throughout this thesis, the domain Ω and spatial coordinates $\boldsymbol{x}$ refer to the macroscale problem. When a multiscale setting is considered, the microscale domain is denoted by Y with local coordinates $\boldsymbol{y}$. In single scale problems, Ω and $\boldsymbol{x}$ are used exclusively. Gradient, divergence, and curl operators are written as ∇_x, $\nabla_x \cdot$, and $\nabla_x \times$, respectively. A non-bold notation for $\boldsymbol{x}$ is adopted to maintain consistency across scalar and vectorial quantities in different spatial dimensions.

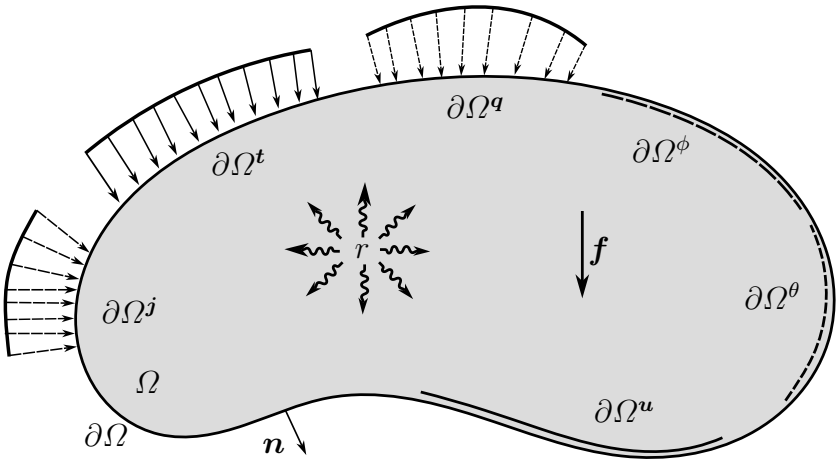

Figure 2.1: Control volume Ω under consideration.

2.2.1 Mechanical subproblem: Balance of linear and angular momentum

The mechanical response is governed by the balance equation of linear momentum

$$\frac{\mathrm{d}}{\mathrm{d}t}\int_{\Omega}\rho\left(\boldsymbol{x}\right)\dot{\boldsymbol{u}}\left(\boldsymbol{x}\right)\,\mathrm{d}x=\int_{\Omega}\rho\left(\boldsymbol{x}\right)\boldsymbol{f}\left(\boldsymbol{x}\right)\,\mathrm{d}x+\int_{\partial\Omega}\boldsymbol{t}\left(\boldsymbol{x}\right)\,\mathrm{d}x\,. \tag{2.24}$$

The volume under consideration is loaded by volume distributed body forces $\boldsymbol{f}:\Omega\rightarrow\mathbb{R}^{d}$ and subjected to surface tractions, $\boldsymbol{t}:\Omega\rightarrow\mathbb{R}^{d}$

$$\boldsymbol{t}\left(\boldsymbol{x}\right)=\boldsymbol{\sigma}\left(\boldsymbol{x}\right)\cdot\boldsymbol{n}\left(\boldsymbol{x}\right), \tag{2.25}$$

where $\boldsymbol{\sigma}:\Omega\rightarrow\mathrm{Lin}\left(\mathbb{R}^{d},\mathbb{R}^{d}\right)$ denotes the Cauchy stress tensor which maps the normal to a surface to the traction vector acting on that surface. By applying the divergence theorem, one can obtain the local form of (2.24)

$$\rho\left(\boldsymbol{x}\right)\ddot{\boldsymbol{u}}\left(\boldsymbol{x}\right)=\nabla_{x}\cdot\boldsymbol{\sigma}\left(\boldsymbol{x}\right)+\rho\left(\boldsymbol{x}\right)\boldsymbol{f}\left(\boldsymbol{x}\right)\qquad\text{in }\Omega\,. \tag{2.26}$$

In analogy with balance of linear momentum, balance of angular momentum reads

$$\frac{\mathrm{d}}{\mathrm{d}t}\int_{\Omega}\boldsymbol{x}\times\rho\left(\boldsymbol{x}\right)\dot{\boldsymbol{u}}\left(\boldsymbol{x}\right)\,\mathrm{d}x=\int_{\Omega}\boldsymbol{x}\times\rho\left(\boldsymbol{x}\right)\boldsymbol{f}\left(\boldsymbol{x}\right)\,\mathrm{d}x+\int_{\partial\Omega}\boldsymbol{x}\times\boldsymbol{t}\left(\boldsymbol{x}\right)\,\mathrm{d}x\,. \tag{2.27}$$

Localisation of balance of angular momentum gives rise to the classic symmetry condition of the stress tensor

$$\boldsymbol{\epsilon}:\boldsymbol{\sigma}\left(\boldsymbol{x}\right)=\boldsymbol{0}\quad\rightarrow\quad\boldsymbol{\sigma}:\Omega\rightarrow\mathrm{Sym}\left(\mathbb{R}^{d\times d}\right). \tag{2.28}$$

2.2.2 Electrical subproblem: Continuity equation for electric charge

In the context of electrical processes, the general electromagnetic problem simplifies to the continuity equation for the electric charge

$$-\frac{\mathrm{d}}{\mathrm{d}t}\int_{\Omega}\rho_{\mathrm{f}}\left(\boldsymbol{x}\right)\,\mathrm{d}x=\int_{\partial\Omega}\boldsymbol{j}\left(\boldsymbol{x}\right)\cdot\boldsymbol{n}\left(\boldsymbol{x}\right)\,\mathrm{d}x\,, \tag{2.29a}$$

and to Faraday's law of induction

$$-\frac{\mathrm{d}}{\mathrm{d}t}\int_{\mathcal{A}} \boldsymbol{b}\left(\boldsymbol{x}\right)\cdot\boldsymbol{n}\left(\boldsymbol{x}\right)\,\mathrm{d}x = \int_{\partial\mathcal{A}} \boldsymbol{e}\left(\boldsymbol{x}\right)\cdot\,\mathrm{d}x\,, \tag{2.29b}$$

where $\rho_{\mathrm{f}} : \Omega \to \mathbb{R}$ denotes the free charge density, $\boldsymbol{j} : \Omega \to \mathbb{R}^d$, $\boldsymbol{e} : \Omega \to \mathbb{R}^d$, $\boldsymbol{b} : \Omega \to \mathbb{R}^d$ represent the electric current density vector, the electric field vector and the magnetic flux density vector, respectively. Moreover, $\boldsymbol{n} : \Omega \to \mathbb{R}^d$ is the outward unit surface normal to domain Ω, and $\partial\mathcal{A}$ is the boundary curve to an arbitrary surface $\mathcal{A} \subset \mathbb{R}^d$. Localisation of the set of equations (2.29) results in

$$\nabla_x\cdot\boldsymbol{j}\left(\boldsymbol{x}\right) + \dot{\rho}_{\mathrm{f}}\left(\boldsymbol{x}\right) = 0 \qquad \text{in } \Omega\,, \tag{2.30a}$$

$$\nabla_x\times\boldsymbol{e}\left(\boldsymbol{x}\right) = -\dot{\boldsymbol{b}}\left(\boldsymbol{x}\right) \qquad \text{in } \Omega\,, \tag{2.30b}$$

with (2.30b) being naturally fulfilled by the introduction of a scalar-valued electric potential field $\phi : \Omega \to \mathbb{R}$ such that $\boldsymbol{e}\left(\boldsymbol{x}\right) = -\nabla_x\phi\left(\boldsymbol{x}\right)$.

2.2.3 Thermal subproblem: Conservation of energy

The balance equation of energy governs the temperature evolution and is given by

$$\frac{\mathrm{d}}{\mathrm{d}t}\int_{\Omega}\rho\left(\boldsymbol{x}\right)\,e\left(\boldsymbol{x}\right)\,\mathrm{d}x + \frac{\mathrm{d}}{\mathrm{d}t}\int_{\Omega}\frac{1}{2}\rho\left(\boldsymbol{x}\right)\dot{\boldsymbol{u}}\left(\boldsymbol{x}\right)\cdot\dot{\boldsymbol{u}}\left(\boldsymbol{x}\right)\,\mathrm{d}x = \mathcal{P}^{\boldsymbol{u}} + \mathcal{P}^{\phi} + \mathcal{P}^{\theta} \tag{2.31}$$

where $e : \Omega \to \mathbb{R}$ is the mass-specific internal energy density. The respective contributions to (2.31) are specified as the external mechanical power

$$\begin{aligned}\mathcal{P}^{\boldsymbol{u}} &= \int_{\Omega}\dot{\boldsymbol{u}}\left(\boldsymbol{x}\right)\cdot\rho\left(\boldsymbol{x}\right)\boldsymbol{f}\left(\boldsymbol{x}\right)\,\mathrm{d}x + \int_{\partial\Omega}\dot{\boldsymbol{u}}\left(\boldsymbol{x}\right)\cdot\boldsymbol{t}\left(\boldsymbol{x}\right)\,\mathrm{d}x\\ &= \int_{\Omega}\nabla\dot{\boldsymbol{u}}\left(\boldsymbol{x}\right):\boldsymbol{\sigma}\left(\boldsymbol{x}\right)\,\mathrm{d}x + \int_{\Omega}\dot{\boldsymbol{u}}\left(\boldsymbol{x}\right)\cdot\left[\nabla_x\cdot\boldsymbol{\sigma}\left(\boldsymbol{x}\right) + \rho\left(\boldsymbol{x}\right)\boldsymbol{f}\left(\boldsymbol{x}\right)\right]\,\mathrm{d}x\,,\end{aligned} \tag{2.32a}$$

the external electrical power

$$\mathcal{P}^{\phi} = \int_{\Omega}\boldsymbol{j}\left(\boldsymbol{x}\right)\cdot\boldsymbol{e}\left(\boldsymbol{x}\right)\,\mathrm{d}x\,, \tag{2.32b}$$

and external thermal power,

$$\mathcal{P}^{\theta} = -\int_{\partial\Omega}\boldsymbol{q}\left(\boldsymbol{x}\right)\cdot\boldsymbol{n}\left(\boldsymbol{x}\right)\,\mathrm{d}x + \int_{\Omega}r\left(\boldsymbol{x}\right)\,\mathrm{d}x\,, \tag{2.32c}$$

where $r : \Omega \to \mathbb{R}$ denotes the heat source per unit volume, and $\boldsymbol{q} : \Omega \to \mathbb{R}^d$ is the heat flux vector. Equation (2.31) states that the rate of change of the sum of internal and kinetic energy over time t arises from mechanical, electrical, and thermal contributions. Localising (2.31), with the definition of strain tensor $\boldsymbol{\varepsilon} : \Omega \to \mathrm{Sym}\left(\mathbb{R}^{d\times d}\right)$

$$\boldsymbol{\varepsilon}\left(\boldsymbol{x}\right) = \left[\nabla_x\boldsymbol{u}\left(\boldsymbol{x}\right)\right]^{\mathrm{sym}} = \frac{1}{2}\left[\nabla_x\boldsymbol{u}\left(\boldsymbol{x}\right) + \left[\nabla_x\boldsymbol{u}\left(\boldsymbol{x}\right)\right]^{\mathrm{t}}\right] \tag{2.33}$$

while assuming a (quasi-)stationary problem setting yields

$$\rho\left(\boldsymbol{x}\right)\dot{e}\left(\boldsymbol{x}\right)=\boldsymbol{\sigma}\left(\boldsymbol{x}\right):\dot{\boldsymbol{\varepsilon}}\left(\boldsymbol{x}\right)-\nabla_{x}\cdot\boldsymbol{q}\left(\boldsymbol{x}\right)+r\left(\boldsymbol{x}\right)+\boldsymbol{j}\left(\boldsymbol{x}\right)\cdot\boldsymbol{e}\left(\boldsymbol{x}\right)\qquad\text{in }\Omega\,. \tag{2.34}$$

The electrical contribution $\boldsymbol{j}\cdot\boldsymbol{e}$ in (2.34) is purely dissipative and acts as a heat source driving the temperature evolution. This effect is typically referred to as Joule heating.

2.2.4 Dissipation inequality: The second law of thermodynamics

Furthermore, introducing mass-specific entropy density $s:\Omega\to\mathbb{R}$ and absolute temperature $\theta:\Omega\to\mathbb{R}^{+}$, the dissipation inequality takes the form

$$\frac{\mathrm{d}}{\mathrm{d}t}\int_{\Omega}\rho\left(\boldsymbol{x}\right)\,s\left(\boldsymbol{x}\right)\,\mathrm{d}x\geq\int_{\Omega}\frac{r\left(\boldsymbol{x}\right)}{\theta\left(\boldsymbol{x}\right)}\,\mathrm{d}x-\int_{\partial\Omega}\frac{\boldsymbol{q}\left(\boldsymbol{x}\right)\cdot\boldsymbol{n}\left(\boldsymbol{x}\right)}{\theta\left(\boldsymbol{x}\right)}\,\mathrm{d}x\,. \tag{2.35}$$

By using Gauß's theorem, the dissipation inequality (2.35),

$$\rho\left(\boldsymbol{x}\right)\dot{s}\left(\boldsymbol{x}\right)\geq\frac{r\left(\boldsymbol{x}\right)}{\theta\left(\boldsymbol{x}\right)}-\frac{1}{\theta\left(\boldsymbol{x}\right)}\nabla_{x}\cdot\boldsymbol{q}\left(\boldsymbol{x}\right)+\frac{1}{\theta\left(\boldsymbol{x}\right)}\boldsymbol{q}\left(\boldsymbol{x}\right)\cdot\nabla_{x}\ln\left(\theta\left(\boldsymbol{x}\right)\right) \tag{2.36}$$

is obtained in the local form. After rearranging, (2.36) can be written in the form, which is commonly referred as Clausius–Duhem inequality (CDI)

$$\underbrace{\rho\left(\boldsymbol{x}\right)\theta\left(\boldsymbol{x}\right)\dot{s}\left(\boldsymbol{x}\right)-r\left(\boldsymbol{x}\right)+\nabla_{x}\cdot\boldsymbol{q}\left(\boldsymbol{x}\right)-\boldsymbol{q}\left(\boldsymbol{x}\right)\cdot\nabla_{x}\ln\left(\theta\left(\boldsymbol{x}\right)\right)}_{:=\mathcal{D}}\geq0\,. \tag{2.37}$$

By inserting the energy equation (2.34) into (2.37), the local form of the dissipation inequality

$$\rho\left(\boldsymbol{x}\right)\theta\left(\boldsymbol{x}\right)\dot{s}\left(\boldsymbol{x}\right)-\rho\left(\boldsymbol{x}\right)\dot{e}\left(\boldsymbol{x}\right)+\boldsymbol{\sigma}\left(\boldsymbol{x}\right):\dot{\boldsymbol{\varepsilon}}\left(\boldsymbol{x}\right)+\boldsymbol{j}\left(\boldsymbol{x}\right)\cdot\boldsymbol{e}\left(\boldsymbol{x}\right)-\boldsymbol{q}\left(\boldsymbol{x}\right)\cdot\nabla_{x}\ln\left(\theta\left(\boldsymbol{x}\right)\right)\geq0 \tag{2.38}$$

is obtained with the intrinsic, electrical and thermal parts

$$\mathcal{D}=\mathcal{D}_{\mathrm{mech}}+\mathcal{D}_{\mathrm{elec}}+\mathcal{D}_{\mathrm{therm}}\geq0\,. \tag{2.39}$$

Accordingly, we impose the stronger requirement that each term be non-negative, i.e.

$$\mathcal{D}_{\mathrm{mech}}=\rho\left(\boldsymbol{x}\right)\theta\left(\boldsymbol{x}\right)\dot{s}\left(\boldsymbol{x}\right)-\rho\left(\boldsymbol{x}\right)\dot{e}\left(\boldsymbol{x}\right)+\boldsymbol{\sigma}\left(\boldsymbol{x}\right):\dot{\boldsymbol{\varepsilon}}\left(\boldsymbol{x}\right)\geq0\,, \tag{2.40a}$$

$$\mathcal{D}_{\mathrm{elec}}=\boldsymbol{j}\left(\boldsymbol{x}\right)\cdot\boldsymbol{e}\left(\boldsymbol{x}\right)\geq0\,, \tag{2.40b}$$

$$\mathcal{D}_{\mathrm{therm}}=-\boldsymbol{q}\left(\boldsymbol{x}\right)\cdot\nabla_{x}\ln\left(\theta\left(\boldsymbol{x}\right)\right)\geq0\,. \tag{2.40c}$$

in place of the condition in (2.37). The inequalities provide thermodynamic constraints that must be satisfied by the constitutive relations for the mechanical, electrical and thermal subproblems, respectively. Relation (2.40a) is related to the Clausius–Planck inequality, and (2.40b)-(2.40c) constrain the form of the conduction relations.

Moreover, by defining the mass-specific Helmholtz free energy via the Legendre–Fenchel transform

$$\psi\left(\boldsymbol{\varepsilon},\theta,k\right)=\inf\left\{e(\boldsymbol{\varepsilon},s,k)-\theta\,s\right\} \tag{2.41}$$

with the functional dependence of the free energy density function $\psi(\boldsymbol{\varepsilon}, \theta, k)$ on strain, temperature and (possibly a set of) internal variables $k : \Omega \to \mathbb{R}^n$, where n is a non-negative integer. The time derivative of the mass-specific Helmholtz free energy can be expressed as

$$\dot{\psi}\left(\boldsymbol{\varepsilon}\left(\boldsymbol{x}\right), \theta\left(\boldsymbol{x}\right), k\left(\boldsymbol{x}\right)\right) = \dot{e}\left(\boldsymbol{x}\right) - \dot{\theta}\left(\boldsymbol{x}\right) s\left(\boldsymbol{x}\right) - \dot{s}\left(\boldsymbol{x}\right) \theta\left(\boldsymbol{x}\right) . \tag{2.42}$$

By inserting (2.42) into (2.40a), the local (intrinsic) dissipation inequality

$$\mathcal{D}_{\text{mech}} = \boldsymbol{\sigma}\left(\boldsymbol{x}\right) : \dot{\boldsymbol{\varepsilon}}\left(\boldsymbol{x}\right) - \rho\left(\boldsymbol{x}\right) \left[\dot{\psi}\left(\boldsymbol{x}\right) + s\left(\boldsymbol{x}\right) \dot{\theta}\left(\boldsymbol{x}\right)\right] \geq 0 \qquad \text{in } \Omega \tag{2.43}$$

is eventually obtained. Differentiating the mass-specific Helmholtz free energy with respect to time with the functional dependencies

$$\dot{\psi}\left(\boldsymbol{\varepsilon}\left(\boldsymbol{x}\right), \theta\left(\boldsymbol{x}\right), k\left(\boldsymbol{x}\right)\right) = \frac{\partial \psi\left(\boldsymbol{x}\right)}{\partial \boldsymbol{\varepsilon}\left(\boldsymbol{x}\right)} : \dot{\boldsymbol{\varepsilon}}\left(\boldsymbol{x}\right) + \frac{\partial \psi\left(\boldsymbol{x}\right)}{\partial \theta\left(\boldsymbol{x}\right)} \dot{\theta}\left(\boldsymbol{x}\right) + \frac{\partial \psi\left(\boldsymbol{x}\right)}{\partial k\left(\boldsymbol{x}\right)} \dot{k}\left(\boldsymbol{x}\right) \tag{2.44}$$

and substituting (2.44) into (2.43) results in

$$\boldsymbol{\sigma}\left(\boldsymbol{x}\right) : \dot{\boldsymbol{\varepsilon}}\left(\boldsymbol{x}\right) - \rho\left(\boldsymbol{x}\right) \left[\frac{\partial \psi\left(\boldsymbol{x}\right)}{\partial \boldsymbol{\varepsilon}\left(\boldsymbol{x}\right)} : \dot{\boldsymbol{\varepsilon}}\left(\boldsymbol{x}\right) + \frac{\partial \psi\left(\boldsymbol{x}\right)}{\partial \theta\left(\boldsymbol{x}\right)} \dot{\theta}\left(\boldsymbol{x}\right) + \frac{\partial \psi\left(\boldsymbol{x}\right)}{\partial k\left(\boldsymbol{x}\right)} \dot{k}\left(\boldsymbol{x}\right) + s\left(\boldsymbol{x}\right) \dot{\theta}\left(\boldsymbol{x}\right)\right] \geq 0 . \tag{2.45}$$

After rearranging (2.45) in the form

$$\left[\boldsymbol{\sigma}\left(\boldsymbol{x}\right) - \rho\left(\boldsymbol{x}\right) \frac{\partial \psi\left(\boldsymbol{x}\right)}{\partial \boldsymbol{\varepsilon}\left(\boldsymbol{x}\right)}\right] : \dot{\boldsymbol{\varepsilon}}\left(\boldsymbol{x}\right) - \rho\left(\boldsymbol{x}\right) \left[s\left(\boldsymbol{x}\right) + \frac{\partial \psi\left(\boldsymbol{x}\right)}{\partial \theta\left(\boldsymbol{x}\right)}\right] \dot{\theta}\left(\boldsymbol{x}\right) - \rho\left(\boldsymbol{x}\right) \frac{\partial \psi\left(\boldsymbol{x}\right)}{\partial k\left(\boldsymbol{x}\right)} \dot{k}\left(\boldsymbol{x}\right) \geq 0 , \tag{2.46}$$

evaluation of the Coleman-Noll procedure yields the constitutive relations

$$\boldsymbol{\sigma} = \rho \frac{\partial \psi\left(\boldsymbol{\varepsilon}, \theta, k\right)}{\partial \boldsymbol{\varepsilon}} \qquad s = -\frac{\partial \psi\left(\boldsymbol{\varepsilon}, \theta, k\right)}{\partial \theta} \qquad \kappa = -\rho \frac{\partial \psi\left(\boldsymbol{\varepsilon}, \theta, k\right)}{\partial k} . \tag{2.47}$$

Incorporating the obtained constitutive relation for entropy (2.47) and time derivative expression of the Helmholtz free energy (2.44), i.e.

$$\begin{aligned} \rho\left(\boldsymbol{x}\right) \dot{s}\left(\boldsymbol{x}\right) &= -\frac{\mathrm{d}}{\mathrm{d}t} \left[\rho\left(\boldsymbol{x}\right) \frac{\partial \psi\left(\boldsymbol{x}\right)}{\partial \theta\left(\boldsymbol{x}\right)}\right] = \frac{\partial}{\partial \theta\left(\boldsymbol{x}\right)} \left[\rho\left(\boldsymbol{x}\right) \dot{\psi}\left(\boldsymbol{x}\right)\right] \\ &= -\frac{\partial \boldsymbol{\sigma}\left(\boldsymbol{x}\right)}{\partial \theta\left(\boldsymbol{x}\right)} : \dot{\boldsymbol{\varepsilon}}\left(\boldsymbol{x}\right) + \rho\left(\boldsymbol{x}\right) \frac{\partial s\left(\boldsymbol{x}\right)}{\partial \theta\left(\boldsymbol{x}\right)} \dot{\theta}\left(\boldsymbol{x}\right) + \frac{\partial \kappa\left(\boldsymbol{x}\right)}{\partial \theta\left(\boldsymbol{x}\right)} \dot{k}\left(\boldsymbol{x}\right) , \end{aligned} \tag{2.48}$$

into the energy equation (2.34) yields

$$\begin{aligned} \rho\left(\boldsymbol{x}\right) c_{\text{v}}\left(\boldsymbol{x}\right) \dot{\theta}\left(\boldsymbol{x}\right) + \theta\left(\boldsymbol{x}\right) \boldsymbol{\beta}_{\text{v}}\left(\boldsymbol{x}\right) : \dot{\boldsymbol{\varepsilon}}\left(\boldsymbol{x}\right) - \left[\kappa\left(\boldsymbol{x}\right) - \theta\left(\boldsymbol{x}\right) \frac{\partial \kappa\left(\boldsymbol{x}\right)}{\partial \theta\left(\boldsymbol{x}\right)}\right] \dot{k}\left(\boldsymbol{x}\right) \\ - \left[-\nabla_x \cdot \boldsymbol{q}\left(\boldsymbol{x}\right) + r\left(\boldsymbol{x}\right) + \boldsymbol{j}\left(\boldsymbol{x}\right) \cdot \boldsymbol{e}\left(\boldsymbol{x}\right)\right] = 0 \end{aligned} \tag{2.49}$$

where $c_\mathrm{v} : \Omega \to \mathbb{R}$ and $\boldsymbol{\beta}_\mathrm{v} : \Omega \to \mathbb{R}^{d\times d}$ denote the heat capacity and thermal stress respectively

$$\begin{aligned} c_\mathrm{v} &= \theta \frac{\partial s\left(\boldsymbol{\varepsilon}, \theta, k\right)}{\partial \theta} = -\theta \frac{\partial^2 \psi\left(\boldsymbol{\varepsilon}, \theta, k\right)}{\partial \theta \partial \theta}\,, \\ \boldsymbol{\beta}_\mathrm{v} &= -\frac{\partial \boldsymbol{\sigma}\left(\boldsymbol{\varepsilon}, \theta, k\right)}{\partial \theta} = -\rho \frac{\partial \psi\left(\boldsymbol{\varepsilon}, \theta, k\right)}{\partial \boldsymbol{\varepsilon} \partial \theta}\,. \end{aligned} \tag{2.50}$$

Investigating the local electrical dissipation term (2.40b) motivates the form of constitutive relation for electric current density as

$$\boldsymbol{j}\left(\boldsymbol{x}\right) = \boldsymbol{\mathcal{S}}\left(\theta, \boldsymbol{x}\right) \cdot \boldsymbol{e}\left(\boldsymbol{x}\right) = -\boldsymbol{\mathcal{S}}\left(\theta, \boldsymbol{x}\right) \cdot \nabla_x \phi\left(\boldsymbol{x}\right) \tag{2.51}$$

where $\boldsymbol{\mathcal{S}} : \mathbb{R}^+ \times \Omega \to \mathrm{Lin}\left(\mathbb{R}^d, \mathbb{R}^d\right)$ denotes the electrical conductivity tensor. Insertion of the constitutive relation (2.51) into (2.40b) yields

$$\mathcal{D}_\mathrm{elec} = \boldsymbol{j}\left(\boldsymbol{x}\right) \cdot \boldsymbol{e}\left(\boldsymbol{x}\right) = \nabla_x \phi\left(\boldsymbol{x}\right) \cdot \boldsymbol{\mathcal{S}}\left(\theta, \boldsymbol{x}\right) \cdot \nabla_x \phi\left(\boldsymbol{x}\right) \geq 0 \quad \text{in } \Omega\,. \tag{2.52}$$

If the electrical conductivity tensor $\boldsymbol{\mathcal{S}}$ is positive semi-definite, such that $\boldsymbol{\mathcal{S}} : [\nabla_x \phi \otimes \nabla_x \phi] \geq 0$, the dissipation inequality for the electrical problem is automatically satisfied.

Similarly, by adopting the linear relation between the heat flux vector and the (negative) temperature gradient

$$\boldsymbol{q}\left(\boldsymbol{x}\right) = -\boldsymbol{\mathcal{K}}\left(\theta, \boldsymbol{x}\right) \cdot \nabla_x \theta\left(\boldsymbol{x}\right) \tag{2.53}$$

where $\boldsymbol{\mathcal{K}} : \mathbb{R}^+ \times \Omega \to \mathrm{Lin}\left(\mathbb{R}^d, \mathbb{R}^d\right)$ denotes the positive semi-definite thermal conductivity tensor, thermodynamic consistency of the thermal part of the dissipation inequality (2.40c)

$$\begin{aligned} \mathcal{D}_\mathrm{therm} = \; -\boldsymbol{q}\left(\boldsymbol{x}\right) \cdot \nabla_x \ln\left(\theta\left(\boldsymbol{x}\right)\right) &= -\frac{1}{\theta\left(\boldsymbol{x}\right)} \boldsymbol{q}\left(\boldsymbol{x}\right) \cdot \nabla_x \theta\left(\boldsymbol{x}\right) \\ &= \frac{1}{\theta\left(\boldsymbol{x}\right)} \nabla_x \theta\left(\boldsymbol{x}\right) \cdot \boldsymbol{\mathcal{K}}\left(\theta, \boldsymbol{x}\right) \cdot \nabla_x \theta\left(\boldsymbol{x}\right) \geq 0 \quad \text{in } \Omega \end{aligned} \tag{2.54}$$

is established.

2.3 Finite element implementation

Before turning to the simulation results and validation studies, we introduce the finite element framework employed to solve the coupled thermo-electro-mechanical problem formulated in the preceding sections. Section 2.3.1 presents the weak formulations of the governing equations derived earlier. Section 2.3.2 discusses the discretisation of the problem using standard finite element techniques. Finally, Section 2.3.3 outlines the linearisation strategy used to solve the resulting nonlinear system of equations.

2.3.1 Weak form of governing equations

This section focuses on the weak form of the coupled thermo-electro-mechanical problem. In Section 2.2 strong forms of the partial differential equations are derived. Here and throughout, $\overline{\Omega}$ denotes the closure of Ω in $\mathbb{R}^d$, i.e. $\overline{\Omega} = \Omega \cup \partial\Omega$. We are seeking strong solutions of the coupled systems, namely $\boldsymbol{u} \in \mathrm{C}^2(\Omega) \cap \mathrm{C}\big(\overline{\Omega}\big)\,, \phi \in \mathrm{C}^2(\Omega) \cap \mathrm{C}\big(\overline{\Omega}\big)$ and $\theta \in \mathrm{C}^2(\Omega) \cap \mathrm{C}\big(\overline{\Omega}\big)$. The system of equations can be reformulated so as to look for solutions in distributional sense by testing the equations against sufficiently regular functions. This procedure "relaxes" the requirement of pointwise differentiability – i.e. classical C^2 regularity – to Sobolev or Lebesgue-space regularity, in which derivatives are understood in the sense of distributions.

The weak forms are derived by multiplying the field equations (2.26), (2.30a) and (2.34) with smooth and admissible test functions and integrating over the domain.

For the mechanical problem, the balance of linear momentum (2.26) is multiplied with an arbitrary test function $\boldsymbol{\varphi}^{\boldsymbol{u}} \in \mathrm{C}^\infty(\Omega)$, i.e.

$$\int_\Omega \boldsymbol{\varphi}^{\boldsymbol{u}}(\boldsymbol{x}) \cdot [\rho(\boldsymbol{x})\, \ddot{\boldsymbol{u}}(\boldsymbol{x})]\, \mathrm{d}x = \int_\Omega \boldsymbol{\varphi}^{\boldsymbol{u}}(\boldsymbol{x}) \cdot [\nabla_x \cdot \boldsymbol{\sigma}(\boldsymbol{x}) + \rho(\boldsymbol{x})\, \boldsymbol{f}(\boldsymbol{x})]\, \mathrm{d}x\,. \tag{2.55}$$

Since $\boldsymbol{u} \in \mathrm{C}^2(\Omega)$, divergence of the stress is well defined. After applying the divergence theorem, the mechanical problem reads

$$\begin{aligned}\int_\Omega \boldsymbol{\varphi}^{\boldsymbol{u}}(\boldsymbol{x}) \cdot [\rho(\boldsymbol{x})\, \ddot{\boldsymbol{u}}(\boldsymbol{x})]\, \mathrm{d}x = -\int_\Omega \nabla_x \boldsymbol{\varphi}^{\boldsymbol{u}}(\boldsymbol{x}) : \boldsymbol{\sigma}(\boldsymbol{x})\, \mathrm{d}x + \int_{\partial\Omega} \boldsymbol{\varphi}^{\boldsymbol{u}}(\boldsymbol{x}) \cdot \boldsymbol{t}(\boldsymbol{x})\, \mathrm{d}x \\ + \int_\Omega \boldsymbol{\varphi}^{\boldsymbol{u}}(\boldsymbol{x}) \cdot [\rho(\boldsymbol{x})\, \boldsymbol{f}(\boldsymbol{x})]\, \mathrm{d}x\,.\end{aligned} \tag{2.56}$$

For quasi-static settings, the weak form of the mechanical problem can be written as follows:

Find $\boldsymbol{u} \in H^1(\Omega)$ such that

$$\int_\Omega \nabla_x \boldsymbol{\varphi}^{\boldsymbol{u}}(\boldsymbol{x}) : \boldsymbol{\sigma}(\boldsymbol{x})\, \mathrm{d}x = \int_{\partial\Omega} \boldsymbol{\varphi}^{\boldsymbol{u}}(\boldsymbol{x}) \cdot \boldsymbol{t}(\boldsymbol{x})\, \mathrm{d}x + \int_\Omega \boldsymbol{\varphi}^{\boldsymbol{u}}(\boldsymbol{x}) \cdot [\rho(\boldsymbol{x})\, \boldsymbol{f}(\boldsymbol{x})]\, \mathrm{d}x \tag{2.57}$$

for all $\boldsymbol{\varphi}^{\boldsymbol{u}} \in H^1_0(\Omega)$.

Similar to he mechanical problem, the continuity equation of electric charge (2.30a) is multiplied with an arbitrary test function $\varphi^\phi \in \mathrm{C}^\infty(\Omega)$, and integrated over the domain Ω, i.e.

$$-\int_\Omega \varphi^\phi(\boldsymbol{x})\, \dot{\rho}_{\mathrm{f}}(\boldsymbol{x})\, \mathrm{d}x = \int_\Omega \varphi^\phi(\boldsymbol{x})\, [\nabla_x \cdot \boldsymbol{j}(\boldsymbol{x})]\, \mathrm{d}x\,. \tag{2.58}$$

Using the divergence theorem and identifying the resulting boundary terms on $\partial\Omega$, (2.58) takes the form

$$-\int_\Omega \varphi^\phi(\boldsymbol{x})\, \dot{\rho}_{\mathrm{f}}(\boldsymbol{x})\, \mathrm{d}x = -\int_\Omega \nabla_x \varphi^\phi(\boldsymbol{x}) \cdot \boldsymbol{j}(\boldsymbol{x})\, \mathrm{d}x + \int_{\partial\Omega} \varphi^\phi(\boldsymbol{x})\, i(\boldsymbol{x})\, \mathrm{d}x \tag{2.59}$$

with the definition of projected current density vector $i : \Omega \to \mathbb{R}$

$$i(\boldsymbol{x}) = \boldsymbol{j}(\boldsymbol{x}) \cdot \boldsymbol{n}(\boldsymbol{x}) \ . \tag{2.60}$$

For quasi-stationary settings, the weak form of the electrical problem is obtained as

Find $\phi \in H^1(\Omega)$ such that

$$\int_\Omega \nabla_x \varphi^\phi(\boldsymbol{x}) \cdot \boldsymbol{j}(\boldsymbol{x}) \, \mathrm{d}x = \int_{\partial\Omega} \varphi^\phi(\boldsymbol{x}) \, i(\boldsymbol{x}) \, \mathrm{d}x \tag{2.61}$$

for all $\varphi^\phi \in H^1_0(\Omega)$.

Finally, and for the sake of completeness, we are interested in thermal problem (2.34) and multiply the energy equation with an arbitrary test function $\varphi^\theta \in \mathrm{C}^\infty(\Omega)$, i.e.

$$\int_\Omega \varphi^\theta(\boldsymbol{x}) \left[\rho(\boldsymbol{x}) \, \dot{e}(\boldsymbol{x})\right] \mathrm{d}x = \int_\Omega \varphi^\theta(\boldsymbol{x}) \left[\boldsymbol{\sigma}(\boldsymbol{x}) : \dot{\boldsymbol{\varepsilon}}(\boldsymbol{x}) - \nabla_x \cdot \boldsymbol{q}(\boldsymbol{x}) + r(\boldsymbol{x}) + \boldsymbol{j}(\boldsymbol{x}) \cdot \boldsymbol{e}(\boldsymbol{x})\right] \mathrm{d}x \tag{2.62}$$

and arrive at

$$\begin{aligned} \int_\Omega \varphi^\theta(\boldsymbol{x}) \left[\rho(\boldsymbol{x}) \, \dot{e}(\boldsymbol{x})\right] \mathrm{d}x = \int_\Omega \varphi^\theta(\boldsymbol{x}) \left[\boldsymbol{\sigma}(\boldsymbol{x}) : \dot{\boldsymbol{\varepsilon}}(\boldsymbol{x})\right] \mathrm{d}x + \int_\Omega \nabla_x \varphi^\theta(\boldsymbol{x}) \cdot \boldsymbol{q}(\boldsymbol{x}) \, \mathrm{d}x \\ + \int_{\partial\Omega} \varphi^\theta(\boldsymbol{x}) \, q(\boldsymbol{x}) \, \mathrm{d}x + \int_\Omega \varphi^\theta(\boldsymbol{x}) \, r(\boldsymbol{x}) \, \mathrm{d}x + \int_\Omega \varphi^\theta(\boldsymbol{x}) \left[\boldsymbol{j}(\boldsymbol{x}) \cdot \boldsymbol{e}(\boldsymbol{x})\right] \mathrm{d}x \end{aligned} \tag{2.63}$$

with the definition of projected heat flux vector $q : \Omega \to \mathbb{R}$

$$q(\boldsymbol{x}) = -\boldsymbol{q}(\boldsymbol{x}) \cdot \boldsymbol{n}(\boldsymbol{x}) \ . \tag{2.64}$$

For quasi-static and quasi-stationary settings, the weak form of the thermal problem reads:

Find $\theta \in H^1(\Omega)$ such that

$$\int_\Omega \nabla_x \varphi^\theta(\boldsymbol{x}) \cdot \boldsymbol{q}(\boldsymbol{x}) \, \mathrm{d}x = -\int_{\partial\Omega} \varphi^\theta(\boldsymbol{x}) \, q(\boldsymbol{x}) \, \mathrm{d}x - \int_\Omega \varphi^\theta(\boldsymbol{x}) \left[r(\boldsymbol{x}) + \boldsymbol{j}(\boldsymbol{x}) \cdot \boldsymbol{e}(\boldsymbol{x})\right] \mathrm{d}x \tag{2.65}$$

for all $\varphi^\theta \in H^1_0(\Omega)$.

Remark 3. To provide a rigorous foundation for the weak forms introduced previously, we now justify the choice of function spaces used in our formulation. In the case of linear elasticity and so-called dead external loading, if we choose $\boldsymbol{\varphi}^{\boldsymbol{u}}$ to vanish on $\partial\Omega$, we obtain the variational problem

$$a(\boldsymbol{u}(\boldsymbol{x}), \boldsymbol{\varphi}^{\boldsymbol{u}}(\boldsymbol{x})) = F(\boldsymbol{\varphi}^{\boldsymbol{u}}(\boldsymbol{x})) \tag{2.66}$$

in abstract notation, with

$$a\left(\boldsymbol{u}\left(\boldsymbol{x}\right),\boldsymbol{\varphi}^{\boldsymbol{u}}\left(\boldsymbol{x}\right)\right)=\int_{\Omega}\left[\mathbf{E}\left(\theta,\boldsymbol{x}\right):\nabla_{x}\boldsymbol{u}^{\mathrm{sym}}\left(\boldsymbol{x}\right)\right]\cdot\nabla_{x}\boldsymbol{\varphi}^{\boldsymbol{u}}\left(\boldsymbol{x}\right)\,\mathrm{d}x\,, \tag{2.67a}$$

$$F\left(\boldsymbol{\varphi}^{\boldsymbol{u}}\right)=\int_{\Omega}\boldsymbol{\varphi}^{\boldsymbol{u}}\left(\boldsymbol{x}\right)\cdot\left[\rho\left(\boldsymbol{x}\right)\boldsymbol{f}\left(\boldsymbol{x}\right)\right]\,\mathrm{d}x\,. \tag{2.67b}$$

We define the function space V such that the problem is well defined for $\boldsymbol{u},\boldsymbol{\varphi}^{\boldsymbol{u}}\in V$

$$V=\{\boldsymbol{\varphi}^{\boldsymbol{u}}:\Omega\to\mathbb{R}^{d}\mid a\left(\boldsymbol{\varphi}^{\boldsymbol{u}},\boldsymbol{\varphi}^{\boldsymbol{u}}\right)<\infty\quad\text{and}\quad F\left(\boldsymbol{\varphi}^{\boldsymbol{u}}\right)<\infty\quad\text{and}\quad\boldsymbol{\varphi}^{\boldsymbol{u}}\mid_{\partial\Omega}=\mathbf{0}\}\,. \tag{2.68}$$

Let $\boldsymbol{u},\boldsymbol{\varphi}^{\boldsymbol{u}}\in V$ be

$$V=\{\boldsymbol{\varphi}^{\boldsymbol{u}}\in H_{0}^{1}\left(\Omega;\mathbb{R}^{d}\right):\boldsymbol{\varphi}^{\boldsymbol{u}}\mid_{\partial\Omega}=\mathbf{0}\} \tag{2.69}$$

and the bilinear form $a:H^{1}\left(\Omega;\mathbb{R}^{d}\right)\times H^{1}\left(\Omega;\mathbb{R}^{d}\right)\to\mathbb{R}$ is coercive, symmetric and bounded on V. We can now apply the Lax–Milgram theorem to demonstrate the existence and uniqueness of a solution within the defined function space V. The use of the Sobolev space $W_{2}^{1}=H^{1}$ ensures that the functions within the space have finite energy, which is a crucial requirement for the variational problem to be well-posed. This variational formulation serves as the foundation for the Galerkin method.

2.3.2 Discretised weak form

The weak form is discretised using standard finite element approximations, enabling numerical simulation of complex domains. For the discretisation of the primary fields (displacements, electric potential and temperature) and the related test functions, Legendre polynomials are employed as

$$\boldsymbol{u}^{\mathrm{h}}=\sum_{D=1}^{\mathrm{n_{en}}}N_{D}\,\boldsymbol{u}_{D},\quad\boldsymbol{\varphi}^{\boldsymbol{u}\mathrm{h}}=\sum_{A=1}^{\mathrm{n_{en}}}N_{A}\,\boldsymbol{\varphi}_{A}^{\boldsymbol{u}}\,, \tag{2.70a}$$

$$\phi^{\mathrm{h}}=\sum_{E=1}^{\mathrm{n_{en}}}N_{E}\,\phi_{E},\quad\varphi^{\phi\mathrm{h}}=\sum_{B=1}^{\mathrm{n_{en}}}N_{B}\,\varphi_{B}^{\phi} \tag{2.70b}$$

$$\theta^{\mathrm{h}}=\sum_{F=1}^{\mathrm{n_{en}}}N_{F}\,\theta_{F},\quad\varphi^{\theta\mathrm{h}}=\sum_{C=1}^{\mathrm{n_{en}}}N_{C}\,\varphi_{C}^{\theta}\,, \tag{2.70c}$$

where $\mathrm{n_{en}}$ and $N_{\bullet}$ are the number of element nodes and the shape functions, respectively. Furthermore, we employ an isoparametric approximation, where identical shape functions discretise both the geometry and the spatial placement field. Furthermore, identical shape functions are used for all primary fields, displacement, electric potential, and temperature, ensuring a consistent approximation across the coupled problem.

Given the assembly operator $\mathbf{A}$ and the total number of elements, $\mathrm{n_{el}}$, the discrete force vectors can be formulated. Specifically, for the mechanical subproblem, the internal force vector reads

$$\boldsymbol{f}_{\mathrm{int}}^{\boldsymbol{u}\,\mathrm{h}}=\mathop{\mathbf{A}}_{e=1}^{\mathrm{n_{el}}}\int_{\Omega^{\mathrm{e}}}\nabla_{x}N_{A}\cdot\boldsymbol{\sigma}\,\mathrm{d}x\,. \tag{2.71}$$

The contributions of the volumetric forces are given by

$$\boldsymbol{f}_{\mathrm{vol}}^{\boldsymbol{u}\,\mathrm{h}} = \mathop{\mathsf{A}}_{e=1}^{\mathrm{n_{el}}} \int_{\Omega^e} N_A \, \rho \, \boldsymbol{f} \, \mathrm{d}x \,, \tag{2.72}$$

and the surface force vector is defined as

$$\boldsymbol{f}_{\mathrm{sur}}^{\boldsymbol{u}\,\mathrm{h}} = \mathop{\mathsf{A}}_{e=1}^{\mathrm{n_{el}}} \int_{\partial\Omega^e} N_A \, \boldsymbol{t} \, \mathrm{d}x \,. \tag{2.73}$$

For the electrical subproblem, the internal force vector takes the form

$$\boldsymbol{f}_{\mathrm{int}}^{\phi\,\mathrm{h}} = \mathop{\mathsf{A}}_{e=1}^{\mathrm{n_{el}}} \int_{\Omega^e} \nabla_x N_B \cdot \boldsymbol{j} \, \mathrm{d}x \,, \tag{2.74}$$

and the surface force vector reads

$$\boldsymbol{f}_{\mathrm{sur}}^{\phi\,\mathrm{h}} = \mathop{\mathsf{A}}_{e=1}^{\mathrm{n_{el}}} \int_{\partial\Omega^e} N_B \, \boldsymbol{j} \cdot \boldsymbol{n} \, \mathrm{d}x \,. \tag{2.75}$$

Analogous to the electrical and mechanical subproblem, the internal force vector of the thermal problem takes the form

$$\boldsymbol{f}_{\mathrm{int}}^{\theta\,\mathrm{h}} = \mathop{\mathsf{A}}_{e=1}^{\mathrm{n_{el}}} \int_{\Omega^e} \nabla_x N_C \cdot \boldsymbol{q} \, \mathrm{d}x \,. \tag{2.76}$$

The contribution of the source terms is given by

$$\boldsymbol{f}_{\mathrm{vol}}^{\theta\,\mathrm{h}} = \mathop{\mathsf{A}}_{e=1}^{\mathrm{n_{el}}} \int_{\Omega^e} N_C \, r + N_C \, \boldsymbol{j} \cdot \boldsymbol{e} \, \mathrm{d}x, \tag{2.77}$$

and the surface force vector reads

$$\boldsymbol{f}_{\mathrm{sur}}^{\theta\,\mathrm{h}} = \mathop{\mathsf{A}}_{e=1}^{\mathrm{n_{el}}} \int_{\partial\Omega^e} -N_C \, \boldsymbol{q} \cdot \boldsymbol{n} \, \mathrm{d}x \;. \tag{2.78}$$

2.3.3 Linearisation

The solution of the discrete system of equations is performed in an iterative manner, with the residuum

$$\boldsymbol{r}^{\bullet\,\mathrm{h}} = \boldsymbol{f}_{\mathrm{int}}^{\bullet\,\mathrm{h}} - \boldsymbol{f}_{\mathrm{ext}}^{\bullet\,\mathrm{h}} \tag{2.79}$$

and its linearisation at iteration step q,

$$\boldsymbol{r}_{\mathrm{q+1}}^{\bullet\,\mathrm{h}} = \boldsymbol{r}_{\mathrm{q}}^{\bullet\,\mathrm{h}} + \Delta \boldsymbol{r}^{\bullet\,\mathrm{h}} \;. \tag{2.80}$$

The increment can further be specified as

$$\Delta \boldsymbol{r}^{\bullet\,\mathrm{h}} = \frac{\mathrm{d}\boldsymbol{r}^{\bullet\,\mathrm{h}}}{\mathrm{d}\widehat{\boldsymbol{u}}} \cdot \Delta\widehat{\boldsymbol{u}} + \frac{\mathrm{d}\boldsymbol{r}^{\bullet\,\mathrm{h}}}{\mathrm{d}\widehat{\boldsymbol{\phi}}} \cdot \Delta\widehat{\boldsymbol{\phi}} + \frac{\mathrm{d}\boldsymbol{r}^{\bullet\,\mathrm{h}}}{\mathrm{d}\widehat{\boldsymbol{\theta}}} \cdot \Delta\widehat{\boldsymbol{\theta}} \tag{2.81}$$

such that the system of equations solve for the increments referred to the list of nodal degrees of freedom, i.e. ($\widehat{\boldsymbol{u}}$, $\widehat{\boldsymbol{\phi}}$ and $\widehat{\boldsymbol{\theta}}$), reads

$$\begin{bmatrix} \mathbf{K}^{\boldsymbol{u}\boldsymbol{u}} & \mathbf{K}^{\boldsymbol{u}\phi} & \mathbf{K}^{\boldsymbol{u}\theta} \\ \mathbf{K}^{\phi\boldsymbol{u}} & \mathbf{K}^{\phi\phi} & \mathbf{K}^{\phi\theta} \\ \mathbf{K}^{\theta\boldsymbol{u}} & \mathbf{K}^{\theta\phi} & \mathbf{K}^{\theta\theta} \end{bmatrix}_{\mathrm{q}} \cdot \begin{bmatrix} \Delta\widehat{\boldsymbol{u}} \\ \Delta\widehat{\boldsymbol{\phi}} \\ \Delta\widehat{\boldsymbol{\theta}} \end{bmatrix}_{\mathrm{q}} = - \begin{bmatrix} \boldsymbol{r}^{\boldsymbol{u}\,\mathrm{h}} \\ \boldsymbol{r}^{\phi\,\mathrm{h}} \\ \boldsymbol{r}^{\theta\,\mathrm{h}} \end{bmatrix}_{\mathrm{q}} . \tag{2.82}$$

In (2.82), $\mathbf{K}^{\bullet *}$ denotes the tangent stiffness contributions of the generalised global stiffness matrix. With these definitions in hand, the residual force vectors $\boldsymbol{r}^{\bullet\,\mathrm{h}}$ are specified next. By inserting (2.70a) into the weak form of the mechanical subproblem (2.57), the residual force vector

$$\boldsymbol{r}^{\boldsymbol{u}\,\mathrm{h}} = \boldsymbol{f}^{\boldsymbol{u}\,\mathrm{h}}_{\mathrm{int}} - \boldsymbol{f}^{\boldsymbol{u}\,\mathrm{h}}_{\mathrm{sur}} - \boldsymbol{f}^{\boldsymbol{u}\,\mathrm{h}}_{\mathrm{vol}} \tag{2.83}$$

is obtained. For the electrical subproblem, inserting (2.70b) into (2.61) yields the residual vector

$$\boldsymbol{r}^{\phi\,\mathrm{h}} = \boldsymbol{f}^{\phi\,\mathrm{h}}_{\mathrm{int}} - \boldsymbol{f}^{\phi\,\mathrm{h}}_{\mathrm{sur}} . \tag{2.84}$$

Likewise, the residual vector for the thermal problem is obtained by inserting (2.70c) in (2.65), i.e.

$$\boldsymbol{r}^{\theta\,\mathrm{h}} = \boldsymbol{f}^{\theta\,\mathrm{h}}_{\mathrm{int}} - \boldsymbol{f}^{\theta\,\mathrm{h}}_{\mathrm{sur}} - \boldsymbol{f}^{\theta\,\mathrm{h}}_{\mathrm{vol}} . \tag{2.85}$$

The relevant tangent stiffness contributions are presented in Appendix A.1.

2.4 Validation by analytical solution

This section focuses on the validation of the finite element implementation proposed in Section 2.3 based on the analytical solutions derived in Section 2.4. To this end, the elementary boundary value problem depicted in Figure 2.2 is discretised by means of 10 four-node quadrilateral elements. First the thermo-electrical problem is investigated to study the effect of Joule heating. Subsequently, a thermo-elastic problem is analysed to study the effect of the thermo-mechanical coupling. Finally a fully coupled thermo-electro-elastic problem is derived and compared with a proposed three-field finite element analysis results.

Let $\Omega \subset \mathbb{R}$ represent a bar with domain $\Omega \in [0, l]$. The corresponding boundary value problem for the fully coupled case is illustrated in Figure 2.2. For the thermo-electrical and fully coupled cases, a zero heat flux boundary condition $\overline{q} = 0\,\mathrm{W/mm^2}$ is applied at the right end of the bar. In contrast, for the thermo-mechanical problem, a non-zero Neumann boundary condition of $\overline{q} = 100\,\mathrm{W/mm^2}$ is prescribed.

Table 2.1: Material parameters used in the analytical and finite element-based simulations.

E	ν	κ_θ	κ_ϕ	α
$100\,000\,\mathrm{N/mm^2}$	0.0 [-]	$2000\,\mathrm{W/mK}$	$1450\,\mathrm{A/[Vmm]}$	$1 \times 10^{-2}\,\mathrm{K^{-1}}$

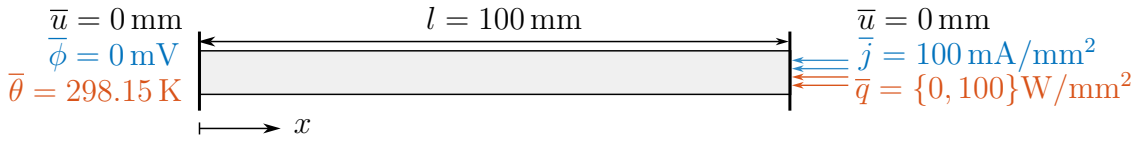

Figure 2.2: Bar of length $l = 100\,\mathrm{mm}$, subjected to mechanical, electrical and thermal boundary conditions.

Although the boundary value problem considered is one-dimensional, it is discretised using two-dimensional linear, quadrilateral elements. To restrict the problem to the one-dimensional case, the transverse displacement ν is constrained to zero across the domain, see Table 2.1. This strategy allows validating the fully coupled thermo-electro-mechanical finite element formulation implemented for general settings while enabling direct comparison with one-dimensional analytical solutions.

2.4.1 Thermo-electrical problem

For the electrical problem at hand, a linear relation between the (longitudinal) electric field $e : \Omega \to \mathbb{R}$ and (longitudinal) electric current density $j : \Omega \to \mathbb{R}$ is assumed as derived in (2.51). For the time being, however, the temperature dependence of electrical conductivity is dropped, namely

$$j = \kappa_\phi\, e = -\kappa_\phi \frac{\mathrm{d}\phi}{\mathrm{d}x}\,, \tag{2.86}$$

with κ_ϕ being constant and electric field $e = -\frac{\mathrm{d}\phi}{\mathrm{d}x}$. Similarly, a linear relation between the heat flux $q : \Omega \to \mathbb{R}$ and (negative) temperature gradient is adopted as

$$q = -\kappa_\theta \frac{\mathrm{d}\theta}{\mathrm{d}x}\,. \tag{2.87}$$

In (2.86)–(2.87), $\kappa_\phi : \Omega \to \mathbb{R}^+$ and $\kappa_\theta : \Omega \to \mathbb{R}^+$ denote the electrical and thermal conductivities. The governing equation of the electrical problem simplifies to a one-dimensional form and the corresponding electric potential field and the electric current take the form

$$\phi\,(x) = -\frac{\bar{j}}{\kappa_\phi}\, x + \bar{\phi} \quad \text{with} \quad \bar{\phi} = 0\,, \tag{2.88a}$$

$$j\,(x) = \bar{j}\,. \tag{2.88b}$$

As shown in Figure 2.2, the beam under consideration has Dirichlet boundary conditions on its left end with free heat flux condition at its right end. Observing the electric potential field, a linearly increasing electric potential profile is expected. Due to the Neumann

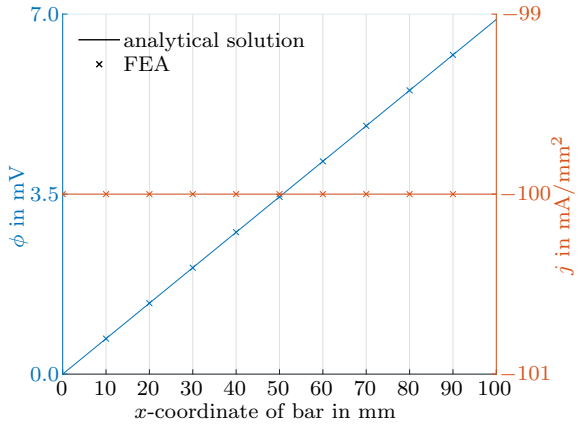

(a) Electric potential and current profile along the bar

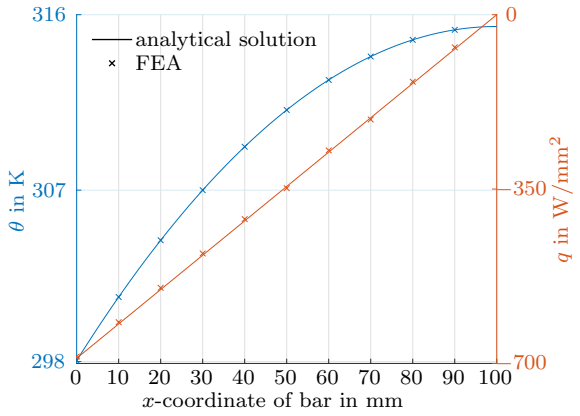

(b) Temperature and heat flux profile along the bar

Figure 2.3: Comparison of analytical solution and finite element results for thermo-electrical boundary value problem.

boundary condition, where the current density $\bar{j}$ is applied at the right boundary, an increasing profile is obtained from the analytical solution, as illustrated in Figure 2.3a. The finite element approximation of the electric potential field matches the analytical solution exactly. Additionally, the electric current is identical to the analytical solution, as it must remain constant along the bar.

The energy equation governs the temperature evolution and associated temperature and heat flux fields are derived as

$$\theta(x) = -\frac{1}{2}\frac{\bar{j}^2}{\kappa_\phi\,\kappa_\theta}\,x^2 + \frac{\bar{j}^2\,l}{\kappa_\phi\,\kappa_\theta}\,x + \bar{\theta} \quad \text{with} \quad \bar{\theta} = 298.15\,\mathrm{K} \tag{2.89a}$$

$$q(x) = \frac{\bar{j}^2}{\kappa_\phi}\,x - \frac{\bar{j}^2\,l}{\kappa_\phi}\,. \tag{2.89b}$$

Figure 2.3b shows a comparison of the analytical and finite element results for the thermal fields. The temperature field is approximated exactly at the nodes. However, due to the quadratic nature of the temperature field, the resulting linear heat flux field cannot be exactly represented due to constant gradient contributions within the elements. Increasing mesh density could improve the approximation.

2.4.2 Thermo-elastic problem

The thermo-mechanical response is assumed to be governed by the volume specific Helmholtz free energy density function $\Psi : \Omega \to \mathbb{R}$

$$\rho\,\psi(\varepsilon,\theta) = \Psi(\varepsilon,\theta) = \frac{1}{2}\,E\,\varepsilon^2 - \alpha\,E\,\varepsilon\,[\theta - \theta_0] \tag{2.90}$$

where $E : \Omega \to \mathbb{R}$ and $\alpha : \Omega \to \mathbb{R}$ are the material specific Young's modulus and thermal expansion coefficients. Furthermore, $\varepsilon : \Omega \to \mathbb{R}$ is the one dimensional total strain,

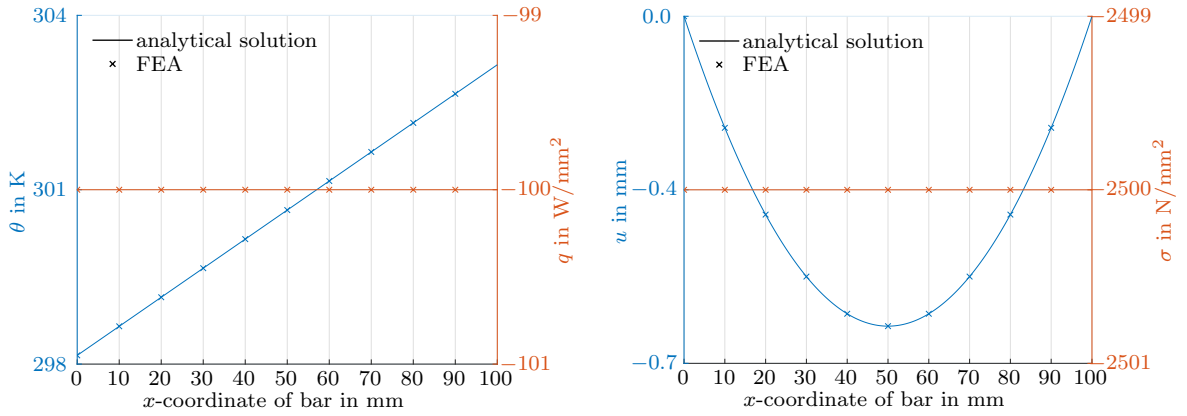

(a) Temperature and heat flux profile along the bar

(b) Displacement and stress profile along the bar

Figure 2.4: Comparison of analytical solution and finite element results for thermo-elastic boundary value problem.

with the definition $\varepsilon = \mathrm{d}u/\,\mathrm{d}x$ at hand. By evaluating (2.47) for the volume specific Helmholtz free energy density, the stress reads

$$\sigma = E\,\varepsilon - \alpha\,E\,[\theta - \theta_0] = E\,\frac{\mathrm{d}u}{\mathrm{d}x} - \alpha\,E\,[\theta - \theta_0]\;. \tag{2.91}$$

In the absence of electrical field, the temperature evolution is governed by the heat equation and the corresponding temperature together with the heat flux fields take the form

$$\theta\,(x) = -\frac{\bar{q}}{\kappa_\theta}\,x + \bar{\theta} \quad \text{with} \quad \bar{\theta} = 298.15\,\mathrm{K}\,, \tag{2.92a}$$

$$q\,(x) = \bar{q}\,. \tag{2.92b}$$

Figure 2.4 presents a comparison between analytical and finite element analysis results for the specified thermo-elastic boundary value problem. Figure 2.4a illustrates a linear increase in temperature resulting from constant heat flux along the bar. Given that the bar is fixed at the boundaries and subjected to thermal expansion without mechanical loading, thermal stresses and corresponding displacements are expected. Respective displacement and stress fields are derived as

$$u\,(x) = -\frac{1}{2}\,\alpha\,\frac{\bar{q}}{\kappa_\theta}\,x^2 + \frac{1}{2}\,\alpha\frac{\bar{q}}{\kappa_\theta}\,l\,x + \bar{u} \quad \text{with} \quad \bar{u} = 0\,, \tag{2.93a}$$

$$\sigma\,(x) = E\,\left[\frac{1}{2}\,\alpha\frac{\bar{q}}{\kappa_\theta}\,l\right] - \alpha\,E\,\left[\bar{\theta} - \theta_0\right] \quad \text{with} \quad \bar{\theta} = \theta_0 = 298.15\,\mathrm{K}\,. \tag{2.93b}$$

Figure 2.4b shows a clear agreement between analytical and finite element results. As expected, compressive strains and stresses are present along the bar due to thermal expansion.

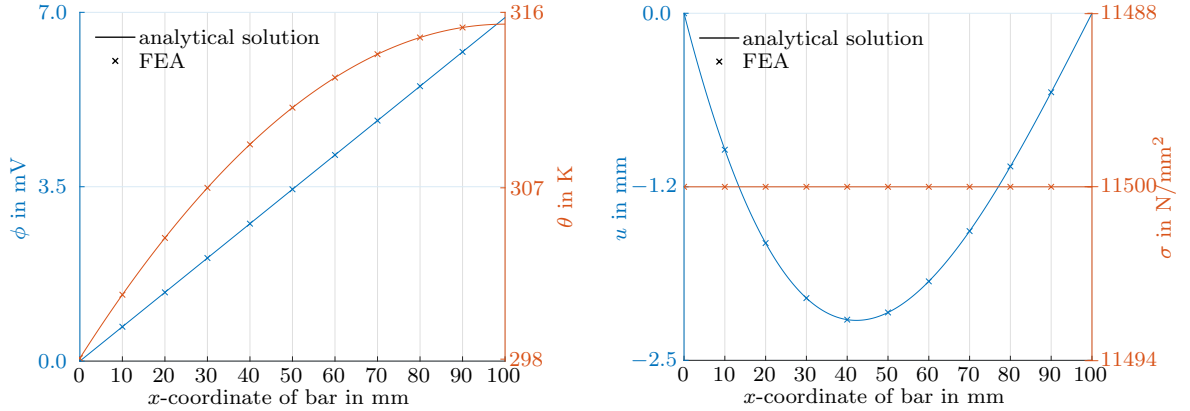

(a) Electric potential and temperature profile along the bar

(b) Displacement and stress profile along the bar

Figure 2.5: Comparison of analytical solution and finite element results for thermo-electro-elastic boundary value problem.

2.4.3 Thermo-electro-mechanical problem

In the fully coupled thermo-electro-mechanical problem sketched in Figure 2.2, the electric potential and temperature fields match those in Section 2.4.1, with the resulting displacement field being the only variation. Figure 2.5a illustrates that the finite element results of the electric potential and temperature fields compared to (2.88a) and (2.89a), respectively. The analytical solution for displacement and stress field are calculated as follows

$$u(x) = -\frac{1}{6}\,\alpha\,\frac{\bar{j}^2}{\kappa_\phi\,\kappa_\theta}\,x^3 + \frac{1}{2}\,\alpha\,\frac{\bar{j}^2}{\kappa_\phi\,\kappa_\theta}\,l\,x^2 - \frac{1}{3}\,\frac{\bar{j}^2}{\kappa_\phi\,\kappa_\theta}\,l^2\,x + \bar{u} \quad \text{with} \quad \bar{u} = 0\,, \tag{2.94a}$$

$$\sigma(x) = -E\,\frac{1}{3}\,\frac{\bar{j}^2}{\kappa_\phi\,\kappa_\theta}\,l^2 - \alpha\,E\,\left[\bar{\theta} - \theta_0\right] \quad \text{with} \quad \bar{\theta} = \theta_0 = 298.15\,\mathrm{K}\,, \tag{2.94b}$$

and plotted against finite element result in Figure 2.5b.

2.5 Representative simulation results

Following the validation of the finite element implementation, a microchip is simulated under electrical loading, motivated by the thermal stresses occurring due to Joule heating. Accurate prediction and control of thermal profiles in microchips are essential for ensuring device reliability. In this section, finite element analysis is employed to simulate the effects of Joule heating in a microchip (or integrated circuit). To this end, Section 2.5.1 provides a brief summary of constitutive relations that are used to model the coupled thermo-electro-mechanical response of the material, respectively device. Two-dimensional representative examples are presented in Section 2.5.2. Material parameters used in the simulations are tabulated in Table 2.2 and plane strain conditions are assumed. Boundary conditions are given in Figure 2.6. The geometry is discretised linear quadrilateral elements. The mesh consists of 16524 linear, quadrilateral elements.

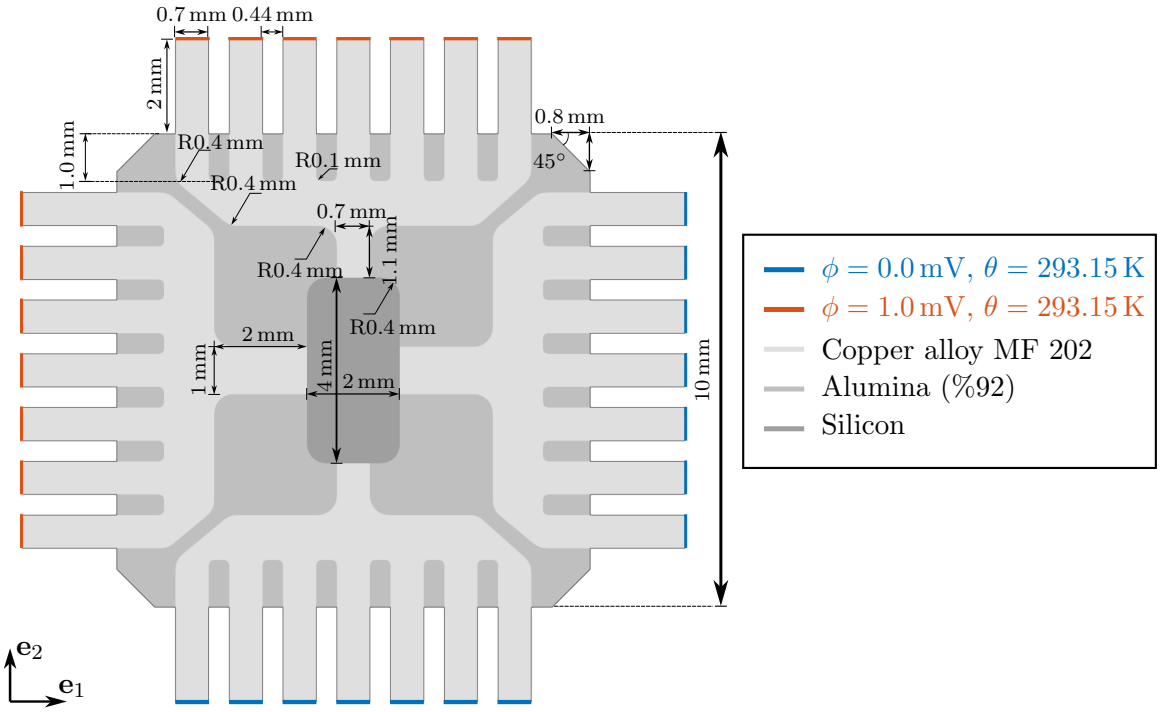

Figure 2.6: Geometrical dimensions and boundary conditions of the two-dimensional boundary value problem discussed in Section 2.5.2. Additionally, fixed boundary conditions are applied on the red and blue boundaries for the mechanical problem.

2.5.1 Constitutive relations

The thermo-mechanical response of the bulk material is assumed to be governed by the volume specific Helmholtz free energy density function Ψ. Specifically speaking, an additive decomposition according to

$$\rho\,\psi\left(\boldsymbol{\varepsilon},\theta\right) = \Psi\left(\boldsymbol{\varepsilon},\theta\right) = \Psi^{\boldsymbol{u}}_{\mathrm{vol}}\left(\boldsymbol{\varepsilon}\right) + \Psi^{\boldsymbol{u}}_{\mathrm{dev}}\left(\boldsymbol{\varepsilon}_{\mathrm{dev}}\right) + \Psi^{\boldsymbol{u}\theta}_{\mathrm{vol}}\left(\boldsymbol{\varepsilon},\theta\right) + \Psi^{\theta}\left(\theta\right) \tag{2.95}$$

is assumed with the elastic volumetric, $\Psi^{\boldsymbol{u}}_{\mathrm{vol}}$, the elastic deviatoric, $\Psi^{\boldsymbol{u}}_{\mathrm{dev}}$, the thermoelastic coupling, $\Psi^{\boldsymbol{u}\theta}_{\mathrm{vol}}$, and the thermal, Ψ^{θ}, parts. The respective contributions to (2.95) are specified as

$$\Psi^{\boldsymbol{u}}_{\mathrm{vol}}\left(\boldsymbol{\varepsilon}\left(\boldsymbol{x}\right)\right) = \frac{1}{2}\,K\left(\boldsymbol{x}\right)\mathrm{tr}^2\left(\boldsymbol{\varepsilon}\left(\boldsymbol{x}\right)\right)\,, \tag{2.96a}$$

$$\Psi^{\boldsymbol{u}}_{\mathrm{dev}}\left(\boldsymbol{\varepsilon}_{\mathrm{dev}}\left(\boldsymbol{x}\right)\right) = G\left(\boldsymbol{x}\right)\boldsymbol{\varepsilon}_{\mathrm{dev}}\left(\boldsymbol{x}\right) : \boldsymbol{\varepsilon}_{\mathrm{dev}}\left(\boldsymbol{x}\right)\,, \tag{2.96b}$$

$$\Psi^{\boldsymbol{u}\theta}_{\mathrm{vol}}\left(\boldsymbol{\varepsilon}\left(\boldsymbol{x}\right),\theta\left(\boldsymbol{x}\right)\right) = 3\,\alpha\left(\boldsymbol{x}\right)K\left(\boldsymbol{x}\right)\left[\theta\left(\boldsymbol{x}\right)-\theta_0\right]\mathrm{tr}\left(\boldsymbol{\varepsilon}\left(\boldsymbol{x}\right)\right)\,, \tag{2.96c}$$

$$\Psi^{\theta}\left(\theta\left(\boldsymbol{x}\right)\right) = c_{\mathrm{v}}\left(\boldsymbol{x}\right)\left[\left[\theta\left(\boldsymbol{x}\right)-\theta_0\right]-\theta\left(\boldsymbol{x}\right)\ln\left(\frac{\theta\left(\boldsymbol{x}\right)}{\theta_0}\right)\right]. \tag{2.96d}$$

In the set of equations above, $K : \Omega \to \mathbb{R}^+$ is the bulk modulus, $G : \Omega \to \mathbb{R}^+$ is the shear modulus, α is the thermal expansion coefficient, c_{v} is the heat capacity and θ_0 is

the reference temperature. The deviatoric part of the strain is defined as $\boldsymbol{\varepsilon}_{\mathrm{dev}} = \mathbf{I}^{\mathrm{dev}} : \boldsymbol{\varepsilon}$, with $\mathbf{I}^{\mathrm{dev}}$ denoting the fourth-order deviatoric projection tensor. By evaluating (2.47) for the volume specific Helmholtz free energy density (2.95), the bulk stress tensor

$$\boldsymbol{\sigma}(\boldsymbol{x}) = K(\boldsymbol{x}) \left[\operatorname{tr}(\boldsymbol{\varepsilon}(\boldsymbol{x})) - 3\,\alpha(\boldsymbol{x}) \left[\theta(\boldsymbol{x}) - \theta_0 \right] \right] \boldsymbol{I} + 2\,G(\boldsymbol{x})\, \boldsymbol{\varepsilon}_{\mathrm{dev}}(\boldsymbol{x}) \,, \tag{2.97}$$

is obtained. Accordingly, the fourth-order stiffness tensor $\mathbf{E} : \Omega \to \operatorname{Sym}\left(\mathbb{R}^{d\times d\times d\times d}\right)$ reads

$$\mathbf{E}(\boldsymbol{x}) = K(\boldsymbol{x})\, \boldsymbol{I} \otimes \boldsymbol{I} + 2\,G(\boldsymbol{x})\, \mathbf{I}^{\mathrm{dev}} \,. \tag{2.98}$$

A linear relation between the electric field vector and the electric current density vector is assumed in the bulk following the restrictions posed by the dissipation inequalities (2.51), i.e.

$$\boldsymbol{j}(\boldsymbol{x}) = \boldsymbol{\mathcal{S}}(\theta, \boldsymbol{x}) \cdot \boldsymbol{e}(\boldsymbol{x}) \,. \tag{2.99}$$

For the sake of simplicity, an isotropic electrical conductivity tensor is assumed with the positive definite electrical conductivity tensor

$$\boldsymbol{\mathcal{S}}(\theta, \boldsymbol{x}) = \kappa_\phi(\theta, \boldsymbol{x})\; \boldsymbol{I} \,, \qquad \text{with} \qquad \kappa_\phi(\theta, \boldsymbol{x}) = \frac{\kappa_{\phi 0}(\boldsymbol{x})}{1 + \mu(\boldsymbol{x}) \left[\theta(\boldsymbol{x}) - \theta_0 \right]} \tag{2.100}$$

where $\kappa_\phi : \mathbb{R}^+ \times \Omega \to \mathbb{R}$ denotes a scalar-valued electrical conductivity parameter. In (2.100), $\kappa_{\phi 0} : \Omega \to \mathbb{R}$ denotes the reference conductivity at temperature θ_0 and $\mu : \Omega \to \mathbb{R}$ is the temperature coefficient of resistivity.

Analogous to the electrical problem, in this example a linear relation between the temperature gradient and the heat flux vector in the bulk is assumed, i.e.

$$\boldsymbol{q}(\boldsymbol{x}) = -\boldsymbol{\mathcal{K}}(\boldsymbol{x}) \cdot \nabla\, \theta(\boldsymbol{x}) \,, \tag{2.101}$$

including the positive definite thermal conductivity tensor

$$\boldsymbol{\mathcal{K}}(\boldsymbol{x}) = \kappa_\theta(\boldsymbol{x})\, \boldsymbol{I} \tag{2.102}$$

with the scalar-valued thermal conductivity parameter $\kappa_\theta : \Omega \to \mathbb{R}$. All the related sensitivities are summarised in Appendix A.2

2.5.2 Simulation of thermo-electro-mechanical fields in microchips

The coupled thermo-electro-mechanical response of the microchip configuration is illustrated in Figures 2.7–2.9, each showing the steady-state solution under an applied potential difference of $\overline{\Delta\phi} = 1.0\,\mathrm{mV}$. Figure 2.7 depicts the electric potential and current density fields, while Figure 2.8 shows the resulting temperature distribution due to Joule heating, along with the corresponding heat flux. The rise in temperature due to electrical response leads to nonuniform thermal expansion within the microchip, which in turn induces mechanical deformation. This is visualised in Figure 2.9, where the displacement and stress fields are shown. The stress field reveals localized concentrations near the pin connections and at internal corners, indicating regions of elevated mechanical response due to both geometric constraints and thermal gradients. The results clearly demonstrate the strong field coupling in the proposed formulation and its ability to capture realistic behaviour in microelectronic components under electrical loading.

Table 2.2: Material parameters used in the finite element-based microchip simulations.

	Copper alloy MF 202	Alumina (%92)	Silicon
E	$113\,000\,\mathrm{N/mm^2}$	$55\,000\,\mathrm{N/mm^2}$	$168\,900\,\mathrm{N/mm^2}$
ν	0.340 [-]	0.210 [-]	0.265 [-]
κ_θ	$160\,\mathrm{W/mK}$	$27.5\,\mathrm{W/mK}$	$239\,\mathrm{W/mK}$
κ_ϕ	$17\,500\,\mathrm{A/[Vmm]}$	$2040\,\mathrm{A/[Vmm]}$	$20\,\mathrm{A/[Vmm]}$
α	$1.7 \times 10^{-5}\,\mathrm{K^{-1}}$	$5.3 \times 10^{-6}\,\mathrm{K^{-1}}$	$2.6 \times 10^{-6}\,\mathrm{K^{-1}}$

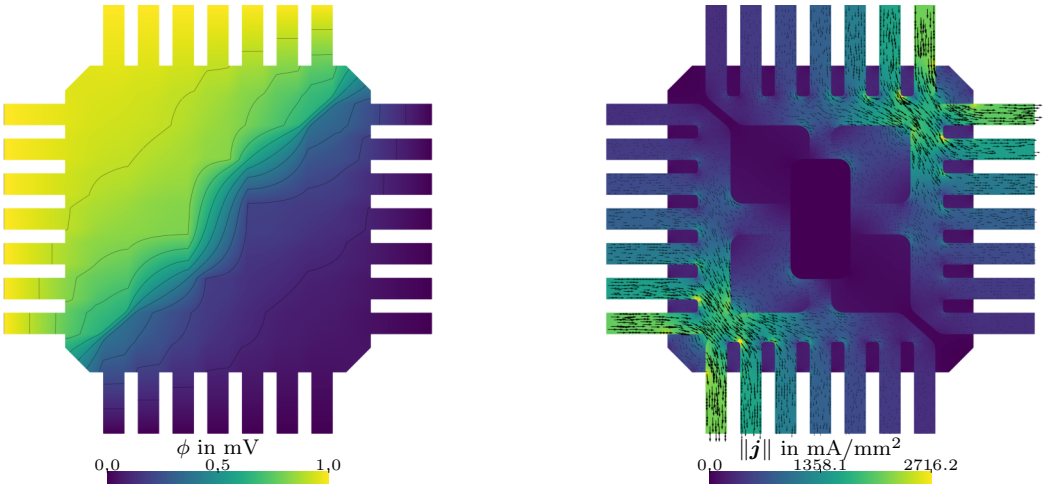

(a) ϕ for $\Delta\phi = 1.0\,\mathrm{mV}$ **(b)** $\boldsymbol{j}$ for $\Delta\phi = 1.0\,\mathrm{mV}$

Figure 2.7: Electric potential ϕ and electric current field $\boldsymbol{j}$ of the boundary value problem, showing the final stage under electrical loading of $\overline{\Delta\phi} = 1.0\,\mathrm{mV}$. In Figure 2.7a, electric potential isolines are included. In Figure 2.7b electric current density vectors are indicated by black arrows.

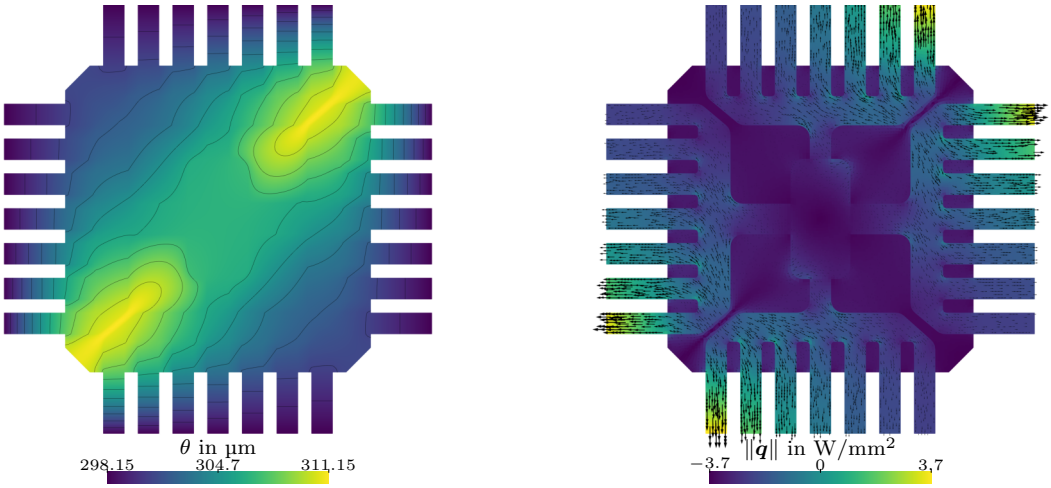

(a) θ for $\Delta\phi = 1.0\,\mathrm{mV}$ **(b)** $\boldsymbol{q}$ for $\Delta\phi = 1.0\,\mathrm{mV}$

Figure 2.8: Temperature θ and heat flux field $\boldsymbol{q}$ of the boundary value problem, showing the final stage under electrical loading of $\overline{\Delta\phi} = 1.0\,\mathrm{mV}$. In Figure 2.8a, temperature isolines are included. In Figure 2.8b heat flux vectors are indicated by black arrows.

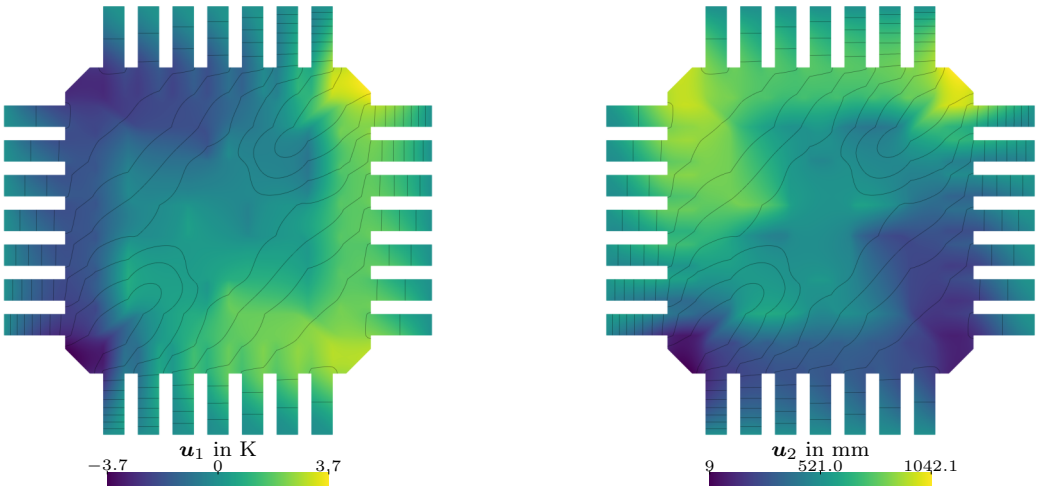

(a) θ for $\Delta\phi = 1.0\,\mathrm{mV}$

(b) $\boldsymbol{u}_2$ for $\Delta\phi = 1.0\,\mathrm{mV}$

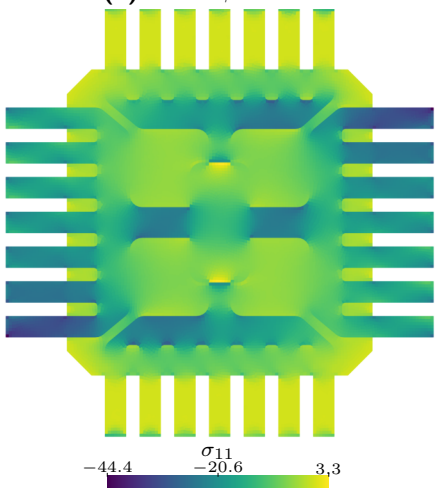

(c) σ_{11} for $\Delta\phi = 1.0\,\mathrm{mV}$

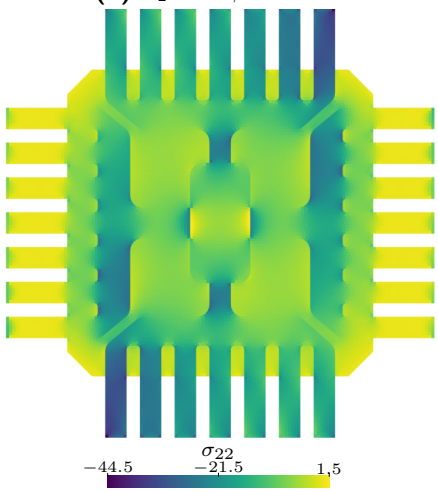

(d) σ_{22} for $\Delta\phi = 1.0\,\mathrm{mV}$

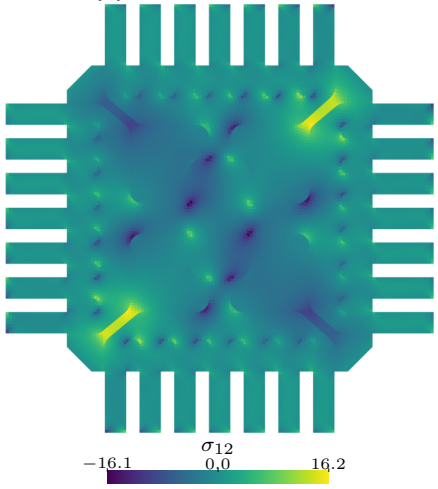

(e) σ_{12} for $\Delta\phi = 1.0\,\mathrm{mV}$

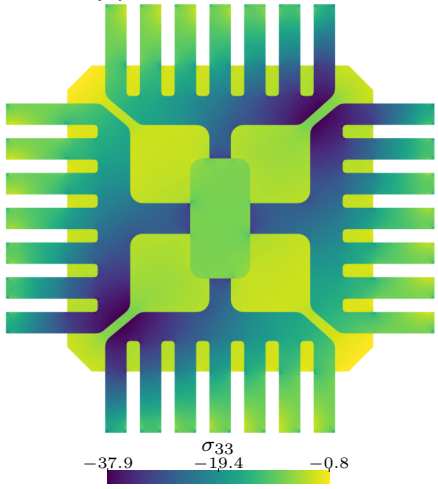

(f) σ_{33} for $\Delta\phi = 1.0\,\mathrm{mV}$

Figure 2.9: Displacement field $\boldsymbol{u}$ and stress field $\boldsymbol{\sigma}$ of the boundary value problem, showing the final stage under electrical loading of $\overline{\Delta\phi} = 1.0\,\mathrm{mV}$. In Figure 2.9a and 2.9b, temperature isolines are included to visualise thermal expansion.

A Appendix

In the following sections, all tangent contributions employed in Section 2.3.3 are derived. Appendix A.1 presents the algorithmic tangent stiffness contributions in their most general form for the finite element framework, while Appendix A.2 discusses the specific tangent operators.

A.1 Derivation of algorithmic tangent stiffness

The contributions to the global stiffness matrix that result from the linearisation of (2.71) can be derived with respect to the displacement field,

$$\mathbf{K}^{\boldsymbol{u}\boldsymbol{u}} = \frac{\mathrm{d}\boldsymbol{f}^{\boldsymbol{u}\,\mathrm{h}}_{\mathrm{int}}}{\mathrm{d}\widehat{\boldsymbol{u}}} = \mathop{\mathbf{A}}_{e=1}^{\mathrm{n_{el}}} \int_{\Omega^e} \nabla_x N_A \cdot \frac{\mathrm{d}\boldsymbol{\sigma}}{\mathrm{d}\boldsymbol{\varepsilon}} \cdot \nabla_x N_D \,\mathrm{d}x \,, \tag{2.103}$$

with respect to the electric potential

$$\mathbf{K}^{\boldsymbol{u}\phi} = \frac{\mathrm{d}\boldsymbol{f}^{\boldsymbol{u}\,\mathrm{h}}_{\mathrm{int}}}{\mathrm{d}\widehat{\boldsymbol{\phi}}} = \mathop{\mathbf{A}}_{e=1}^{\mathrm{n_{el}}} \int_{\Omega^e} -\nabla_x N_A \cdot \frac{\mathrm{d}\boldsymbol{\sigma}}{\mathrm{d}\boldsymbol{e}} \cdot \nabla_x N_E \,\mathrm{d}x \,, \tag{2.104}$$

and with respect to the temperature

$$\mathbf{K}^{\boldsymbol{u}\theta} = \frac{\mathrm{d}\boldsymbol{f}^{\boldsymbol{u}\,\mathrm{h}}_{\mathrm{int}}}{\mathrm{d}\widehat{\boldsymbol{\theta}}} = \mathop{\mathbf{A}}_{e=1}^{\mathrm{n_{el}}} \int_{\Omega^e} \nabla_x N_A \cdot \frac{\mathrm{d}\boldsymbol{\sigma}}{\mathrm{d}\theta} \cdot N_F \,\mathrm{d}x \,. \tag{2.105}$$

Moreover, for the electrical subproblem, the contributions to the global stiffness matrix that result from the linearisation of (2.74) read

$$\mathbf{K}^{\phi\boldsymbol{u}} = \frac{\mathrm{d}\boldsymbol{f}^{\phi\,\mathrm{h}}_{\mathrm{int}}}{\mathrm{d}\widehat{\boldsymbol{u}}} = \mathop{\mathbf{A}}_{e=1}^{\mathrm{n_{el}}} \int_{\Omega^e} \nabla_x N_B \cdot \frac{\mathrm{d}\boldsymbol{j}}{\mathrm{d}\boldsymbol{\varepsilon}} \cdot \nabla_x N_D \,\mathrm{d}x \,, \tag{2.106}$$

and

$$\mathbf{K}^{\phi\phi} = \frac{\mathrm{d}\boldsymbol{f}^{\phi\,\mathrm{h}}_{\mathrm{int}}}{\mathrm{d}\widehat{\boldsymbol{\phi}}} = \mathop{\mathbf{A}}_{e=1}^{\mathrm{n_{el}}} \int_{\Omega^e} -\nabla_x N_B \cdot \frac{\mathrm{d}\boldsymbol{j}}{\mathrm{d}\boldsymbol{e}} \cdot \nabla_x N_E \,\mathrm{d}x \,, \tag{2.107}$$

as well as

$$\mathbf{K}^{\phi\theta} = \frac{\mathrm{d}\boldsymbol{f}^{\phi\,\mathrm{h}}_{\mathrm{int}}}{\mathrm{d}\widehat{\boldsymbol{\theta}}} = \mathop{\mathbf{A}}_{e=1}^{\mathrm{n_{el}}} \int_{\Omega^e} \nabla_x N_B \cdot \frac{\mathrm{d}\boldsymbol{j}}{\mathrm{d}\theta} N_F \,\mathrm{d}x \,. \tag{2.108}$$

The contributions to the global stiffness matrix that result from the linearisation of (2.76) with respect to displacement field,

$$\mathbf{K}^{\theta\boldsymbol{u}} = \frac{\mathrm{d}\boldsymbol{f}^{\theta\,\mathrm{h}}_{\mathrm{int}}}{\mathrm{d}\widehat{\boldsymbol{u}}} = \mathop{\mathbf{A}}_{e=1}^{\mathrm{n_{el}}} \int_{\Omega^e} \nabla_x N_C \cdot \frac{\mathrm{d}\boldsymbol{q}}{\mathrm{d}\boldsymbol{\varepsilon}} \cdot \nabla_x N_D \,\mathrm{d}x \,, \tag{2.109}$$

as well as electric potential field,

$$\mathbf{K}^{\theta\phi} = \frac{\mathrm{d}\boldsymbol{f}_{\mathrm{int}}^{\theta\,\mathrm{h}}}{\mathrm{d}\widehat{\boldsymbol{\phi}}} = \mathop{\mathbf{A}}_{e=1}^{\mathrm{n_{el}}} \int_{\Omega^e} \nabla_x N_C \cdot \frac{\mathrm{d}\left[\boldsymbol{q}\right]}{\mathrm{d}\boldsymbol{e}} \cdot \nabla_x N_E \,\mathrm{d}x\,, \tag{2.110}$$

and temperature field

$$\mathbf{K}^{\theta\theta} = \frac{\mathrm{d}\boldsymbol{f}_{\mathrm{int}}^{\theta\,\mathrm{h}}}{\mathrm{d}\widehat{\boldsymbol{\theta}}} = \mathop{\mathbf{A}}_{e=1}^{\mathrm{n_{el}}} \int_{\Omega^e} \nabla_x N_C \cdot \frac{\mathrm{d}\boldsymbol{q}}{\mathrm{d}\nabla_x\theta} \cdot \nabla_x N_F \,\mathrm{d}x\,. \tag{2.111}$$

are obtained. Finally, the contributions to the global stiffness matrix that result from the linearisation of volumetric source terms (2.77) are given

$$\mathbf{K}^{\theta\boldsymbol{u}} = \frac{\mathrm{d}\boldsymbol{f}_{\mathrm{vol}}^{\theta\,\mathrm{h}}}{\mathrm{d}\widehat{\boldsymbol{u}}} = \mathop{\mathbf{A}}_{e=1}^{\mathrm{n_{el}}} \int_{\Omega^e} N_C \,\frac{\mathrm{d}\left[\rho\, r + \boldsymbol{j}\cdot\boldsymbol{e}\right]}{\mathrm{d}\boldsymbol{\varepsilon}} \cdot \nabla_x N_D \,\mathrm{d}x\,, \tag{2.112}$$

and

$$\mathbf{K}^{\theta\phi} = \frac{\mathrm{d}\boldsymbol{f}_{\mathrm{vol}}^{\theta\,\mathrm{h}}}{\mathrm{d}\widehat{\boldsymbol{\phi}}} = \mathop{\mathbf{A}}_{e=1}^{\mathrm{n_{el}}} \int_{\Omega^e} N_C \frac{\mathrm{d}\left[\rho\, r + \boldsymbol{j}\cdot\boldsymbol{e}\right]}{\mathrm{d}\boldsymbol{e}} \cdot \nabla_x N_E \,\mathrm{d}x\,, \tag{2.113}$$

as well as

$$\mathbf{K}^{\theta\theta} = \frac{\mathrm{d}\boldsymbol{f}_{\mathrm{vol}}^{\theta\,\mathrm{h}}}{\mathrm{d}\widehat{\boldsymbol{\theta}}} = \mathop{\mathbf{A}}_{e=1}^{\mathrm{n_{el}}} \int_{\Omega^e} N_C \,\frac{\mathrm{d}\left[\rho\, r + \boldsymbol{j}\cdot\boldsymbol{e}\right]}{\mathrm{d}\nabla_x\theta} \cdot \nabla_x N_F \,\mathrm{d}x\,. \tag{2.114}$$

A.2 Derivation of sensitivities

Based on the constitutive relations described in Section 2.5.1, the sensitivities of stress, electric current density and heat flux are derived. The non-zero sensitivities of stress read

$$\frac{\mathrm{d}\,\boldsymbol{\sigma}}{\mathrm{d}\,\boldsymbol{\varepsilon}}\left(\boldsymbol{x}\right) = K\left(\boldsymbol{x}\right)\boldsymbol{I}\otimes\boldsymbol{I} + 2\,G\left(\boldsymbol{x}\right)\mathbf{I}^{\mathrm{dev}}\,, \tag{2.115}$$

$$\frac{\mathrm{d}\boldsymbol{\sigma}}{\mathrm{d}\theta}\left(\boldsymbol{x}\right) = -3\,\alpha\left(\boldsymbol{x}\right)K\left(\boldsymbol{x}\right)\;\boldsymbol{I}\,. \tag{2.116}$$

It is observed that there is no direct coupling between stress and the electric field vector for electrical conductors. Consequently, electrical phenomena do not directly influence the mechanical behaviour within this formulation.

To derive the specific form of the sensitivities in the electrical subproblem, the temperature dependence of the electrical conductivity must first be specified. Here, a simple functional relationship between the electrical conductivity tensor and temperature, typical for metals, is adopted as given in (2.100). Physically speaking, electrical conductivity

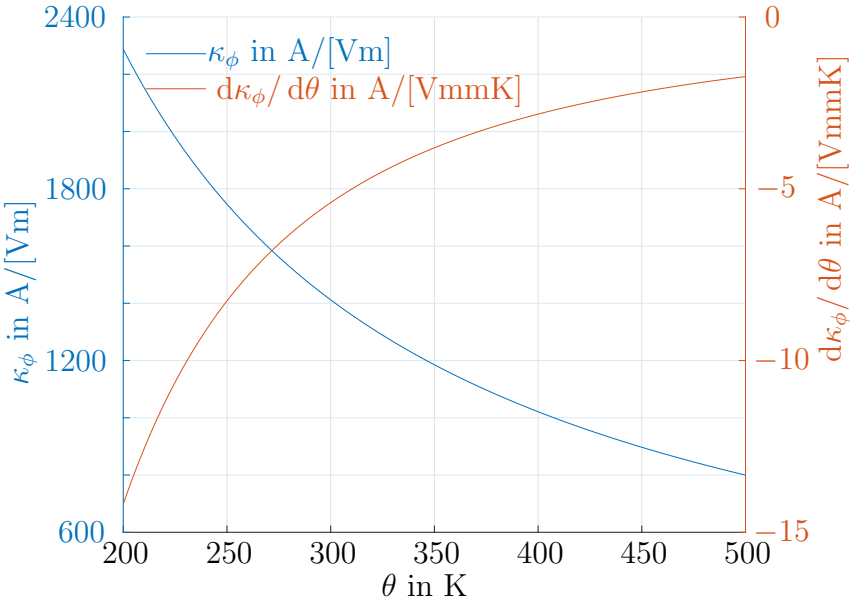

Figure 2.10: Temperature-dependent electrical conductivity of copper over the range 200 K to 500 K, based on the derivative expressions (2.117) and (2.118).

decreases with increasing temperature which is further illustrated in Figure 2.10. The resulting non-zero sensitivities are expressed as

$$\frac{\mathrm{d}\boldsymbol{j}}{\mathrm{d}\boldsymbol{e}}\left(\theta,\boldsymbol{x}\right)=\kappa_\phi\left(\theta,\boldsymbol{x}\right)\,\boldsymbol{I}=\frac{\kappa_{\phi 0}}{1+\mu\left[\theta-\theta_0\right]}\,\boldsymbol{I}\,, \tag{2.117}$$

$$\frac{\mathrm{d}\boldsymbol{j}}{\mathrm{d}\theta}\left(\theta,\boldsymbol{x}\right)=\frac{\mathrm{d}\kappa_\phi\left(\theta,\boldsymbol{x}\right)}{\mathrm{d}\theta}\,\boldsymbol{e}\left(\boldsymbol{x}\right)=-\frac{\kappa_{\phi 0}\,\mu}{\left[1+\mu\left[\theta-\theta_0\right]\right]^2}\,\boldsymbol{e}\left(\boldsymbol{x}\right)\,. \tag{2.118}$$

The current formulation assumes no coupling between the electric current density vector and the strain tensor. However, in models with deformation-dependent conductivity or within a finite-strain framework, this coupling yields additional non-zero sensitivity contributions.

Finally, the non-zero sensitivities of heat flux

$$\frac{\mathrm{d}\boldsymbol{q}}{\mathrm{d}\nabla_x\theta}\left(\boldsymbol{x}\right)=-\kappa_\theta\left(\boldsymbol{x}\right)\boldsymbol{I}\,, \tag{2.119}$$

and the source term due to Joule heating

$$\frac{\mathrm{d}\left[\boldsymbol{j}\cdot\boldsymbol{e}\right]}{\mathrm{d}\boldsymbol{e}}\left(\boldsymbol{x}\right)=\boldsymbol{j}\left(\boldsymbol{x}\right), \tag{2.120}$$

are calculated. The proposed small-strain framework assumes no coupling between heat flux vector and the strain tensor.

3 A thermo-electro-mechanically cohesive zone model for damage predictions

Every material exhibits heterogeneous behaviour at a certain scale. Focusing for instance on classic problems of materials science, multiphase microstructures that contain grain and phase boundaries, and, possibly, microcracks are studied. In these intrinsically heterogeneous materials, the effective material response is significantly influenced by the presence of material interfaces. Grain boundaries are, for instance, an example of material interfaces which influence electrical properties, such as resistivity. Moreover, predicting the evolution of interfacial damage is essential in order to optimise the material's performance and reliability.

Motivated by the change of electrical properties due to damage evolution, an electro-mechanically coupled cohesive zone formulation for electrical conductors was proposed by Kaiser and Menzel [98], which provides the basis for the current work. In the current chapter, an extension of the proposed framework to additionally account for thermal coupling is considered. The scope of the present chapter is twofold:

- *It establishes a thermodynamically consistent cohesive zone formulation for coupled thermo-electro-mechanical processes in the presence of material interfaces, including the derivation of balance laws, interface-specific dissipation inequalities, and the associated finite element framework.*

- *It demonstrates the applicability of the proposed model through numerical simulations ranging from analytical benchmark problems to realistic two-dimensional interface failure scenarios, thereby laying the foundation for further developments such as interface elasticity or large deformation formulations.*

In Section 3.1, the thermodynamic fundamentals for the mechanical, electrical and thermal subproblems are summarised, and the constitutive restrictions resulting from the dissipation inequality are investigated. With the fundamental set of balance equations at hand, a weak form of the problem is derived and a finite element implementation is proposed in Section 3.2. Section 3.3 deals with the specific constitutive relations for bulk and interface, before representative simulation results are studied in Section 3.4 to

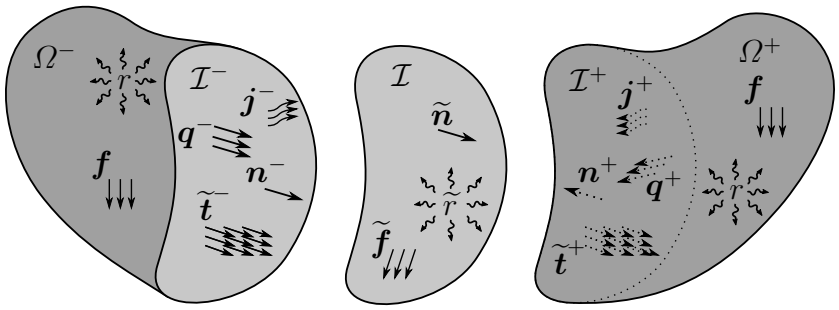

Figure 3.1: Specification of quantities in the control volume Ω and on the interface $\mathcal{I}$ for thermo-electro-mechanical interface problems. Reprinted from [74] under the terms of the Creative Commons Attribution License (CC BY).

demonstrate the capabilities of the proposed framework. In particular, an analytical solution in a quasi-one-dimensional setting is derived for validation purposes, and thermo-electro-mechanically-induced failure processes in wire bonds are exemplarily studied in a two-dimensional setting.

3.1 Continuum thermo-electrodynamics

$^{\text{qtd.}}_{[74]}\{$The governing equations for electro-mechanically coupled cohesive zone formulations were derived in [98] and detailed studies of the principle model properties were carried out. Against this background, the derivations for the mechanical and electrical subproblems are briefly summarised in the following and not presented in detail to avoid repetitiveness.

In particular, the mechanical subproblem is discussed in Section 3.1.1, the electrical subproblem in Section 3.1.2 and the thermal problem in Section 3.1.3, before the restrictions that result from the evaluation of the dissipation inequality are eventually studied in Section 3.1.4. A graphical illustration of the thermo-electro-mechanical problem considered is provided in Figure 3.1. Furthermore, quantities at the two opposing sides of an interface will be indicated by superscripts $\bullet^-$ and $\bullet^+$ such that the jump of a quantity across the interface follows as

$$[\![\bullet]\!] = \bullet^+ - \bullet^- \quad , \tag{3.1}$$

the interfacial mean value reads

$$\{\!\{\bullet\}\!\} = \frac{1}{2}\left[\bullet^+ + \bullet^-\right] \quad , \tag{3.2}$$

and the identity

$$[\![\bullet *]\!] = [\![\bullet]\!]\,\{\!\{*\}\!\} + \{\!\{\bullet\}\!\}\,[\![*]\!] \quad , \tag{3.3}$$

holds. As this work proceeds a small strain setting shall be considered.$\}^{\text{qtd.}}_{[74]}$

3.1.1 Mechanical subproblem

qtd. [74] {The control volume $\Omega \subset \mathbb{R}^d$ with material interface $\mathcal{I} \subset \mathbb{R}^{d-1}$ is assumed to be loaded by tractions

$$\boldsymbol{t}(\boldsymbol{x}) = \boldsymbol{\sigma}(\boldsymbol{x}) \cdot \boldsymbol{n}(\boldsymbol{x}) \,, \tag{3.4}$$

where $\boldsymbol{\sigma} : \Omega \to \mathrm{Lin}\left(\mathbb{R}^d, \mathbb{R}^d\right)$ and $\boldsymbol{n} : \Omega \to \mathbb{R}^d$ correspond to the stress tensor and the outward unit normal vector, respectively, and by volume distributed forces $\boldsymbol{f} : \Omega \to \mathbb{R}^d$ in the bulk as well as surface distributed forces $\widetilde{\boldsymbol{f}} : \mathcal{I} \to \mathbb{R}^d$ at the interface. The specific integral form of the balance equation of linear momentum in quasi-static representation is obtained when neglecting the tangential forces on $\partial\mathcal{I}$ as follows

$$\boldsymbol{0} = \int_\Omega \rho(\boldsymbol{x})\, \boldsymbol{f}(\boldsymbol{x}) \,\mathrm{d}x + \int_{\mathcal{I}} \widetilde{\rho}(\widetilde{\boldsymbol{x}})\, \widetilde{\boldsymbol{f}}(\widetilde{\boldsymbol{x}}) \,\mathrm{d}x + \int_{\partial\Omega} \boldsymbol{t}(\boldsymbol{x}) \,\mathrm{d}x \,, \tag{3.5}$$

where $\rho : \Omega \to \mathbb{R}$ and $\widetilde{\rho} : \mathcal{I} \to \mathbb{R}$ are the mass density of bulk and interface. } qtd. [74] Following the derivation in [98], utilising the divergence theorem results in

$$\begin{aligned}
\int_{\partial\Omega} \boldsymbol{t}(\boldsymbol{x}) \,\mathrm{d}x &= \int_{\partial\Omega} \boldsymbol{t}(\boldsymbol{x}) \,\mathrm{d}x + [-1+1] \int_{\mathcal{I}^+ \cup \mathcal{I}^-} \boldsymbol{t}(\boldsymbol{x}) \,\mathrm{d}x \\
&= \int_{\partial\Omega^+} \boldsymbol{t}(\boldsymbol{x}) \,\mathrm{d}x + \int_{\partial\Omega^-} \boldsymbol{t}(\boldsymbol{x}) \,\mathrm{d}x + \int_{\mathcal{I}} [\![\widetilde{\boldsymbol{t}}]\!](\widetilde{\boldsymbol{x}}) \,\mathrm{d}x \\
&= \int_{\Omega^+} \nabla_x \cdot \boldsymbol{\sigma}(\boldsymbol{x}) \,\mathrm{d}x \int_{\Omega^-} \nabla_x \cdot \boldsymbol{\sigma}(\boldsymbol{x}) \,\mathrm{d}x + \int_{\mathcal{I}} [\![\widetilde{\boldsymbol{t}}]\!](\widetilde{\boldsymbol{x}}) \,\mathrm{d}x \,.
\end{aligned} \tag{3.6}$$

qtd. [74] {Carrying out the localisation of the balance equation for a continuum featuring material interfaces, the local form of the balance equation of linear momentum for the bulk and the interface

$$\nabla_x \cdot \boldsymbol{\sigma}(\boldsymbol{x}) + \rho(\boldsymbol{x})\, \boldsymbol{f}(\boldsymbol{x}) = \boldsymbol{0} \quad \text{(in bulk)} \,, \tag{3.7a}$$

$$[\![\widetilde{\boldsymbol{t}}]\!](\widetilde{\boldsymbol{x}}) + \widetilde{\rho}(\boldsymbol{x})\, \widetilde{\boldsymbol{f}}(\boldsymbol{x}) = \boldsymbol{0} \quad \text{(at interface)} \,, \tag{3.7b}$$

are obtained. By neglecting body forces at the interface, (3.7b) simplifies to the condition that the tractions at the opposing sides of the interface must be equal, i.e.

$$[\![\widetilde{\boldsymbol{t}}]\!](\widetilde{\boldsymbol{x}}) = \widetilde{\boldsymbol{t}}^{+}(\widetilde{\boldsymbol{x}}) - \widetilde{\boldsymbol{t}}^{-}(\widetilde{\boldsymbol{x}}) \,, \quad \widetilde{\boldsymbol{t}}^{+}(\widetilde{\boldsymbol{x}}) = \boldsymbol{\sigma}^{+}\left(\boldsymbol{x}^{+}\right) \cdot \widetilde{\boldsymbol{n}}(\widetilde{\boldsymbol{x}}) \,, \quad \widetilde{\boldsymbol{t}}^{-}(\widetilde{\boldsymbol{x}}) = \boldsymbol{\sigma}^{-}\left(\boldsymbol{x}^{-}\right) \cdot \widetilde{\boldsymbol{n}}(\widetilde{\boldsymbol{x}}) \,. \tag{3.8}$$

In a small deformation setting, the balance equations are evaluated in the undeformed configuration, namely $\widetilde{\boldsymbol{x}} = \boldsymbol{x}^{+} = \boldsymbol{x}^{-}$. Under the same assumptions, the conservation of angular momentum in integral form is written as } qtd. [74]

$$\boldsymbol{0} = \int_\Omega \boldsymbol{x} \times \rho(\boldsymbol{x})\, \boldsymbol{f}(\boldsymbol{x}) \,\mathrm{d}x + \int_{\mathcal{I}} \boldsymbol{x} \times \widetilde{\rho}(\widetilde{\boldsymbol{x}})\, \widetilde{\boldsymbol{f}}(\widetilde{\boldsymbol{x}}) \,\mathrm{d}x + \int_{\partial\Omega} \boldsymbol{x} \times \boldsymbol{t}(\boldsymbol{x}) \,\mathrm{d}x \,. \tag{3.9}$$

Similar to the balance of linear momentum, (3.9) takes the form

$$\begin{aligned}\mathbf{0} = &\int_{\Omega^+} \boldsymbol{x} \times [\nabla_x \cdot \boldsymbol{\sigma}(\boldsymbol{x}) + \rho(\boldsymbol{x})\, \boldsymbol{f}(\boldsymbol{x})] + \boldsymbol{\epsilon} : \boldsymbol{\sigma}^{\mathrm{t}}(\boldsymbol{x})\, \mathrm{d}x \\ &+ \int_{\Omega^-} \boldsymbol{x} \times [\nabla_x \cdot \boldsymbol{\sigma}(\boldsymbol{x}) + \rho(\boldsymbol{x})\, \boldsymbol{f}(\boldsymbol{x})] + \boldsymbol{\epsilon} : \boldsymbol{\sigma}^{\mathrm{t}}(\boldsymbol{x})\, \mathrm{d}x \\ &+ \int_{\mathcal{I}} \boldsymbol{x} \times \left[[\![\widetilde{\boldsymbol{t}}]\!](\widetilde{\boldsymbol{x}}) + \widetilde{\rho}(\widetilde{\boldsymbol{x}})\, \widetilde{\boldsymbol{f}}(\widetilde{\boldsymbol{x}}) \right] \mathrm{d}x\,. \end{aligned} \tag{3.10}$$

{qtd. [74]}{After localisation (3.10) simplifies to the classic symmetry condition of the bulk stress tensor, namely}{qtd. [74]}

$$\boldsymbol{\sigma}(\boldsymbol{x}) = \boldsymbol{\sigma}^{\mathrm{t}}(\boldsymbol{x}) \quad \text{(in bulk)}\,. \tag{3.11}$$

3.1.2 Electrical subproblem

{qtd. [74]}{The control volume Ω with material interface $\mathcal{I}$ is assumed to be loaded by

$$i(\boldsymbol{x}) = \boldsymbol{j}(\boldsymbol{x}) \cdot \boldsymbol{n}(\boldsymbol{x})\ , \tag{3.12}$$

where $\boldsymbol{j} : \Omega \to \mathbb{R}^d$ corresponds to the electric current density vector. The specific form of the continuity equation for the electric charge is obtained by neglecting the tangential component of the electric current density vector on $\partial\mathcal{I}$ as follows}{qtd. [74]}

$$0 = \int_{\partial\Omega} \boldsymbol{j}(\boldsymbol{x}) \cdot \boldsymbol{n}(\boldsymbol{x})\, \mathrm{d}x\,. \tag{3.13}$$

Following the same procedure as in Section 3.1.1, one obtains

$$\begin{aligned} 0 &= \int_{\partial\Omega} \boldsymbol{j}(\boldsymbol{x}) \cdot \boldsymbol{n}(\boldsymbol{x})\, \mathrm{d}x + [-1+1] \int_{\mathcal{I}^+ \cup \mathcal{I}^-} \boldsymbol{j}(\boldsymbol{x}) \cdot \boldsymbol{n}(\boldsymbol{x})\, \mathrm{d}x \\ &= \int_{\partial\Omega^+} \boldsymbol{j}(\boldsymbol{x}) \cdot \boldsymbol{n}(\boldsymbol{x})\, \mathrm{d}x + \int_{\partial\Omega^-} \boldsymbol{j}(\boldsymbol{x}) \cdot \boldsymbol{n}(\boldsymbol{x})\, \mathrm{d}x + \int_{\mathcal{I}} [\![\widetilde{i}]\!](\widetilde{\boldsymbol{x}})\, \mathrm{d}x \\ &= \int_{\Omega^+} \nabla_x \cdot \boldsymbol{j}(\boldsymbol{x})\, \mathrm{d}x + \int_{\Omega^-} \nabla_x \cdot \boldsymbol{j}(\boldsymbol{x})\, \mathrm{d}x + \int_{\mathcal{I}} [\![\widetilde{i}]\!](\widetilde{\boldsymbol{x}})\, \mathrm{d}x \end{aligned} \tag{3.14}$$

and {qtd. [74]}{the local versions of the continuity equation for the electric charge for the bulk and the interface read

$$\nabla_x \cdot \boldsymbol{j}(\boldsymbol{x}) = 0 \quad \text{(in bulk)}\,, \tag{3.15a}$$

$$[\![\widetilde{i}]\!](\widetilde{\boldsymbol{x}}) = 0 \quad \text{(at interface)}\,. \tag{3.15b}$$

Similar to (3.7b), relation (3.15b) stipulates that the electric current at the opposing sides of the interface is equal, i.e.

$$[\![\widetilde{i}]\!](\widetilde{\boldsymbol{x}}) = \widetilde{i}^{+}(\widetilde{\boldsymbol{x}}) - \widetilde{i}^{-}(\widetilde{\boldsymbol{x}})\ , \quad \widetilde{i}^{+}(\widetilde{\boldsymbol{x}}) = \boldsymbol{j}^{+}\left(\boldsymbol{x}^{+}\right) \cdot \widetilde{\boldsymbol{n}}(\widetilde{\boldsymbol{x}})\,, \quad \widetilde{i}^{-}(\widetilde{\boldsymbol{x}}) = \boldsymbol{j}^{-}\left(\boldsymbol{x}^{+}\right) \cdot \widetilde{\boldsymbol{n}}(\widetilde{\boldsymbol{x}})\ . \tag{3.16}$$

Under the assumption of a (quasi-)stationary state, Faraday's law of induction simplifies and can naturally be fulfilled by the introduction of a scalar-valued electric potential field ϕ with

$$\boldsymbol{e}\left(\boldsymbol{x}\right) = -\nabla_x \phi\left(\boldsymbol{x}\right) \quad \text{(in bulk)}\,, \tag{3.17}$$

where $\boldsymbol{e} : \Omega \to \mathbb{R}^d$ corresponds to the electric field vector. The localisation of Faraday's law of induction at the interface yields no additional condition for cohesive zone formulations. For a detailed derivation of the local form of Faraday's law of induction the reader may refer to [98].}$^{\text{qtd.}}_{[74]}$

3.1.3 Thermal problem

$^{\text{qtd.}}_{[74]}${In the following, focus is set on thermo-electro-mechanical problems with emphasis on the fundamentals of thermo-electro-mechanically coupled cohesive zone formulations. The governing form of the balance equation of energy for a continuum with interfaces that is subjected to mechanical, electrical and thermal loads is summarised in the following.

The (quasi-static) balance equation of energy for a continuum with interfaces reads

$$\frac{\mathrm{d}}{\mathrm{d}t}\int_{\Omega} \rho\left(\boldsymbol{x}\right) e\left(\boldsymbol{x}\right)\,\mathrm{d}x + \frac{\mathrm{d}}{\mathrm{d}t}\int_{\mathcal{I}} \widetilde{\rho}\left(\boldsymbol{x}\right) \widetilde{e}\left(\boldsymbol{x}\right)\,\mathrm{d}x = \mathcal{P}^{\boldsymbol{u}}\left(\boldsymbol{x}\right) + \mathcal{P}^{\theta}\left(\boldsymbol{x}\right) + \mathcal{P}^{\phi}\left(\boldsymbol{x}\right) \tag{3.18}$$

where $e : \Omega \to \mathbb{R}$ and $\widetilde{e} : \mathcal{I} \to \mathbb{R}$ correspond to the mass-specific internal energy densities of the bulk and the interface, respectively, and t denotes time. The single contributions to the mechanical power $\mathcal{P}^{\boldsymbol{u}}$, the electrical power $\mathcal{P}^{\phi}$, and the thermal power $\mathcal{P}^{\theta}$ are specified under the assumption of a quasi-stationary electrical problem. The mechanical power $\mathcal{P}^{\boldsymbol{u}}$ reads

$$\begin{aligned}
\mathcal{P}^{\boldsymbol{u}} &= \int_{\Omega} \dot{\boldsymbol{u}}\left(\boldsymbol{x}\right) \cdot \rho\left(\boldsymbol{x}\right) \boldsymbol{f}\left(\boldsymbol{x}\right)\,\mathrm{d}x + \int_{\mathcal{I}} \dot{\widetilde{\boldsymbol{u}}}\left(\widetilde{\boldsymbol{x}}\right) \cdot \widetilde{\rho}\left(\widetilde{\boldsymbol{x}}\right) \widetilde{\boldsymbol{f}}\left(\widetilde{\boldsymbol{x}}\right)\,\mathrm{d}x + \int_{\partial\Omega} \dot{\boldsymbol{u}}\left(\boldsymbol{x}\right) \cdot \boldsymbol{t}\left(\boldsymbol{x}\right)\,\mathrm{d}x \\
&= \int_{\Omega\setminus\mathcal{I}} \nabla_x \dot{\boldsymbol{u}}\left(\boldsymbol{x}\right) : \boldsymbol{\sigma}\left(\boldsymbol{x}\right)\,\mathrm{d}x + \int_{\Omega\setminus\mathcal{I}} \dot{\boldsymbol{u}}\left(\boldsymbol{x}\right) \cdot \left[\nabla_x \cdot \boldsymbol{\sigma}\left(\boldsymbol{x}\right) + \rho\left(\boldsymbol{x}\right) \boldsymbol{f}\left(\boldsymbol{x}\right)\right]\,\mathrm{d}x \\
&+ \int_{\mathcal{I}} [\![\dot{\boldsymbol{u}}]\!]\left(\widetilde{\boldsymbol{x}}\right) \cdot \{\!\{\widetilde{\boldsymbol{t}}\}\!\}\left(\widetilde{\boldsymbol{x}}\right)\,\mathrm{d}x + \int_{\mathcal{I}} \dot{\widetilde{\boldsymbol{u}}}\left(\widetilde{\boldsymbol{x}}\right) \cdot \widetilde{\rho}\left(\widetilde{\boldsymbol{x}}\right) \widetilde{\boldsymbol{f}}\left(\widetilde{\boldsymbol{x}}\right) + \{\!\{\dot{\boldsymbol{u}}\}\!\}\left(\widetilde{\boldsymbol{x}}\right) \cdot [\![\widetilde{\boldsymbol{t}}]\!]\left(\widetilde{\boldsymbol{x}}\right)\,\mathrm{d}x\,,
\end{aligned} \tag{3.19}$$

where $\dot{\boldsymbol{u}} : \Omega \to \mathbb{R}^d$ and $\dot{\widetilde{\boldsymbol{u}}} : \mathcal{I} \to \mathbb{R}^d$ are velocity fields. Following the specific assumption adopted in [98] with regard to the interface position, namely $\widetilde{\boldsymbol{u}} = \{\!\{\boldsymbol{u}\}\!\}$, the mechanical power term simplifies to

$$\mathcal{P}^{\boldsymbol{u}}\left(\boldsymbol{x}\right) = \int_{\Omega\setminus\mathcal{I}} \nabla_x \dot{\boldsymbol{u}}\left(\boldsymbol{x}\right) : \boldsymbol{\sigma}\left(\boldsymbol{x}\right)\,\mathrm{d}x + \int_{\mathcal{I}} [\![\dot{\boldsymbol{u}}]\!]\left(\widetilde{\boldsymbol{x}}\right) \cdot \{\!\{\widetilde{\boldsymbol{t}}\}\!\}\left(\widetilde{\boldsymbol{x}}\right)\,\mathrm{d}x\,. \tag{3.20}$$

The electrical power $\mathcal{P}^{\phi}$ is assumed to be of purely dissipative type and reads

$$\mathcal{P}^{\phi}\left(\boldsymbol{x}\right) = \int_{\Omega\setminus\mathcal{I}} \boldsymbol{j}\left(\boldsymbol{x}\right) \cdot \boldsymbol{e}\left(\boldsymbol{x}\right)\,\mathrm{d}x + \int_{\mathcal{I}} -\{\!\{\widetilde{i}\}\!\}\left(\widetilde{\boldsymbol{x}}\right) [\![\phi]\!]\left(\widetilde{\boldsymbol{x}}\right)\,\mathrm{d}x\,. \tag{3.21}$$

The thermal power $\mathcal{P}^{\theta}$ is given by

$$\mathcal{P}^{\theta}(\boldsymbol{x}) = \int_{\Omega} \rho(\boldsymbol{x})\, r(\boldsymbol{x})\, \mathrm{d}x - \int_{\partial\Omega} \boldsymbol{q}(\boldsymbol{x}) \cdot \boldsymbol{n}(\boldsymbol{x})\, \mathrm{d}x + \int_{\mathcal{I}} \widetilde{\rho}(\widetilde{\boldsymbol{x}})\, \widetilde{r}(\widetilde{\boldsymbol{x}})\, \mathrm{d}x\,, \tag{3.22}$$

where $\boldsymbol{q} : \Omega \to \mathbb{R}^d$ denotes the heat flux vector, and where $r : \Omega \to \mathbb{R}$ and $\widetilde{r} : \mathcal{I} \to \mathbb{R}$ correspond to the mass-specific heat source in the bulk and the mass-specific heat source at the interface. Similar to the mechanical and the electrical problem, the tangential component of the heat flux vector on $\partial\mathcal{I}$ is neglected and an alternative representation of (3.22) is obtained as

$$\mathcal{P}^{\theta}(\boldsymbol{x}) = \int_{\Omega\setminus\mathcal{I}} \rho(\boldsymbol{x})\, r(\boldsymbol{x}) - \nabla_x \cdot \boldsymbol{q}(\boldsymbol{x})\, \mathrm{d}x + \int_{\mathcal{I}} \widetilde{\rho}(\widetilde{\boldsymbol{x}})\, \widetilde{r}(\widetilde{\boldsymbol{x}}) - [\![\boldsymbol{q} \cdot \widetilde{\boldsymbol{n}}]\!](\widetilde{\boldsymbol{x}})\, \mathrm{d}x\,. \tag{3.23}$$

By inserting (3.20), (3.21) and (3.23) into (3.18), localising the related equation and additionally assuming that the heat source $\widetilde{r}$ at the interface $\partial\mathcal{I}$ is negligible, the thermal problem for the continuum with interfaces takes the form$\}^{\text{qtd.}}_{[74]}$

$$\rho(\boldsymbol{x})\, \dot{e}(\boldsymbol{x}) = \boldsymbol{\sigma}(\boldsymbol{x}) : \dot{\boldsymbol{\varepsilon}}(\boldsymbol{x}) + \rho(\boldsymbol{x})\, r(\boldsymbol{x}) - \nabla_x \cdot \boldsymbol{q}(\boldsymbol{x}) + \boldsymbol{j}(\boldsymbol{x}) \cdot \boldsymbol{e}(\boldsymbol{x}) \quad \text{(in bulk)}\,, \tag{3.24a}$$

$$\widetilde{\rho}(\widetilde{\boldsymbol{x}})\, \dot{\widetilde{e}}(\widetilde{\boldsymbol{x}}) = \{\!\{\widetilde{\boldsymbol{t}}\}\!\}(\widetilde{\boldsymbol{x}}) \cdot [\![\dot{\boldsymbol{u}}]\!](\widetilde{\boldsymbol{x}}) - [\![\boldsymbol{q} \cdot \widetilde{\boldsymbol{n}}]\!](\widetilde{\boldsymbol{x}}) - \{\!\{\widetilde{i}\}\!\}(\widetilde{\boldsymbol{x}})\, [\![\phi]\!](\widetilde{\boldsymbol{x}}) \quad \text{(at interface)}\,. \tag{3.24b}$$

3.1.4 Dissipation inequality

$^{\text{qtd.}}_{[74]}\{$For standard solids, the global form of the second law of thermodynamics states that

$$\int_{\Omega} \rho(\boldsymbol{x})\, \dot{s}(\boldsymbol{x})\, \mathrm{d}x - R_{\text{ext}}(\boldsymbol{x}) \geq 0\,. \tag{3.25}$$

In (3.25), $s : \Omega \to \mathbb{R}$ and $R_{\text{ext}} : \Omega \to \mathbb{R}$ denote the mass-specific entropy density of the bulk and the rate of entropy input which takes the form

$$R_{\text{ext}}(\boldsymbol{x}) = \int_{\Omega} \frac{\rho(\boldsymbol{x})\, r(\boldsymbol{x})}{\theta(\boldsymbol{x})}\, \mathrm{d}x - \int_{\partial\Omega} \frac{\boldsymbol{q}(\boldsymbol{x}) \cdot \boldsymbol{n}(\boldsymbol{x})}{\theta(\boldsymbol{x})}\, \mathrm{d}x\,. \tag{3.26}$$

Similar to the rate of internal energy, the entropy rate is extended by the contributions of the interface according to

$$\frac{\mathrm{d}}{\mathrm{d}t} \int_{\Omega} \rho(\boldsymbol{x})\, s(\boldsymbol{x})\, \mathrm{d}x + \frac{\mathrm{d}}{\mathrm{d}t} \int_{\mathcal{I}} \widetilde{\rho}(\widetilde{\boldsymbol{x}})\, \widetilde{s}(\boldsymbol{x})\, \mathrm{d}x \geq \int_{\Omega} \frac{\rho(\boldsymbol{x})\, r(\boldsymbol{x})}{\theta(\boldsymbol{x})}\, \mathrm{d}x - \int_{\partial\Omega} \frac{\boldsymbol{q}(\boldsymbol{x}) \cdot \boldsymbol{n}(\boldsymbol{x})}{\theta(\boldsymbol{x})}\, \mathrm{d}x\,, \tag{3.27}$$

where $\theta : \Omega \to \mathbb{R}$ and $\widetilde{s} : \mathcal{I} \to \mathbb{R}$ are the absolute temperature and the mass-specific entropy density of the interface.

In the following, focus is laid on the evaluation of the dissipation inequality for the bulk, before the dissipation inequality at the interface is evaluated. To avoid repetition, the dissipation analysis for bulk follows the derivations presented in Section 2.2.4. For the transient case, one eventually arrives at the local form of dissipation equality, namely

$$\begin{aligned}\rho\left(\boldsymbol{x}\right)c_{\mathrm{v}}\left(\boldsymbol{x}\right)\dot{\theta}\left(\boldsymbol{x}\right)+\theta\left(\boldsymbol{x}\right)\boldsymbol{\beta}_{\mathrm{v}}\left(\boldsymbol{x}\right):\dot{\boldsymbol{\varepsilon}}\left(\boldsymbol{x}\right)-\left[\boldsymbol{\kappa}\left(\boldsymbol{x}\right)-\theta\left(\boldsymbol{x}\right)\frac{\partial\boldsymbol{\kappa}\left(\boldsymbol{x}\right)}{\partial\theta\left(\boldsymbol{x}\right)}\right]\cdot\dot{\boldsymbol{k}}\left(\boldsymbol{x}\right)\\-\left[-\nabla_{x}\cdot\boldsymbol{q}\left(\boldsymbol{x}\right)+\rho\left(\boldsymbol{x}\right)r\left(\boldsymbol{x}\right)+\boldsymbol{j}\left(\boldsymbol{x}\right)\cdot\boldsymbol{e}\left(\boldsymbol{x}\right)\right]=0\end{aligned}\tag{3.28}$$

In this work, the evolution of internal variables associated with irreversible processes (e.g., plasticity, damage) is assumed to be negligible, i.e., $\dot{\boldsymbol{k}}=\boldsymbol{0}$. Consequently, the corresponding internal dissipation term in the thermal energy balance is neglected. Additionally, under the quasi-static assumption with negligible elastic strain rates, the thermoelastic coupling term $\boldsymbol{\beta}_{\mathrm{v}}:\dot{\boldsymbol{\varepsilon}}$ is considered insignificant and is therefore omitted from the thermal energy balance. The final result takes the form

$$\nabla_{x}\cdot\boldsymbol{q}\left(\boldsymbol{x}\right)-\boldsymbol{j}\left(\boldsymbol{x}\right)\cdot\boldsymbol{e}\left(\boldsymbol{x}\right)-\rho\left(\boldsymbol{x}\right)r\left(\boldsymbol{x}\right)=0\,.\tag{3.29}$$

Moreover, the interface related local form of balance of entropy takes the form

$$\widetilde{\rho}\left(\widetilde{\boldsymbol{x}}\right)\dot{\widetilde{s}}\left(\widetilde{\boldsymbol{x}}\right)+\left\{\!\!\left\{\theta^{-1}\right\}\!\!\right\}\left(\widetilde{\boldsymbol{x}}\right)\left[\!\left[\boldsymbol{q}\cdot\widetilde{\boldsymbol{n}}\right]\!\right]\left(\widetilde{\boldsymbol{x}}\right)+\left\{\!\!\left\{\boldsymbol{q}\cdot\widetilde{\boldsymbol{n}}\right\}\!\!\right\}\left(\widetilde{\boldsymbol{x}}\right)\left[\!\left[\theta^{-1}\right]\!\right]\left(\widetilde{\boldsymbol{x}}\right)\geq0\,.\tag{3.30}$$

By analogy with the bulk, the Legendre–Fenchel transformation defines the free energy density for the interface, i.e.

$$\widetilde{\psi}\left(\left[\!\left[\boldsymbol{u}\right]\!\right]\left(\widetilde{\boldsymbol{x}}\right),\widetilde{\theta}\left(\widetilde{\boldsymbol{x}}\right),\widetilde{k}\left(\widetilde{\boldsymbol{x}}\right)\right)=\inf_{\widetilde{s}}\left\{\widetilde{e}\left(\left[\!\left[\boldsymbol{u}\right]\!\right]\left(\widetilde{\boldsymbol{x}}\right),\widetilde{s}\left(\widetilde{\boldsymbol{x}}\right),\widetilde{k}\left(\widetilde{\boldsymbol{x}}\right)\right)-\widetilde{\theta}\left(\widetilde{\boldsymbol{x}}\right)\widetilde{s}\left(\widetilde{\boldsymbol{x}}\right)\right\}\tag{3.31}$$

where $\widetilde{\theta}$ denotes the interface temperature. Inserting (3.24b) into (3.30) results in

$$\begin{aligned}\left[\!\left[\dot{\boldsymbol{u}}\right]\!\right]\left(\widetilde{\boldsymbol{x}}\right)\cdot\left\{\!\!\left\{\widetilde{\boldsymbol{t}}\right\}\!\!\right\}\left(\widetilde{\boldsymbol{x}}\right)-\widetilde{\rho}\left(\widetilde{\boldsymbol{x}}\right)\left[\dot{\widetilde{\psi}}\left(\widetilde{\boldsymbol{x}}\right)+\widetilde{s}\left(\widetilde{\boldsymbol{x}}\right)\dot{\widetilde{\theta}}\left(\widetilde{\boldsymbol{x}}\right)\right]-\left\{\!\!\left\{\widetilde{i}\right\}\!\!\right\}\left(\widetilde{\boldsymbol{x}}\right)\left[\!\left[\phi\right]\!\right]\left(\widetilde{\boldsymbol{x}}\right)\\+\widetilde{\theta}\left(\widetilde{\boldsymbol{x}}\right)\left[\left\{\!\!\left\{\boldsymbol{q}\cdot\widetilde{\boldsymbol{n}}\right\}\!\!\right\}\left(\widetilde{\boldsymbol{x}}\right)\left[\!\left[\theta^{-1}\right]\!\right]\left(\widetilde{\boldsymbol{x}}\right)+\left[\left\{\!\!\left\{\theta^{-1}\right\}\!\!\right\}\left(\widetilde{\boldsymbol{x}}\right)-\widetilde{\theta}^{-1}\left(\widetilde{\boldsymbol{x}}\right)\right]\left[\!\left[\boldsymbol{q}\cdot\widetilde{\boldsymbol{n}}\right]\!\right]\left(\widetilde{\boldsymbol{x}}\right)\right]\geq0\,.\end{aligned}\tag{3.32}$$

By applying the Coleman-Noll-type procedure, one obtains the constitutive relations

$$\left\{\!\!\left\{\widetilde{\boldsymbol{t}}\right\}\!\!\right\}=\widetilde{\rho}\frac{\partial\widetilde{\psi}}{\partial\left[\!\left[\boldsymbol{u}\right]\!\right]}\quad,\quad\widetilde{s}=-\frac{\partial\widetilde{\psi}}{\partial\widetilde{\theta}}\quad,\quad\widetilde{\kappa}=-\widetilde{\rho}\frac{\partial\widetilde{\psi}}{\partial\widetilde{k}}\,,\tag{3.33}$$

so that

$$\dot{\widetilde{\psi}}\left(\widetilde{\boldsymbol{x}}\right)=\frac{1}{\widetilde{\rho}\left(\widetilde{\boldsymbol{x}}\right)}\left\{\!\!\left\{\widetilde{\boldsymbol{t}}\right\}\!\!\right\}\left(\widetilde{\boldsymbol{x}}\right)\cdot\left[\!\left[\dot{\boldsymbol{u}}\right]\!\right]\left(\widetilde{\boldsymbol{x}}\right)-\widetilde{s}\left(\widetilde{\boldsymbol{x}}\right)\dot{\widetilde{\theta}}\left(\widetilde{\boldsymbol{x}}\right)-\frac{1}{\widetilde{\rho}\left(\widetilde{\boldsymbol{x}}\right)}\widetilde{\kappa}\left(\widetilde{\boldsymbol{x}}\right)\dot{\widetilde{k}}\left(\widetilde{\boldsymbol{x}}\right)\,.\tag{3.34}$$

Inserting (3.31), (3.33) and (3.34) into the energy equation (3.24b) finally yields

$$\begin{aligned}\widetilde{\rho}\left(\widetilde{\boldsymbol{x}}\right)\widetilde{c}_{\mathrm{v}}\left(\widetilde{\boldsymbol{x}}\right)\dot{\widetilde{\theta}}\left(\widetilde{\boldsymbol{x}}\right)+\widetilde{\theta}\left(\widetilde{\boldsymbol{x}}\right)\widetilde{\boldsymbol{\beta}_{\mathrm{v}}}\left(\widetilde{\boldsymbol{x}}\right)\cdot\left[\!\left[\dot{\boldsymbol{u}}\right]\!\right]\left(\widetilde{\boldsymbol{x}}\right)-\left[\widetilde{\kappa}\left(\widetilde{\boldsymbol{x}}\right)-\widetilde{\theta}\left(\widetilde{\boldsymbol{x}}\right)\frac{\partial\widetilde{\kappa}\left(\widetilde{\boldsymbol{x}}\right)}{\partial\widetilde{\theta}\left(\widetilde{\boldsymbol{x}}\right)}\right]\dot{\widetilde{k}}\left(\widetilde{\boldsymbol{x}}\right)\\+\left[\left[\!\left[\boldsymbol{q}\cdot\widetilde{\boldsymbol{n}}\right]\!\right]\left(\widetilde{\boldsymbol{x}}\right)+\left\{\!\!\left\{\widetilde{i}\right\}\!\!\right\}\left(\widetilde{\boldsymbol{x}}\right)\left[\!\left[\phi\right]\!\right]\left(\widetilde{\boldsymbol{x}}\right)\right]=0\end{aligned}\tag{3.35}$$

where $\widetilde{c_{\mathrm{v}}} : \mathcal{I} \to \mathbb{R}$ and $\widetilde{\boldsymbol{\beta}_{\mathrm{v}}} : \mathcal{I} \to \mathbb{R}^d$ denote the heat capacity of the interface

$$\widetilde{c_{\mathrm{v}}} = \widetilde{\theta}\,\frac{\partial\,\widetilde{s}\left(\llbracket \boldsymbol{u} \rrbracket, \widetilde{\theta}, k\right)}{\partial\,\widetilde{\theta}} = -\widetilde{\theta}\,\frac{\partial^2\,\widetilde{\psi}\left(\llbracket \boldsymbol{u} \rrbracket, \widetilde{\theta}, \widetilde{k}\right)}{\partial\,\widetilde{\theta}\partial\,\widetilde{\theta}} \tag{3.36a}$$

and thermal stresses

$$\widetilde{\boldsymbol{\beta}_{\mathrm{v}}} = -\frac{\partial\,\{\!\{\widetilde{\boldsymbol{t}}\}\!\}\left(\llbracket \boldsymbol{u} \rrbracket, \widetilde{\theta}, \widetilde{k}\right)}{\partial\,\widetilde{\theta}} = -\widetilde{\rho}\,\frac{\partial^2\,\widetilde{\psi}\left(\llbracket \boldsymbol{u} \rrbracket, \widetilde{\theta}, \widetilde{k}\right)}{\partial\,\llbracket \boldsymbol{u} \rrbracket\partial\,\widetilde{\theta}} \tag{3.36b}$$

at the interface, respectively. Analogous to the assumptions made in bulk, the evolution of internal variables associated with interfaces is neglected, i.e., $\dot{\widetilde{\boldsymbol{k}}} = \boldsymbol{0}$. Under the quasi-static, quasi-stationary approximation we also assume the interfacial thermoelastic coupling term $\widetilde{\boldsymbol{\beta}_{\mathrm{v}}} \cdot \llbracket \dot{\boldsymbol{u}} \rrbracket$ to be negligible. Hence, (3.35) reduces to

$$\llbracket \boldsymbol{q} \cdot \widetilde{\boldsymbol{n}} \rrbracket\,(\widetilde{\boldsymbol{x}}) + \{\!\{\widetilde{i}\}\!\}\,(\widetilde{\boldsymbol{x}})\,\llbracket \phi \rrbracket\,(\widetilde{\boldsymbol{x}}) = 0\,. \tag{3.37}$$

Application of the Coleman-Noll procedure to further specify (3.29) and (3.32) naturally gives rise to the constitutive restrictions for the electrical subproblem, i.e.

$$\boldsymbol{j}\,(\boldsymbol{x}) \cdot \boldsymbol{e}\,(\boldsymbol{x}) \quad \geq 0 \quad \text{(in bulk)} \quad , \tag{3.38a}$$

$$-\{\!\{\widetilde{i}\}\!\}\,(\widetilde{\boldsymbol{x}})\,\llbracket \phi \rrbracket\,(\widetilde{\boldsymbol{x}}) \geq 0 \quad \text{(at interface)}\,. \tag{3.38b}$$

By analogy with (3.38), the reduced dissipation inequality for the thermal subproblem takes the form

$$-\frac{1}{\theta\,(\boldsymbol{x})}\,\boldsymbol{q}\,(\boldsymbol{x}) \cdot \nabla_x \theta\,(\boldsymbol{x}) \geq 0 \qquad \text{(in bulk)}\,, \tag{3.39a}$$

$$\widetilde{\theta}\,(\widetilde{\boldsymbol{x}})\left[\{\!\{q\}\!\}\,(\widetilde{\boldsymbol{x}})\,\llbracket \theta^{-1} \rrbracket\,(\widetilde{\boldsymbol{x}}) + \left[\{\!\{\theta^{-1}\}\!\}\,(\widetilde{\boldsymbol{x}}) - \widetilde{\theta}^{-1}\,(\widetilde{\boldsymbol{x}})\right]\llbracket q \rrbracket\,(\widetilde{\boldsymbol{x}})\right] \geq 0 \qquad \text{(at interface)}\,. \tag{3.39b}$$

with the definition of $\boldsymbol{q} \cdot \widetilde{\boldsymbol{n}} = -q$ at hand. In order to evaluate the constitutive restrictions stipulated by (3.39b), an additional relation between the bulk and interface temperature needs to be assumed. There are (at least) two alternatives to define the interface temperature. Firstly, the interface temperature may be chosen as the average temperature of the two bounding surfaces according to

$$\widetilde{\theta} = \{\!\{\theta\}\!\}\,. \tag{3.40}$$

Alternatively, the interface temperature may be introduced as average coldness inverse

$$\widetilde{\theta} = \{\!\{\theta^{-1}\}\!\}^{-1}\,. \tag{3.41}$$

By inserting (3.41) into (3.39b) and by using

$$\llbracket \theta\,\theta^{-1} \rrbracket = \llbracket \theta \rrbracket\{\!\{\theta^{-1}\}\!\} + \{\!\{\theta\}\!\}\llbracket \theta^{-1} \rrbracket = 0 \tag{3.42}$$

the relation

$$\widetilde{\mathcal{D}}_{\text{con}} = -[\![\theta]\!] \frac{\{\!\{\boldsymbol{q} \cdot \widetilde{\boldsymbol{n}}\}\!\}}{\{\!\{\theta\}\!\}} \geq 0 \tag{3.43}$$

is obtained, which can be satisfied by assuming a Fourier-type behaviour for the average heat flux across the interface, namely

$$\{\!\{\boldsymbol{q} \cdot \widetilde{\boldsymbol{n}}\}\!\} = \{\!\{\widetilde{q}\}\!\} \propto -[\![\theta]\!] \,. \tag{3.44}$$

On the other hand, choosing the interface temperature as the mean temperature according to (3.40) results in a non-trivial form of the reduced dissipation inequality. More specifically speaking, inserting (3.40) into (3.39b) and applying (3.3) yields

$$\widetilde{\mathcal{D}}_{\text{con}} = -\left\{\!\!\left\{ \frac{\boldsymbol{q} \cdot \widetilde{\boldsymbol{n}}}{\theta} \right\}\!\!\right\} [\![\theta]\!] \geq 0 \,. \tag{3.45}$$

Condition (3.45) can be fulfilled by choosing the average entropy flux across the interface, $\widetilde{h}$, proportional to the negative temperature jump

$$\left\{\!\!\left\{ \frac{\boldsymbol{q} \cdot \widetilde{\boldsymbol{n}}}{\theta} \right\}\!\!\right\} = \widetilde{h} \propto -[\![\theta]\!] \,. \tag{3.46}$$

Both interface temperature definitions result in a Fourier-type behaviour and satisfy the dissipation inequality across the interface. In this contribution, the average coldness-based definition is adopted since the focus is not on the particular material model and (3.44) turns out to be a more convenient definition from a computational viewpoint as discussed in [169].

Remark 4. In the current contribution, a thermal cohesive zone formulation is assumed which attaches a Kapitza-type resistance to the interface. However, in general, an interface can be classified according to its thermal properties and generalised formulations exist. In the case of generic imperfect interfaces, the temperature field and the heat flux across the interface can both exhibit jump discontinuities. Weakly conducting (Kapitza) interfaces and highly conducting (HC) interfaces are limit cases of generic imperfect interfaces. Kapitza interfaces allow for temperature jumps across the interface whereas the heat flux across the interface is continuous. In the case of HC interfaces, the temperature across the interface is continuous whereas the heat flux across the interface may exhibit a jump discontinuity. For a detailed review and discussion, the reader may refer to [91, 92] and references cite therein.$\}^{\text{qtd.}}_{[74]}$

3.2 Weak form of the coupled problem

$^{\text{qtd.}}_{[74]}\{$This section focuses on the weak form of the coupled problem. The weak form of the mechanical, electrical and thermal subproblems are derived in Sections 3.2.1, 3.2.2 and 3.2.3 by multiplying the field equations with test functions and by fulfilling the field equations only in an integral sense. Eventually, the corresponding finite element formulation for the coupled problem is discussed in Section 3.2.4.$\}^{\text{qtd.}}_{[74]}$

3.2.1 Mechanical subproblem

qtd. [74] {For the mechanical problem, the balance equation of linear momentum (3.7a) is multiplied with test function $\boldsymbol{\varphi}^{\boldsymbol{u}}$ and integrated on the region where the problem is defined, the continuum Ω, which consists of subdomains Ω^- and Ω^+ as well as the interface $\mathcal{I}$ between these so that

$$0 = \int_{\Omega^+} \boldsymbol{\varphi}^{\boldsymbol{u}}(\boldsymbol{x}) \cdot [\nabla_x \cdot \boldsymbol{\sigma}(\boldsymbol{x}) + \rho(\boldsymbol{x})\, \boldsymbol{f}(\boldsymbol{x})]\, \mathrm{d}x + \int_{\Omega^-} \boldsymbol{\varphi}^{\boldsymbol{u}}(\boldsymbol{x}) \cdot [\nabla_x \cdot \boldsymbol{\sigma}(\boldsymbol{x}) + \rho \boldsymbol{f}(\boldsymbol{x})]\, \mathrm{d}x \quad (3.47)$$

Using the divergence theorem, (3.47) takes the form

$$\begin{aligned} 0 = &\int_{\Omega} \boldsymbol{\varphi}^{\boldsymbol{u}}(\boldsymbol{x}) \cdot \rho(\boldsymbol{x})\, \boldsymbol{f}(\boldsymbol{x})\, \mathrm{d}x - \int_{\Omega^+ \cup \Omega^-} \nabla_x \boldsymbol{\varphi}^{\boldsymbol{u}}(\boldsymbol{x}) : \boldsymbol{\sigma}(\boldsymbol{x})\, \mathrm{d}x + \int_{\partial\Omega} \boldsymbol{\varphi}^{\boldsymbol{u}}(\boldsymbol{x}) \cdot \boldsymbol{t}(\boldsymbol{x})\, \mathrm{d}x \\ &- \int_{\mathcal{I}} [\![\boldsymbol{\varphi}^{\boldsymbol{u}}]\!](\widetilde{\boldsymbol{x}}) \cdot \{\!\{\widetilde{\boldsymbol{t}}\}\!\}(\widetilde{\boldsymbol{x}}) + \{\!\{\boldsymbol{\varphi}^{\boldsymbol{u}}\}\!\}(\widetilde{\boldsymbol{x}}) \cdot [\![\widetilde{\boldsymbol{t}}]\!](\widetilde{\boldsymbol{x}})\, \mathrm{d}x\,. \end{aligned} \quad (3.48)$$

The detailed derivation of (3.48) is provided in Appendix B.1. By inserting (3.7b) into (3.48), the governing equation for the mechanical subproblem in weak form reads} qtd. [74]

Find $\boldsymbol{u} \in [H^1(\Omega^+)]^d \times [H^1(\Omega^-)]^d$ such that

$$\begin{aligned} \int_{\Omega^+ \cup \Omega^-} \nabla_x \boldsymbol{\varphi}^{\boldsymbol{u}}(\boldsymbol{x}) : \boldsymbol{\sigma}(\boldsymbol{x})\, \mathrm{d}x = &\int_{\Omega} \boldsymbol{\varphi}^{\boldsymbol{u}}(\boldsymbol{x}) \cdot \rho(\boldsymbol{x})\, \boldsymbol{f}(\boldsymbol{x})\, \mathrm{d}x + \int_{\partial\Omega} \boldsymbol{\varphi}^{\boldsymbol{u}}(\boldsymbol{x}) \cdot \boldsymbol{t}(\boldsymbol{x})\, \mathrm{d}x \\ &- \int_{\mathcal{I}} [\![\boldsymbol{\varphi}^{\boldsymbol{u}}]\!](\widetilde{\boldsymbol{x}}) \cdot \{\!\{\widetilde{\boldsymbol{t}}\}\!\}(\widetilde{\boldsymbol{x}})\, \mathrm{d}x + \int_{\mathcal{I}} \{\!\{\boldsymbol{\varphi}^{\boldsymbol{u}}\}\!\}(\widetilde{\boldsymbol{x}}) \cdot \widetilde{\rho}(\widetilde{\boldsymbol{x}})\, \widetilde{\boldsymbol{f}}(\widetilde{\boldsymbol{x}})\, \mathrm{d}x \end{aligned} \quad (3.49)$$

for all $\boldsymbol{\varphi}^{\boldsymbol{u}} \in \Phi = \{\boldsymbol{\varphi}^{\boldsymbol{u}} \in [H^1(\Omega^+)]^d \times [H^1(\Omega^-)]^d : \boldsymbol{\varphi}^{\boldsymbol{u}} = \boldsymbol{0} \text{ on } \partial\Omega^{\boldsymbol{u}}\}$.

Remark 5. Rather than specifying a particular form for the test functions, a term involving the mean of the traction against the jump of a test function is derived through the application of the divergence theorem and the mean jump identity. As an alternative, the test functions $\{\!\{\boldsymbol{\varphi}^{\boldsymbol{u}}\}\!\}$, $\{\!\{\varphi^{\phi}\}\!\}$ and $\{\!\{\varphi^{\theta}\}\!\}$ can be directly chosen, following the approach in [93, 98].

3.2.2 Electrical subproblem

qtd. [74] {For the electrical problem, the continuity equation for electric charge (3.15a) is multiplied with test function φ^{ϕ} and integrated over body Ω,

$$0 = \int_{\Omega^+} \varphi^{\phi}(\boldsymbol{x})\, \nabla_x \cdot \boldsymbol{j}(\boldsymbol{x})\, \mathrm{d}x + \int_{\Omega^-} \varphi^{\phi}(\boldsymbol{x})\, \nabla_x \cdot \boldsymbol{j}(\boldsymbol{x})\, \mathrm{d}x\,. \quad (3.50)$$

Employing the divergence theorem, (3.50) takes the form

$$\begin{aligned} 0 = &- \int_{\Omega^+ \cup \Omega^-} \nabla_x \varphi^\phi (\boldsymbol{x}) \cdot \boldsymbol{j} (\boldsymbol{x}) \, \mathrm{d}x + \int_{\partial\Omega} \varphi^\phi (\boldsymbol{x}) \, \boldsymbol{j} (\boldsymbol{x}) \cdot \boldsymbol{n} (\boldsymbol{x}) \, \mathrm{d}x \\ &- \int_{\mathcal{I}} [\![\varphi^\phi]\!] (\widetilde{\boldsymbol{x}}) \, \{\!\{ \widetilde{i} \}\!\} (\widetilde{\boldsymbol{x}}) + \{\!\{ \varphi^\phi \}\!\} (\widetilde{\boldsymbol{x}}) \, [\![\widetilde{i}]\!] (\widetilde{\boldsymbol{x}}) \, \mathrm{d}x \, . \end{aligned} \tag{3.51}$$

By combining (3.15b) with (3.51), the governing equation for the electrical subproblem is derived as}$^{\text{qtd.}}_{[74]}$

Find $\phi \in H^1 (\Omega^+) \times H^1 (\Omega^-)$ such that

$$\int_{\Omega^+ \cup \Omega^-} \nabla_x \varphi^\phi (\boldsymbol{x}) \cdot \boldsymbol{j} (\boldsymbol{x}) \, \mathrm{d}x = \varphi^\phi (\boldsymbol{x}) \, \boldsymbol{j} (\boldsymbol{x}) \cdot \boldsymbol{n} (\boldsymbol{x}) \, \mathrm{d}x - \int_{\mathcal{I}} [\![\varphi^\phi]\!] (\widetilde{\boldsymbol{x}}) \, \{\!\{ \widetilde{i} \}\!\} (\widetilde{\boldsymbol{x}}) \, \mathrm{d}x \tag{3.52}$$

for all $\varphi^\phi \in \Phi = \{ \varphi^\phi \in H^1 (\Omega^+) \times H^1 (\Omega^-) : \varphi^\phi = 0 \text{ on } \partial\Omega^\phi \}$.

3.2.3 Thermal problem

$^{\text{qtd.}}_{[74]}${For the thermal problem, the (quasi-stationary) balance equation of energy (3.29) is multiplied with test function φ^θ and integrated over body Ω, resulting in

$$0 = \int_{\Omega^+} \varphi^\theta (\boldsymbol{x}) \left[\nabla_x \cdot \boldsymbol{q} (\boldsymbol{x}) - \boldsymbol{j} (\boldsymbol{x}) \cdot \boldsymbol{e} (\boldsymbol{x}) \right] \mathrm{d}x + \int_{\Omega^-} \varphi^\theta (\boldsymbol{x}) \left[\nabla_x \cdot \boldsymbol{q} (\boldsymbol{x}) - \boldsymbol{j} (\boldsymbol{x}) \cdot \boldsymbol{e} (\boldsymbol{x}) \right] \mathrm{d}x \tag{3.53}$$

Making use of the divergence theorem, (3.53) takes the form

$$\begin{aligned} 0 = &- \int_{\Omega} \varphi^\theta (\boldsymbol{x}) \, \boldsymbol{j} (\boldsymbol{x}) \cdot \boldsymbol{e} (\boldsymbol{x}) \, \mathrm{d}x - \int_{\Omega^+ \cup \Omega^-} \nabla_x \varphi^\theta (\boldsymbol{x}) \cdot \boldsymbol{q} (\boldsymbol{x}) \, \mathrm{d}x + \int_{\partial\Omega} \varphi^\theta (\boldsymbol{x}) \, \boldsymbol{q} (\boldsymbol{x}) \cdot \boldsymbol{n} (\boldsymbol{x}) \, \mathrm{d}x \\ &- \int_{\mathcal{I}} [\![\varphi^\theta]\!] (\widetilde{\boldsymbol{x}}) \cdot \{\!\{ \widetilde{q} \}\!\} (\widetilde{\boldsymbol{x}}) + \{\!\{ \varphi^\theta \}\!\} (\widetilde{\boldsymbol{x}}) \, [\![\boldsymbol{q} \cdot \widetilde{\boldsymbol{n}}]\!] (\widetilde{\boldsymbol{x}}) \, \mathrm{d}x \, . \end{aligned} \tag{3.54}$$

By inserting (3.37) into (3.54), one obtains the governing equation for the thermal problem in weak form, i.e.}$^{\text{qtd.}}_{[74]}$

Find $\theta \in H^1(\Omega^+) \times H^1(\Omega^-)$ such that

$$\int_{\Omega^+ \cup \Omega^-} \nabla_x \varphi^\theta(\boldsymbol{x}) \cdot \boldsymbol{q}(\boldsymbol{x}) \, \mathrm{d}x = -\int_\Omega \varphi^\theta(\boldsymbol{x}) \, \boldsymbol{j}(\boldsymbol{x}) \cdot \boldsymbol{e}(\boldsymbol{x}) \, \mathrm{d}x + \int_{\partial\Omega} \varphi^\theta(\boldsymbol{x}) \, \boldsymbol{q}(\boldsymbol{x}) \cdot \boldsymbol{n}(\boldsymbol{x}) \, \mathrm{d}x - \int_{\mathcal{I}} [\![\varphi^\theta]\!](\widetilde{\boldsymbol{x}}) \cdot \{\!\{\widetilde{q}\}\!\}(\widetilde{\boldsymbol{x}}) \, \mathrm{d}x + \int_{\mathcal{I}} \{\!\{\varphi^\theta\}\!\}(\widetilde{\boldsymbol{x}}) \, \{\!\{\widetilde{i}\}\!\}(\widetilde{\boldsymbol{x}}) \, [\![\phi]\!](\widetilde{\boldsymbol{x}}) \, \mathrm{d}x \tag{3.55}$$

for all $\varphi^\theta \in \Phi = \{\varphi^\theta \in H^1(\Omega^+) \times H^1(\Omega^-) : \varphi^\theta = 0 \text{ on } \partial\Omega^\theta\}$.

3.2.4 Finite element formulation

qtd. [74]{This section focuses on the finite element formulation of the thermo-electro-mechanically coupled cohesive zone formulation proposed. The numerical treatment of continua with interfaces includes finite element formulations that are able to account for a discrete separation of material points. For the discretisation of the primary fields (displacements, electric potential and temperature) and the related test functions, Legendre polynomials are employed as

$$\boldsymbol{u}^{\mathrm{h}} = \sum_{D=1}^{\mathrm{n_{en}}} N_D \, \boldsymbol{u}_D, \quad \boldsymbol{\varphi}^{\boldsymbol{u}\mathrm{h}} = \sum_{A=1}^{\mathrm{n_{en}}} N_A \, \boldsymbol{\varphi}_A^{\boldsymbol{u}}, \tag{3.56a}$$

$$\phi^{\mathrm{h}} = \sum_{E=1}^{\mathrm{n_{en}}} N_E \, \phi_E, \quad \varphi^{\phi\mathrm{h}} = \sum_{B=1}^{\mathrm{n_{en}}} N_B \, \varphi_B^{\phi} \tag{3.56b}$$

$$\theta^{\mathrm{h}} = \sum_{F=1}^{\mathrm{n_{en}}} N_F \, \theta_F, \quad \varphi^{\theta\mathrm{h}} = \sum_{C=1}^{\mathrm{n_{en}}} N_C \, \varphi_C^{\theta}, \tag{3.56c}$$

where $\mathrm{n_{en}}$ and $N_\bullet$ are the number of element nodes and the shape functions, respectively. By inserting (3.56) into the weak form of the mechanical subproblem (3.48), the residual force vector

$$\boldsymbol{r}^{\boldsymbol{u}\,\mathrm{h}} = \boldsymbol{f}_{\mathrm{int}}^{\boldsymbol{u}\,\mathrm{h}} + \tilde{\boldsymbol{f}}_{\mathrm{int}}^{\boldsymbol{u}\,\mathrm{h}} - \boldsymbol{f}_{\mathrm{sur}}^{\boldsymbol{u}\,\mathrm{h}} - \boldsymbol{f}_{\mathrm{vol}}^{\boldsymbol{u}\,\mathrm{h}} - \tilde{\boldsymbol{f}}_{\mathrm{vol}}^{\boldsymbol{u}\,\mathrm{h}} \tag{3.57}$$

is obtained. For the electrical subproblem, inserting (3.56) into (3.51) yields the residual vector

$$\boldsymbol{r}^{\phi\,\mathrm{h}} = \boldsymbol{f}_{\mathrm{int}}^{\phi\,\mathrm{h}} + \tilde{\boldsymbol{f}}_{\mathrm{int}}^{\phi\,\mathrm{h}} - \boldsymbol{f}_{\mathrm{sur}}^{\phi\,\mathrm{h}}. \tag{3.58}$$

Likewise, the residual vector for the thermal problem is obtained by inserting (3.56) in (3.54), i.e.

$$\boldsymbol{r}^{\theta\,\mathrm{h}} = \boldsymbol{f}_{\mathrm{int}}^{\theta\,\mathrm{h}} + \tilde{\boldsymbol{f}}_{\mathrm{int}}^{\theta\,\mathrm{h}} - \boldsymbol{f}_{\mathrm{sur}}^{\theta\,\mathrm{h}} - \boldsymbol{f}_{\mathrm{vol}}^{\theta\,\mathrm{h}} - \tilde{\boldsymbol{f}}_{\mathrm{vol}}^{\theta\,\mathrm{h}}. \tag{3.59}$$

The (in general) nonlinear coupled problem is solved by using Newton's method. The system of equations to be solved for the increments in the list of nodal degrees of freedom, ($\widehat{\boldsymbol{u}}$, $\widehat{\boldsymbol{\phi}}$ and $\widehat{\boldsymbol{\theta}}$) reads

$$\begin{bmatrix} \mathbf{K}^{\boldsymbol{u}\boldsymbol{u}} + \widetilde{\mathbf{K}}^{\boldsymbol{u}\boldsymbol{u}} & \mathbf{K}^{\boldsymbol{u}\phi} + \widetilde{\mathbf{K}}^{\boldsymbol{u}\phi} & \mathbf{K}^{\boldsymbol{u}\theta} + \widetilde{\mathbf{K}}^{\boldsymbol{u}\theta} \\ \mathbf{K}^{\phi\boldsymbol{u}} + \widetilde{\mathbf{K}}^{\phi\boldsymbol{u}} & \mathbf{K}^{\phi\phi} + \widetilde{\mathbf{K}}^{\phi\phi} & \mathbf{K}^{\phi\theta} + \widetilde{\mathbf{K}}^{\phi\theta} \\ \mathbf{K}^{\theta\boldsymbol{u}} + \widetilde{\mathbf{K}}^{\theta\boldsymbol{u}} & \mathbf{K}^{\theta\phi} + \widetilde{\mathbf{K}}^{\theta\phi} & \mathbf{K}^{\theta\theta} + \widetilde{\mathbf{K}}^{\theta\theta} \end{bmatrix} \cdot \begin{bmatrix} \Delta\widehat{\boldsymbol{u}} \\ \Delta\widehat{\boldsymbol{\phi}} \\ \Delta\widehat{\boldsymbol{\theta}} \end{bmatrix} = - \begin{bmatrix} \boldsymbol{r}^{\boldsymbol{u}\,\mathrm{h}} \\ \boldsymbol{r}^{\phi\,\mathrm{h}} \\ \boldsymbol{r}^{\theta\,\mathrm{h}} \end{bmatrix} . \tag{3.60}$$

In (3.60), $\mathbf{K}^{\bullet *}$ and $\widetilde{\mathbf{K}}^{\bullet *}$ denote the tangent stiffness contributions of the bulk and interface to the generalised global stiffness matrix, which are specified in Appendix B.2.

For the mechanical subproblem, the contributions of the bulk and the interface to the internal force vector read

$$\boldsymbol{f}^{\boldsymbol{u}\,\mathrm{h}}_{\mathrm{int}} = \mathop{\mathsf{A}}_{e=1}^{\mathrm{n_{el}}} \int_{\Omega^e} \nabla_x N_A \cdot \boldsymbol{\sigma} \, \mathrm{d}x \,, \tag{3.61}$$

$$\widetilde{\boldsymbol{f}}^{\boldsymbol{u}\,\mathrm{h}}_{\mathrm{int}} = \mathop{\mathsf{A}}_{e=1}^{\widetilde{\mathrm{n}}_{\mathrm{el}}} \int_{\mathcal{I}^e} N_A \, \{\!\{\widetilde{\boldsymbol{t}}\}\!\} \, \mathrm{d}x \,, \tag{3.62}$$

where $\widetilde{\mathrm{n}}_{\mathrm{el}}$ is the number of interface element nodes. The contributions of the volumetric and surface distributed forces are given by

$$\boldsymbol{f}^{\boldsymbol{u}\,\mathrm{h}}_{\mathrm{vol}} = \mathop{\mathsf{A}}_{e=1}^{\mathrm{n_{el}}} \int_{\Omega^e} N_A \, \rho \, \boldsymbol{f} \, \mathrm{d}x \,, \tag{3.63}$$

$$\widetilde{\boldsymbol{f}}^{\boldsymbol{u}\,\mathrm{h}}_{\mathrm{vol}} = \mathop{\mathsf{A}}_{e=1}^{\widetilde{\mathrm{n}}_{\mathrm{el}}} \int_{\mathcal{I}^e} N_A \, \widetilde{\rho} \, \widetilde{\boldsymbol{f}} \, \mathrm{d}x \,, \tag{3.64}$$

and the surface force vector is defined as

$$\boldsymbol{f}^{\boldsymbol{u}\,\mathrm{h}}_{\mathrm{sur}} = \mathop{\mathsf{A}}_{e=1}^{\mathrm{n_{el}}} \int_{\partial\Omega^e} N_A \, \boldsymbol{t} \, \mathrm{d}x \,. \tag{3.65}$$

For the electrical subproblem, the contributions of the bulk and the interface to the internal force vector take the form

$$\boldsymbol{f}^{\phi\,\mathrm{h}}_{\mathrm{int}} = \mathop{\mathsf{A}}_{e=1}^{\mathrm{n_{el}}} \int_{\Omega^e} \nabla_x N_B \cdot \boldsymbol{j} \, \mathrm{d}x \,, \tag{3.66}$$

$$\widetilde{\boldsymbol{f}}^{\phi\,\mathrm{h}}_{\mathrm{int}} = \mathop{\mathsf{A}}_{e=1}^{\widetilde{\mathrm{n}}_{\mathrm{el}}} \int_{\mathcal{I}^e} N_B \, \{\!\{\widetilde{i}\}\!\} \, \mathrm{d}x \,, \tag{3.67}$$

and the surface force vector reads

$$\boldsymbol{f}_{\mathrm{sur}}^{\phi\,\mathrm{h}} = \mathop{\mathsf{A}}_{e=1}^{\mathrm{n_{el}}} \int_{\partial\Omega^e} N_B\, \boldsymbol{j}\cdot\boldsymbol{n}\,\mathrm{d}x\,. \tag{3.68}$$

Analogous to the electrical and mechanical subproblem, the contributions of the bulk and the interface to the internal force vector of the thermal problem take the form

$$\boldsymbol{f}_{\mathrm{int}}^{\theta\,\mathrm{h}} = \mathop{\mathsf{A}}_{e=1}^{\mathrm{n_{el}}} \int_{\Omega^e} \nabla_x N_C\cdot\boldsymbol{q}\,\mathrm{d}x\,, \tag{3.69}$$

$$\widetilde{\boldsymbol{f}}_{\mathrm{int}}^{\theta\,\mathrm{h}} = \mathop{\mathsf{A}}_{e=1}^{\widetilde{\mathrm{n}}_{\mathrm{el}}} \int_{\mathcal{I}^e} N_C\,\{\!\{\widetilde{q}\}\!\}\,\mathrm{d}x\,. \tag{3.70}$$

The contribution of the volumetric distributed forces in bulk and at the interface are given by

$$\boldsymbol{f}_{\mathrm{vol}}^{\theta\,\mathrm{h}} = \mathop{\mathsf{A}}_{e=1}^{\mathrm{n_{el}}} \int_{\Omega^e} N_C\,\rho\,r + N_C\,\boldsymbol{j}\cdot\boldsymbol{e}\,\mathrm{d}x\,, \tag{3.71}$$

$$\widetilde{\boldsymbol{f}}_{\mathrm{vol}}^{\theta\,\mathrm{h}} = \mathop{\mathsf{A}}_{e=1}^{\widetilde{\mathrm{n}}_{\mathrm{el}}} \int_{\mathcal{I}^e} N_C\,\{\!\{\widetilde{i}\}\!\}\,[\![\phi]\!]\,\mathrm{d}x\,, \tag{3.72}$$

and the surface force vector reads$\}^{\mathrm{qtd.}}_{[74]}$

$$\boldsymbol{f}_{\mathrm{sur}}^{\theta\,\mathrm{h}} = \mathop{\mathsf{A}}_{e=1}^{\mathrm{n_{el}}} \int_{\partial\Omega^e} -N_C\,\boldsymbol{q}\cdot\boldsymbol{n}\,\mathrm{d}x\,. \tag{3.73}$$

3.3 Material models

$^{\mathrm{qtd.}}_{[74]}\{$This section focuses on the specific form of the bulk and interface material model used in the simulations. In particular, the (thermo-)mechanical material behaviour and the evolution of interface damage is studied in Section 3.3.1 before Fourier-type relations for the electrical and thermal subproblems are discussed in Section 3.3.2 and Section 3.3.3, respectively. The specific form of the mechanical and electrical material model is adopted from [98] and extended by additionally taking thermal coupling into account. In particular, it is noted that the constitutive relations are of purely academic nature and not adopted based on experimental data. They are chosen to demonstrate the fully coupled behaviour and to show the applicability of the proposed framework.$\}^{\mathrm{qtd.}}_{[74]}$

3.3.1 Mechanical material models

As the thermo-mechanical response of the bulk material is described in Section 2.5.1, only the final results are summarised here to avoid redundancy. The bulk stress tensor is given as

$$\boldsymbol{\sigma} = K\big[\mathrm{tr}\,(\boldsymbol{\varepsilon}) - 3\,\alpha\,[\theta-\theta_0]\,\big]\boldsymbol{I} + 2\,G\boldsymbol{\varepsilon}_{\mathrm{dev}}\,. \tag{3.74}$$

Accordingly, the fourth-order stiffness tensor $\mathbf{E} : \Omega \to \mathrm{Sym}\left(\mathbb{R}^{d\times d\times d\times d}\right)$ reads

$$\mathbf{E} = K\,\boldsymbol{I}\otimes\boldsymbol{I} + 2\,G\,\mathbf{I}^{\mathrm{dev}}\,. \tag{3.75}$$

qtd. [74] {A linear-elastic thermo-mechanical material response accounting for a brittle damage formulation is used for the interface. More specifically speaking, the area-specific interface Helmholtz free energy density

$$\widetilde{\rho}\,\widetilde{\psi}\left(\llbracket\boldsymbol{u}\rrbracket,\widetilde{\theta},\widetilde{d}\right) = \widetilde{\Psi}\left(\llbracket\boldsymbol{u}\rrbracket,\widetilde{\theta},\widetilde{d}\right) \tag{3.76}$$

depending on displacement jump $\llbracket\boldsymbol{u}\rrbracket$, interface temperature $\widetilde{\theta}$ as defined in (3.41) and interface damage variable $\widetilde{d}$ is introduced. It is assumed that the mechanical stiffness of the interface $\widetilde{E}$ is reduced in the tensile region due to the evolution of interfacial damage, whereas the original mechanical stiffness is regained under compressive loadings. By introducing the elastic displacement jump

$$\llbracket\boldsymbol{u}\rrbracket^{\mathrm{e}} = \llbracket\boldsymbol{u}\rrbracket - \widetilde{\alpha}\left[\widetilde{\theta}-\widetilde{\theta}_0\right]\llbracket\boldsymbol{u}\rrbracket \tag{3.77}$$

one can formulate the area-specific Helmholtz free energy density function for the tensile region ($\llbracket\boldsymbol{u}\rrbracket^{\mathrm{e}}\cdot\widetilde{\boldsymbol{n}} > 0$)

$$\widetilde{\Psi}\left(\llbracket\boldsymbol{u}\rrbracket,\widetilde{\theta},\widetilde{d}\right) = \frac{1}{2}\,\widetilde{E}\,\left[1-\widetilde{d}\right]\,\llbracket\boldsymbol{u}\rrbracket^{\mathrm{e}}\cdot\boldsymbol{I}\cdot\llbracket\boldsymbol{u}\rrbracket^{\mathrm{e}}\,, \tag{3.78a}$$

and for the compressive region ($\llbracket\boldsymbol{u}\rrbracket^{\mathrm{e}}\cdot\widetilde{\boldsymbol{n}} \le 0$)

$$\widetilde{\Psi}\left(\llbracket\boldsymbol{u}\rrbracket,\widetilde{\theta},\widetilde{d}\right) = \frac{1}{2}\,\widetilde{E}\,\llbracket\boldsymbol{u}\rrbracket^{\mathrm{e}}\cdot\left[1-\widetilde{d}\right]\,[\boldsymbol{I}-\widetilde{\boldsymbol{n}}\otimes\widetilde{\boldsymbol{n}}]\cdot\llbracket\boldsymbol{u}\rrbracket^{\mathrm{e}} + \frac{1}{2}\widetilde{E}\,\llbracket\boldsymbol{u}\rrbracket^{\mathrm{e}}\cdot\widetilde{\boldsymbol{n}}\otimes\widetilde{\boldsymbol{n}}\cdot\llbracket\boldsymbol{u}\rrbracket^{\mathrm{e}}\,. \tag{3.78b}$$

Analogous to the bulk, by evaluating the constitutive relations at the interface, (3.33), the mean interface traction vector for the tensile region ($\llbracket\boldsymbol{u}\rrbracket^{\mathrm{e}}\cdot\widetilde{\boldsymbol{n}} > 0$)

$$\{\!\{\widetilde{\boldsymbol{t}}\}\!\} = \left[1-\widetilde{d}\right]\,\widetilde{E}\,\llbracket\boldsymbol{u}\rrbracket^{\mathrm{e}}\,, \tag{3.79}$$

and for the compressive region ($\llbracket\boldsymbol{u}\rrbracket^{\mathrm{e}}\cdot\widetilde{\boldsymbol{n}} \le 0$)

$$\{\!\{\widetilde{\boldsymbol{t}}\}\!\} = \widetilde{E}\,\left[1-\widetilde{d}\right]\,[\boldsymbol{I}-\widetilde{\boldsymbol{n}}\otimes\widetilde{\boldsymbol{n}}]\cdot\llbracket\boldsymbol{u}\rrbracket^{\mathrm{e}} + \widetilde{E}\,\widetilde{\boldsymbol{n}}\otimes\widetilde{\boldsymbol{n}}\cdot\llbracket\boldsymbol{u}\rrbracket^{\mathrm{e}} \tag{3.80}$$

are obtained.

It can be observed from (3.78) that the mechanical stiffness reduction is modelled by means of a classic $\left[1-\widetilde{d}\right]$ formulation. For the damage evolution, an exponential form of the interface damage variable

$$\widetilde{d} = 1 - \frac{\chi_0}{\chi}\exp\left(-\left[\chi-\chi_0\right]\,\frac{\widetilde{E}\,\chi_0}{G_{\mathrm{F}}-\frac{1}{2}\,\widetilde{E}\,\chi_0^2}\right) \tag{3.81}$$

is assumed, where G_{F}, χ and χ_0 are the fracture energy, a displacement jump-type internal variable and the critical interface opening, respectively. The critical interface opening relates the fracture strength Q_0 and mechanical stiffness $\widetilde{E}$ of the interface as $\chi_0 = Q_0/\widetilde{E}$, holds. Moreover, variable χ at time t^* is defined as

$$\chi = \max\left\{ \max_{0<t\leq t^*} \left\{ \operatorname{sgn}\left([\![\boldsymbol{u}]\!]^{\mathrm{e}} \cdot \widetilde{\boldsymbol{n}} \right) [\![\boldsymbol{u}]\!]^{\mathrm{e}} \right\} \, , \, \chi_0 \right\} . \tag{3.82}$$

Conceptually speaking, until damage evolution starts, χ takes the value of χ_0 and $\widetilde{d} = 0$ holds. However, once the opening of the interface exceeds the critical value χ_0, damage starts to evolve.$\}^{\text{qtd.}}_{[74]}$

3.3.2 Electrical material models

$^{\text{qtd.}}_{[74]}\{$A linear relation between the electric field vector and the electric current density vector is assumed in the bulk following the restrictions posed by the dissipation inequalities (3.38), i.e.

$$\boldsymbol{j} = \boldsymbol{\mathcal{S}} \cdot \boldsymbol{e} \, . \tag{3.83}$$

For the sake of simplicity, an isotropic electrical conductivity tensor is assumed with the positive definite electrical conductivity tensor

$$\boldsymbol{\mathcal{S}} = \kappa \, \boldsymbol{I} \, , \tag{3.84}$$

where κ denotes a scalar-valued electrical conductivity parameter.

A linear relation between the jump of the electric potential and the mean value of the electric current is considered at the interface. Similar to the mechanical material response, the electrical conductivity is assumed to be influenced by damage evolution at the interface. To this end, a $\left[1 - \widetilde{d}\right]$ formulation is employed as

$$\{\!\{\widetilde{i}\}\!\} = \begin{cases} -\left[1 - \widetilde{d}\right] \widetilde{\kappa} \, [\![\phi]\!] & \text{if } [\![\boldsymbol{u}]\!]^{\mathrm{e}} \cdot \widetilde{\boldsymbol{n}} > 0 \\ -\widetilde{\kappa} \, [\![\phi]\!] & \text{if } [\![\boldsymbol{u}]\!]^{\mathrm{e}} \cdot \widetilde{\boldsymbol{n}} \leq 0 \end{cases} , \tag{3.85}$$

where $\widetilde{\kappa}$ denotes the idealised conductivity of the interface. The $\left[1 - \widetilde{d}\right]$ term introduces a coupling between the electrical and mechanical field equations after the damage starts to evolve. Moreover, the specific form of the constitutive equation (3.85) is physically motivated in [98] by assuming that the effective conducting interface area in the tensile region (where microcracks open) is reduced due to the damage processes. In contrast, the interface recovers its initial conductivity under compressive loads.$\}^{\text{qtd.}}_{[74]}$

3.3.3 Thermal material models

$^{\text{qtd.}}_{[74]}\{$The Fourier inequalities in the bulk (3.38a) and at the interface (3.44) yield restrictions to the heat flux vector. In this work a linear relation between the temperature gradient and the heat flux vector in the bulk is assumed, i.e.

$$\boldsymbol{q} = -\boldsymbol{\mathcal{K}} \cdot \nabla \, \theta \quad , \tag{3.86}$$

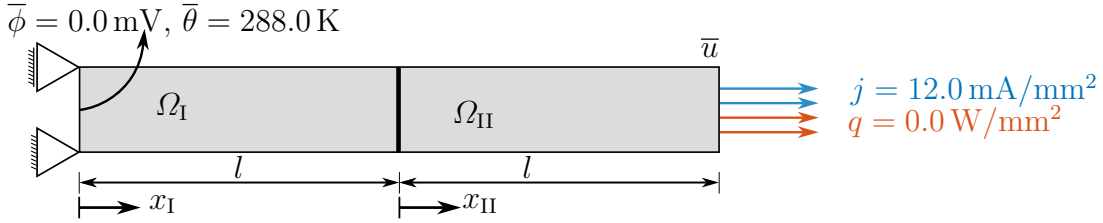

Figure 3.2: Geometrical dimensions and boundary conditions of the one-dimensional boundary value problem discussed in Section 3.4.1. Reproduced from [74] under the terms of the Creative Commons Attribution License (CC BY).

including the positive definite thermal conductivity tensor

$$\boldsymbol{\mathcal{K}} = \kappa_\theta \, \boldsymbol{I} \tag{3.87}$$

with the scalar-valued thermal conductivity parameter κ_θ.

Analogous to the electrical problem, the constitutive equation for the heat flux at the interface is assumed to take the form

$$\{\!\{\widetilde{q}\}\!\} = \begin{cases} -\left[1-\widetilde{d}\right] \widetilde{\kappa}_\theta \, [\![\theta]\!] & \text{if } [\![\boldsymbol{u}]\!]^\mathrm{e} \cdot \widetilde{\boldsymbol{n}} > 0 \\ -\widetilde{\kappa}_\theta \, [\![\theta]\!] & \text{if } [\![\boldsymbol{u}]\!]^\mathrm{e} \cdot \widetilde{\boldsymbol{n}} \leq 0 \end{cases} , \tag{3.88}$$

with $\widetilde{\kappa}_\theta$ denoting the idealised conductivity of the interface. Relation (3.88) establishes a coupling between the thermal and mechanical field equations via the $\left[1-\widetilde{d}\right]$ term. In particular (3.88) states that under tensile loadings, when damage evolves, the effective thermal conductivity is reduced, whereas the effective conductivity is assumed to regain its initial value under compressive loading.}$^{\text{qtd.}}_{[74]}$

3.4 Representative simulation results

$^{\text{qtd.}}_{[74]}${This section deals with a study of representative boundary value problems. In particular, an analytical solution is provided in Section 3.4.1 for validation purposes of the finite element formulation proposed, and thermo-electrically-induced failure processes in material interfaces are studied in a two-dimensional setting in Section 3.4.2. The material parameters used in this work are summarised in Table 3.1. Moreover, the reference temperature for bulk and interface is set to $\theta_0 = \widetilde{\theta}_0 = 288.0\,\mathrm{K}$ and an initial temperature of 288.0 K is assumed.}$^{\text{qtd.}}_{[74]}$

3.4.1 Analytical solution of one-dimensional bar

$^{\text{qtd.}}_{[74]}${This section deals with the derivation of an analytical solution for the one-dimensional sample boundary value problem of a bar with $l = 50.0\,\mathrm{mm}$ depicted in Figure 3.2. Assuming monotonic loading, a parametrisation of the analytical solution

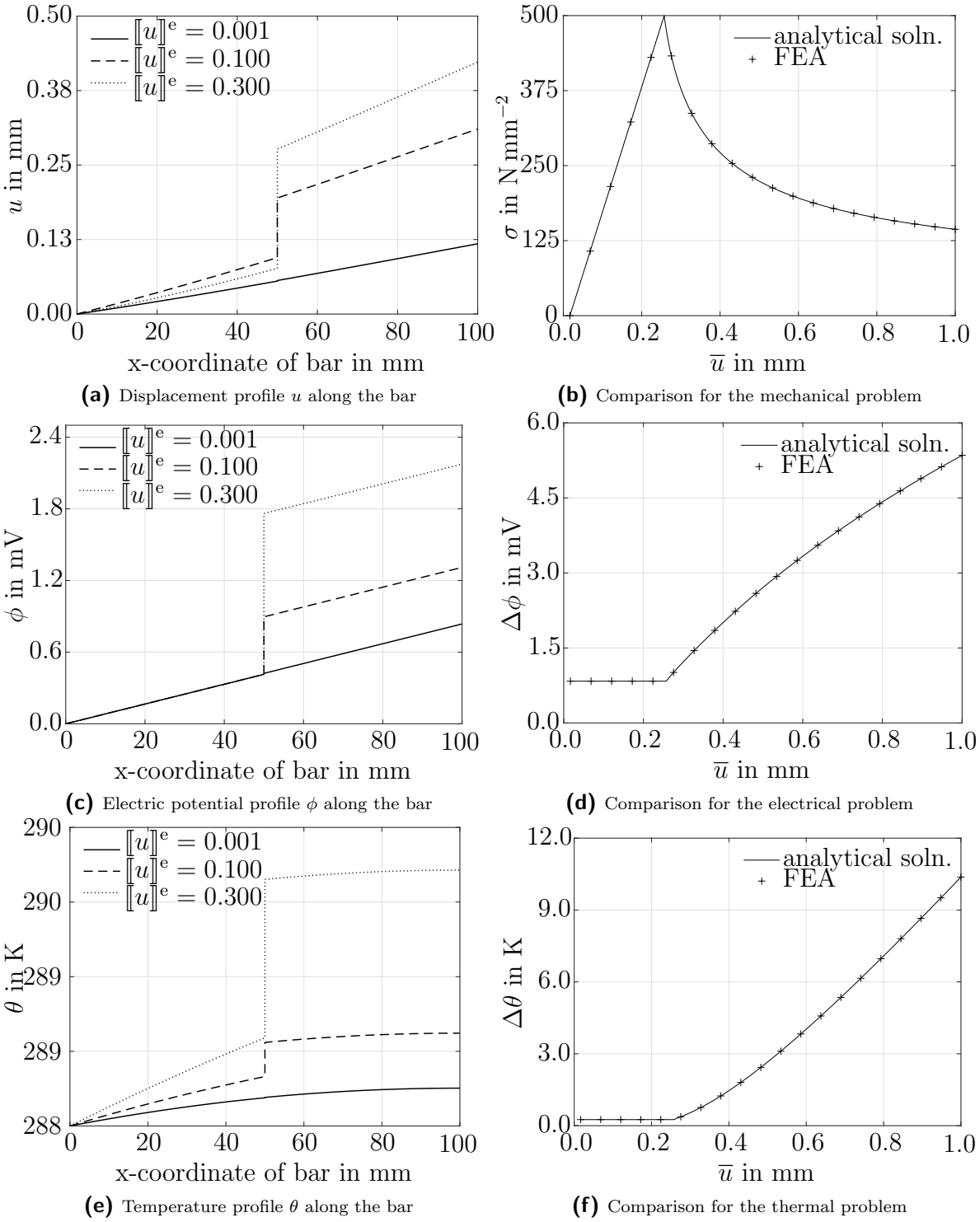

(a) Displacement profile u along the bar

(b) Comparison for the mechanical problem

(c) Electric potential profile ϕ along the bar

(d) Comparison for the electrical problem

(e) Temperature profile θ along the bar

(f) Comparison for the thermal problem

Figure 3.3: Comparison of finite element-based and analytical solutions for the representative boundary value problem analysed in Section 5.4.2. Figures (a), (c), (e) show the analytical profiles according to Section 5.4.2 for $[\![u]\!]^{\mathrm{e}} = 0.001$mm, $[\![u]\!]^{\mathrm{e}} = 0.100$mm and $[\![u]\!]^{\mathrm{e}} = 0.300$mm. In Figures (b), (d), (f) the comparison between analytical and finite element-based solutions for thermo-electro-mechanical problem is exemplarily provided. Reprinted from [74] under the terms of the Creative Commons Attribution License (CC BY).

Table 3.1: Material parameters used in the analytical and finite element-based simulations.

E, $\widetilde{E}$	$210\,000\,\mathrm{N/mm^2}$	$210\,000\,\mathrm{N/mm^3}$
ν	0.3	-
κ, $\widetilde{\kappa}$	$1450\,\mathrm{A/[Vmm]}$	$1450\,\mathrm{A/[Vmm^2]}$
κ_θ, $\widetilde{\kappa_\theta}$	$2000\,\mathrm{W/[mmK]}$	$2000\,\mathrm{W/[mm^2K]}$
α, $\widetilde{\alpha}$	$0.001\,1/\mathrm{K}$	$0.000\,01\,1/\mathrm{K}$
Q_0	-	$500\,\mathrm{N/mm^2}$
G_F	-	$200\,\mathrm{N/mm}$

with respect to $[\![u]\!]^\mathrm{e}$ (elastic displacement jump contribution in longitudinal direction) according to

$$\chi \overset{\text{mon. loading}}{=} [\![u]\!]^\mathrm{e} = [\![u]\!] - \widetilde{\alpha}\left[\widetilde{\theta} - \widetilde{\theta}_0\right][\![u]\!] \tag{3.89}$$

is adopted. With (3.89) at hand and by taking (3.81) into account, the closed-form solution for the (spatially constant) stress reads

$$\sigma = \left[1 - \widetilde{d}\,(\chi)\right]\widetilde{E}\,[\![u]\!]^\mathrm{e}\,. \tag{3.90}$$

The electric potential field in the domains Ω_I and Ω_II is obtained analytically by integrating (3.15a) and takes the form

$$\phi = \begin{cases} \phi_\mathrm{I}(x_\mathrm{I}) & = \dfrac{c_{1\phi}}{\kappa}\,x_\mathrm{I} + \dfrac{c_{2\phi}}{\kappa} \\ \phi_\mathrm{II}(x_\mathrm{II}) & = \dfrac{c_{3\phi}}{\kappa}\,x_\mathrm{II} + \dfrac{c_{4\phi}}{\kappa} \end{cases}. \tag{3.91}$$

To obtain the problem-specific integration constants ($c_{1\phi}$, $c_{2\phi}$, $c_{3\phi}$ and $c_{4\phi}$), the boundary conditions are investigated. In the representative problem, ϕ is prescribed at the left boundary, while the electric current density is prescribed at the right boundary as j. There is an additional set of boundary conditions due to the balance equation at the interface, cf. (3.15b). The continuity equation for the electric charge at the interface states that the jump of electric current density must vanish across the interface, cf. (3.16). Considering these boundary conditions, the integration constant can be specified as

$$c_{1\phi} = -j\,, \tag{3.92a}$$

$$c_{2\phi} = \kappa\,\overline{\phi}\,, \tag{3.92b}$$

$$c_{3\phi} = -j\,, \tag{3.92c}$$

$$c_{4\phi} = \left[c_{1\phi}\left[1 + \frac{\left[1-\widetilde{d}\right]\widetilde{\kappa}}{\kappa}\right]l + c_{2\phi}\,\frac{\left[1-\widetilde{d}\right]\widetilde{\kappa}}{\kappa}\right]\frac{\kappa}{\left[1-\widetilde{d}\right]\widetilde{\kappa}}\,. \tag{3.92d}$$

After obtaining a closed-form solution for the electrical field, the temperature field can be determined by following a similar procedure. More specifically speaking, integrating the quasi-static, quasi-stationary form of the balance of energy, (3.29), yields

$$\theta = \begin{cases} \theta_{\mathrm{I}}(x_{\mathrm{I}}) & = -\dfrac{j\,e}{2\kappa_\theta} x_{\mathrm{I}}^2 + c_{1\theta}\, x_{\mathrm{I}} + c_{2\theta} \\ \theta_{\mathrm{II}}(x_{\mathrm{II}}) & = -\dfrac{j\,e}{2\kappa_\theta} x_{\mathrm{II}}^2 + c_{3\theta}\, x_{\mathrm{II}} + c_{4\theta} \end{cases} . \tag{3.93}$$

The thermal field is strongly coupled with the electrical field since the term $j\,e$ acts as an additional source term for the thermal problem. As a result of the coupling between the electrical and thermal subproblems, the temperature field is quadratic in x_{I}, respectively x_{II}, within the subdomains. To obtain the integration constants, the boundary conditions are examined. For the thermal problem, the temperature at the left side is prescribed, similar to the electrical problem, while the right side is assumed to be thermally insulated. The relation between the heat flux at the interface and the quasi-static, quasi-stationary form of the balance of energy, (3.37), yields an additional boundary condition. Specifically speaking, balance equation (3.37) stipulates that the heat flux across the interface changes according to the dissipation associated with jump of the electric potential and the mean value of the electric current. Analogous to the bulk, these terms act as a source term. The integration constants $c_{1\theta}$, $c_{2\theta}$, $c_{3\theta}$ and $c_{4\theta}$ follow as

$$c_{1\theta} = \frac{\{\!\{\widetilde{i}\}\!\}\,[\![\phi]\!] + 2j\,e\,l}{\kappa_\theta}\,, \tag{3.94a}$$

$$c_{2\theta} = \overline{\theta}\,, \tag{3.94b}$$

$$c_{3\theta} = \frac{j\,e\,l}{\kappa_\theta}\,, \tag{3.94c}$$

$$c_{4\theta} = \frac{1}{2\widetilde{\kappa}_\theta}\left[\{\!\{\widetilde{i}\}\!\}\,[\![\phi]\!] + 2j\,e\,l\right] + \frac{5\,j\,e\,l^2 + 2\{\!\{\widetilde{i}\}\!\}\,[\![\phi]\!]}{2\kappa_\theta} + \overline{\theta}\,. \tag{3.94d}$$

In (3.94), $\{\!\{\widetilde{i}\}\!\}$ and $[\![\phi]\!]$ are obtained from the solution of the field equations for the electric potential field (3.91)–(3.92). After obtaining the temperature distribution along the bar, the displacement field due to thermal effects can be calculated. For the mechanical field, the balance of linear momentum (3.7a) is integrated, while neglecting body forces. The displacement field for the respective subdomains reads

$$u = \begin{cases} u_{\mathrm{I}}(x_{\mathrm{I}}) & = c_{1\mathrm{u}}\, x_{\mathrm{I}} + c_{2\mathrm{u}} + \alpha\left[-\dfrac{j\,e}{6\kappa_\theta} l^3 + c_{1\theta}\,\dfrac{x_{\mathrm{I}}^2}{2} + c_{2\theta}\, x_{\mathrm{I}} - \theta_0\, x_{\mathrm{I}}\right] \\ u_{\mathrm{II}}(x_{\mathrm{II}}) & = c_{3\mathrm{u}}\, x_{\mathrm{II}} + c_{4\mathrm{u}} + \alpha\left[-\dfrac{j\,e}{6\kappa_\theta} l^3 + c_{3\theta}\dfrac{x_{\mathrm{II}}^2}{2} + c_{4\theta}\, x_{\mathrm{II}} - \theta_0\, x_{\mathrm{II}}\right] \end{cases} \tag{3.95}$$

where $c_{1\mathrm{u}}$, $c_{2\mathrm{u}}$, $c_{3\mathrm{u}}$ and $c_{4\mathrm{u}}$ are defined as

$$c_{1\mathrm{u}} = \sigma\,, \tag{3.96a}$$

$$c_{2\mathrm{u}} = 0\,, \tag{3.96b}$$

$$c_{3\mathrm{u}} = \sigma\,, \tag{3.96c}$$

$$c_{4\mathrm{u}} = \frac{\sigma}{\widetilde{E}} + \frac{c_{1\mathrm{u}}}{E} l + c_{2\mathrm{u}} + \alpha \left[-\frac{je}{6\kappa_\theta} l^3 + c_{1\theta} \frac{l^2}{2} + c_{2\theta}\, l - \theta_0\, l \right] + \widetilde{\alpha} \left[2 \left[\frac{1}{\theta_{\mathrm{I}}(x_{\mathrm{I}} = l)} + \frac{1}{\theta_{\mathrm{II}}(x_{\mathrm{II}} = 0)} \right]^{-1} - \widetilde{\theta}_0 \right]. \tag{3.96d}$$

The integration constants in (3.96) are derived by investigating the boundary conditions. The bar is clamped at the left side resulting in $u\,(x_{\mathrm{I}} = 0) = 0$. The stress σ along the bar follows from (3.90).

Figure 3.3 illustrates that the proposed finite element framework is capable of capturing the analytical solution for coupled thermo-electro-mechanical problems. For comparison purposes, the geometry given in Figure 3.2 is discretised with three-dimensional linear brick elements for the bulk Ω_{I} and Ω_{II}, and the interface is discretised by means of four-node linear quadrilateral elements. Figures 3.3a, 3.3c and 3.3e are based on the analytical solution of the field equations derived in Section 3.4.1. Figures 3.3b, 3.3d and 3.3f provide a detailed comparison of the analytical solution and the finite element based simulation results. In particular, Figures 3.3d and 3.3f show the overall electric potential difference $\Delta\phi$ and temperature difference $\Delta\theta$ between the free and clamped boundary as a function of the prescribed elongation of the bar, $\Delta u = \overline{u}.\}^{\text{qtd.}}_{[74]}$

3.4.2 Finite element simulation of a wire bonding example

$^{\text{qtd.}}_{[74]}\{$Wire bonding failures present a considerable concern in semiconductor manufacturing as they significantly affect the bond's mechanical strength and electrical conductivity. Some of the reasons of failure are voids in the bonds, the presence of contaminants and bonding between electronic components issues. The types of failure include micro-cracks under the pad or complete chip-out, as exemplified in Figure 3.5. There is an extensive amount of literature on the mechanisms of wire bonding failures focusing on both experimental and numerical investigations, cf. [15, 31, 58, 84, 173, 187].

Motivated by wire bonding failure that initiates at the interface between the pad and soldered wire, the two-dimensional sample boundary value problem depicted in Figure 3.4 is studied in this section. The sample boundary value problem is chosen to show the capabilities of the proposed framework. The material parameters and the geometry do not directly correspond to the real physical system. Rather, the main goal is to show the failure initiation at the interface in coupled thermo-electro-mechanical response. For this purpose, a representative wire bonding problem of pad length $l = 60\,\mathrm{mm}$, pad height $h = 20\,\mathrm{mm}$, radius of the solder $r = 10\,\mathrm{mm}$ and the angle $\vartheta = 30°$ and with the dimensions of the wire $h_w = 6\,\mathrm{mm}$ and $w_w = 4\,\mathrm{mm}$ is considered. The wire and the pad are assumed to have the same material properties as provided in Table 3.1, except

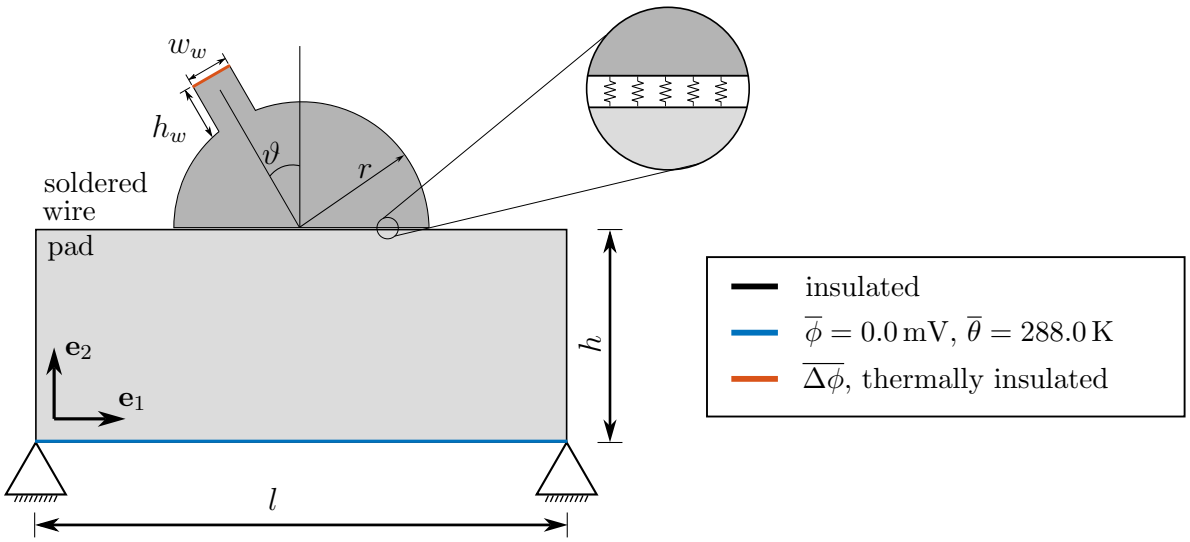

Figure 3.4: Geometrical dimensions and boundary conditions of the two-dimensional boundary value problem discussed in Section 3.4.2. Black surfaces are thermally and electrically insulated, while red indicates the surface where the electric potential boundary condition is applied. The blue indicated bottom boundary is restricted from moving in any direction. The interface is placed between the pad and soldered wire. Reproduced from [74] under the terms of the Creative Commons Attribution License (CC BY).

for the thermal expansion coefficient. The thermal coefficient of the pad is assumed to be $\alpha_{\text{pad}} = 0.000\,01\,1/\text{K}$, whereas the thermal coefficient of the soldered wire is assumed to take the value $\alpha_{\text{wire}} = 0.0001\,1/\text{K}$. The material models are chosen according to Section 3.3 and plane strain conditions are assumed. The pad and the soldered wire are discretised with four-node linear quadrilateral elements, and the interface between the pad and soldered wire is discretised with linear, four-node interface elements.

The pad is restricted from moving in any direction at the bottom boundary. Moreover, an electric potential difference $\overline{\Delta\phi}$ between the bottom boundary and the wire is prescribed. More specifically speaking, the potential difference is linearly increased from $\overline{\Delta\phi} = 0.0\,\text{mV}$ to $\overline{\Delta\phi} = 5.0\,\text{mV}$. In addition, the temperature is set to $\overline{\theta} = 288.0\,\text{K}$ at the bottom boundary. The remaining boundaries are assumed to be electrically and thermally insulated and traction free.

Three different stages of the boundary value problem are depicted in Figures 3.6 and 3.7, focusing on the electrical, thermal and mechanical fields, respectively. The first stage corresponds to $\overline{\Delta\phi} = 1.0\,\text{mV}$, where damage evolution has not been activated. During the second stage, as exemplarily shown for $\overline{\Delta\phi} = 3.5\,\text{mV}$, damage starts to evolve in the middle of the interface. Eventually, the maximum prescribed electric potential difference $\overline{\Delta\phi} = 5.0\,\text{mV}$ is reached and an almost complete decohesion of the interface is observed in the last stage.

Figures 3.6b, 3.6d and 3.6f illustrate the temperature field evolution due to the electro-thermal coupling as discussed in Section 3.1.3. In Figures 3.6a, 3.6c and 3.6e, the electric current density is visualised. Moreover, electric current density vectors are indicated by black arrows.

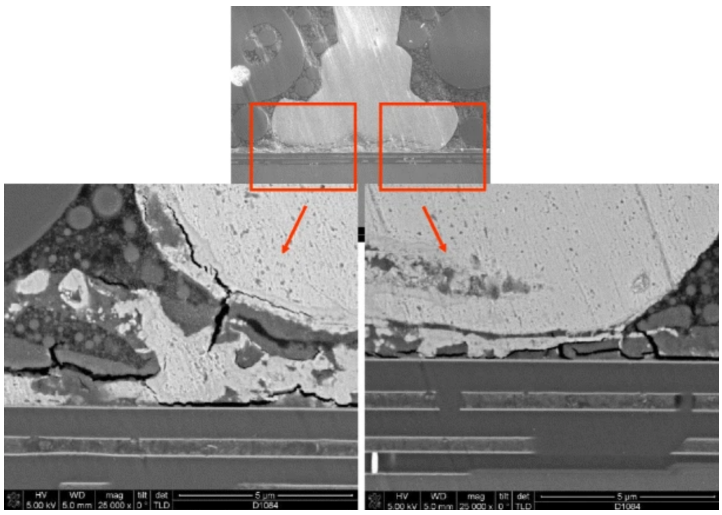

Figure 3.5: SEM image showing microcracking along the interface in a Cu ball bond. Reprinted from "Extended reliability of gold and copper ball bonds in microelectronic packaging" by C. L. Gan, C. Francis, B. L. Chan and U. Hashim, 2013, *Gold Bulletin 46 (2)*, 103–115.

The stress contributions σ_{22} and σ_{12} are depicted in Figure 3.7. Thermal stresses arise in the bulk due to the (local) increase in temperature caused by the electrical source term. Vice versa, the mechanical field is coupled with the electrical and thermal field via the damage variable $\widetilde{d}$. It can be observed from Figure 3.7 that the pad and the soldered wire in the vicinity of the interface are subjected to tensile and compressive loadings, respectively, when the interface starts to fail. Similar observations are made for the shear component of the stress tensor, as shown in Figures 3.7b, 3.7d and 3.7f.}$^{\text{qtd.}}_{[74]}$

B Appendix

Appendix B.1 compiles the technical details relevant to the derivation and implementation of the weak form in the presence of material interfaces. Appendix B.2 provides the associated tangent contributions used in the numerical solution procedure.

B.1 Derivation of weak form with interface contributions

In contrast to standard formulations, the present derivation of the weak form accounts not only for the bulk contributions but also for interfacial contributions. This is essential in order to capture discontinuities in fields such as displacement, electric potential or temperature across interfaces within the domain.

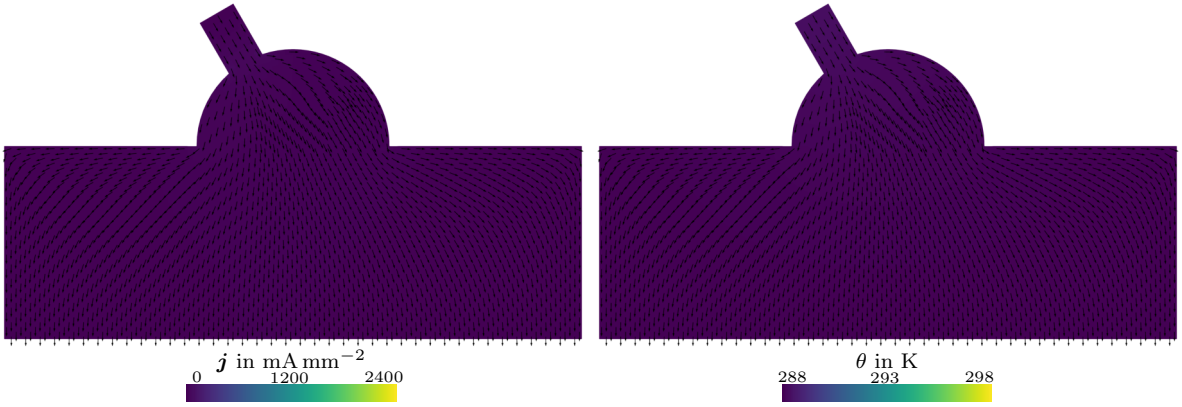

(a) Electric current density field $\boldsymbol{j}$ for $\overline{\Delta\phi} = 1.0\,\mathrm{mV}$ **(b)** Temperature field θ for $\overline{\Delta\phi} = 1.0\,\mathrm{mV}$

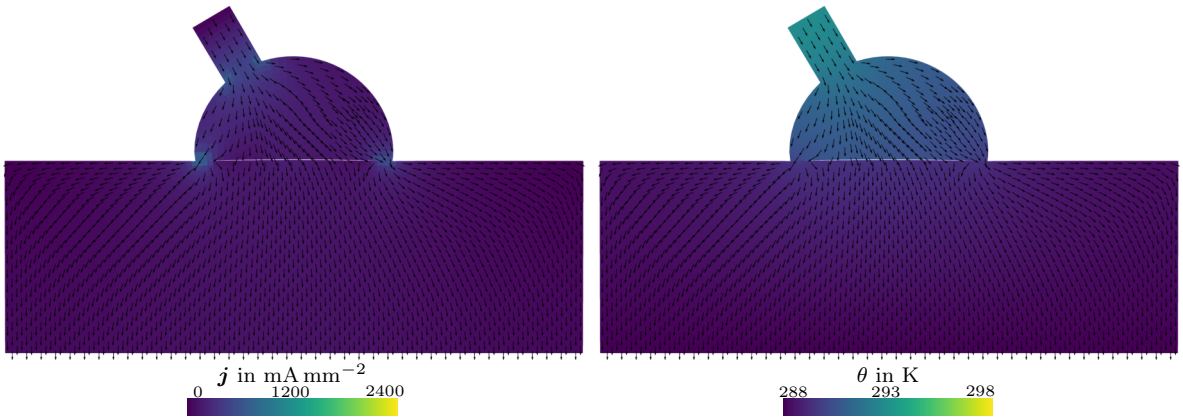

(c) Electric current density field $\boldsymbol{j}$ for $\overline{\Delta\phi} = 3.5\,\mathrm{mV}$ **(d)** Temperature θ for $\overline{\Delta\phi} = 3.5\,\mathrm{mV}$

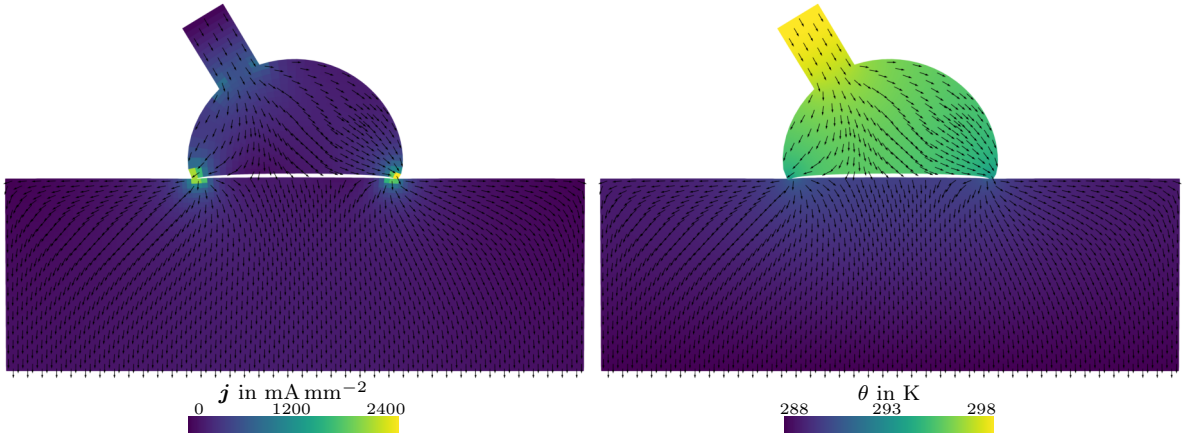

(e) Electric current density field $\boldsymbol{j}$ for $\overline{\Delta\phi} = 5.0\,\mathrm{mV}$ **(f)** Temperature θ for $\overline{\Delta\phi} = 5.0\,\mathrm{mV}$

Figure 3.6: Electric current density field $\boldsymbol{j}$ and temperature field θ of the boundary value problem depicted in Figure 3.4, showing three different loading stages. In particular, Figures 3.6a and 3.6b correspond to the stage where damage evolution has not yet been initiated. In Figures 3.6c and 3.6d, damage evolution at the middle of interface is observed. Finally, a load state where the wire is almost completely detached from the pad is shown in Figures 3.6e and 3.6f. Electric current density vectors are indicated by black arrows and the deformation is scaled by a factor of 20 for visualisation purposes. Reproduced from [74] under the terms of the Creative Commons Attribution License (CC BY).

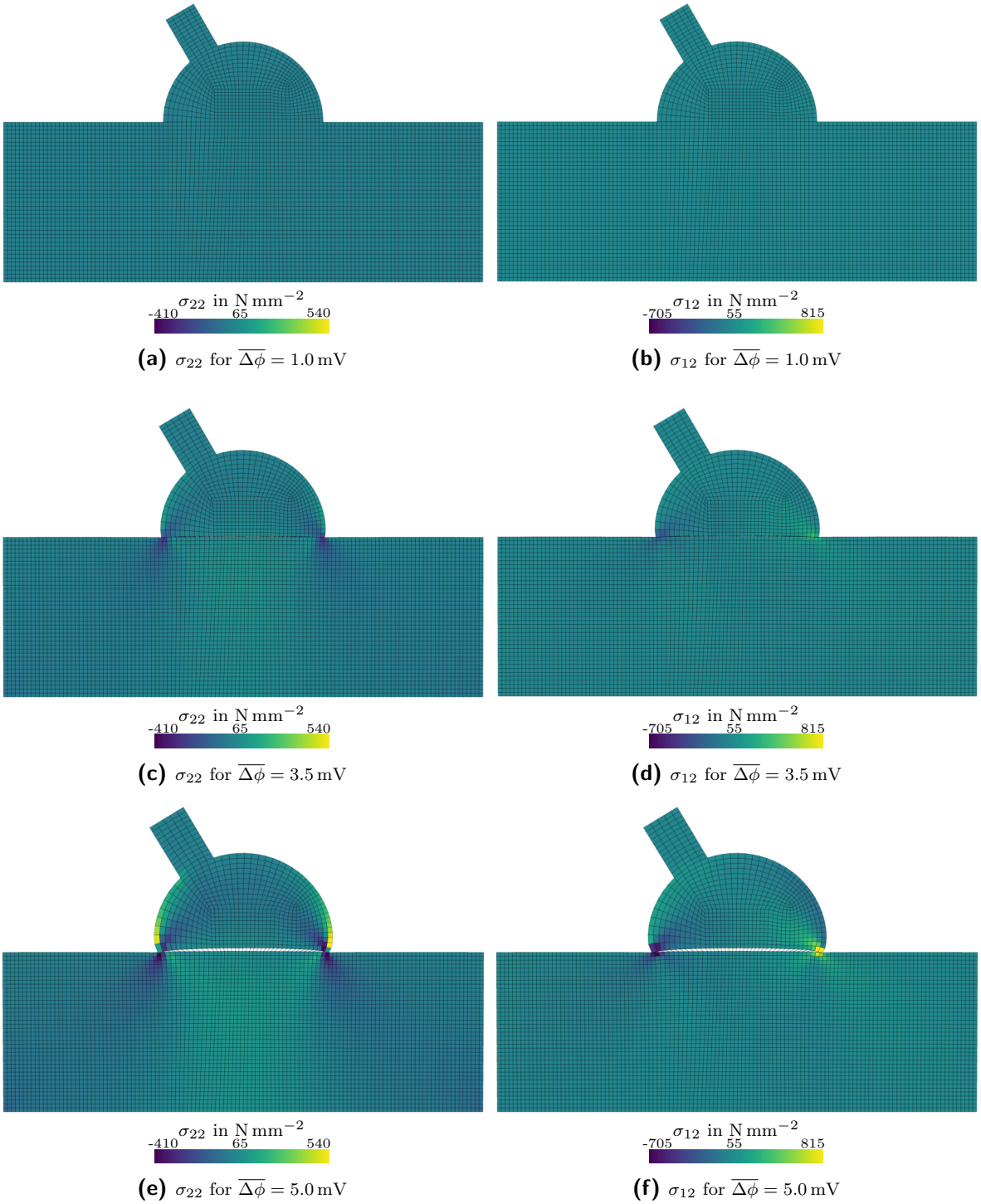

(a) σ_{22} for $\overline{\Delta\phi} = 1.0\,\mathrm{mV}$ **(b)** σ_{12} for $\overline{\Delta\phi} = 1.0\,\mathrm{mV}$

(c) σ_{22} for $\overline{\Delta\phi} = 3.5\,\mathrm{mV}$ **(d)** σ_{12} for $\overline{\Delta\phi} = 3.5\,\mathrm{mV}$

(e) σ_{22} for $\overline{\Delta\phi} = 5.0\,\mathrm{mV}$ **(f)** σ_{12} for $\overline{\Delta\phi} = 5.0\,\mathrm{mV}$

Figure 3.7: Stress distribution for the boundary value problem depicted in Figure 3.4, for three different load states. For visualisation purposes, the deformation is scaled by a factor of 20. Reproduced from [74] under the terms of the Creative Commons Attribution License (CC BY).

Multiplying the strong form of the balance of linear momentum and integrating over the domain $\Omega^- \cup \mathcal{I} \cup \Omega^+$, (3.47), we obtain

$$\begin{aligned} 0 &= \int_{\Omega^+} \boldsymbol{\varphi}^{\boldsymbol{u}}(\boldsymbol{x}) \cdot [\nabla_x \cdot \boldsymbol{\sigma}(\boldsymbol{x}) + \rho(\boldsymbol{x})\, \boldsymbol{f}(\boldsymbol{x})]\, \mathrm{d}x + \int_{\Omega^-} \boldsymbol{\varphi}^{\boldsymbol{u}}(\boldsymbol{x}) \cdot [\nabla_x \cdot \boldsymbol{\sigma}(\boldsymbol{x}) + \rho \boldsymbol{f}(\boldsymbol{x})]\, \mathrm{d}x \\ &= \int_{\Omega} \boldsymbol{\varphi}^{\boldsymbol{u}}(\boldsymbol{x}) \cdot \rho(\boldsymbol{x})\, \boldsymbol{f}(\boldsymbol{x})\, \mathrm{d}x + \int_{\Omega^+ \cup \Omega^-} \nabla_x \cdot [\boldsymbol{\varphi}^{\boldsymbol{u}}(\boldsymbol{x}) \cdot \boldsymbol{\sigma}(\boldsymbol{x})] - \nabla_x \boldsymbol{\varphi}^{\boldsymbol{u}}(\boldsymbol{x}) : \boldsymbol{\sigma}(\boldsymbol{x})\, \mathrm{d}x\,. \end{aligned} \tag{3.97}$$

After applying the divergence theorem, the second term in (3.97) can be expressed as a surface integral

$$\begin{aligned} \int_{\Omega^+ \cup \Omega^-} \nabla_x \cdot [\boldsymbol{\varphi}^{\boldsymbol{u}}(\boldsymbol{x}) \cdot \boldsymbol{\sigma}(\boldsymbol{x})]\, \mathrm{d}x &= \int_{\partial\Omega^+} \boldsymbol{\varphi}^{\boldsymbol{u}}(\boldsymbol{x}) \cdot \boldsymbol{\sigma}(\boldsymbol{x}) \cdot \boldsymbol{n}^+\left(\boldsymbol{x}^+\right) \mathrm{d}x \\ &\quad + \int_{\partial\Omega^-} \boldsymbol{\varphi}^{\boldsymbol{u}}(\boldsymbol{x}) \cdot \boldsymbol{\sigma}(\boldsymbol{x}) \cdot \boldsymbol{n}^-\left(\boldsymbol{x}^-\right) \mathrm{d}x \\ &= \int_{\partial\Omega} \boldsymbol{\varphi}^{\boldsymbol{u}}(\boldsymbol{x}) \cdot \boldsymbol{t}(\boldsymbol{x})\, \mathrm{d}x \\ &\quad - \int_{\mathcal{I}} \boldsymbol{\varphi}^{\boldsymbol{u}}_+\left(\boldsymbol{x}^+\right) \cdot \boldsymbol{\sigma}^+\left(\boldsymbol{x}^+\right) \cdot \widetilde{\boldsymbol{n}}(\widetilde{\boldsymbol{x}}) - \boldsymbol{\varphi}^{\boldsymbol{u}}_-\left(\boldsymbol{x}^-\right) \cdot \boldsymbol{\sigma}^-\left(\boldsymbol{x}^-\right) \cdot \widetilde{\boldsymbol{n}}(\widetilde{\boldsymbol{x}})\, \mathrm{d}x\,. \end{aligned} \tag{3.98}$$

Moreover, the integral over the interface can be further rearranged as

$$\begin{aligned} \int_{\mathcal{I}} \boldsymbol{\varphi}^{\boldsymbol{u}}_+\left(\boldsymbol{x}^+\right) \cdot \widetilde{\boldsymbol{t}^+}(\widetilde{\boldsymbol{x}}) - \boldsymbol{\varphi}^{\boldsymbol{u}}_-\left(\boldsymbol{x}^-\right) \cdot \widetilde{\boldsymbol{t}^-}(\widetilde{\boldsymbol{x}})\, \mathrm{d}x &= \int_{\mathcal{I}} [\![\boldsymbol{\varphi}^{\boldsymbol{u}} \cdot \widetilde{\boldsymbol{t}}]\!](\widetilde{\boldsymbol{x}})\, \mathrm{d}x \\ &= \int_{\mathcal{I}} [\![\boldsymbol{\varphi}^{\boldsymbol{u}}]\!](\widetilde{\boldsymbol{x}}) \cdot \{\!\{\widetilde{\boldsymbol{t}}\}\!\}(\widetilde{\boldsymbol{x}}) + \{\!\{\boldsymbol{\varphi}^{\boldsymbol{u}}\}\!\}(\widetilde{\boldsymbol{x}}) \cdot [\![\widetilde{\boldsymbol{t}}]\!](\widetilde{\boldsymbol{x}})\, \mathrm{d}x\,. \end{aligned} \tag{3.99}$$

Substituting (3.98) and (3.99) into (3.97) yields the final form of weak form as in (3.49). The same procedure can analogously be applied to derive the weak forms for the electrical and thermal subproblems.

B.2 Tangent stiffness contributions

qtd. [74] {This section provides the specific form of the tangent stiffness contributions. The contributions to the global stiffness matrix that result from the linearisation of (3.61) and (3.62) can be derived with respect to the displacement field,

$$\mathbf{K}^{\boldsymbol{uu}} = \frac{\mathrm{d}\boldsymbol{f}^{\boldsymbol{u}\,\mathrm{h}}_{\mathrm{int}}}{\mathrm{d}\widehat{\boldsymbol{u}}} = \mathop{\mathbf{A}}_{e=1}^{\mathrm{n_{el}}} \int_{\Omega^e} \nabla_x N_A \cdot \frac{\mathrm{d}\boldsymbol{\sigma}}{\mathrm{d}\boldsymbol{\varepsilon}} \cdot \nabla_x N_D\, \mathrm{d}x\,, \tag{3.100}$$

$$\widetilde{\mathbf{K}}^{\boldsymbol{uu}} = \frac{\mathrm{d}\widetilde{\boldsymbol{f}}^{\boldsymbol{u}\,\mathrm{h}}_{\mathrm{int}}}{\mathrm{d}\widehat{\boldsymbol{u}}} = \mathop{\mathbf{A}}_{e=1}^{\widetilde{\mathrm{n}}_{\mathrm{el}}} \int_{\mathcal{I}^e} N_A \frac{\mathrm{d}\{\!\{\widetilde{\boldsymbol{t}}\}\!\}}{\mathrm{d}[\![\boldsymbol{u}]\!]} N_D\, \mathrm{d}x\,, \tag{3.101}$$

with respect to the electric potential

$$\mathbf{K}^{\boldsymbol{u}\phi} = \frac{\mathrm{d}\tilde{\boldsymbol{f}}^{\boldsymbol{u}\,\mathrm{h}}_{\mathrm{int}}}{\mathrm{d}\widehat{\boldsymbol{\phi}}} = \bigwedge_{e=1}^{\mathrm{n_{el}}} \int_{\Omega^e} -\nabla_x N_A \cdot \frac{\mathrm{d}\boldsymbol{\sigma}}{\mathrm{d}\boldsymbol{e}} \cdot \nabla_x N_E \,\mathrm{d}x\,, \tag{3.102}$$

$$\widetilde{\mathbf{K}}^{\boldsymbol{u}\phi} = \frac{\mathrm{d}\tilde{\boldsymbol{f}}^{\boldsymbol{u}\,\mathrm{h}}_{\mathrm{int}}}{\mathrm{d}\widehat{\boldsymbol{\phi}}} = \bigwedge_{e=1}^{\widetilde{\mathrm{n}}_{\mathrm{el}}} \int_{\mathcal{I}^e} N_A \frac{\mathrm{d}\{\!\{\widetilde{\boldsymbol{t}}\}\!\}}{\mathrm{d}[\![\phi]\!]} N_E \,\mathrm{d}x\,. \tag{3.103}$$

and with respect to the temperature

$$\mathbf{K}^{\boldsymbol{u}\theta} = \frac{\mathrm{d}\tilde{\boldsymbol{f}}^{\boldsymbol{u}\,\mathrm{h}}_{\mathrm{int}}}{\mathrm{d}\widehat{\boldsymbol{\theta}}} = \bigwedge_{e=1}^{\mathrm{n_{el}}} \int_{\Omega^e} -\nabla_x N_A \cdot \frac{\mathrm{d}\boldsymbol{\sigma}}{\mathrm{d}\theta} \cdot N_F \,\mathrm{d}x\,, \tag{3.104}$$

$$\widetilde{\mathbf{K}}^{\boldsymbol{u}\theta} = \frac{\mathrm{d}\tilde{\boldsymbol{f}}^{\boldsymbol{u}\,\mathrm{h}}_{\mathrm{int}}}{\mathrm{d}\widehat{\boldsymbol{\theta}}} = \bigwedge_{e=1}^{\widetilde{\mathrm{n}}_{\mathrm{el}}} \int_{\mathcal{I}^e} N_A \frac{\mathrm{d}\{\!\{\widetilde{\boldsymbol{t}}\}\!\}}{\mathrm{d}[\![\theta]\!]} N_F \,\mathrm{d}x\,, \tag{3.105}$$

Moreover, the contributions to the global stiffness matrix that result from the linearisation of (3.66) and (3.67) read

$$\mathbf{K}^{\phi\boldsymbol{u}} = \frac{\mathrm{d}\boldsymbol{f}^{\phi\,\mathrm{h}}_{\mathrm{int}}}{\mathrm{d}\widehat{\boldsymbol{u}}} = \bigwedge_{e=1}^{\mathrm{n_{el}}} \int_{\Omega^e} \nabla_x N_B \cdot \frac{\mathrm{d}\boldsymbol{j}}{\mathrm{d}\boldsymbol{\varepsilon}} \cdot \nabla_x N_D \,\mathrm{d}x\,, \tag{3.106}$$

$$\widetilde{\mathbf{K}}^{\phi\boldsymbol{u}} = \frac{\mathrm{d}\tilde{\boldsymbol{f}}^{\phi\,\mathrm{h}}_{\mathrm{int}}}{\mathrm{d}\widehat{\boldsymbol{u}}} = \bigwedge_{e=1}^{\widetilde{\mathrm{n}}_{\mathrm{el}}} \int_{\mathcal{I}^e} N_B \frac{\mathrm{d}\{\!\{\widetilde{i}\}\!\}}{\mathrm{d}[\![\boldsymbol{u}]\!]} N_D \,\mathrm{d}x\,, \tag{3.107}$$

and

$$\mathbf{K}^{\phi\phi} = \frac{\mathrm{d}\boldsymbol{f}^{\phi\,\mathrm{h}}_{\mathrm{int}}}{\mathrm{d}\widehat{\boldsymbol{\phi}}} = \bigwedge_{e=1}^{\mathrm{n_{el}}} \int_{\Omega^e} -\nabla_x N_B \cdot \frac{\mathrm{d}\boldsymbol{j}}{\mathrm{d}\boldsymbol{e}} \cdot \nabla_x N_E \,\mathrm{d}x\,, \tag{3.108}$$

$$\widetilde{\mathbf{K}}^{\phi\phi} = \frac{\mathrm{d}\tilde{\boldsymbol{f}}^{\phi\,\mathrm{h}}_{\mathrm{int}}}{\mathrm{d}\widehat{\boldsymbol{\phi}}} = \bigwedge_{e=1}^{\widetilde{\mathrm{n}}_{\mathrm{el}}} \int_{\mathcal{I}^e} N_B \frac{\mathrm{d}\{\!\{\widetilde{i}\}\!\}}{\mathrm{d}[\![\phi]\!]} N_E \,\mathrm{d}x\,, \tag{3.109}$$

as well as

$$\mathbf{K}^{\phi\theta} = \frac{\mathrm{d}\boldsymbol{f}^{\phi\,\mathrm{h}}_{\mathrm{int}}}{\mathrm{d}\widehat{\boldsymbol{\theta}}} = \bigwedge_{e=1}^{\mathrm{n_{el}}} \int_{\Omega^e} \nabla_x N_B \cdot \frac{\mathrm{d}\boldsymbol{j}}{\mathrm{d}\theta} N_F \,\mathrm{d}x\,, \tag{3.110}$$

$$\widetilde{\mathbf{K}}^{\phi\theta} = \frac{\mathrm{d}\tilde{\boldsymbol{f}}^{\phi\,\mathrm{h}}_{\mathrm{int}}}{\mathrm{d}\widehat{\boldsymbol{\theta}}} = \bigwedge_{e=1}^{\widetilde{\mathrm{n}}_{\mathrm{el}}} \int_{\mathcal{I}^e} N_B \frac{\mathrm{d}\{\!\{\widetilde{i}\}\!\}}{\mathrm{d}[\![\theta]\!]} N_F \,\mathrm{d}x\,. \tag{3.111}$$

The contributions to the global stiffness matrix that result from the linearisation of (3.69) and (3.70) result in

$$\mathbf{K}^{\theta\boldsymbol{u}} = \frac{\mathrm{d}\boldsymbol{f}^{\theta\,\mathrm{h}}_{\mathrm{int}}}{\mathrm{d}\widehat{\boldsymbol{u}}} = \bigwedge_{e=1}^{\mathrm{n_{el}}} \int_{\Omega^e} \nabla_x N_C \cdot \frac{\mathrm{d}\boldsymbol{q}}{\mathrm{d}\boldsymbol{\varepsilon}} \cdot \nabla_x N_D \,\mathrm{d}x\,, \tag{3.112}$$

$$\widetilde{\mathbf{K}}^{\theta\boldsymbol{u}} = \frac{\mathrm{d}\tilde{\boldsymbol{f}}^{\theta\,\mathrm{h}}_{\mathrm{int}}}{\mathrm{d}\widehat{\boldsymbol{u}}} = \bigwedge_{e=1}^{\widetilde{\mathrm{n}}_{\mathrm{el}}} \int_{\mathcal{I}^e} N_C \frac{\mathrm{d}\{\!\{\widetilde{q}\}\!\}}{\mathrm{d}[\![\boldsymbol{u}]\!]} N_D \,\mathrm{d}x\,, \tag{3.113}$$

as well as

$$\mathbf{K}^{\theta\phi} = \frac{\mathrm{d}\boldsymbol{f}^{\theta\,\mathrm{h}}_{\mathrm{int}}}{\mathrm{d}\widehat{\boldsymbol{\phi}}} = \mathop{\mathbf{A}}_{e=1}^{\mathrm{n_{el}}} \int_{\Omega^e} \nabla_x N_C \cdot \frac{\mathrm{d}\boldsymbol{q}}{\mathrm{d}\boldsymbol{e}} \cdot \nabla_x N_E \,\mathrm{d}x\,, \tag{3.114}$$

$$\widetilde{\mathbf{K}}^{\theta\phi} = \frac{\mathrm{d}\tilde{\boldsymbol{f}}^{\theta\,\mathrm{h}}_{\mathrm{int}}}{\mathrm{d}\widehat{\boldsymbol{\phi}}} = \mathop{\mathbf{A}}_{e=1}^{\widetilde{\mathrm{n}}_{\mathrm{el}}} \int_{\mathcal{I}^e} N_C \,\frac{\mathrm{d}\{\!\{\widetilde{q}\}\!\}}{\mathrm{d}[\![\phi]\!]}\, N_E \,\mathrm{d}x\,, \tag{3.115}$$

and}$^{\mathrm{qtd.}}_{[74]}$

$$\mathbf{K}^{\theta\theta} = \frac{\mathrm{d}\boldsymbol{f}^{\theta\,\mathrm{h}}_{\mathrm{int}}}{\mathrm{d}\widehat{\boldsymbol{\theta}}} = \mathop{\mathbf{A}}_{e=1}^{\mathrm{n_{el}}} \int_{\Omega^e} \nabla_x N_C \,\cdot \frac{\mathrm{d}\boldsymbol{q}}{\mathrm{d}\nabla_x\theta} \cdot \nabla_x N_F \,\mathrm{d}x\,, \tag{3.116}$$

$$\widetilde{\mathbf{K}}^{\theta\theta} = \frac{\mathrm{d}\tilde{\boldsymbol{f}}^{\theta\,\mathrm{h}}_{\mathrm{int}}}{\mathrm{d}\widehat{\boldsymbol{\theta}}} = \mathop{\mathbf{A}}_{e=1}^{\widetilde{\mathrm{n}}_{\mathrm{el}}} \int_{\mathcal{I}^e} N_C \,\frac{\mathrm{d}\{\!\{\widetilde{q}\}\!\}}{\mathrm{d}[\![\theta]\!]}\, N_F \,\mathrm{d}x\,. \tag{3.117}$$

Finally, the contributions to the global stiffness matrix that result from the linearisation of (3.71) and (3.72) are given

$$\mathbf{K}^{\theta\boldsymbol{u}} = \frac{\mathrm{d}\boldsymbol{f}^{\theta\,\mathrm{h}}_{\mathrm{vol}}}{\mathrm{d}\widehat{\boldsymbol{u}}} = \mathop{\mathbf{A}}_{e=1}^{\mathrm{n_{el}}} \int_{\Omega^e} N_C \,\frac{\mathrm{d}\left[\rho\, r + \boldsymbol{j}\cdot\boldsymbol{e}\right]}{\mathrm{d}\boldsymbol{\varepsilon}} \cdot \nabla_x N_D \,\mathrm{d}x\,, \tag{3.118}$$

$$\widetilde{\mathbf{K}}^{\theta\boldsymbol{u}} = \frac{\mathrm{d}\tilde{\boldsymbol{f}}^{\theta\,\mathrm{h}}_{\mathrm{vol}}}{\mathrm{d}\widehat{\boldsymbol{u}}} = \mathop{\mathbf{A}}_{e=1}^{\widetilde{\mathrm{n}}_{\mathrm{el}}} \int_{\mathcal{I}^e} N_C \frac{\mathrm{d}\,\{\!\{\widetilde{i}\}\!\}\,[\![\phi]\!]}{\mathrm{d}[\![\boldsymbol{u}]\!]} N_D \,\mathrm{d}x\,, \tag{3.119}$$

as well as

$$\mathbf{K}^{\theta\phi} = \frac{\mathrm{d}\boldsymbol{f}^{\theta\,\mathrm{h}}_{\mathrm{vol}}}{\mathrm{d}\widehat{\boldsymbol{\phi}}} = \mathop{\mathbf{A}}_{e=1}^{\mathrm{n_{el}}} \int_{\Omega^e} N_C \frac{\mathrm{d}\left[\rho\, r + \boldsymbol{j}\cdot\boldsymbol{e}\right]}{\mathrm{d}\boldsymbol{e}} \cdot \nabla_x N_E \,\mathrm{d}x\,, \tag{3.120}$$

$$\widetilde{\mathbf{K}}^{\theta\phi} = \frac{\mathrm{d}\tilde{\boldsymbol{f}}^{\theta\,\mathrm{h}}_{\mathrm{vol}}}{\mathrm{d}\widehat{\boldsymbol{\phi}}} = \mathop{\mathbf{A}}_{e=1}^{\widetilde{\mathrm{n}}_{\mathrm{el}}} \int_{\mathcal{I}^e} N_C \frac{\mathrm{d}\,\{\!\{\widetilde{i}\}\!\}[\![\phi]\!]}{\mathrm{d}[\![\phi]\!]}\, N_E \,\mathrm{d}x\,, \tag{3.121}$$

and

$$\mathbf{K}^{\theta\theta} = \frac{\mathrm{d}\boldsymbol{f}^{\theta\,\mathrm{h}}_{\mathrm{vol}}}{\mathrm{d}\widehat{\boldsymbol{\theta}}} = \mathop{\mathbf{A}}_{e=1}^{\mathrm{n_{el}}} \int_{\Omega^e} N_C \,\frac{\mathrm{d}\left[\rho\, r + \boldsymbol{j}\cdot\boldsymbol{e}\right]}{\mathrm{d}\nabla_x\theta} \cdot \nabla_x N_F \,\mathrm{d}x\,, \tag{3.122}$$

$$\widetilde{\mathbf{K}}^{\theta\theta} = \frac{\mathrm{d}\tilde{\boldsymbol{f}}^{\theta\,\mathrm{h}}_{\mathrm{vol}}}{\mathrm{d}\widehat{\boldsymbol{\theta}}} = \mathop{\mathbf{A}}_{e=1}^{\widetilde{\mathrm{n}}_{\mathrm{el}}} \int_{\mathcal{I}^e} N_C \,\frac{\mathrm{d}\,\{\!\{\widetilde{i}\}\!\}[\![\phi]\!]}{\mathrm{d}[\![\theta]\!]}\, N_F \,\mathrm{d}x\,. \tag{3.123}$$

4 Computational homogenisation: Thermo-electro-mechanical problem

Materials often exhibit complex microstructural feature – such as pores, inclusions, and grain boundaries – that significantly influence their macroscopic behaviour. Under coupled thermo-electro-mechanical loading, these heterogeneities can induce localised variations in the stress tensor, the heat flux vector, and the electric current density vector, ultimately altering the global material response. Of particular interest is their impact on electrical resistance, which can serve as a sensitive indicator – or fingerprint – of internal damage evolution.

Figure 4.1 illustrates the experimental concept behind resistance-based damage characterisation in metals. As the specimen is subjected to mechanical loading, localised changes in electrical resistance can be measured using a four-point probe setup. These resistance changes are directly influenced by microstructural features such as voids, inclusions, and microcracks, whose evolution alters the local conductivity. The correlation between spatial resistance measurements and microstructural damage states enables a non-destructive assessment of material degradation. This motivates the need for a computational multiscale framework capable of resolving such microstructural features and predicting their influence on macroscopic resistance. By explicitly resolving microstructural features within representative volume elements (RVEs), these approaches enable accurate evaluation of the effective macroscopic response under coupled thermal, electrical, and mechanical loading conditions. Instead of relying on closed-form constitutive laws, classical material evaluations are replaced with finite element simulations at the microscale, making it possible to bridge spatial scales and capture the influence of evolving microstructural phenomena under realistic operating conditions.

Motivated by the temperature-dependent electrical and mechanical behaviour of conductors, the present chapter extends existing computational multiscale methods [98] to a thermo-electro-mechanically coupled setting. The resulting framework enables accurate simulations of materials where field couplings cannot be neglected – such as in advanced electronic components, microelectromechanical systems (MEMS), and functional materials exposed to complex environments.

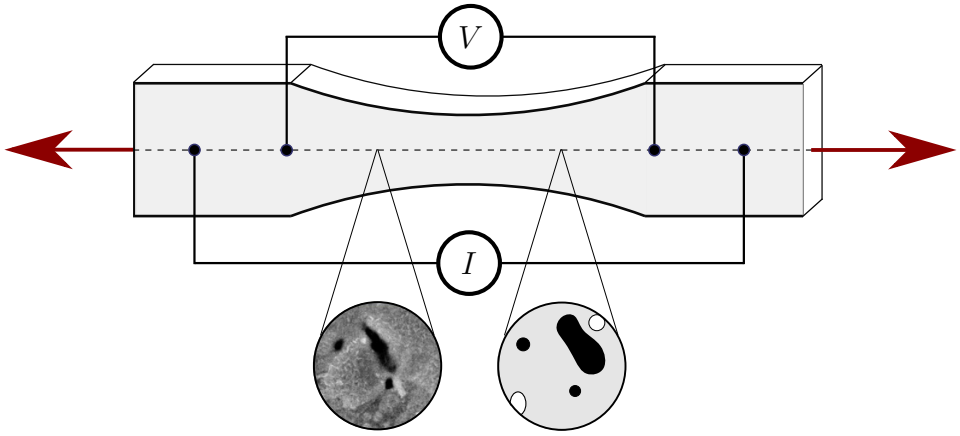

Figure 4.1: Schematic representation of a resistance measurement setup for a tensile specimen under uniaxial loading. A four-point probe configuration is employed to monitor changes in electrical resistance across the gauge section. Insets show experimental SEM image of evolving pore deformation under tensile loading reproduced from [39], alongside a representative volume element used in finite element simulations.

The scope of the present chapter is:

- *It establishes a small-strain, multiscale computational framework for thermo-electro-mechanically coupled problems, including the derivation of governing equations, boundary conditions, and energy consistency criteria.*

The chapter is organised as follows: We begin by defining the microscale problem in Section 4.1. Averaging theorems are discussed in Section 4.2, followed by the derivation of a generalised Hill–Mandel condition in Section 4.3 and the presentation of suitable boundary conditions. Based on the findings of previous sections, the coupled macroscale problem and associated macroscopic effective material properties are defined in Section 4.4. With the fundamental set of balance equations and corresponding weak forms at hand, a finite element implementation for the multiscale framework is detailed in Section 4.5.

4.1 Microscale problem

Let $\boldsymbol{y} \in \mathbb{R}^d$ denote the position in the unit cell $Y \subset \mathbb{R}^d$, as illustrated in Figure 4.2. The local displacement, electric potential and temperature fields are decomposed into macroscopic averages $\{\bullet\}_0$ and superimposed microfluctuations $\{\widetilde{\bullet}\}$, resulting in

$$\boldsymbol{u}(\boldsymbol{y}) = \boldsymbol{\varepsilon}_0(\boldsymbol{x}) \cdot \boldsymbol{y} + \widetilde{\boldsymbol{u}}(\boldsymbol{x}, \boldsymbol{y}) \qquad \forall \boldsymbol{y} \in Y\,, \tag{4.1a}$$

$$\phi(\boldsymbol{y}) = -\boldsymbol{e}_0(\boldsymbol{x}) \cdot \boldsymbol{y} + \widetilde{\phi}(\boldsymbol{x}, \boldsymbol{y}) \qquad \forall \boldsymbol{y} \in Y\,, \tag{4.1b}$$

$$\theta(\boldsymbol{y}) = \nabla_x \theta_0(\boldsymbol{x}) \cdot \boldsymbol{y} + \widetilde{\theta}(\boldsymbol{x}, \boldsymbol{y}) \qquad \forall \boldsymbol{y} \in Y\,, \tag{4.1c}$$

and

$$\boldsymbol{\varepsilon}(\boldsymbol{y}) = \quad \boldsymbol{\varepsilon}_0(\boldsymbol{x}) + \nabla_y \widetilde{\boldsymbol{u}}(\boldsymbol{x}, \boldsymbol{y}) \qquad \forall \boldsymbol{y} \in Y\,, \tag{4.1d}$$

$$\boldsymbol{e}(\boldsymbol{y}) = \quad \boldsymbol{e}_0(\boldsymbol{x}) - \nabla_y \widetilde{\phi}(\boldsymbol{x}, \boldsymbol{y}) \qquad \forall \boldsymbol{y} \in Y\,, \tag{4.1e}$$

$$\nabla_y \theta(\boldsymbol{y}) = \nabla_x \theta_0(\boldsymbol{x}) + \nabla_y \widetilde{\theta}(\boldsymbol{x}, \boldsymbol{y}) \qquad \forall \boldsymbol{y} \in Y\,. \tag{4.1f}$$

Resorting to a classic separation of scales argument, the governing equations at the microscale are solved subject to the assumptions of (quasi-)stationary processes. Moreover, source terms are neglected and constitutive relations are evaluated at "fixed" macroscale temperature. Accordingly, for the type of constitutive relations considered

the thermo-electrically coupled microscale boundary value problem reads

$$\nabla_y \cdot \boldsymbol{\sigma}(\boldsymbol{y}) = \quad \nabla_y \cdot [\mathbf{E}(\theta_0, \boldsymbol{y}) : \boldsymbol{\varepsilon}(\boldsymbol{y})] \quad = \mathbf{0} \qquad \forall \boldsymbol{y} \in Y\,, \tag{4.2a}$$

$$\nabla_y \cdot \boldsymbol{j}(\boldsymbol{y}) = -\nabla_y \cdot [\boldsymbol{\mathcal{S}}(\theta_0, \boldsymbol{y}) \cdot \nabla_y \phi(\boldsymbol{y})] = 0 \qquad \forall \boldsymbol{y} \in Y\,, \tag{4.2b}$$

$$\nabla_y \cdot \boldsymbol{q}(\boldsymbol{y}) = -\nabla_y \cdot [\boldsymbol{\mathcal{K}}(\theta_0, \boldsymbol{y}) \cdot \nabla_y \theta(\boldsymbol{y})] = 0 \qquad \forall \boldsymbol{y} \in Y\,. \tag{4.2c}$$

Having defined the field variables and governing equations at the microscale, the next step is to understand how these local quantities relate to macroscopic responses. This is achieved through appropriate averaging theorems, discussed in the following section.

Remark 6. The present multiscale framework relies on the assumption of scale separation, wherein the characteristic length of the microstructure is significantly smaller than that of the macroscopic domain. Mathematically, this implies $\ell \ll L$, allowing for a clear distinction between local (microscale) and global (macroscale) behaviour. Under this assumption, each material point in the macroscale domain can be associated with a RVE, whose response is governed by locally periodic or statistically homogeneous microstructures. This scale separation justifies the application of first-order computational homogenisation and ensures that information from the microstructure can be consistently upscaled without invoking memory effects or nonlocality. In the absence of scale separation – e.g., near localisation zones or in the presence of strong gradients – higher-order or enriched homogenisation schemes may be required [60].

4.2 Averaging theorems

Throughout this thesis, the definition $v = \mathrm{vol}(Y)$ holds. In energy-based computational multiscale formulations, macroscopic quantities are related to their microscopic counterparts through volume averages over unit cells, namely

$$\{\bullet\}_0(\boldsymbol{x}) = \frac{1}{v} \int_Y \{\bullet\}(\boldsymbol{y})\, \mathrm{d}y\,. \tag{4.3}$$

In this regard, energetic consistency of the two-scales is ensured by postulating appropriate Hill–Mandel energy equivalence conditions. To evaluate these and to simplify the

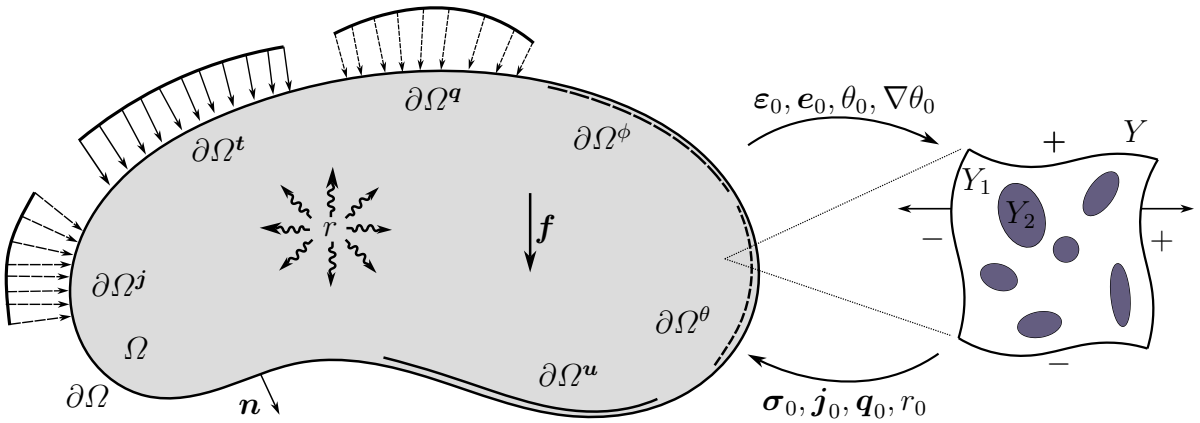

Figure 4.2: Control volume Ω under consideration. The underlying microstructure Y, represented by a unit cell at each material point, dictates the effective macroscale material response.

implementation, it is advantageous to convert the volume integrals into surface integrals using Gauß's theorem. Accordingly, the macroscopic strain tensor results in

$$\boldsymbol{\varepsilon}_0 = \frac{1}{v}\int_Y \boldsymbol{\varepsilon}(\boldsymbol{y})\,\mathrm{d}y = \frac{1}{v}\left[\int_{\partial Y} \boldsymbol{u}(\boldsymbol{y}) \otimes \boldsymbol{n}(\boldsymbol{y})\,\mathrm{d}y\right]^{\mathrm{sym}} . \tag{4.4}$$

The representation of the macroscopic electric field vector

$$\boldsymbol{e}_0 = \frac{1}{v}\int_Y \boldsymbol{e}(\boldsymbol{y})\,\mathrm{d}y = \frac{1}{v}\int_{\partial Y} -\phi(\boldsymbol{y})\,\boldsymbol{n}(\boldsymbol{y})\,\mathrm{d}y \tag{4.5}$$

is obtained in terms of the electric potential field at the boundary. Analogously, the effective macroscopic temperature gradient is given by

$$\nabla\theta_0 = \frac{1}{v}\int_Y \nabla_y\theta(\boldsymbol{y})\,\mathrm{d}y = \frac{1}{v}\int_{\partial Y} \theta(\boldsymbol{y})\,\boldsymbol{n}(\boldsymbol{y})\,\mathrm{d}y . \tag{4.6}$$

The effective macroscopic stress tensor can be expressed as

$$\boldsymbol{\sigma}_0 = \frac{1}{v}\int_Y \boldsymbol{\sigma}(\boldsymbol{y})\,\mathrm{d}y = \frac{1}{v}\int_{\partial Y} \boldsymbol{t}(\boldsymbol{y}) \otimes \boldsymbol{y}\,\mathrm{d}y , \tag{4.7}$$

where use was made of the definition of surface tractions $\boldsymbol{t}(\boldsymbol{y}) = \boldsymbol{\sigma}(\boldsymbol{y})\cdot\boldsymbol{n}(\boldsymbol{y})$. Moreover, the governing equation for the effective macroscopic electric current density vector results in

$$\boldsymbol{j}_0 = \frac{1}{v}\int_Y \boldsymbol{j}(\boldsymbol{y})\,\mathrm{d}y = \frac{1}{v}\int_{\partial Y} \boldsymbol{y}\,i(\boldsymbol{y})\,\mathrm{d}y \tag{4.8}$$

where the definition of the projected current density vector $i(\boldsymbol{y}) = \boldsymbol{j}(\boldsymbol{y})\cdot\boldsymbol{n}(\boldsymbol{y})$ was used. Furthermore, by introducing the projected heat flux $q(\boldsymbol{y}) = -\boldsymbol{q}(\boldsymbol{y})\cdot\boldsymbol{n}(\boldsymbol{y})$, the effective macroscopic heat flux vector takes the form

$$\boldsymbol{q}_0 = \frac{1}{v}\int_Y \boldsymbol{q}(\boldsymbol{y})\,\mathrm{d}y = \frac{1}{v}\int_{\partial Y} -\boldsymbol{y}\,q(\boldsymbol{y})\,\mathrm{d}y . \tag{4.9}$$

While the averaging theorems provide the basis for scale transition, the formulation must also satisfy energetic consistency between the micro- and macroscales. This requirement is addressed by the Hill–Mandel principle, which is introduced in the following section.

4.3 Generalised Hill–Mandel conditions

The Hill–Mandel condition establishes a rigorous energy consistency requirement, stipulating that the macroscopic energy must be equivalent to the average microscopic energy within a unit cell. In this regard, (2.34) leads to a generalised average dissipation theorem. Specifically speaking, the classic Hill–Mandel condition for the mechanical problem reads

$$\begin{aligned}
\boldsymbol{\sigma}_0 : \delta\boldsymbol{\varepsilon}_0 &\overset{!}{=} \frac{1}{v}\int_Y \boldsymbol{\sigma}(\boldsymbol{y}) : \nabla_y \delta\boldsymbol{\varepsilon}(\boldsymbol{y})\,\mathrm{d}y \\
&= \frac{1}{v}\int_Y \nabla_y \cdot [\delta\boldsymbol{u}(\boldsymbol{y}) \cdot \boldsymbol{\sigma}(\boldsymbol{y})]\,\mathrm{d}y \quad - \frac{1}{v}\int_Y \delta\boldsymbol{u}(\boldsymbol{y}) \cdot [\nabla_y \boldsymbol{\sigma}(\boldsymbol{y})]\,\mathrm{d}y \\
&= \frac{1}{v}\int_{\partial Y} \delta\boldsymbol{u}(\boldsymbol{y}) \cdot \underbrace{\boldsymbol{\sigma}(\boldsymbol{y}) \cdot \boldsymbol{n}(\boldsymbol{y})}_{=\boldsymbol{t}(\boldsymbol{y})}\,\mathrm{d}y - \frac{1}{v}\int_Y \delta\boldsymbol{u}(\boldsymbol{y}) \underbrace{[\nabla_y \cdot \boldsymbol{\sigma}(\boldsymbol{y})]}_{=\mathbf{0}}\,\mathrm{d}y\,.
\end{aligned} \tag{4.10}$$

The energy equivalence condition for the electrical problem takes the form

$$\begin{aligned}
\boldsymbol{j}_0 \cdot \delta\boldsymbol{e}_0 &\overset{!}{=} -\frac{1}{v}\int_Y \boldsymbol{j}(\boldsymbol{y}) \cdot \nabla_y \delta\phi(\boldsymbol{y})\,\mathrm{d}y \\
&= -\frac{1}{v}\int_Y \nabla_y \cdot [\delta\phi(\boldsymbol{y})\ \boldsymbol{j}(\boldsymbol{y})]\,\mathrm{d}y \quad + \frac{1}{v}\int_Y \delta\phi(\boldsymbol{y})\,[\nabla_y \cdot \boldsymbol{j}(\boldsymbol{y})]\,\mathrm{d}y \\
&= -\frac{1}{v}\int_{\partial Y} \delta\phi(\boldsymbol{y})\ \underbrace{\boldsymbol{j}(\boldsymbol{y}) \cdot \boldsymbol{n}(\boldsymbol{y})}_{=i(\boldsymbol{y})}\,\mathrm{d}y + \frac{1}{v}\int_Y \delta\phi(\boldsymbol{y}) \underbrace{[\nabla_y \cdot \boldsymbol{j}(\boldsymbol{y})]}_{=0}\,\mathrm{d}y
\end{aligned} \tag{4.11}$$

and the one for the thermal problem reads

$$\begin{aligned}
\boldsymbol{q}_0 \cdot \nabla_x \delta\theta_0 &\overset{!}{=} \frac{1}{v}\int_Y \boldsymbol{q}(\boldsymbol{y}) \cdot \nabla_y \delta\theta(\boldsymbol{y})\,\mathrm{d}y \\
&= \frac{1}{v}\int_Y \nabla_y \cdot [\delta\theta(\boldsymbol{y})\ \boldsymbol{q}(\boldsymbol{y})]\,\mathrm{d}y \quad - \frac{1}{v}\int_Y \delta\theta(\boldsymbol{y})\,[\nabla_y \cdot \boldsymbol{q}(\boldsymbol{y})]\,\mathrm{d}y \\
&= \frac{1}{v}\int_{\partial Y} \delta\theta(\boldsymbol{y})\ \underbrace{\boldsymbol{q}(\boldsymbol{y}) \cdot \boldsymbol{n}(\boldsymbol{y})}_{=-q(\boldsymbol{y})}\,\mathrm{d}y - \frac{1}{v}\int_Y \delta\theta(\boldsymbol{y}) \underbrace{[\nabla_y \cdot \boldsymbol{q}(\boldsymbol{y})]}_{=0}\,\mathrm{d}y\,.
\end{aligned} \tag{4.12}$$

In view of (4.1), we observe that (4.10)–(4.12) can alternatively be expressed as

$$\begin{aligned}\boldsymbol{\sigma}_0 : \delta\boldsymbol{\varepsilon}_0 &= \frac{1}{v}\int_{\partial Y} \delta\boldsymbol{u}\,(\boldsymbol{y}) \cdot \boldsymbol{t}\,(\boldsymbol{y})\ \mathrm{d}y \\ &= \frac{1}{v}\int_{\partial Y} [\delta\boldsymbol{\varepsilon}_0 \cdot \boldsymbol{y} + \delta\,\widetilde{\boldsymbol{u}}\,(\boldsymbol{x},\boldsymbol{y})] \cdot \boldsymbol{t}\,(\boldsymbol{y})\ \mathrm{d}y \\ &= \underbrace{\frac{1}{v}\int_{\partial Y} \boldsymbol{t}\,(\boldsymbol{y}) \otimes \boldsymbol{y}\,\mathrm{d}y}_{=\,\boldsymbol{\sigma}_0} : \delta\boldsymbol{\varepsilon}_0 + \frac{1}{v}\int_{\partial Y} \delta\,\widetilde{\boldsymbol{u}}\,(\boldsymbol{y}) \cdot \boldsymbol{t}\,(\boldsymbol{y})\ \mathrm{d}y\end{aligned} \tag{4.13}$$

and

$$\begin{aligned}\boldsymbol{j}_0 \cdot \delta\boldsymbol{e}_0 &= \frac{1}{v}\int_{\partial Y} -\delta\phi\,(\boldsymbol{y})\ i\,(\boldsymbol{y})\ \mathrm{d}y \\ &= -\frac{1}{v}\int_{\partial Y} \left[\nabla_x \delta\phi_0 \cdot \boldsymbol{y} + \delta\,\widetilde{\phi}\,(\boldsymbol{x},\boldsymbol{y})\right]\ i\,(\boldsymbol{y})\ \mathrm{d}y \\ &= \underbrace{\frac{1}{v}\int_{\partial Y} \boldsymbol{y}\, i\,(\boldsymbol{y})\,\mathrm{d}y}_{=\,\boldsymbol{j}_0} \cdot \delta\boldsymbol{e}_0 - \frac{1}{v}\int_{\partial Y} \delta\,\widetilde{\phi}\,(\boldsymbol{y})\ i\,(\boldsymbol{y})\ \mathrm{d}y\end{aligned} \tag{4.14}$$

as well as

$$\begin{aligned}\boldsymbol{q}_0 \cdot \nabla_x \delta\theta_0 &= \frac{1}{v}\int_{\partial Y} -\delta\theta\,(\boldsymbol{y})\ q\,(\boldsymbol{y})\ \mathrm{d}y \\ &= -\frac{1}{v}\int_{\partial Y} \left[\nabla_x \delta\theta_0 \cdot \boldsymbol{y} + \delta\,\widetilde{\theta}\,(\boldsymbol{x},\boldsymbol{y})\right]\ q\,(\boldsymbol{y})\ \mathrm{d}y \\ &= \underbrace{\frac{1}{v}\int_{\partial Y} -\boldsymbol{y}\, q\,(\boldsymbol{y})\,\mathrm{d}y}_{=\,\boldsymbol{q}_0} \cdot \nabla_x\, \delta\theta_0 - \frac{1}{v}\int_{\partial Y} \delta\,\widetilde{\theta}\,(\boldsymbol{x},\boldsymbol{y})\ q\,(\boldsymbol{y})\ \mathrm{d}y\end{aligned} \tag{4.15}$$

which implies that the microfluctuations do not contribute to the overall energy balance. To satisfy (4.10)-(4.12) *a priori*, boundary conditions must be carefully chosen. It can be observed that the boundary conditions on the unit cell must be chosen such that microfluctuation fields vanish.

4.3.1 Affine boundary conditions

In order to satisfy the scale transition relations, the microfluctations on the unit cell boundary are assumed to be suppressed

$$\widetilde{\boldsymbol{u}}\,(\boldsymbol{x},\boldsymbol{y}) = \boldsymbol{0} \quad \text{such that} \quad \boldsymbol{u}\,(\boldsymbol{y}) = \boldsymbol{\varepsilon}_0\,(\boldsymbol{x}) \cdot \boldsymbol{y} \qquad \forall \boldsymbol{y} \in \partial Y\,, \tag{4.16a}$$

$$\widetilde{\phi}\,(\boldsymbol{x},\boldsymbol{y}) = 0 \quad \text{such that} \quad \phi\,(\boldsymbol{y}) = -\boldsymbol{e}_0\,(\boldsymbol{x}) \cdot \boldsymbol{y} \qquad \forall \boldsymbol{y} \in \partial Y\,, \tag{4.16b}$$

$$\widetilde{\theta}\,(\boldsymbol{x},\boldsymbol{y}) = 0 \quad \text{such that} \quad \theta\,(\boldsymbol{y}) = \nabla_x \theta_0\,(\boldsymbol{x}) \cdot \boldsymbol{y} \qquad \forall \boldsymbol{y} \in \partial Y\,. \tag{4.16c}$$

With these conditions, the displacement, electric potential and temperature fields of the unit cell are fully prescribed according to given macroscopic contributions $\boldsymbol{\varepsilon}_0, \boldsymbol{e}_0, \nabla_x \theta_0$. Alternatively, the consistency can be demonstrated through the following derivation. By inserting affine boundary conditions into the Hill–Mandel condition for the mechanical problem yields

$$\begin{aligned} \frac{1}{v}\int_Y \boldsymbol{\sigma}(\boldsymbol{y}) : \delta\boldsymbol{\varepsilon}(\boldsymbol{y})\,\mathrm{d}y &= \frac{1}{v}\int_{\partial Y} \boldsymbol{t}(\boldsymbol{y}) \cdot \delta\left[\boldsymbol{\varepsilon}_0(\boldsymbol{x}) \cdot \boldsymbol{y}\right]\mathrm{d}y \\ &= \frac{1}{v}\int_{\partial Y} \boldsymbol{t}(\boldsymbol{y}) \otimes \boldsymbol{y}\,\mathrm{d}y : \delta\boldsymbol{\varepsilon}_0(\boldsymbol{x}) = \boldsymbol{\sigma}_0 : \delta\boldsymbol{\varepsilon}_0\,, \end{aligned} \tag{4.17a}$$

and the electrical problem is expressed as

$$\begin{aligned} \frac{1}{v}\int_Y \boldsymbol{j}(\boldsymbol{y}) \cdot \delta\boldsymbol{e}(\boldsymbol{y})\,\mathrm{d}y &= -\frac{1}{v}\int_{\partial Y} i(\boldsymbol{y})\,\delta\left[-\boldsymbol{e}_0(\boldsymbol{x}) \cdot \boldsymbol{y}\right]\mathrm{d}y \\ &= \frac{1}{v}\int_{\partial Y} \boldsymbol{y}\, i(\boldsymbol{y})\,\mathrm{d}y \cdot \delta\boldsymbol{e}_0(\boldsymbol{x}) = \boldsymbol{j}_0 \cdot \delta\boldsymbol{e}_0\,. \end{aligned} \tag{4.17b}$$

Similarly, the generalised Hill–Mandel condition for the thermal problem reads

$$\begin{aligned} \frac{1}{v}\int_Y \boldsymbol{q}(\boldsymbol{y}) \cdot \delta\nabla_y\theta(\boldsymbol{y})\,\mathrm{d}y &= \frac{1}{v}\int_{\partial Y} i(\boldsymbol{y})\,\delta\left[\nabla_x\theta_0(\boldsymbol{x}) \cdot \boldsymbol{y}\right]\mathrm{d}y \\ &= \frac{1}{v}\int_{\partial Y} \boldsymbol{y}\, q(\boldsymbol{y})\,\mathrm{d}y \cdot \delta\nabla_x\theta_0(\boldsymbol{x}) = \boldsymbol{q}_0 \cdot \delta\nabla_x\theta_0\,. \end{aligned} \tag{4.17c}$$

4.3.2 Periodic boundary conditions

The set of scale bridging relations (4.10)-(4.12) is trivially fulfilled for the assumed periodic setting with

$$\widetilde{\boldsymbol{u}}^+(\boldsymbol{y}) = \widetilde{\boldsymbol{u}}^-(\boldsymbol{y}) \quad \text{and} \quad \boldsymbol{t}^+(\boldsymbol{y}) = -\boldsymbol{t}^-(\boldsymbol{y}) \quad \forall \boldsymbol{y} \in \partial Y\,, \tag{4.18a}$$

$$\widetilde{\phi}^+(\boldsymbol{y}) = \widetilde{\phi}^-(\boldsymbol{y}) \quad \text{and} \quad i^+(\boldsymbol{y}) = -i^-(\boldsymbol{y}) \quad \forall \boldsymbol{y} \in \partial Y\,, \tag{4.18b}$$

$$\widetilde{\theta}^+(\boldsymbol{y}) = \widetilde{\theta}^-(\boldsymbol{y}) \quad \text{and} \quad q^+(\boldsymbol{y}) = -q^-(\boldsymbol{y}) \quad \forall \boldsymbol{y} \in \partial Y\,. \tag{4.18c}$$

A different approach to showing consistency is outlined below. The formulation of the periodic boundary conditions in terms of the position vectors of the boundary points

$$\boldsymbol{u}^+(\boldsymbol{y}) - \boldsymbol{u}^-(\boldsymbol{y}) = \boldsymbol{\varepsilon}_0(\boldsymbol{x}) \cdot \left[\boldsymbol{y}^+ - \boldsymbol{y}^-\right] \quad \forall \boldsymbol{y} \in \partial Y \tag{4.19a}$$

$$\phi^+(\boldsymbol{y}) - \phi^-(\boldsymbol{y}) = -\boldsymbol{e}_0(\boldsymbol{x}) \cdot \left[\boldsymbol{y}^+ - \boldsymbol{y}^-\right] \quad \forall \boldsymbol{y} \in \partial Y \tag{4.19b}$$

$$\theta^+(\boldsymbol{y}) - \theta^-(\boldsymbol{y}) = \nabla_x\theta_0(\boldsymbol{x}) \cdot \left[\boldsymbol{y}^+ - \boldsymbol{y}^-\right] \quad \forall \boldsymbol{y} \in \partial Y \tag{4.19c}$$

is obtained. To this end, let $\bullet^+$ and $\bullet^-$ indicate quantities at opposing parts of the boundary ∂Y^+ and ∂Y^-. By inserting specified boundary conditions into generalised Hill–Mandel conditions yield

$$\begin{aligned}\frac{1}{v}\int_Y \boldsymbol{\sigma}(\boldsymbol{y}) : \delta\boldsymbol{\varepsilon}(\boldsymbol{y})\,\mathrm{d}y &= \frac{1}{v}\left[\int_{\partial Y^+} \boldsymbol{t}^+(\boldsymbol{y})\cdot\delta\boldsymbol{u}^+(\boldsymbol{y})\,\mathrm{d}y + \int_{\partial Y^-} \boldsymbol{t}^-(\boldsymbol{y})\cdot\delta\boldsymbol{u}^-(\boldsymbol{y})\,\mathrm{d}y\right]\\ &= \frac{1}{v}\int_{\partial Y^+} \boldsymbol{t}^+(\boldsymbol{y})\cdot\left[\delta\boldsymbol{\varepsilon}_0(\boldsymbol{x})\cdot\left[\boldsymbol{y}^+-\boldsymbol{y}^-\right]\right]\mathrm{d}y\\ &= \frac{1}{v}\int_{\partial Y} \boldsymbol{t}(\boldsymbol{y})\otimes\boldsymbol{y}\,\mathrm{d}y : \delta\boldsymbol{\varepsilon}_0(\boldsymbol{x}) = \boldsymbol{\sigma}_0 : \delta\boldsymbol{\varepsilon}_0\,,\end{aligned} \tag{4.20a}$$

so that the average microscopic mechanical work done within the unit cell is equal to the macroscopic work done. Moreover, the Hill–Mandel conditions for the electrical problem

$$\begin{aligned}\frac{1}{v}\int_Y \boldsymbol{j}(\boldsymbol{y})\cdot\delta\boldsymbol{e}(\boldsymbol{y})\,\mathrm{d}y &= -\frac{1}{v}\left[\int_{\partial Y^+} i^+(\boldsymbol{y})\,\delta\phi^+(\boldsymbol{y})\,\mathrm{d}y + \int_{\partial Y^-} i^-(\boldsymbol{y})\;\delta\phi^-(\boldsymbol{y})\,\mathrm{d}y\right]\\ &= \frac{1}{v}\int_{\partial Y^+} i^+(\boldsymbol{y})\left[\delta\boldsymbol{e}_0(\boldsymbol{x})\cdot\left[\boldsymbol{y}^+-\boldsymbol{y}^-\right]\right]\mathrm{d}y\\ &= \frac{1}{v}\int_{\partial Y} \boldsymbol{y}\,i(\boldsymbol{y})\,\mathrm{d}y\cdot\delta\boldsymbol{e}_0(\boldsymbol{x}) = \boldsymbol{j}_0\cdot\delta\boldsymbol{e}_0\,,\end{aligned} \tag{4.20b}$$

and for the thermal problem

$$\begin{aligned}\frac{1}{v}\int_Y \boldsymbol{q}(\boldsymbol{y})\cdot\delta\nabla_y\theta(\boldsymbol{y})\,\mathrm{d}y &= \frac{1}{v}\left[\int_{\partial Y^+} q^+(\boldsymbol{y})\,\delta\theta^+(\boldsymbol{y})\,\mathrm{d}y + \int_{\partial Y^-} q^-(\boldsymbol{y})\,\delta\theta^-(\boldsymbol{y})\,\mathrm{d}y\right]\\ &= \frac{1}{v}\int_{\partial Y^+} q^+(\boldsymbol{y})\left[\delta\nabla_x\theta_0(\boldsymbol{x})\cdot\left[\boldsymbol{y}^+-\boldsymbol{y}^-\right]\right]\mathrm{d}y\\ &= \frac{1}{v}\int_{\partial Y} \boldsymbol{y}\,q(\boldsymbol{y})\,\mathrm{d}y\cdot\delta\nabla_x\theta_0(\boldsymbol{x}) = \boldsymbol{q}_0\cdot\delta\nabla_x\theta_0\,.\end{aligned} \tag{4.20c}$$

are obtained.

4.3.3 Uniform flux boundary conditions

Another boundary condition used in the literature is the uniform flux boundary condition. However, it does not satisfy the condition of vanishing microfluctuation fields; in other words, it does not follow the kinematics-driven macro-micro scale transition of fields. The uniform traction boundary conditions are prescribed at the boundary of unit cell, namely

$$\boldsymbol{t}(\boldsymbol{y}) = \boldsymbol{\sigma}_0(\boldsymbol{x})\cdot\boldsymbol{n}(\boldsymbol{y}) \quad \forall\boldsymbol{y}\in\partial Y \tag{4.21a}$$

$$i(\boldsymbol{y}) = \boldsymbol{j}_0(\boldsymbol{x})\cdot\boldsymbol{n}(\boldsymbol{y}) \quad \forall\boldsymbol{y}\in\partial Y \tag{4.21b}$$

$$q(\boldsymbol{y}) = \boldsymbol{q}_0(\boldsymbol{x})\cdot\boldsymbol{n}(\boldsymbol{y}) \quad \forall\boldsymbol{y}\in\partial Y\,, \tag{4.21c}$$

In view of (4.21), the Hill–Mandel condition yields

$$\begin{aligned}\frac{1}{v}\int_Y \boldsymbol{\sigma}(\boldsymbol{y}) : \delta\boldsymbol{\varepsilon}(\boldsymbol{y})\,\mathrm{d}y &= \frac{1}{v}\int_{\partial Y} \delta\boldsymbol{u}(\boldsymbol{y})\cdot\boldsymbol{\sigma}_0(\boldsymbol{x})\cdot\boldsymbol{n}(\boldsymbol{y})\,\mathrm{d}y \\ &= \boldsymbol{\sigma}_0(\boldsymbol{x}) : \left[\frac{1}{v}\int_{\partial Y} \delta\boldsymbol{u}(\boldsymbol{y})\otimes\boldsymbol{n}(\boldsymbol{y})\,\mathrm{d}y\right]^{\mathrm{sym}} = \boldsymbol{\sigma}_0\cdot\delta\boldsymbol{\varepsilon}_0\,.\end{aligned} \tag{4.22a}$$

Similarly, the electrical problem

$$\begin{aligned}\frac{1}{v}\int_Y \boldsymbol{j}(\boldsymbol{y})\cdot\delta\boldsymbol{e}(\boldsymbol{y})\,\mathrm{d}y &= -\frac{1}{v}\int_{\partial Y} \delta\phi(\boldsymbol{y})\,[\boldsymbol{j}_0(\boldsymbol{x})\cdot\boldsymbol{n}(\boldsymbol{y})]\,\mathrm{d}y \\ &= \boldsymbol{j}_0(\boldsymbol{x})\cdot\left[\frac{1}{v}\int_{\partial Y} -\delta\phi(\boldsymbol{y})\;\boldsymbol{n}(\boldsymbol{y})\,\mathrm{d}y\right] = \boldsymbol{j}_0\cdot\delta\boldsymbol{e}_0\,.\end{aligned} \tag{4.22b}$$

is obtained. The consistency condition for the thermal problem is expressed as

$$\begin{aligned}\frac{1}{v}\int_Y \boldsymbol{q}(\boldsymbol{y})\cdot\delta\nabla\theta(\boldsymbol{y})\,\mathrm{d}y &= \frac{1}{v}\int_{\partial Y} \delta\theta(\boldsymbol{y})\,[\boldsymbol{q}_0(\boldsymbol{x})\cdot\boldsymbol{n}(\boldsymbol{y})]\,\mathrm{d}y \\ &= \boldsymbol{q}_0(\boldsymbol{x})\cdot\left[\frac{1}{v}\int_{\partial Y} \delta\theta(\boldsymbol{y})\;\boldsymbol{n}(\boldsymbol{y})\,\mathrm{d}y\right] = \boldsymbol{q}_0\cdot\delta\nabla_x\theta_0\,.\end{aligned} \tag{4.22c}$$

With the condition of energetic equivalence established, the framework permits the derivation of effective macroscopic constitutive relations. These are developed in the next section, forming the foundation of the macroscale problem.

Remark 7. In addition to boundary conditions used in computational homogenisation, such as affine displacement, uniform flux, and periodic conditions, the assumptions of constant strain (Voigt bound) and constant stress (Reuss bound) offer classical estimates for bounding effective material responses. These assumptions do not stem from boundary value problems posed on RVEs but rather from uniform field approximations applied to idealised microstructures. The Voigt assumption prescribes a constant strain across all constituents, leading to an upper bound on the effective stiffness. The Reuss assumption enforces constant stress throughout the microstructure, resulting in a lower bound on the effective stiffness. While conceptually related to affine displacement and uniform flux boundary conditions, Voigt and Reuss models are more approximate and are generally not used in full-field computational homogenisation. Instead, they serve as theoretical extremes, against which more refined multiscale methods can be benchmarked. Notably, periodic boundary conditions typically yield effective responses that lie between these classical bounds, especially for periodic or statistically representative RVEs.

4.4 Macroscale problem

Having established the energy equivalence between scales, we can define the coupled macroscale problem as

$$\nabla_x\cdot\boldsymbol{\sigma}_0(\boldsymbol{x}) = -\rho^*(\boldsymbol{x})\,\boldsymbol{f}_0(\boldsymbol{x}) \qquad \forall\boldsymbol{x}\in\Omega\,, \tag{4.23a}$$

$$\nabla_x\cdot\boldsymbol{j}_0(\boldsymbol{x}) = 0 \qquad \forall\boldsymbol{x}\in\Omega\,, \tag{4.23b}$$

$$\nabla_x\cdot\boldsymbol{q}_0(\boldsymbol{x}) = \boldsymbol{j}_0(\boldsymbol{x})\cdot\boldsymbol{e}_0(\boldsymbol{x}) + r_0(\boldsymbol{x}) \qquad \forall\boldsymbol{x}\in\Omega\,, \tag{4.23c}$$

with its alternative form

$$\nabla_x \cdot \left[\mathbf{E}^* \left(\theta_0, \boldsymbol{x}\right) : \nabla_x \boldsymbol{u}_0 \left(\boldsymbol{x}\right)\right] = -\rho^* \left(\boldsymbol{x}\right) \boldsymbol{f}_0 \left(\boldsymbol{x}\right) \qquad \forall \boldsymbol{x} \in \Omega\,, \tag{4.24a}$$

$$-\nabla_x \cdot \left[\boldsymbol{\mathcal{S}}^* \left(\theta_0, \boldsymbol{x}\right) \cdot \nabla_x \phi_0 \left(\boldsymbol{x}\right)\right] = 0 \qquad \forall \boldsymbol{x} \in \Omega\,, \tag{4.24b}$$

$$-\nabla_x \cdot \left[\boldsymbol{\mathcal{K}}^* \left(\theta_0, \boldsymbol{x}\right) \cdot \nabla_x \theta_0 \left(\boldsymbol{x}\right)\right] = \nabla_x \phi_0 \left(\boldsymbol{x}\right) \cdot \boldsymbol{\mathcal{S}}^* \left(\theta_0, \boldsymbol{x}\right) \cdot \nabla_x \phi_0 \left(\boldsymbol{x}\right) + r_0 \left(\boldsymbol{x}\right) \qquad \forall \boldsymbol{x} \in \Omega\,, \tag{4.24c}$$

where $\mathbf{E}^* : \mathbb{R}^+ \times \Omega \to \mathrm{Lin}\left(\mathbb{R}^{d\times d}, \mathbb{R}^{d\times d}\right)$ is the 4th order effective mechanical stiffness tensor, $\boldsymbol{\mathcal{S}}^* : \mathbb{R}^+ \times \Omega \to \mathrm{Lin}\left(\mathbb{R}^d, \mathbb{R}^d\right)$ and $\boldsymbol{\mathcal{K}}^* : \mathbb{R}^+ \times \Omega \to \mathrm{Lin}\left(\mathbb{R}^d, \mathbb{R}^d\right)$ denote the effective electrical and thermal conductivity tensor, respectively. In (4.23c), macroscopic body forces $\boldsymbol{f}_0 : \Omega \to \mathbb{R}^d$ and the heat source $r_0 : \Omega \to \mathbb{R}$ are calculated through volume averages (4.3). Furthermore the effective density $\rho^* : \Omega \to \mathbb{R}$ relies on conservation of mass

$$\rho^* \left(\boldsymbol{x}\right) = \frac{1}{v} \int_Y \rho \left(\boldsymbol{y}\right) \, \mathrm{d}y \tag{4.25}$$

and can be obtained through volume average. Once the local problem (4.2) is solved, the effective fluxes can be calculated using (4.7), (4.8) and (4.9). The effective stiffness tensor can be expressed as

$$\begin{aligned} \mathbf{E}^* \left(\theta_0, \boldsymbol{x}\right) : \boldsymbol{\varepsilon}_0 \left(\boldsymbol{x}\right) = \boldsymbol{\sigma}_0 \left(\boldsymbol{x}\right) &= \frac{1}{v} \int_Y \boldsymbol{\sigma} \left(\boldsymbol{y}\right) \mathrm{d}y \\ &= \frac{1}{v} \int_Y \mathbf{E} \left(\theta_0, \boldsymbol{y}\right) : \left[\boldsymbol{\varepsilon}_0 \left(\boldsymbol{x}\right) + \nabla_y \widetilde{\boldsymbol{u}} \left(\boldsymbol{x}, \boldsymbol{y}\right)\right] \mathrm{d}y \\ &= \underbrace{\frac{1}{v} \int_Y \mathbf{E} \left(\theta_0, \boldsymbol{y}\right) : \left[\mathbf{I} + \mathbf{M}^u \left(\boldsymbol{x}, \boldsymbol{y}\right)\right] \mathrm{d}y}_{\mathbf{E}^* \left(\theta_0, \, \boldsymbol{x}\right)} : \, \boldsymbol{\varepsilon}_0 \left(\boldsymbol{x}\right) \,, \end{aligned} \tag{4.26a}$$

where the 4th order structure tensor $\mathbf{M}^u : \Omega \times Y \to \mathrm{Lin}\left(\mathbb{R}^{d\times d}, \mathbb{R}^{d\times d}\right)$ defines the relation between the fluctuation field and the applied macroscopic field, specifically speaking $\nabla_y \widetilde{\boldsymbol{u}} = \mathbf{M}^u : \boldsymbol{\varepsilon}_0$. Moreover, the effective electrical conductivity tensor can be determined through the relation

$$\begin{aligned} \boldsymbol{\mathcal{S}}^* \left(\theta_0, \boldsymbol{x}\right) \cdot \boldsymbol{e}_0 \left(\boldsymbol{x}\right) = \boldsymbol{j}_0 \left(\boldsymbol{x}\right) &= \frac{1}{v} \int_Y \boldsymbol{j} \left(\boldsymbol{y}\right) \mathrm{d}y \\ &= \frac{1}{v} \int_Y \boldsymbol{\mathcal{S}} \left(\theta_0, \boldsymbol{y}\right) \cdot \left[\boldsymbol{e}_0 \left(\boldsymbol{x}\right) - \nabla_y \widetilde{\phi} \left(\boldsymbol{x}, \boldsymbol{y}\right)\right] \mathrm{d}y \\ &= \underbrace{\frac{1}{v} \int_Y \boldsymbol{\mathcal{S}} \left(\theta_0, \boldsymbol{y}\right) \cdot \left[\boldsymbol{I} - \boldsymbol{\mathcal{M}}^\phi \left(\boldsymbol{x}, \boldsymbol{y}\right)\right] \mathrm{d}y}_{\boldsymbol{\mathcal{S}}^* \left(\theta_0, \, \boldsymbol{x}\right)} \cdot \boldsymbol{e}_0 \left(\boldsymbol{x}\right) \,, \end{aligned} \tag{4.26b}$$

where $\boldsymbol{\mathcal{M}}^{\phi} : \Omega \times Y \to \mathrm{Lin}\left(\mathbb{R}^d, \mathbb{R}^d\right)$ denotes the structure tensor that defines the relation between the (gradient of the) fluctuation field and the applied macroscopic field, namely $\nabla_y \widetilde{\phi} = \boldsymbol{\mathcal{M}}^{\phi} \cdot \boldsymbol{e}_0$. Similarly, the effective thermal conductivity tensor is derived as

$$\begin{aligned}\boldsymbol{\mathcal{K}}^{*}\left(\theta_0, \boldsymbol{x}\right) \cdot \nabla_x \theta_0\left(\boldsymbol{x}\right) = \boldsymbol{q}_0\left(\boldsymbol{x}\right) &= \frac{1}{v}\int_Y \boldsymbol{q}\left(\boldsymbol{y}\right) \mathrm{d}y \\ &= -\frac{1}{v}\int_Y \boldsymbol{\mathcal{K}}\left(\theta_0, \boldsymbol{y}\right) \cdot \left[\nabla_x \theta_0\left(\boldsymbol{x}\right) + \nabla_y \widetilde{\theta}\left(\boldsymbol{x}, \boldsymbol{y}\right)\right] \mathrm{d}y \\ &= \underbrace{-\frac{1}{v}\int_Y \boldsymbol{\mathcal{K}}\left(\theta_0, \boldsymbol{y}\right) \cdot \left[\boldsymbol{I} + \boldsymbol{\mathcal{M}}^{\theta}\left(\boldsymbol{x}, \boldsymbol{y}\right)\right] \mathrm{d}y}_{\boldsymbol{\mathcal{K}}^{*}\left(\theta_0, \boldsymbol{x}\right)} \cdot \nabla_x \theta_0\left(\boldsymbol{x}\right) \ .\end{aligned} \tag{4.26c}$$

The corresponding relation between the (gradient of the) temperature fluctuation field and the macroscopic gradient of temperature is defined through the structure tensor $\boldsymbol{\mathcal{M}}^{\theta} : \Omega \times Y \to \mathrm{Lin}\left(\mathbb{R}^d, \mathbb{R}^d\right)$, namely $\nabla_y \widetilde{\theta} = \boldsymbol{\mathcal{M}}^{\theta} \cdot \nabla_x \theta_0$.

Remark 8. An alternate form of effective tensors can be obtained by means of Hill's lemma

$$\mathbf{E}^{*}\left(\theta_0, \boldsymbol{x}\right) = \frac{1}{v}\int_Y \left[\mathbf{I} + \mathbf{M}^{u}\left(\boldsymbol{x}, \boldsymbol{y}\right)\right]^{\mathrm{T}} : \mathbf{E}\left(\theta_0, \boldsymbol{y}\right) : \left[\mathbf{I} + \mathbf{M}^{u}\left(\boldsymbol{x}, \boldsymbol{y}\right)\right] \mathrm{d}y \tag{4.27a}$$

It follows from (4.27a) that $\mathbf{E}^{*}$ possess minor and mojor symmetry, i.e. $\mathsf{E}^{*}_{ijkl} = \mathsf{E}^{*}_{jikl} = \mathsf{E}^{*}_{klij}$. Similarly, the effective electrical conductivity tensor

$$\boldsymbol{\mathcal{S}}^{*}\left(\theta_0, \boldsymbol{x}\right) = \frac{1}{v}\int_Y \left[\boldsymbol{I} - \boldsymbol{\mathcal{M}}^{\phi}\left(\boldsymbol{x}, \boldsymbol{y}\right)\right]^{\mathrm{t}} \cdot \boldsymbol{\mathcal{S}}\left(\theta_0, \boldsymbol{y}\right) \cdot \left[\boldsymbol{I} - \boldsymbol{\mathcal{M}}^{\phi}\left(\boldsymbol{x}, \boldsymbol{y}\right)\right] \mathrm{d}y \tag{4.27b}$$

and the effective thermal conductivity tensor

$$\boldsymbol{\mathcal{K}}^{*}\left(\theta_0, \boldsymbol{x}\right) = \frac{1}{v}\int_Y \left[\boldsymbol{I} + \boldsymbol{\mathcal{M}}^{\theta}\left(\boldsymbol{x}, \boldsymbol{y}\right)\right]^{\mathrm{t}} \cdot \boldsymbol{\mathcal{K}}\left(\theta_0, \boldsymbol{y}\right) \cdot \left[\boldsymbol{I} + \boldsymbol{\mathcal{M}}^{\theta}\left(\boldsymbol{x}, \boldsymbol{y}\right)\right] \mathrm{d}y \tag{4.27c}$$

are obtained. The effective conductivity tensors have the symmetry properties $\mathcal{S}^{*}_{ij} = \mathcal{S}^{*}_{ji}$ and $\mathcal{K}^{*}_{ij} = \mathcal{K}^{*}_{ji}$, as observed from (4.27b) and (4.27c).

Remark 9. The first-order computational homogenisation framework developed herein assumes a classical macroscopic kinematic description, which is suitable for many engineering applications. An alternative to the classical first-order computational homogenisation scheme involves enriching the macroscopic kinematic description to incorporate higher-order gradients. This results in a more complex microscale boundary value problem, capable of capturing additional microstructural effects such as strain gradients and size dependencies. In this framework, homogenisation yields not only the classical Cauchy stress tensor but also higher-order stress measures and their corresponding tangent operators [107, 108, 188].

4.5 Finite element implementation

This section addresses the finite element implementation of the proposed multiscale formulation for electrical conductors. In particular, the focus is on discrete closed-form solutions for homogenised macroscale fields, and the associated tangent stiffness contributions. The microscale boundary value problems are formulated using weak forms based on Section 2.3.1, neglecting body forces and source terms. The discretised weak form and corresponding finite element implementation that is derived in Section 4.5 is employed for the microscale problems.

The discussion within this thesis is limited to affine and periodic boundary conditions. In the case of periodic boundary conditions, the generalised stiffness matrices and generalised reaction force vectors are substituted by reduced versions that result from enforcing linear constraints between opposing RVE boundaries. Specifically speaking, the reduced generalised stiffness matrix $\mathbf{K}^*$ and the reduced generalised reaction force vector are expressed via

$$\mathbf{K}^* = \boldsymbol{\mathcal{T}}^{\mathrm{t}} \cdot \mathbf{K} \cdot \boldsymbol{\mathcal{T}}\,, \quad \boldsymbol{f}^* = \boldsymbol{\mathcal{T}}^{\mathrm{t}} \cdot \boldsymbol{f} \quad \text{and} \quad \begin{bmatrix} \boldsymbol{\chi}_{\mathrm{i}} \\ \boldsymbol{\chi}_{\mathrm{d}} \end{bmatrix} = \boldsymbol{\mathcal{T}} \cdot \boldsymbol{\chi}_{\mathrm{i}} \tag{4.28}$$

using the transformation matrix $\boldsymbol{\mathcal{T}}$ that relates dependent degrees of freedom $\boldsymbol{\chi}_{\mathrm{d}}$ to independent degrees of freedom $\boldsymbol{\chi}_{\mathrm{i}}$. With the definitions of reduced forms at hand, the system

$$\mathbf{K}^* \cdot \Delta\boldsymbol{\chi}_{\mathrm{i}} = \Delta\boldsymbol{f}^* \tag{4.29}$$

is obtained.

4.5.1 Calculation of macroscopic stress tensor, electric current density vector and heat flux vector

Upon solving the microscale boundary value problems, macroscopic quantities are determined through volume averaging. The discrete version of the macroscopic stress tensor (4.7)

$$\boldsymbol{\sigma}_0 = \frac{1}{v} \int_{\partial Y} \boldsymbol{t}\,(\boldsymbol{y}) \otimes \boldsymbol{y}\, \mathrm{d}y \approx \frac{1}{v} \sum_{i=1}^{\mathrm{n_{pn}}} {}^{(i)}\boldsymbol{f}^{\boldsymbol{u}} \otimes {}^{(i)}\boldsymbol{y} \tag{4.30}$$

and the macroscopic electric current density vector (4.8)

$$\boldsymbol{j}_0 = \frac{1}{v} \int_{\partial Y} \boldsymbol{y}\, i\,(\boldsymbol{y})\ \mathrm{d}y \approx \frac{1}{v} \sum_{i=1}^{\mathrm{n_{pn}}} {}^{(i)}f^{\phi}\, {}^{(i)}\boldsymbol{y} \tag{4.31}$$

and the macroscopic heat flux vector (4.9)

$$\boldsymbol{q}_0 = \frac{1}{v} \int_{\partial Y} -\boldsymbol{y}\, q\,(\boldsymbol{y})\ \mathrm{d}y \approx -\frac{1}{v} \sum_{i=1}^{\mathrm{n_{pn}}} {}^{(i)}f^{\theta}\, {}^{(i)}\boldsymbol{y} \tag{4.32}$$

are obtained. In equations above $\mathrm{n_{pn}}$ denotes the number of nodes where the corresponding degrees of freedom are prescribed, and ${}^{(i)}\boldsymbol{y}$ and ${}^{(i)}f^{\bullet}$ are the position vector and the (generalised) reaction forces of node i.

4.5.2 Calculation of macroscopic tangent contributions

Iterative techniques like the Newton-Raphson method require the tangent stiffness to solve nonlinear macroscopic problems. Since the computational homogenisation methods do not provide an explicit form of effective properties, the tangent contributions have to be determined numerically. Tangents are to be calculated from the relation between variations of the macroscopic flux like quantities and macroscopic gradients of fields at every macroscopic (integration) point. To this end, a forward difference approximation can be employed in order to obtain consistent tangent moduli, as demonstrated for finite elasticity in [131]. Alternatively, the so called condensation methods are widely used in the literature [107, 108, 132]. Condensation methods rely on condensed matrices, associated with the boundary, $\partial\Omega$, of the unit cell, to compute macroscopic moduli.

In this section, a direct condensation of the constrained degrees of freedom is outlined. To derive generalised tangent stiffness contributions, changes in generalised reaction forces $\Delta^{(i)}f_{\mathrm{d}}^{\bullet}$ due to perturbations of the prescribed (Dirichlet) degrees of freedom $\Delta\boldsymbol{f}_{\mathrm{d}}$ are studied. The linearised system of equations for the microscale problem is partitioned as

$$\begin{bmatrix}\mathbf{K}_{\mathrm{dd}} & \mathbf{K}_{\mathrm{df}}\\ \mathbf{K}_{\mathrm{fd}} & \mathbf{K}_{\mathrm{ff}}\end{bmatrix}\cdot\begin{bmatrix}\Delta\boldsymbol{\chi}_{\mathrm{d}}\\ \Delta\boldsymbol{\chi}_{\mathrm{f}}\end{bmatrix}=\begin{bmatrix}\Delta\boldsymbol{f}_{\mathrm{d}}\\ \mathbf{0}\end{bmatrix} \tag{4.33}$$

where $\{\bullet\}_{\mathrm{d}}$ and $\{\bullet\}_{\mathrm{f}}$ denote Dirichlet and free degrees of freedom related quantities. Solving the second line of the system of equations for $\Delta\boldsymbol{\chi}_{\mathrm{f}}$ and inserting the ensuing relation in the first line, the closed-form expression

$$\underbrace{\left[\mathbf{K}_{\mathrm{dd}}-\mathbf{K}_{\mathrm{df}}\cdot\mathbf{K}_{\mathrm{ff}}^{-1}\cdot\mathbf{K}_{\mathrm{fd}}\right]}_{\widehat{\mathbf{K}}}\cdot\Delta\boldsymbol{\chi}_{\mathrm{d}}=\Delta\boldsymbol{f}_{\mathrm{d}} \tag{4.34}$$

is obtained, with the definition of the condensed stiffness matrix $\widehat{\mathbf{K}}$. For affine and periodic boundary conditions, the kinematic relations are given as

$$\Delta^{(j)}\boldsymbol{u}_{\mathrm{d}} = \quad \Delta\boldsymbol{\varepsilon}_0\cdot{}^{(j)}\boldsymbol{y} \tag{4.35a}$$
$$\Delta^{(j)}\phi_{\mathrm{d}} = -\Delta\boldsymbol{e}_0\cdot{}^{(j)}\boldsymbol{y} \tag{4.35b}$$
$$\Delta^{(j)}\theta_{\mathrm{d}} = \quad \Delta\nabla_x\theta_0\cdot{}^{(j)}\boldsymbol{y} \tag{4.35c}$$

By partitioning equation (4.33) into mechanical, thermal and electrical contributions and inserting kinematic relations, the discrete representation of generalised reaction force vectors

$$\Delta^{(i)}\boldsymbol{f}^{\boldsymbol{u}} = \sum_{j=1}^{\mathrm{n_{pn}}} {}^{(ij)}\widehat{\mathbf{K}}^{\boldsymbol{uu}}\, \Delta\boldsymbol{\varepsilon}_0\, {}^{(j)}\boldsymbol{y} - \sum_{j=1}^{\mathrm{n_{pn}}} {}^{(ij)}\widehat{\mathbf{K}}^{\boldsymbol{u}\phi} \otimes \Delta\boldsymbol{e}_0\, {}^{(j)}\boldsymbol{y} + \sum_{j=1}^{\mathrm{n_{pn}}} {}^{(ij)}\widehat{\mathbf{K}}^{\boldsymbol{u}\theta} \otimes \Delta\nabla_x\theta_0\, {}^{(j)}\boldsymbol{y} \tag{4.36}$$

$$\Delta^{(i)}f^{\phi} = \sum_{j=1}^{\mathrm{n_{pn}}} {}^{(ij)}\widehat{\mathbf{K}}^{\phi\boldsymbol{u}}\, \Delta\boldsymbol{\varepsilon}_0\, {}^{(j)}\boldsymbol{y} - \sum_{j=1}^{\mathrm{n_{pn}}} {}^{(ij)}\widehat{\mathbf{K}}^{\phi\phi} \otimes \Delta\boldsymbol{e}_0\, {}^{(j)}\boldsymbol{y} + \sum_{j=1}^{\mathrm{n_{pn}}} {}^{(ij)}\widehat{\mathbf{K}}^{\phi\theta} \otimes \Delta\nabla_x\theta_0\, {}^{(j)}\boldsymbol{y} \tag{4.37}$$

$$\Delta^{(i)}f^{\theta} = -\sum_{j=1}^{\mathrm{n_{pn}}} {}^{(ij)}\widehat{\mathbf{K}}^{\theta\boldsymbol{u}}\, \Delta\boldsymbol{\varepsilon}_0\, {}^{(j)}\boldsymbol{y} + \sum_{j=1}^{\mathrm{n_{pn}}} {}^{(ij)}\widehat{\mathbf{K}}^{\theta\phi} \otimes \Delta\boldsymbol{e}_0\, {}^{(j)}\boldsymbol{y} - \sum_{j=1}^{\mathrm{n_{pn}}} {}^{(ij)}\widehat{\mathbf{K}}^{\theta\theta} \otimes \Delta\nabla_x\theta_0\, {}^{(j)}\boldsymbol{y} \tag{4.38}$$

are obtained. Finally, by inserting discrete forms of generalised force vectors at the microscale into the discrete representation of the change in the stress tensor reads

$$\begin{aligned}
\Delta\boldsymbol{\sigma}_0 \approx{}& \left[\frac{1}{\mathrm{vol}(\Omega)}\sum_{i=1}^{\mathrm{n_{pn}}}\sum_{j=1}^{\mathrm{n_{pn}}} {}^{(ij)}\widehat{\mathbf{K}}^{\boldsymbol{uu}}\overline{\otimes}\left[{}^{(i)}\boldsymbol{y}\otimes{}^{(j)}\boldsymbol{y}\right]\right] : \Delta\boldsymbol{\varepsilon}_0 \\
&+ \left[-\frac{1}{\mathrm{vol}(\Omega)}\sum_{i=1}^{\mathrm{n_{pn}}}\sum_{j=1}^{\mathrm{n_{pn}}} {}^{(ij)}\widehat{\mathbf{K}}^{\boldsymbol{u}\phi}\otimes{}^{(i)}\boldsymbol{y}\otimes{}^{(j)}\boldsymbol{y}\right] : \Delta\boldsymbol{e}_0 \\
&+ \left[\frac{1}{\mathrm{vol}(\Omega)}\sum_{i=1}^{\mathrm{n_{pn}}}\sum_{j=1}^{\mathrm{n_{pn}}} {}^{(ij)}\widehat{\mathbf{K}}^{\boldsymbol{u}\theta}\otimes{}^{(i)}\boldsymbol{y}\otimes{}^{(j)}\boldsymbol{y}\right] : \Delta\nabla_x\theta_0 \\
\approx{}& \frac{\mathrm{d}\boldsymbol{\sigma}_0}{\mathrm{d}\boldsymbol{\varepsilon}_0} : \Delta\boldsymbol{\varepsilon}_0 + \frac{\mathrm{d}\boldsymbol{\sigma}_0}{\mathrm{d}\boldsymbol{e}_0}\cdot\Delta\boldsymbol{e}_0 + \frac{\mathrm{d}\boldsymbol{\sigma}_0}{\mathrm{d}\nabla_x\theta_0}\cdot\Delta\nabla_x\theta_0
\end{aligned} \tag{4.39}$$

and the electric current density vector yields the following system

$$\begin{aligned}
\Delta\boldsymbol{j}_0 \approx{}& \left[\frac{1}{\mathrm{vol}(\Omega)}\sum_{i=1}^{\mathrm{n_{pn}}}\sum_{j=1}^{\mathrm{n_{pn}}} {}^{(ij)}\widehat{\mathbf{K}}^{\phi\boldsymbol{u}}\otimes{}^{(i)}\boldsymbol{y}\otimes{}^{(j)}\boldsymbol{y}\right] : \Delta\boldsymbol{\varepsilon}_0 \\
&+ \left[-\frac{1}{\mathrm{vol}(\Omega)}\sum_{i=1}^{\mathrm{n_{pn}}}\sum_{j=1}^{\mathrm{n_{pn}}} {}^{(ij)}\widehat{\mathbf{K}}^{\phi\phi}\otimes{}^{(i)}\boldsymbol{y}\otimes{}^{(j)}\boldsymbol{y}\right] : \Delta\boldsymbol{e}_0 \\
&+ \left[\frac{1}{\mathrm{vol}(\Omega)}\sum_{i=1}^{\mathrm{n_{pn}}}\sum_{j=1}^{\mathrm{n_{pn}}} {}^{(ij)}\widehat{\mathbf{K}}^{\phi\theta}\otimes{}^{(i)}\boldsymbol{y}\otimes{}^{(j)}\boldsymbol{y}\right] : \Delta\nabla_x\theta_0 \\
\approx{}& \frac{\mathrm{d}\boldsymbol{j}_0}{\mathrm{d}\boldsymbol{\varepsilon}_0} : \Delta\boldsymbol{\varepsilon}_0 + \frac{\mathrm{d}\boldsymbol{j}_0}{\mathrm{d}\boldsymbol{e}_0}\cdot\Delta\boldsymbol{e}_0 + \frac{\mathrm{d}\boldsymbol{j}_0}{\mathrm{d}\nabla_x\theta_0}\cdot\Delta\nabla_x\theta_0
\end{aligned} \tag{4.40}$$

Likewise, the change in heat flux can be written as

$$\begin{aligned}\Delta \boldsymbol{q}_0 \approx & \left[-\frac{1}{\mathrm{vol}(\Omega)}\sum_{i=1}^{\mathrm{n_{pn}}}\sum_{j=1}^{\mathrm{n_{pn}}} {}^{(ij)}\widehat{\mathbf{K}}^{\theta \boldsymbol{u}} \otimes {}^{(i)}\boldsymbol{y} \otimes {}^{(j)}\boldsymbol{y}\right] : \Delta \boldsymbol{\varepsilon}_0 \\ & + \left[\frac{1}{\mathrm{vol}(\Omega)}\sum_{i=1}^{\mathrm{n_{pn}}}\sum_{j=1}^{\mathrm{n_{pn}}} {}^{(ij)}\widehat{\mathbf{K}}^{\theta \phi} \otimes {}^{(i)}\boldsymbol{y} \otimes {}^{(j)}\boldsymbol{y}\right] : \Delta \boldsymbol{e}_0 \\ & + \left[-\frac{1}{\mathrm{vol}(\Omega)}\sum_{i=1}^{\mathrm{n_{pn}}}\sum_{j=1}^{\mathrm{n_{pn}}} {}^{(ij)}\widehat{\mathbf{K}}^{\theta \theta} \otimes {}^{(i)}\boldsymbol{y} \otimes {}^{(j)}\boldsymbol{y}\right] : \Delta \nabla_x \theta_0 \\ & \approx \frac{\mathrm{d}\boldsymbol{q}_0}{\mathrm{d}\boldsymbol{\varepsilon}_0} : \Delta \boldsymbol{\varepsilon}_0 + \frac{\mathrm{d}\boldsymbol{q}_0}{\mathrm{d}\boldsymbol{e}_0} \cdot \Delta \boldsymbol{e}_0 + \frac{\mathrm{d}\boldsymbol{q}_0}{\mathrm{d}\nabla_x \theta_0} \cdot \Delta \nabla_x \theta_0\end{aligned} \tag{4.41}$$

Equations (4.39)-(4.41) give rise to the definitions of the macroscale algorithmic tangent stiffness and conductivity tensors.

To summarise, this chapter introduced a computational multiscale framework for modelling coupled thermo-electro-mechanical behaviour in heterogeneous materials. The formulation begins at the microscale, where the governing equations for mechanical equilibrium, heat conduction, and electrical conduction are defined. These local field equations are linked to the macroscopic response through averaging theorems, with the Hill–Mandel condition ensuring energetic consistency across scales. Based on this scale-bridging procedure, effective constitutive relations are derived and incorporated into a finite element implementation of the macroscale problem.

The framework presented here provides the foundation for the subsequent chapters. Importantly, the macroscopic equations derived in this chapter are later shown to be consistent with those obtained from analytical and asymptotic homogenisation techniques, as discussed in Chapter 7, offering a theoretical justification for the computational approach developed here.

5 Computational homogenisation with interfaces: Electro-mechanical problem

Every material in nature exhibits heterogeneous behaviour at some scale. The effective material response is governed by the underlying microstructure. Interfaces, such as phase and grain boundaries, can affect the overall response of the material under consideration. Grain boundaries are particular sources of resistance in polycrystalline materials with empirical evidence suggesting that grain boundaries can substantially influence the electrical properties [23, 145].

To accurately capture such microscale effects, computational multiscale formulations offer a powerful approach by explicitly resolving complex microscale processes, and distinct features such as material interfaces. Motivated by the influence of grain boundaries on effective electrical properties, a computational multiscale framework for electrical conductors is extended to continua with material interfaces at the microscale in the present chapter. Specifically, (lowly-conducting) cohesive-type interfaces are accounted for at the microscale, such that displacement and electrical potential jumps across the interface can be considered.

The scope of the chapter is threefold:

- *It proposes a computational multiscale formulation for electrical conductors featuring cohesive-type material interfaces at the microscale, along with a corresponding finite element implementation.*

- *It demonstrates, through two-dimensional numerical examples, the validity and predictive capability of the proposed framework. This includes validation against analytical benchmark solutions, an investigation of how microstructural features affect the effective conductivity tensor, and the emergence of interface-induced size effects that are beyond the reach of classical first-order homogenisation approaches.*

- *It illustrates the framework's applicability to coupled electro-mechanical processes, with particular focus on mechanically driven interfacial degradation and its influence on the effective electrical response.*

This chapter is organised as follows: In Section 5.1, the thermodynamic fundamentals of continua with interfaces are summarised and the constitutive restrictions resulting

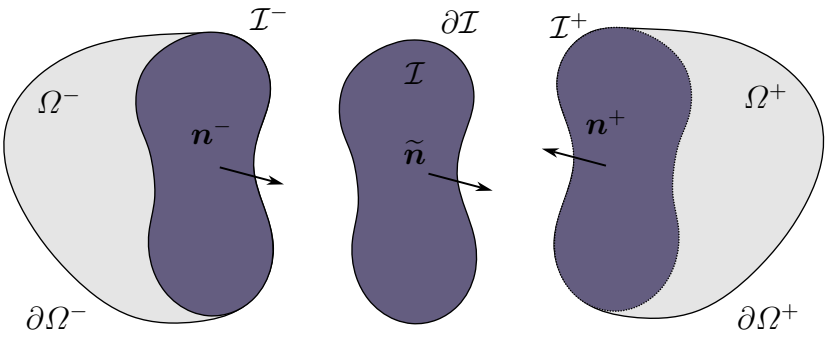

Figure 5.1: Control volume $\Omega = \Omega^- \cup \Omega^+$ under consideration. The interface $\mathcal{I}$ is characterised by its unit surface normal vector $\widetilde{\boldsymbol{n}}$. Reprinted from [76] under the terms of the Creative Commons Attribution License (CC BY).

from the dissipation inequality are investigated. Section 5.2 deals with the theoretical aspects of the electro-mechanical computational multiscale approach in the presence of cohesive interfaces. Specifically speaking, averaging theorems for the mechanical and electrical subproblems are discussed in Section 5.2.1, a generalised Hill–Mandel condition is proposed in Section 5.2.2 and suitable boundary conditions are presented. With the fundamental set of balance equations at hand, a weak form of the problem is derived and a finite element implementation is proposed in Section 5.3. Section 5.4 deals with the specific constitutive relations for the bulk and the interface, before representative boundary value problems are studied to demonstrate the capabilities of the proposed framework.

5.1 Continuum thermodynamics

qtd. [76] {The thermodynamic fundamentals of continua featuring cohesive-type material interfaces in small strain setting are briefly recapitulated in this section. In particular, focus is laid on the mechanical subproblem in Section 5.1.1, on the electrical subproblem in Section 5.1.2, and on the balance equation of energy and the dissipation inequality in Section 5.1.3.

Control volume Ω consists of two disjoint subdomains Ω^+ and Ω^- with material interface $\mathcal{I}$ in between, see Figure 5.1. The interface is a surface connecting the two sides of the bulk. The opposing sides of the interface can be defined as the intersection of the interface with the boundary of each subdomain, namely $\mathcal{I}^+ = \partial\Omega^+ \cap \mathcal{I}$ and $\mathcal{I}^- = \partial\Omega^- \cap \mathcal{I}$. The unit normal vector to the surface of the body $\partial\Omega$ is $\boldsymbol{n}$. The unit normal vectors to the plus side $\mathcal{I}^+$ and minus side $\mathcal{I}^-$ of interface $\mathcal{I}$ are $\boldsymbol{n}^+$ and $\boldsymbol{n}^-$. Furthermore, the interface unit normal is defined as $\widetilde{\boldsymbol{n}}$ which points from $\mathcal{I}^-$ to $\mathcal{I}^+$, i.e.} qtd. [76]

$$\boldsymbol{n}^+ = -\widetilde{\boldsymbol{n}}\,, \quad \boldsymbol{n}^- = \widetilde{\boldsymbol{n}}\,. \tag{5.1}$$

5.1.1 Mechanical subproblem

The governing equations of control volume $\Omega \subset \mathbb{R}^d$ with material interface $\mathcal{I} \subset \mathbb{R}^{(d-1)}$ for thermo-electro-mechanical problems are derived in Chapter 3. Although Sections 3.1 and 5.1 develop essentially the same thermo-electro-mechanical balance laws, in Chapter 5 we simply recapitulate their structure and then – unlike the transient, time-dependent formulation of Chapter 3 – specialise to the electro-mechanical subproblem in its quasi-static form. Based on the formulation presented in the previous chapter, tangential forces on $\partial\mathcal{I}$ are neglected. $^{\text{qtd.}}_{[76]}\{$The integral form of the balance of linear momentum for a quasi-static case reads

$$\mathbf{0} = \int_{\Omega} \rho\,(\boldsymbol{x})\,\boldsymbol{f}\,(\boldsymbol{x})\;\mathrm{d}x + \int_{\mathcal{I}} \widetilde{\rho}\,(\widetilde{\boldsymbol{x}})\,\widetilde{\boldsymbol{f}}\,(\widetilde{\boldsymbol{x}})\;\mathrm{d}x + \int_{\partial\Omega} \boldsymbol{t}\,(\boldsymbol{x})\;\mathrm{d}x\,, \tag{5.2}$$

where $\rho : \Omega \to \mathbb{R}$ and $\widetilde{\rho} : \Omega \to \mathbb{R}$ are the mass density of the bulk and interface. The volume under consideration is subjected to surface tractions

$$\boldsymbol{t}\,(\boldsymbol{x}) = \boldsymbol{\sigma}\,(\boldsymbol{x}) \cdot \boldsymbol{n}\,(\boldsymbol{x})\;, \tag{5.3}$$

and loaded by volume distributed forces $\rho\,\boldsymbol{f}$ in the bulk as well as surface distributed forces $\widetilde{\rho}\,\widetilde{\boldsymbol{f}}$ at the interface. In (5.3), $\boldsymbol{\sigma} : \Omega \to \mathrm{Lin}\left(\mathbb{R}^d, \mathbb{R}^d\right)$ and $\boldsymbol{n} : \Omega \to \mathbb{R}^d$ correspond to the stress tensor and the outward unit normal vector, respectively. Using the divergence theorem and carrying out localisation of (5.2) for continua featuring material interfaces, with the definitions

$$\widetilde{\boldsymbol{t}}^{+}\left(\boldsymbol{x}^{+}\right) = \boldsymbol{\sigma}^{+}\left(\boldsymbol{x}^{+}\right) \cdot \widetilde{\boldsymbol{n}}\,(\widetilde{\boldsymbol{x}}) \quad \text{and} \quad \widetilde{\boldsymbol{t}}^{-}\left(\boldsymbol{x}^{-}\right) = \boldsymbol{\sigma}^{-}\left(\boldsymbol{x}^{-}\right) \cdot \widetilde{\boldsymbol{n}}\,(\widetilde{\boldsymbol{x}})\;, \tag{5.4}$$

the local form of the balance of linear momentum is obtained as

$$\nabla_x \cdot \boldsymbol{\sigma}\,(\boldsymbol{x}) + \rho\,(\boldsymbol{x})\,\boldsymbol{f}\,(\boldsymbol{x}) = \mathbf{0} \quad \text{(in the bulk)}\;, \tag{5.5a}$$

$$[\![\widetilde{\boldsymbol{t}}]\!]\,(\widetilde{\boldsymbol{x}}) + \widetilde{\rho}\,(\widetilde{\boldsymbol{x}})\,\widetilde{\boldsymbol{f}}\,(\widetilde{\boldsymbol{x}}) = \mathbf{0} \quad \text{(at the interface)}\;. \tag{5.5b}$$

Under the same assumptions, localisation of conservation of angular momentum gives rise to the classic symmetry condition of the stress tensor

$$\boldsymbol{\epsilon} : \boldsymbol{\sigma}\,(\boldsymbol{x}) = \mathbf{0} \quad \Longrightarrow\; \boldsymbol{\sigma}\,(\boldsymbol{x}) = \boldsymbol{\sigma}^{\mathrm{t}}\,(\boldsymbol{x}) \quad \text{(in the bulk)}\,. \tag{5.6}$$

Cohesive zone formulations for small strain settings yield no additional condition regarding angular momentum at the interface.$\}^{\text{qtd.}}_{[76]}$

5.1.2 Electrical subproblem

$^{\text{qtd.}}_{[76]}\{$The integral form of the continuity equation for the electrical charge for quasi-stationary processes reads

$$0 = \int_{\partial\Omega} \boldsymbol{j}\,(\boldsymbol{x}) \cdot \boldsymbol{n}\,(\boldsymbol{x})\;\mathrm{d}x \tag{5.7}$$

with

$$i\left(\boldsymbol{x}\right) = \boldsymbol{j}\left(\boldsymbol{x}\right) \cdot \boldsymbol{n}\left(\boldsymbol{x}\right) \tag{5.8}$$

where $\boldsymbol{j} : \Omega \to \mathbb{R}^d$ corresponds to the electric current density vector and where $i : \Omega \to \mathbb{R}$ denotes the projected current density vector. Following the same procedure as in [98] and introducing the definitions

$$\widetilde{i}^{+}\left(\boldsymbol{x}^{+}\right) = \boldsymbol{j}^{+}\left(\boldsymbol{x}^{+}\right) \cdot \widetilde{\boldsymbol{n}}\left(\widetilde{\boldsymbol{x}}\right) \quad \text{and} \quad \widetilde{i}^{-}\left(\boldsymbol{x}^{-}\right) = \boldsymbol{j}^{-}\left(\boldsymbol{x}^{-}\right) \cdot \widetilde{\boldsymbol{n}}\left(\widetilde{\boldsymbol{x}}\right) , \tag{5.9}$$

the local version of the continuity equation for the electric charge is obtained as

$$\nabla_x \cdot \boldsymbol{j}\left(\boldsymbol{x}\right) = 0 \quad \text{(in the bulk)} , \tag{5.10a}$$

$$[\![\widetilde{i}]\!]\left(\widetilde{\boldsymbol{x}}\right) = 0 \quad \text{(at the interface)} . \tag{5.10b}$$

The introduction of a scalar-valued electric potential field $\phi : \Omega \to \mathbb{R}$ can fulfil the requirements of Faraday's law of induction under the assumption of a (quasi-)stationary state, namely

$$\boldsymbol{e}\left(\boldsymbol{x}\right) = -\nabla_x \phi\left(\boldsymbol{x}\right) \quad \text{(in the bulk)} , \tag{5.11}$$

where $\boldsymbol{e} : \Omega \to \mathbb{R}^d$ corresponds to the electric field vector. The localisation of Faraday's law of induction at the interface yields no additional condition for cohesive zone formulations.}$^{\text{qtd.}}_{[76]}$

5.1.3 Balance of energy and dissipation inequality

$^{\text{qtd.}}_{[76]}${Taking into account mechanical, thermal and electrical contributions, the (quasi-static) balance equation of energy for a continuum with interfaces is given by

$$\frac{\mathrm{d}}{\mathrm{d}t}\int_{\Omega} \rho\left(\boldsymbol{x}\right) e\left(\boldsymbol{x}\right) \mathrm{d}x + \frac{\mathrm{d}}{\mathrm{d}t}\int_{\mathcal{I}} \widetilde{\rho}\left(\widetilde{\boldsymbol{x}}\right) \widetilde{e}\left(\widetilde{\boldsymbol{x}}\right) \mathrm{d}x = \mathcal{P}^{\boldsymbol{u}} + \mathcal{P}^{\theta} + \mathcal{P}^{\phi} \tag{5.12}$$

where $e : \Omega \to \mathbb{R}$ and $\widetilde{e} : \mathcal{I} \to \mathbb{R}$ correspond to the mass-specific internal energy densities of the bulk and the interface, respectively, and t denotes time. The respective contributions to (5.12) are specified as

$$\mathcal{P}^{\boldsymbol{u}} = \int_{\Omega\setminus\mathcal{I}} \nabla_x \dot{\boldsymbol{u}}\left(\boldsymbol{x}\right) : \boldsymbol{\sigma}\left(\boldsymbol{x}\right) \mathrm{d}x + \int_{\mathcal{I}} [\![\dot{\boldsymbol{u}}]\!]\left(\widetilde{\boldsymbol{x}}\right) \cdot \{\!\{\widetilde{\boldsymbol{t}}\}\!\}\left(\widetilde{\boldsymbol{x}}\right) \mathrm{d}x , \tag{5.13a}$$

$$\mathcal{P}^{\phi} = \int_{\Omega\setminus\mathcal{I}} \boldsymbol{j}\left(\boldsymbol{x}\right) \cdot \boldsymbol{e}\left(\boldsymbol{x}\right) \mathrm{d}x + \int_{\mathcal{I}} -\{\!\{\widetilde{i}\}\!\}\left(\widetilde{\boldsymbol{x}}\right) [\![\phi]\!]\left(\widetilde{\boldsymbol{x}}\right) \mathrm{d}x , \tag{5.13b}$$

$$\mathcal{P}^{\theta} = \int_{\Omega\setminus\mathcal{I}} \rho\left(\boldsymbol{x}\right) r\left(\boldsymbol{x}\right) - \nabla_x \cdot \boldsymbol{q}\left(\boldsymbol{x}\right) \mathrm{d}x + \int_{\mathcal{I}} -[\![\boldsymbol{q} \cdot \widetilde{\boldsymbol{n}}]\!]\left(\widetilde{\boldsymbol{x}}\right) \mathrm{d}x . \tag{5.13c}$$

In the set of equations (5.13), $\dot{\boldsymbol{u}} : \Omega \to \mathbb{R}^d$ denotes the velocity field whereas $\boldsymbol{q} : \Omega \to \mathbb{R}^d$ and $r : \Omega \to \mathbb{R}$ correspond to the heat flux vector and mass-specific heat source in

the bulk. By inserting (5.13a), (5.13b) and (5.13c) into (5.12), and by localising the ensuing equation, the local form of the balance equation of energy for a continuum with interfaces takes the form

$$\rho(\boldsymbol{x})\,\dot{e}(\boldsymbol{x}) = \boldsymbol{\sigma}(\boldsymbol{x}) : \dot{\boldsymbol{\varepsilon}}(\boldsymbol{x}) + \rho(\boldsymbol{x})\,r(\boldsymbol{x}) - \nabla_x \cdot \boldsymbol{q}(\boldsymbol{x}) + \boldsymbol{j}(\boldsymbol{x}) \cdot \boldsymbol{e}(\boldsymbol{x}) \quad \text{(in the bulk)}\,, \tag{5.14a}$$

$$\widetilde{\rho}(\widetilde{\boldsymbol{x}})\,\dot{\widetilde{e}}(\widetilde{\boldsymbol{x}}) = [\![\dot{\boldsymbol{u}}]\!](\widetilde{\boldsymbol{x}}) \cdot \{\!\{\widetilde{\boldsymbol{t}}\}\!\}(\widetilde{\boldsymbol{x}}) - [\![\boldsymbol{q} \cdot \boldsymbol{n}]\!](\widetilde{\boldsymbol{x}}) - \{\!\{\widetilde{i}\}\!\}(\widetilde{\boldsymbol{x}})\,[\![\phi]\!](\widetilde{\boldsymbol{x}}) \qquad \text{(at the interface)} \tag{5.14b}$$

where the definitions of the small strain deformation tensor $\boldsymbol{\varepsilon} = \nabla_x^{\mathrm{sym}} \boldsymbol{u}$ with the material time derivative $\dot{\bullet}$ are used. Furthermore, localisation of the dissipation inequality

$$\frac{\mathrm{d}}{\mathrm{d}t}\int_\Omega \rho(\boldsymbol{x})\,s(\boldsymbol{x})\,\mathrm{d}x + \frac{\mathrm{d}}{\mathrm{d}t}\int_{\mathcal{I}} \widetilde{\rho}(\widetilde{\boldsymbol{x}})\,\widetilde{s}(\widetilde{\boldsymbol{x}})\,\mathrm{d}x \geq \int_\Omega \frac{\rho(\boldsymbol{x})\,r(\boldsymbol{x})}{\theta(\boldsymbol{x})}\,\mathrm{d}x - \int_{\partial\Omega} \frac{\boldsymbol{q}(\boldsymbol{x}) \cdot \boldsymbol{n}(\boldsymbol{x})}{\theta(\boldsymbol{x})}\,\mathrm{d}x\,, \tag{5.15}$$

with $\theta : \Omega \to \mathbb{R}$, $s : \Omega \to \mathbb{R}$ and $\widetilde{s} : \mathcal{I} \to \mathbb{R}$ denoting the absolute temperature, the mass-specific entropy density of the bulk and the mass-specific entropy density of the interface, respectively, yields

$$\begin{aligned} &\boldsymbol{\sigma}(\boldsymbol{x}) : \dot{\boldsymbol{\varepsilon}}(\boldsymbol{x}) - \rho(\boldsymbol{x})\left[\dot{\psi}(\boldsymbol{x}) + s(\boldsymbol{x})\,\dot{\theta}(\boldsymbol{x})\right] \quad \text{(in the bulk)} \\ &\qquad - \frac{1}{\theta(\boldsymbol{x})}\boldsymbol{q}(\boldsymbol{x}) \cdot \nabla_x\theta(\boldsymbol{x}) + \boldsymbol{j}(\boldsymbol{x}) \cdot \boldsymbol{e}(\boldsymbol{x}) \geq 0 \end{aligned} \tag{5.16a}$$

and

$$\begin{aligned} &[\![\dot{\boldsymbol{u}}]\!](\widetilde{\boldsymbol{x}}) \cdot \{\!\{\widetilde{\boldsymbol{t}}\}\!\}(\widetilde{\boldsymbol{x}}) - \widetilde{\rho}(\widetilde{\boldsymbol{x}})\left[\dot{\widetilde{\psi}}(\widetilde{\boldsymbol{x}}) + \widetilde{s}(\widetilde{\boldsymbol{x}})\,\dot{\widetilde{\theta}}(\widetilde{\boldsymbol{x}})\right] - \{\!\{\widetilde{i}\}\!\}(\widetilde{\boldsymbol{x}})\,[\![\phi]\!](\widetilde{\boldsymbol{x}}) \quad \text{(at the interface)} \\ &\qquad + \widetilde{\theta}(\widetilde{\boldsymbol{x}})\left[\{\!\{\boldsymbol{q} \cdot \boldsymbol{n}\}\!\}(\widetilde{\boldsymbol{x}})\,[\![\theta^{-1}]\!](\widetilde{\boldsymbol{x}}) + \left[\{\!\{\theta^{-1}\}\!\}(\widetilde{\boldsymbol{x}}) - \widetilde{\theta}^{-1}(\widetilde{\boldsymbol{x}})\right][\![\boldsymbol{q} \cdot \boldsymbol{n}]\!](\widetilde{\boldsymbol{x}})\right] \geq 0\,. \end{aligned} \tag{5.16b}$$

In order to derive the dissipation inequality in the form (5.16), the Legendre–Fenchel transformation, relating the internal and free energy densities of the bulk and the interface as

$$\psi(\boldsymbol{\varepsilon}, \theta, \bullet) = \inf_s \{e(\boldsymbol{\varepsilon}, s, \bullet) - \theta\, s\}\,, \tag{5.17a}$$

$$\widetilde{\psi}\left([\![\boldsymbol{u}]\!], \widetilde{\theta}, \bullet\right) = \inf_{\widetilde{s}} \left\{\widetilde{e}([\![\boldsymbol{u}]\!], \widetilde{s}, \bullet) - \widetilde{\theta}\,\widetilde{s}\right\} \tag{5.17b}$$

was invoked, where $\widetilde{\theta} : \mathcal{I} \to \mathbb{R}$ denotes the interface temperature. Evaluation of the Coleman-Noll procedure yields the constitutive relations for the mechanical subproblem

$$\boldsymbol{\sigma} = \rho\,\frac{\partial\psi(\boldsymbol{\varepsilon}, \theta, \bullet)}{\partial\boldsymbol{\varepsilon}} \qquad \text{(in the bulk)}\quad, \tag{5.18a}$$

$$\{\!\{\widetilde{\boldsymbol{t}}\}\!\} = \widetilde{\rho}\,\frac{\partial\widetilde{\psi}\left([\![\boldsymbol{u}]\!], \widetilde{\theta}, \bullet\right)}{\partial[\![\boldsymbol{u}]\!]} \quad \text{(at the interface)}\quad. \tag{5.18b}$$

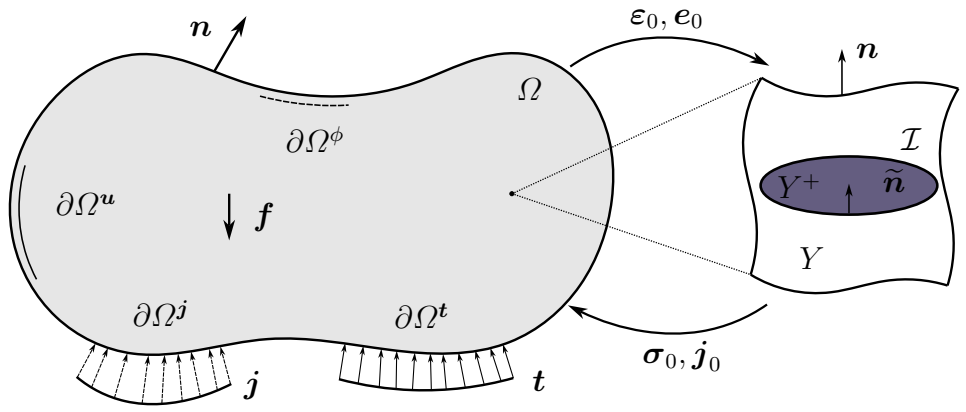

Figure 5.2: The effective macroscale material response is determined by the underlying heterogeneous microstructure. In each material point on the macroscale a representative volume element (RVE) that characterises the material microstructure is considered. Reproduced from [76] under the terms of the Creative Commons Attribution License (CC BY).

For the electrical subproblem, the constitutive restrictions for the electric current density read$\}^{\text{qtd.}}_{[76]}$

$$\boldsymbol{j}(\boldsymbol{x}) \cdot \boldsymbol{e}(\boldsymbol{x}) \geq 0 \qquad \text{(in the bulk)} \quad , \tag{5.19a}$$

$$-\{\!\{\widetilde{i}\}\!\}(\widetilde{\boldsymbol{x}}) \, [\![\phi]\!](\widetilde{\boldsymbol{x}}) \geq 0 \quad \text{(at the interface)} \, . \tag{5.19b}$$

5.2 Computational homogenisation

$\{^{\text{qtd.}}_{[76]}$This section focuses on computational multiscale formulations for electro-mechanical problems in the presence of material interfaces at the microscale. The derivations in this section are based on, and a direct extension of, the multiscale framework for materials with interfaces documented in [93] and the work on multiscale methods for electrical conductors [100]. Whereas the focus in [93] was on purely mechanical problems, the focus in the present contribution is laid on the extension to electro-mechanical coupling. Likewise, material interfaces have not been considered in [100].

Constitutive relations at the microscale are assumed to be known and the objective is to compute the macroscopic response through homogenising the response of the underlying microstructure. In particular, interfaces between different constituents at the microscale are considered and assumed to significantly affect the overall behaviour of the material, see Figure 5.2. The governing equations at the microscale are solved subject to the assumptions of quasi-statics, quasi-stationary and negligible body forces.$\}^{\text{qtd.}}_{[76]}$

5.2.1 Averaging theorems

$\{^{\text{qtd.}}_{[76]}$Macroscopic quantities are related to their microscopic counterparts through volume averages over the representative volume element and additional jump contributions orig-

inating from the material interfaces. In particular, it is observed that the macroscopic strain tensor $\boldsymbol{\varepsilon}_0$, the electric field vector $\boldsymbol{e}_0$, the stress tensor $\boldsymbol{\sigma}_0$ and the electric current density vector $\boldsymbol{j}_0$ can be expressed as surface integrals of microscopic quantities. The definition $v = \mathrm{vol}\,(Y)$ holds. The effective macroscopic strain tensor may be specified in terms of boundary displacements, namely

$$\begin{aligned}
\boldsymbol{\varepsilon}_0(\boldsymbol{x}) &= \frac{1}{v}\int_Y \boldsymbol{\varepsilon}(\boldsymbol{y})\,\mathrm{d}y + \frac{1}{v}\left[\int_{\mathcal{I}} [\![\boldsymbol{u}]\!](\tilde{\boldsymbol{y}}) \otimes \widetilde{\boldsymbol{n}}(\tilde{\boldsymbol{y}})\,\mathrm{d}y\right]^{\mathrm{sym}} \\
&= \frac{1}{v}\left[\int_{\partial Y} \boldsymbol{u}(\boldsymbol{y}) \otimes \boldsymbol{n}(\boldsymbol{y})\,\mathrm{d}y\right]^{\mathrm{sym}} \\
&+ \frac{1}{v}\left[\int_{\mathcal{I}} \boldsymbol{u}^+(\boldsymbol{y}^+) \otimes \boldsymbol{n}^+(\boldsymbol{y}^+) + \boldsymbol{u}^-(\boldsymbol{y}^-) \otimes \boldsymbol{n}^-(\boldsymbol{y}^-) + [\![\boldsymbol{u}]\!](\tilde{\boldsymbol{y}}) \otimes \widetilde{\boldsymbol{n}}(\tilde{\boldsymbol{y}})\,\mathrm{d}y\right]^{\mathrm{sym}} \\
&= \frac{1}{v}\left[\int_{\partial Y} \boldsymbol{u}(\boldsymbol{y}) \otimes \boldsymbol{n}(\boldsymbol{y})\,\mathrm{d}y\right]^{\mathrm{sym}} .
\end{aligned} \tag{5.20}$$

Analogous to (5.20), the effective macroscopic electric field vector

$$\begin{aligned}
\boldsymbol{e}_0(\boldsymbol{x}) &= \frac{1}{v}\int_Y \boldsymbol{e}(\boldsymbol{y})\,\mathrm{d}y + \frac{1}{v}\int_{\mathcal{I}} -[\![\phi]\!](\tilde{\boldsymbol{y}})\,\widetilde{\boldsymbol{n}}(\tilde{\boldsymbol{y}})\,\mathrm{d}y \\
&= \frac{1}{v}\int_{\partial Y} -\phi(\boldsymbol{y})\,\boldsymbol{n}(\boldsymbol{y})\,\mathrm{d}y \\
&+ \frac{1}{v}\int_{\mathcal{I}} -\left[\phi^+(\boldsymbol{y}^+)\,\boldsymbol{n}^+(\boldsymbol{y}^+) + \phi^-(\boldsymbol{y}^-)\,\boldsymbol{n}^-(\boldsymbol{y}^-)\right] - [\![\phi]\!](\tilde{\boldsymbol{y}})\,\widetilde{\boldsymbol{n}}(\tilde{\boldsymbol{y}})\;\mathrm{d}y \\
&= \frac{1}{v}\int_{\partial Y} -\phi(\boldsymbol{y})\,\boldsymbol{n}(\boldsymbol{y})\,\mathrm{d}y
\end{aligned} \tag{5.21}$$

is obtained. In a small strain setting ($\tilde{\boldsymbol{y}} = \boldsymbol{y}^+ = \boldsymbol{y}^-$) and in the absence of interfacial stresses (see [93]), the effective macroscopic stress tensor can be expressed as

$$\begin{aligned}
\boldsymbol{\sigma}_0(\boldsymbol{x}) &= \frac{1}{v}\int_Y \boldsymbol{\sigma}(\boldsymbol{y})\,\mathrm{d}y \\
&= \frac{1}{v}\int_{\partial Y} \boldsymbol{t}(\boldsymbol{y}) \otimes \boldsymbol{y}\,\mathrm{d}y + \frac{1}{v}\int_{\mathcal{I}} \boldsymbol{t}^+(\boldsymbol{y}^+) \otimes \boldsymbol{y}^+ + \boldsymbol{t}^-(\boldsymbol{y}^-) \otimes \boldsymbol{y}^-\mathrm{d}y \\
&= \frac{1}{v}\int_{\partial Y} \boldsymbol{t}(\boldsymbol{y}) \otimes \boldsymbol{y}\,\mathrm{d}y - \frac{1}{v}\int_{\mathcal{I}} \underbrace{[\![\widetilde{\boldsymbol{t}}]\!](\tilde{\boldsymbol{y}})}_{=\,\boldsymbol{0}} \otimes \tilde{\boldsymbol{y}}\,\mathrm{d}y = \frac{1}{v}\int_{\partial Y} \boldsymbol{t}(\boldsymbol{y}) \otimes \boldsymbol{y}\,\mathrm{d}y
\end{aligned} \tag{5.22}$$

where use was made of (5.5b). Analogously and in view of (5.10b), the effective electric current density results in}$^{\text{qtd.}}_{[76]}$

$$\begin{aligned}\boldsymbol{j}_0(\boldsymbol{x}) =& \frac{1}{v}\int_Y \boldsymbol{j}(\boldsymbol{y})\,\mathrm{d}y \\ =& \frac{1}{v}\int_{\partial Y} \boldsymbol{y}\, i(\boldsymbol{y})\,\mathrm{d}y + \frac{1}{v}\int_{\mathcal{I}} \boldsymbol{y}^+ i^+\left(\boldsymbol{y}^+\right) + \boldsymbol{y}^-\, i^-\left(\boldsymbol{y}^-\right)\mathrm{d}y \\ =& \frac{1}{v}\int_{\partial Y} \boldsymbol{y}\, i(\boldsymbol{y})\,\mathrm{d}y - \frac{1}{v}\int_{\mathcal{I}} \tilde{\boldsymbol{y}}\, \underbrace{[\![i]\!](\tilde{\boldsymbol{y}})}_{=0}\,\mathrm{d}y = \frac{1}{v}\int_{\partial Y} \boldsymbol{y}\, i(\boldsymbol{y})\,\mathrm{d}y\,.\end{aligned} \tag{5.23}$$

5.2.2 Generalised Hill–Mandel conditions

$^{\text{qtd.}}_{[76]}$}The Hill–Mandel condition, also known as the micro-macro energy equivalence condition, is a criterion used in homogenisation theory to ensure that the effective material properties of a heterogeneous solid are physically meaningful and well-defined. This criterion postulates that the virtual work on the macroscale is equivalent to the average virtual work on the microscale. In view of (5.12), the classic Hill–Mandel condition for the mechanical problem (5.5) is extended by interface contributions and, by using (3.3), takes the form

$$\begin{aligned}&\boldsymbol{\sigma}_0(\boldsymbol{x}) : \delta\boldsymbol{\varepsilon}_0(\boldsymbol{x}) \overset{!}{=} \frac{1}{v}\int_Y \boldsymbol{\sigma}(\boldsymbol{y}) : \delta\boldsymbol{\varepsilon}(\boldsymbol{y})\,\mathrm{d}y + \frac{1}{v}\int_{\mathcal{I}} \{\!\{\widetilde{\boldsymbol{t}}\}\!\}(\tilde{\boldsymbol{y}}) \cdot \delta[\![\boldsymbol{u}]\!](\tilde{\boldsymbol{y}})\,\mathrm{d}y \\ &= \frac{1}{v}\int_Y \nabla_y \cdot [\delta\boldsymbol{u}(\boldsymbol{y}) \cdot \boldsymbol{\sigma}(\boldsymbol{y})] - \delta\boldsymbol{u}(\boldsymbol{y}) \cdot \underbrace{[\nabla_y \cdot \boldsymbol{\sigma}(\boldsymbol{y})]}_{=\mathbf{0}}\,\mathrm{d}y + \frac{1}{v}\int_{\mathcal{I}} \{\!\{\widetilde{\boldsymbol{t}}\}\!\}(\tilde{\boldsymbol{y}}) \cdot \delta[\![\boldsymbol{u}]\!](\tilde{\boldsymbol{y}})\,\mathrm{d}y \\ &= \frac{1}{v}\int_{\partial Y} \boldsymbol{t}(\boldsymbol{y}) \cdot \delta\boldsymbol{u}(\boldsymbol{y})\,\mathrm{d}y - \frac{1}{v}\int_{\mathcal{I}} [\![\widetilde{\boldsymbol{t}} \cdot \delta\boldsymbol{u}]\!](\tilde{\boldsymbol{y}}) + \frac{1}{v}\int_{\mathcal{I}} \{\!\{\widetilde{\boldsymbol{t}}\}\!\}(\tilde{\boldsymbol{y}}) \cdot \delta[\![\boldsymbol{u}]\!](\tilde{\boldsymbol{y}})\,\mathrm{d}y \\ &= \frac{1}{v}\int_{\partial Y} \boldsymbol{t}(\boldsymbol{y}) \cdot \delta\boldsymbol{u}(\boldsymbol{y})\,\mathrm{d}y\,.\end{aligned} \tag{5.24}$$

Analogous to (5.24), the extended Hill–Mandel condition for the electrical subproblem can be derived as

$$\begin{aligned}&\boldsymbol{j}_0(\boldsymbol{x}) \cdot \delta\boldsymbol{e}_0(\boldsymbol{x}) \overset{!}{=} \frac{1}{v}\int_Y \boldsymbol{j}(\boldsymbol{y}) \cdot \delta\boldsymbol{e}(\boldsymbol{y})\,\mathrm{d}y + \frac{1}{v}\int_{\mathcal{I}} -\{\!\{\widetilde{i}\}\!\}(\tilde{\boldsymbol{y}})\,\delta[\![\phi]\!](\tilde{\boldsymbol{y}})\,\mathrm{d}y \\ &= \frac{1}{v}\int_Y -\nabla_y \cdot [\delta\phi(\boldsymbol{y})\,\boldsymbol{j}(\boldsymbol{y})] + \delta\phi(\boldsymbol{y})\,\underbrace{[\nabla_y \cdot \boldsymbol{j}(\boldsymbol{y})]}_{=\mathbf{0}}\,\mathrm{d}y - \frac{1}{v}\int_{\mathcal{I}} \{\!\{\widetilde{i}\}\!\}(\tilde{\boldsymbol{y}})\,\delta[\![\phi]\!](\tilde{\boldsymbol{y}})\,\mathrm{d}y \\ &= \frac{1}{v}\int_{\partial Y} -i(\boldsymbol{y})\,\delta\phi(\boldsymbol{y})\,\mathrm{d}y + \frac{1}{v}\int_{\mathcal{I}} [\![\widetilde{i}\delta\phi]\!](\tilde{\boldsymbol{y}})\,\mathrm{d}y - \frac{1}{v}\int_{\mathcal{I}} \{\!\{\widetilde{i}\}\!\}(\tilde{\boldsymbol{y}})\,\delta[\![\phi]\!](\tilde{\boldsymbol{y}})\,\mathrm{d}y \\ &= \frac{1}{v}\int_{\partial Y} -i(\boldsymbol{y})\,\delta\phi(\boldsymbol{y})\,\mathrm{d}y\,.\end{aligned} \tag{5.25}$$

In accordance with [93], the representation of the Hill–Mandel condition are expressed as a surface integral, which remains equivalent to its classic form even in the presence of an interface. This has advantages in computational implementations because existing frameworks and subroutines developed for classic homogenisation, i.e. homogenisation without interfacial contributions, can be applied.}$^{\text{qtd.}}_{[76]}$

5.2.2.1 Affine boundary conditions

$^{\text{qtd.}}_{[76]}${Affine displacement boundary conditions are prescribed based on the macroscopic deformation state, namely

$$\boldsymbol{u}(\boldsymbol{y}) = \boldsymbol{\varepsilon}_0(\boldsymbol{x}) \cdot \boldsymbol{y} \quad \text{on} \quad \partial Y\,. \tag{5.26}$$

The affine displacement boundary condition fulfils the averaging theorem for the macroscopic strain tensor (5.20), i.e. inserting (5.26) into (5.20) results in

$$\begin{aligned} \frac{1}{v}\left[\int_{\partial Y} \boldsymbol{u}(\boldsymbol{y}) \otimes \boldsymbol{n}(\boldsymbol{y})\,\mathrm{d}y\right]^{\text{sym}} &= \frac{1}{v}\int_{\partial Y} [\boldsymbol{\varepsilon}_0(\boldsymbol{x}) \cdot \boldsymbol{y}] \otimes \boldsymbol{n}(\boldsymbol{y})\,\mathrm{d}y \\ &= \frac{1}{v}\left[\boldsymbol{\varepsilon}_0(\boldsymbol{x}) \cdot \int_Y \nabla_y \cdot [\boldsymbol{y} \otimes \boldsymbol{I}]\,\mathrm{d}y\right] = \boldsymbol{\varepsilon}_0(\boldsymbol{x})\,. \end{aligned} \tag{5.27}$$

For the electrical subproblem, the particular form of the microscopic electric potential field

$$\phi(\boldsymbol{y}) = -\boldsymbol{e}_0(\boldsymbol{x}) \cdot \boldsymbol{y} \quad \text{on} \quad \partial Y \tag{5.28}$$

is chosen. Analogous to the mechanical problem (5.27), consistency of the boundary condition (5.28) with the scale bridging relation (5.21) is shown by inserting (5.28) into (5.21), namely

$$\begin{aligned} \frac{1}{v}\int_{\partial Y} -\phi(\boldsymbol{y})\,\boldsymbol{n}(\boldsymbol{y})\,\mathrm{d}y &= \frac{1}{v}\int_{\partial Y} -\left[-\boldsymbol{e}_0(\boldsymbol{x}) \cdot \boldsymbol{y}\right]\boldsymbol{n}(\boldsymbol{y})\,\mathrm{d}y \\ &= \frac{1}{v}\left[\boldsymbol{e}_0(\boldsymbol{x}) \cdot \int_\Omega \nabla_y \cdot [\boldsymbol{y} \otimes \boldsymbol{I}]\,\mathrm{d}y\right] = \boldsymbol{e}_0(\boldsymbol{x})\,. \end{aligned} \tag{5.29}$$

By inserting (5.26) into the Hill–Mandel condition for the mechanical problem (5.24)

$$\begin{aligned} \frac{1}{v}\int_Y \boldsymbol{\sigma}(\boldsymbol{y}) : \delta\boldsymbol{\varepsilon}(\boldsymbol{y})\,\mathrm{d}y + \frac{1}{v}\int_{\mathcal{I}} \{\!\{\widetilde{\boldsymbol{t}}\}\!\}(\tilde{\boldsymbol{y}}) \cdot \delta[\![\boldsymbol{u}]\!](\tilde{\boldsymbol{y}})\,\mathrm{d}y &= \frac{1}{v}\int_{\partial Y} \boldsymbol{t}(\boldsymbol{y}) \cdot \delta\boldsymbol{u}(\boldsymbol{y})\,\mathrm{d}y \\ = \frac{1}{v}\int_{\partial Y} \boldsymbol{t}(\boldsymbol{y}) \cdot [\delta\boldsymbol{\varepsilon}_0(\boldsymbol{x}) \cdot \boldsymbol{y}]\,\mathrm{d}y & \\ = \frac{1}{v}\int_{\partial Y} \boldsymbol{t}(\boldsymbol{y}) \otimes \boldsymbol{y}\,\mathrm{d}y : \delta\boldsymbol{\varepsilon}_0(\boldsymbol{x}) &= \boldsymbol{\sigma}_0(\boldsymbol{x}) : \delta\boldsymbol{\varepsilon}_0(\boldsymbol{x}) \end{aligned} \tag{5.30}$$

is obtained. Furthermore, inserting (5.28) into (5.25) shows the consistency of the boundary condition (5.28) and the Hill–Mandel condition for the electrical problem results in}^{\text{qtd.}}_{[76]}

$$\begin{aligned}\frac{1}{v}\int_Y \boldsymbol{j}\left(\boldsymbol{y}\right)\cdot\delta\boldsymbol{e}\left(\boldsymbol{y}\right)\mathrm{d}y-\frac{1}{v}\int_{\mathcal{I}}\widetilde{\{\!\{i\}\!\}}\left(\tilde{\boldsymbol{y}}\right)\delta[\![\phi]\!]\left(\tilde{\boldsymbol{y}}\right)\mathrm{d}y&=-\frac{1}{v}\int_{\partial Y} i\left(\boldsymbol{y}\right)\delta\phi\left(\boldsymbol{y}\right)\mathrm{d}y\\ &=-\frac{1}{v}\int_{\partial Y} i\left(\boldsymbol{y}\right)\left[-\delta\boldsymbol{e}_0\left(\boldsymbol{x}\right)\cdot\boldsymbol{y}\right]\mathrm{d}y\\ &=+\frac{1}{v}\int_{\partial Y} i\left(\boldsymbol{y}\right)\boldsymbol{y}\,\mathrm{d}y\cdot\delta\boldsymbol{e}_0\left(\boldsymbol{x}\right)=\boldsymbol{j}_0\left(\boldsymbol{x}\right)\cdot\delta\boldsymbol{e}_0\left(\boldsymbol{x}\right)\ .\end{aligned}\tag{5.31}$$

5.2.2.2 Periodic boundary conditions

The periodicity conditions for the mechanical subproblem are expressed as

$$\boldsymbol{u}^+\left(\boldsymbol{y}\right)-\boldsymbol{u}^-\left(\boldsymbol{y}\right)=\boldsymbol{\varepsilon}_0\left(\boldsymbol{x}\right)\cdot\left[\boldsymbol{y}^+-\boldsymbol{y}^-\right]\quad\text{on}\quad\partial Y\,,\tag{5.32a}$$

$$\boldsymbol{t}^+\left(\boldsymbol{y}^+\right)=-\boldsymbol{t}^-\left(\boldsymbol{y}^-\right)\quad\text{on}\quad\partial Y\,.\tag{5.32b}$$

The periodic displacement boundary condition fulfils the averaging theorem for the macroscopic strain tensor (5.20), i.e. inserting (5.32) into (5.20) results in

$$\begin{aligned}\frac{1}{v}\left[\int_{\partial Y}\boldsymbol{u}\left(\boldsymbol{y}\right)\otimes\boldsymbol{n}\left(\boldsymbol{y}\right)\mathrm{d}y\right]^{\mathrm{sym}}&=\frac{1}{v}\left[\int_{\partial Y^+}\boldsymbol{u}^+\left(\boldsymbol{y}^+\right)\boldsymbol{n}^+\left(\boldsymbol{y}^+\right)\mathrm{d}y+\int_{\partial Y^-}\boldsymbol{u}^-\left(\boldsymbol{y}^-\right)\boldsymbol{n}^-\left(\boldsymbol{y}^-\right)\mathrm{d}y\right]^{\mathrm{sym}}\\ &=\frac{1}{v}\left[\int_{\partial Y^+}\boldsymbol{\varepsilon}_0\left(\boldsymbol{x}\right)\cdot\left[\boldsymbol{y}^+-\boldsymbol{y}^-\right]\otimes\boldsymbol{n}^+\left(\boldsymbol{y}^+\right)\mathrm{d}y\right]^{\mathrm{sym}}\\ &=\frac{1}{v}\left[\boldsymbol{\varepsilon}_0\left(\boldsymbol{x}\right)\cdot\int_{\partial Y}\boldsymbol{y}\otimes\boldsymbol{I}\cdot\boldsymbol{n}\left(\boldsymbol{y}\right)\mathrm{d}y\right]^{\mathrm{sym}}=\boldsymbol{\varepsilon}_0\left(\boldsymbol{x}\right)\ .\end{aligned}\tag{5.33}$$

Analogously, the periodicity conditions for the electrical problem read

$$\phi^+\left(\boldsymbol{y}\right)-\phi^-\left(\boldsymbol{y}\right)=-\boldsymbol{e}_0\left(\boldsymbol{x}\right)\cdot\left[\boldsymbol{y}^+-\boldsymbol{y}^-\right]\quad\text{on}\quad\partial Y\,,\tag{5.34a}$$

$$i^+\left(\boldsymbol{y}^+\right)=-i^-\left(\boldsymbol{y}^-\right)\quad\text{on}\quad\partial Y\,.\tag{5.34b}$$

By inserting the boundary conditions (5.34) into the effective macroscopic electric field vector (5.21), i.e.

$$\begin{aligned}\frac{1}{v}\int_{\partial Y}-\phi\left(\boldsymbol{y}\right)\boldsymbol{n}\left(\boldsymbol{y}\right)\mathrm{d}y&=-\frac{1}{v}\left[\int_{\partial Y^+}\phi^+\left(\boldsymbol{y}^+\right)\boldsymbol{n}^+\left(\boldsymbol{y}^+\right)\mathrm{d}y+\int_{\partial Y^-}\phi^-\left(\boldsymbol{y}^-\right)\boldsymbol{n}^-\left(\boldsymbol{y}^-\right)\mathrm{d}y\right]\\ &=\frac{1}{v}\left[\int_{\partial Y^+}\boldsymbol{e}_0\left(\boldsymbol{x}\right)\cdot\left[\boldsymbol{y}^+-\boldsymbol{y}^-\right]\otimes\boldsymbol{n}^+\left(\boldsymbol{y}^+\right)\mathrm{d}y\right]\\ &=\frac{1}{v}\left[\boldsymbol{e}_0\left(\boldsymbol{x}\right)\cdot\int_{\partial Y}\boldsymbol{y}\otimes\boldsymbol{I}\cdot\boldsymbol{n}\left(\boldsymbol{y}\right)\mathrm{d}y\right]=\boldsymbol{e}_0\left(\boldsymbol{x}\right)\ ,\end{aligned}\tag{5.35}$$

consistency of scale-bridging relation is shown. In order to fulfil extended Hill–Mandel conditions, mechanical boundary conditions (5.32) are inserted into (5.24), to be specific

$$\begin{aligned}\frac{1}{v}\int_Y \boldsymbol{\sigma}(\boldsymbol{y}) : \delta\boldsymbol{\varepsilon}(\boldsymbol{y})\,\mathrm{d}y + \frac{1}{v}\int_{\mathcal{I}} \widetilde{\{\!\{\boldsymbol{t}\}\!\}}(\tilde{\boldsymbol{y}}) \cdot \delta[\![\boldsymbol{u}]\!](\tilde{\boldsymbol{y}})\,\mathrm{d}y &= \frac{1}{v}\int_{\partial Y} \boldsymbol{t}(\boldsymbol{y}) \cdot \delta\boldsymbol{u}(\boldsymbol{y})\,\mathrm{d}y \\ &= \frac{1}{v}\left[\int_{\partial Y^+} \boldsymbol{t}^+\left(\boldsymbol{y}^+\right)\delta\boldsymbol{u}^+\left(\boldsymbol{y}^+\right)\mathrm{d}y + \int_{\partial Y^-} \boldsymbol{t}^-\left(\boldsymbol{y}^-\right)\delta\boldsymbol{u}^-\left(\boldsymbol{y}^-\right)\mathrm{d}y\right] \\ &= \frac{1}{v}\int_{\partial Y^+} \boldsymbol{t}^+(\boldsymbol{y}) \cdot \left[\delta\boldsymbol{\varepsilon}_0(\boldsymbol{x}) \cdot \left[\boldsymbol{y}^+ - \boldsymbol{y}^-\right]\right]\mathrm{d}y \\ &= \frac{1}{v}\int_{\partial Y} \boldsymbol{t}(\boldsymbol{y}) \otimes \boldsymbol{y}\,\mathrm{d}y : \delta\boldsymbol{\varepsilon}_0(\boldsymbol{x}) = \boldsymbol{\sigma}_0(\boldsymbol{x}) : \delta\boldsymbol{\varepsilon}_0(\boldsymbol{x})\ .\end{aligned} \tag{5.36}$$

Analogously, for the electrical problem, one obtains

$$\begin{aligned}\frac{1}{v}\int_Y \boldsymbol{j}(\boldsymbol{y}) \cdot \delta\boldsymbol{e}(\boldsymbol{y})\,\mathrm{d}y + \frac{1}{v}\int_{\mathcal{I}} -\widetilde{\{\!\{i\}\!\}}(\tilde{\boldsymbol{y}})\,\delta[\![\phi]\!](\tilde{\boldsymbol{y}})\,\mathrm{d}y &= -\frac{1}{v}\int_{\partial Y} i(\boldsymbol{y})\,\delta\phi(\boldsymbol{y})\,\mathrm{d}y \\ &= \frac{1}{v}\left[\int_{\partial Y^+} i^+\left(\boldsymbol{y}^+\right)\delta\phi^+\left(\boldsymbol{y}^+\right)\mathrm{d}y + \int_{\partial Y^-} i^-\left(\boldsymbol{y}^-\right)\delta\phi^-\left(\boldsymbol{y}^-\right)\mathrm{d}y\right] \\ &= -\frac{1}{v}\int_{\partial Y^+} i^+(\boldsymbol{y})\left[-\delta\boldsymbol{e}_0(\boldsymbol{x}) \cdot \left[\boldsymbol{y}^+ - \boldsymbol{y}^-\right]\right]\mathrm{d}y \\ &= \frac{1}{v}\int_{\partial Y} i(\boldsymbol{y})\,\boldsymbol{y}\,\mathrm{d}y \cdot \delta\boldsymbol{e}_0(\boldsymbol{x}) = \boldsymbol{j}_0(\boldsymbol{x}) \cdot \delta\boldsymbol{e}_0(\boldsymbol{x})\ .\end{aligned} \tag{5.37}$$

5.2.2.3 Uniform flux boundary conditions

qtd. [76] {Uniform (constant) traction conditions are prescribed at the boundary of the RVE as

$$\boldsymbol{t}(\boldsymbol{y}) = \boldsymbol{\sigma}_0(\boldsymbol{x}) \cdot \boldsymbol{n}(\boldsymbol{y}) \quad \text{on} \quad \partial Y\,. \tag{5.38}$$

By inserting (5.38) into (5.22), consistency of the uniform flux boundary condition with scale-bridging relation (5.22) can be shown, namely

$$\begin{aligned}&\frac{1}{v}\int_Y \boldsymbol{\sigma}(\boldsymbol{y})\,\mathrm{d}y = \frac{1}{v}\int_{\partial Y} \boldsymbol{t}(\boldsymbol{y}) \otimes \boldsymbol{y}\,\mathrm{d}y \\ &= \frac{1}{v}\int_{\partial Y} \boldsymbol{\sigma}_0(\boldsymbol{x}) \cdot \boldsymbol{n}(\boldsymbol{y}) \otimes \boldsymbol{y}\,\mathrm{d}y - \frac{1}{v}\int_Y \underbrace{\nabla_y \cdot \boldsymbol{\sigma}_0(\boldsymbol{x})}_{=\mathbf{0}} \otimes \boldsymbol{y}\,\mathrm{d}y - \frac{1}{v}\int_{\mathcal{I}} \underbrace{[\![\widetilde{\boldsymbol{t}}]\!](\tilde{\boldsymbol{y}})}_{=\mathbf{0}} \otimes \tilde{\boldsymbol{y}}\,\mathrm{d}y \\ &= \frac{1}{v}\int_Y \boldsymbol{\sigma}_0(\boldsymbol{x})\,\mathrm{d}y = \boldsymbol{\sigma}_0(\boldsymbol{x})\ .\end{aligned} \tag{5.39}$$

Uniform electric current density boundary conditions are given by

$$i(\boldsymbol{y}) = \boldsymbol{j}_0(\boldsymbol{x}) \cdot \boldsymbol{n}(\boldsymbol{y}) \quad \text{on} \quad \partial Y\,. \tag{5.40}$$

By inserting (5.40) into (5.23) and by analogy with the mechanical subproblem, one arrives at

$$\begin{aligned}
&\frac{1}{v}\int_Y \boldsymbol{j}\,(\boldsymbol{y})\,\mathrm{d}y = \frac{1}{v}\int_{\partial Y} i\,(\boldsymbol{y})\,\boldsymbol{y}\,\mathrm{d}y \\
&= \frac{1}{v}\int_{\partial Y} \boldsymbol{y}\otimes\boldsymbol{j}_0\,(\boldsymbol{x})\cdot\boldsymbol{n}\,(\boldsymbol{y})\,\mathrm{d}y - \frac{1}{v}\int_Y \underbrace{\nabla_y\cdot\boldsymbol{j}_0\,(\boldsymbol{x})}_{=0}\,\boldsymbol{y}\,\mathrm{d}y - \frac{1}{v}\int_{\mathcal{I}} \widetilde{\boldsymbol{x}}\,\underbrace{[\![i]\!]\,(\tilde{\boldsymbol{y}})}_{=0}\,\mathrm{d}y \\
&= \frac{1}{v}\int_Y \boldsymbol{j}_0\,(\boldsymbol{x})\,\mathrm{d}y = \boldsymbol{j}_0\,(\boldsymbol{x})
\end{aligned} \tag{5.41}$$

which shows the consistency of the uniform electric current density boundary condition with scale bridging relation (5.23). In view of (5.38) and (5.40), the evaluation of the Hill–Mandel condition for the mechanical subproblem (5.24) results in

$$\begin{aligned}
&\frac{1}{v}\int_Y \boldsymbol{\sigma}\,(\boldsymbol{y}) : \delta\boldsymbol{\varepsilon}\,(\boldsymbol{y})\,\mathrm{d}y + \frac{1}{v}\int_{\mathcal{I}} \{\!\{\widetilde{\boldsymbol{t}}\}\!\}\,(\tilde{\boldsymbol{y}})\cdot\delta[\![\boldsymbol{u}]\!]\,(\tilde{\boldsymbol{y}})\,\mathrm{d}y \\
&\qquad = \frac{1}{v}\int_{\partial Y} \boldsymbol{t}\,(\boldsymbol{y})\cdot\delta\boldsymbol{u}\,(\boldsymbol{y})\,\mathrm{d}y = \frac{1}{v}\int_{\partial Y} \delta\boldsymbol{u}\,(\boldsymbol{y})\cdot[\boldsymbol{\sigma}_0\,(\boldsymbol{x})\cdot\boldsymbol{n}\,(\boldsymbol{y})]\,\mathrm{d}y \\
&\qquad = \boldsymbol{\sigma}_0\,(\boldsymbol{x}) : \left[\frac{1}{v}\int_{\partial Y} \delta\boldsymbol{u}\,(\boldsymbol{y})\otimes\boldsymbol{n}\,(\boldsymbol{y})\,\mathrm{d}y\right] = \boldsymbol{\sigma}_0\,(\boldsymbol{x}) : \delta\boldsymbol{\varepsilon}_0\,(\boldsymbol{x})
\end{aligned} \tag{5.42}$$

and for the electrical subproblem (5.25)

$$\begin{aligned}
&\frac{1}{v}\int_Y \boldsymbol{j}\,(\boldsymbol{y})\cdot\delta\boldsymbol{e}\,(\boldsymbol{y})\,\mathrm{d}y - \frac{1}{v}\int_{\mathcal{I}} \{\!\{\widetilde{i}\}\!\}\,(\tilde{\boldsymbol{y}})\,\delta[\![\phi]\!]\,(\tilde{\boldsymbol{y}})\,\mathrm{d}y \\
&\qquad = -\frac{1}{v}\int_{\partial Y} i\,(\boldsymbol{y})\,\delta\phi\,(\boldsymbol{y})\,\mathrm{d}y = -\frac{1}{v}\int_{\partial Y} \delta\phi\,(\boldsymbol{y})\,[\boldsymbol{j}_0\,(\boldsymbol{x})\cdot\boldsymbol{n}\,(\boldsymbol{y})]\,\mathrm{d}y \\
&\qquad = \boldsymbol{j}_0\,(\boldsymbol{x}) : \left[\frac{1}{v}\int_{\partial Y} -\delta\phi\,(\boldsymbol{y})\,\boldsymbol{n}\,(\boldsymbol{y})\,\mathrm{d}y\right] = \boldsymbol{j}_0\,(\boldsymbol{x}) : \delta\boldsymbol{e}_0\,(\boldsymbol{x})
\end{aligned} \tag{5.43}$$

is obtained.}$^{\text{qtd.}}_{[76]}$

5.3 Finite element implementation

$^{\text{qtd.}}_{[76]}${This section addresses the finite element implementation of the proposed multiscale formulation for electrical conductors in the presence of material interfaces. In particular, the focus is on the weak form of the microscale boundary value problem in Section 5.3.1 before discrete closed-form solutions for the homogenised macroscale fields and the associated tangent stiffness contributions are derived in Section 5.3.2 and Section 5.3.3, respectively.}$^{\text{qtd.}}_{[76]}$

5.3.1 Weak form of the coupled problem

To derive the weak form of the electro-mechanically coupled problem, (5.5a)–(5.10) are multiplied by appropriate test functions $\boldsymbol{\varphi}^{\boldsymbol{u}}$ and φ^{ϕ}, and are integrated over domain

Y, which consists of subdomains Y^- and Y^+. To avoid repetition, only the final weak forms are presented here. Detailed derivations and intermediate steps are addressed in Section 3.2.

The weak form of the mechanical problem is given by:

Find $\boldsymbol{u} \in [H^1(Y^+)]^d \times [H^1(Y^-)]^d$ such that

$$\int_{Y^+ \cup Y^-} \nabla_y \boldsymbol{\varphi}^{\boldsymbol{u}}(\boldsymbol{y}) : \boldsymbol{\sigma}(\boldsymbol{y}) \,\mathrm{d}y = \int_{\partial Y} \boldsymbol{\varphi}^{\boldsymbol{u}}(\boldsymbol{y}) \cdot \boldsymbol{t}(\boldsymbol{y}) \,\mathrm{d}y - \int_{\mathcal{I}} [\![\boldsymbol{\varphi}^{\boldsymbol{u}}]\!](\tilde{\boldsymbol{y}}) \cdot \{\!\{\widetilde{\boldsymbol{t}}\}\!\}(\tilde{\boldsymbol{y}}) \,\mathrm{d}y \tag{5.44}$$

for all $\boldsymbol{\varphi}^{\boldsymbol{u}} \in \Phi = \{\boldsymbol{\varphi}^{\boldsymbol{u}} \in [H^1(Y^+)]^d \times [H^1(Y^-)]^d : \boldsymbol{\varphi}^{\boldsymbol{u}} = \mathbf{0} \text{ on } \partial Y^{\boldsymbol{u}}\}$.

Similarly, the weak form of the electrical problem reads

Find $\phi \in H^1(Y^+) \times H^1(Y^-)$ such that

$$\int_{Y^+ \cup Y^-} \nabla_y \varphi^{\phi}(\boldsymbol{y}) \cdot \boldsymbol{j}(\boldsymbol{y}) \,\mathrm{d}y = \varphi^{\phi}(\boldsymbol{y})\, \boldsymbol{j}(\boldsymbol{y}) \cdot \boldsymbol{n}(\boldsymbol{y}) \,\mathrm{d}y - \int_{\mathcal{I}} [\![\varphi^{\phi}]\!](\tilde{\boldsymbol{y}})\, \{\!\{\widetilde{i}\}\!\}(\tilde{\boldsymbol{y}}) \,\mathrm{d}y \tag{5.45}$$

for all $\varphi^{\phi} \in \Phi = \{\varphi^{\phi} \in H^1(Y^+) \times H^1(Y^-) : \varphi^{\phi} = 0 \text{ on } \partial Y^{\phi}\}$.

5.3.2 Homogenisation

qtd. [76] {The finite element implementation of continua with interfaces is adopted from [98]. The primary fields and test functions are discretised as follows

$$\boldsymbol{u}^{\mathrm{h}} = \sum_{C=1}^{\mathrm{n_{en}}} \boldsymbol{u}_C \, N_C, \quad \boldsymbol{\eta}^{\boldsymbol{u}\,\mathrm{h}} = \sum_{A=1}^{\mathrm{n_{en}}} \boldsymbol{\eta}^{\boldsymbol{u}} \, N_A \,, \tag{5.46a}$$

$$\phi^{\mathrm{h}} = \sum_{D=1}^{\mathrm{n_{en}}} \phi_D \, N_D, \quad \eta^{\phi\,\mathrm{h}} = \sum_{B=1}^{\mathrm{n_{en}}} \eta_B^{\phi} \, N_B \tag{5.46b}$$

where $\mathrm{n_{en}}$ and $N_\bullet$ are the number of element nodes and the shape functions, respectively. The linearised system of equations for the coupled problem with affine boundary conditions takes the form

$$\begin{bmatrix} \mathbf{K}^{\boldsymbol{u}\boldsymbol{u}} + \widetilde{\mathbf{K}}^{\boldsymbol{u}\boldsymbol{u}} & \mathbf{K}^{\boldsymbol{u}\phi} + \widetilde{\mathbf{K}}^{\boldsymbol{u}\phi} \\ \mathbf{K}^{\phi\boldsymbol{u}} + \widetilde{\mathbf{K}}^{\phi\boldsymbol{u}} & \mathbf{K}^{\phi\phi} + \widetilde{\mathbf{K}}^{\phi\phi} \end{bmatrix}_q \cdot \begin{bmatrix} \Delta\widehat{\boldsymbol{u}} \\ \Delta\widehat{\boldsymbol{\phi}} \end{bmatrix}_q = \begin{bmatrix} \Delta\boldsymbol{f}^{\boldsymbol{u}} + \Delta\widetilde{\boldsymbol{f}}^{\boldsymbol{u}} \\ \Delta\boldsymbol{f}^{\phi} + \Delta\widetilde{\boldsymbol{f}}^{\phi} \end{bmatrix}_q , \tag{5.47}$$

for Newton iteration step q, where $\widehat{\boldsymbol{u}}$ and $\widehat{\boldsymbol{\phi}}$ denote the global lists of nodal degrees of freedom. In (5.47), $\mathbf{K}^{\bullet *}$ and $\widetilde{\mathbf{K}}^{\bullet *}$ are the generalised stiffness matrices of bulk and

interface. Similarly, $\boldsymbol{f}^{\bullet}$ and $\widetilde{\boldsymbol{f}}^{\bullet}$ are the contributions of bulk and interface to the generalised reaction force vector. By collecting the contributions of the individual fields in the matrix $\mathbf{K}$ and the vectors $\boldsymbol{\mathcal{X}}$ and $\boldsymbol{f}$, system (5.47) can be written as

$$\mathbf{K} \cdot \Delta\boldsymbol{\mathcal{X}} = \Delta\boldsymbol{f}\,. \tag{5.48}$$

In the case of periodic boundary conditions, the generalised stiffness matrices and generalised reaction force vectors are substituted by reduced versions that result from enforcing linear constraints between opposing RVE boundaries, see e.g. [100]. The proposed finite element implementation uses scale-bridging relations that rely on equations (5.22) and (5.23). Accordingly, the discrete versions of the macroscopic stress tensor

$$\boldsymbol{\sigma}_0 = \frac{1}{v}\int_{\partial Y} \boldsymbol{t}\,(\boldsymbol{y}) \otimes \boldsymbol{y}\,\mathrm{d}y \approx \frac{1}{v}\sum_{i=1}^{\mathrm{n_{pn}}} {}^{(i)}\boldsymbol{f}^{\boldsymbol{u}} \otimes {}^{(i)}\boldsymbol{y} \tag{5.49}$$

and the electric current density vector

$$\boldsymbol{j}_0 = \frac{1}{v}\int_{\partial Y} i\,(\boldsymbol{y})\,\boldsymbol{y}\,\mathrm{d}y \approx \frac{1}{v}\sum_{i=1}^{\mathrm{n_{pn}}} {}^{(i)}f^{\phi}\,{}^{(i)}\boldsymbol{y} \tag{5.50}$$

are obtained. In (5.49), $\mathrm{n_{pn}}$ denotes the number of Dirichlet nodes, and ${}^{(i)}\boldsymbol{y}$ and ${}^{(i)}\boldsymbol{f}^{\boldsymbol{u}}$ are the position and the reaction force vector of node i, corresponding to the mechanical problem. Similarly, ${}^{(i)}f^{\phi}$ represents the generalised reaction force of node i for the electrical problem.}$^{\text{qtd.}}_{[76]}$

5.3.3 Consistent tangent stiffness tensors

$^{\text{qtd.}}_{[76]}${In order to derive consistent algorithmic tangent stiffness operators, the linear system (5.48) is partitioned into Dirichlet $\boldsymbol{\mathcal{X}}_{\mathrm{d}}$ and free $\boldsymbol{\mathcal{X}}_{\mathrm{f}}$ degrees of freedom

$$\begin{bmatrix}\mathbf{K}_{\mathrm{dd}} & \mathbf{K}_{\mathrm{df}}\\ \mathbf{K}_{\mathrm{fd}} & \mathbf{K}_{\mathrm{ff}}\end{bmatrix} \cdot \begin{bmatrix}\Delta\boldsymbol{\mathcal{X}}_{\mathrm{d}}\\ \Delta\boldsymbol{\mathcal{X}}_{\mathrm{f}}\end{bmatrix} = \begin{bmatrix}\Delta\boldsymbol{f}_{\mathrm{d}}\\ \mathbf{0}\end{bmatrix}\,. \tag{5.51}$$

Solving the second line of the system of equations for $\boldsymbol{\mathcal{X}}_{\mathrm{f}}$ and inserting the ensuing relation in the first line, the closed-form expression

$$\left[\mathbf{K}_{\mathrm{dd}} - \mathbf{K}_{\mathrm{df}} \cdot \mathbf{K}_{\mathrm{ff}}^{-1} \cdot \mathbf{K}_{\mathrm{fd}}\right] \cdot \Delta\boldsymbol{\mathcal{X}}_{\mathrm{d}} = \Delta\boldsymbol{f}_{\mathrm{d}} \tag{5.52}$$

is obtained. For affine and periodic boundary conditions, the kinematic relations are given as

$$\Delta^{(j)}\boldsymbol{u}_{\mathrm{d}} = \Delta\boldsymbol{\varepsilon}_0 \cdot {}^{(j)}\boldsymbol{y}\,, \tag{5.53a}$$

$$\Delta^{(j)}\phi_{\mathrm{d}} = -\Delta\boldsymbol{e}_0 \cdot {}^{(j)}\boldsymbol{y}\,. \tag{5.53b}$$

By partitioning (5.51) into mechanical and electrical contributions and after inserting (5.53), the relations

$$\Delta^{(i)}\boldsymbol{f}^{\boldsymbol{u}} = \sum_{j=1}^{\mathrm{n_{pn}}} {}^{(ij)}\widehat{\mathbf{K}}^{\boldsymbol{uu}} \cdot \Delta\boldsymbol{\varepsilon}_0 \cdot {}^{(j)}\boldsymbol{y} - \sum_{j=1}^{\mathrm{n_{pn}}} {}^{(ij)}\widehat{\mathbf{K}}^{\boldsymbol{u}\phi} \otimes \Delta\boldsymbol{e}_0 \cdot {}^{(j)}\boldsymbol{y} \tag{5.54}$$

and

$$\Delta^{(i)}f^{\phi} = \sum_{j=1}^{\mathrm{n_{pn}}} {}^{(ij)}\widehat{\mathbf{K}}^{\phi\boldsymbol{u}} \cdot \Delta\boldsymbol{\varepsilon}_0 \cdot {}^{(j)}\boldsymbol{y} - \sum_{j=1}^{\mathrm{n_{pn}}} {}^{(ij)}\widehat{\mathbf{K}}^{\phi\phi} \otimes \Delta\boldsymbol{e}_0 \cdot {}^{(j)}\boldsymbol{y} \tag{5.55}$$

between increments in the generalised reaction force vectors at the microscale and changes in $\boldsymbol{\varepsilon}_0$ and $\boldsymbol{e}_0$ are obtained. Finally, by inserting (5.54) into the discrete representation of the stress tensor (5.49), one arrives at

$$\Delta\boldsymbol{\sigma}_0 \approx \underbrace{\frac{1}{v}\sum_{i=1}^{\mathrm{n_{pn}}}\sum_{j=1}^{\mathrm{n_{pn}}} {}^{(ij)}\widehat{\mathbf{K}}^{\boldsymbol{uu}} \overline{\otimes} \left[{}^{(i)}\boldsymbol{y} \otimes {}^{(j)}\boldsymbol{y}\right]}_{=\dfrac{\mathrm{d}\boldsymbol{\sigma}_0}{\mathrm{d}\boldsymbol{\varepsilon}_0}} : \Delta\boldsymbol{\varepsilon}_0 \underbrace{-\frac{1}{v}\sum_{i=1}^{\mathrm{n_{pn}}}\sum_{j=1}^{\mathrm{n_{pn}}} {}^{(ij)}\widehat{\mathbf{K}}^{\boldsymbol{u}\phi} \otimes \left[{}^{(i)}\boldsymbol{y} \otimes {}^{(j)}\boldsymbol{y}\right]}_{=\dfrac{\mathrm{d}\boldsymbol{\sigma}_0}{\mathrm{d}\boldsymbol{e}_0}} \cdot \Delta\boldsymbol{e}_0 \,. \tag{5.56}$$

Analogously, inserting (5.55) into the discrete representation of the electric current density vector (5.50) yields}$^{\mathrm{qtd.}}_{[76]}$

$$\Delta\boldsymbol{j}_0 \approx \underbrace{\frac{1}{v}\sum_{i=1}^{\mathrm{n_{pn}}}\sum_{j=1}^{\mathrm{n_{pn}}} {}^{(i)}\boldsymbol{y} \otimes {}^{(ij)}\widehat{\mathbf{K}}^{\phi\boldsymbol{u}} \otimes {}^{(j)}\boldsymbol{y}}_{=\dfrac{\mathrm{d}\boldsymbol{j}_0}{\mathrm{d}\boldsymbol{\varepsilon}_0}} : \Delta\boldsymbol{\varepsilon}_0 \underbrace{-\frac{1}{v}\sum_{i=1}^{\mathrm{n_{pn}}}\sum_{j=1}^{\mathrm{n_{pn}}} {}^{(ij)}\widehat{\mathbf{K}}^{\phi\phi(i)}\boldsymbol{y} \otimes {}^{(j)}\boldsymbol{y}}_{=\dfrac{\mathrm{d}\boldsymbol{j}_0}{\mathrm{d}\boldsymbol{e}_0}} \cdot \Delta\boldsymbol{e}_0 \,. \tag{5.57}$$

5.4 Representative simulation results

$^{\mathrm{qtd.}}_{[76]}\{$This section deals with a study of representative boundary value problems. Constitutive relations that are employed in the current work for the bulk and interface are discussed in Section 5.4.1. In particular, the electrical and mechanical material models are adopted from [98] for demonstration purposes. An analytical solution for the effective conductivity in a (quasi-) one-dimensional setting is provided in Section 5.4.2. Various microstructures are studied and the effective macroscopic conductivity tensors are obtained and compared in Section 5.4.3. Moreover, the internal length scale is discussed in Section 5.4.4 and the coupled electro-mechanical response due to mechanically-induced microscale damage processes is exemplarily studied in Section 5.4.5. The specific material parameters are summarised in Table 5.1, a plane strain setting is assumed, and quadrilateral bulk and linear interface elements are used.$\}^{\mathrm{qtd.}}_{[76]}$

Table 5.1: Material parameters used in the analytical solution and finite element-based simulations.

E, $\widetilde{E}$	$210\,000\,\mathrm{N/mm^2}$	$210\,000\,\mathrm{N/mm^3}$
ν	0.3	-
κ, $\widetilde{\kappa}$	$1450\,\mathrm{A/[Vmm]}$	$1450\,\mathrm{A/[Vmm^2]}$
Q_0	-	$500\,\mathrm{N/mm^2}$
G_F	-	$200\,\mathrm{N/mm}$

5.4.1 Constitutive relations

The mechanical response of the bulk material is assumed to be governed by the volume specific Helmholtz free energy density function

$$\rho\,\psi = \Psi\left(\boldsymbol{\varepsilon}\right) = \frac{K}{2}\,\mathrm{tr}^2\left(\boldsymbol{\varepsilon}\right) + G\,\boldsymbol{\varepsilon}_\mathrm{dev} : \boldsymbol{\varepsilon}_\mathrm{dev}\,. \tag{5.58}$$

In (5.58), $\boldsymbol{\varepsilon}_\mathrm{dev}$ is the deviatoric part of the strain tensor, $K = \frac{E}{3[1-2\,\nu]}$ is the bulk modulus and $G = \frac{E}{2[1+\nu]}$ is the shear modulus. Evaluation of the constitutive equation (5.18) for the volume specific Helmholtz free energy density (5.58) results in

$$\boldsymbol{\sigma} = \frac{\partial \Psi}{\partial \boldsymbol{\varepsilon}} = K\,\mathrm{tr}\left(\boldsymbol{\varepsilon}\right)\,\boldsymbol{I} + 2\,G\,\boldsymbol{\varepsilon}_\mathrm{dev}\,. \tag{5.59}$$

qtd. [76]{The interface incorporates a model that accounts for brittle damage, along with a linear-elastic material response. More specifically speaking, the area-specific interface Helmholtz free energy density is taken as a function of displacement jump $[\![\boldsymbol{u}]\!]$ and interface damage variable $\widetilde{d}$. The mechanical response at the interface is assumed to show different behaviour patterns under tensile and compressive loadings. The interface elastic stiffness $\widetilde{E}$ is assumed to reduce due to damage evolution in the tensile region ($[\![\boldsymbol{u}]\!] \cdot \widetilde{\boldsymbol{n}} > 0$)

$$\widetilde{\rho}\,\widetilde{\psi} = \widetilde{\Psi}\left([\![\boldsymbol{u}]\!], \widetilde{d}\right) = \frac{1}{2}\,\left[1-\widetilde{d}\right]\,\widetilde{E}\,[\![\boldsymbol{u}]\!] \cdot \boldsymbol{I} \cdot [\![\boldsymbol{u}]\!]\,, \tag{5.60a}$$

whereas the interface is assumed to regain its normal stiffness under compressive loadings ($[\![\boldsymbol{u}]\!] \cdot \widetilde{\boldsymbol{n}} \leq 0$)

$$\begin{aligned}\widetilde{\rho}\,\widetilde{\psi} = \widetilde{\Psi}\left([\![\boldsymbol{u}]\!], \widetilde{d}\right) = \frac{1}{2}\widetilde{E}\,[\![\boldsymbol{u}]\!] \cdot \left[1-\widetilde{d}\right]\,[\boldsymbol{I} - \widetilde{\boldsymbol{n}} \otimes \widetilde{\boldsymbol{n}}] \cdot [\![\boldsymbol{u}]\!] \\ + \frac{1}{2}\widetilde{E}\,[\![\boldsymbol{u}]\!] \cdot \widetilde{\boldsymbol{n}} \otimes \widetilde{\boldsymbol{n}} \cdot [\![\boldsymbol{u}]\!]\,.\end{aligned} \tag{5.60b}$$

The corresponding traction-separation law at the interface

$$\{\!\{\widetilde{\boldsymbol{t}}\}\!\} = \frac{\partial \widetilde{\Psi}}{\partial [\![\boldsymbol{u}]\!]} = \begin{cases} \left[1-\widetilde{d}\right]\,\widetilde{E}\,[\![\boldsymbol{u}]\!] & \text{if } [\![\boldsymbol{u}]\!] \cdot \widetilde{\boldsymbol{n}} > 0 \\ \widetilde{E}\,\left[\left[1-\widetilde{d}\right]\,\boldsymbol{I} + \widetilde{d}\,\widetilde{\boldsymbol{n}} \otimes \widetilde{\boldsymbol{n}}\right] \cdot [\![\boldsymbol{u}]\!] & \text{if } [\![\boldsymbol{u}]\!] \cdot \widetilde{\boldsymbol{n}} \leq 0 \end{cases} \tag{5.61}$$

is derived by evaluating (5.18) for (5.60). For the damage evolution, an exponential form of the interface damage variable

$$\widetilde{d} = 1 - \frac{\chi_0}{\chi} \exp\left(- \left[\chi - \chi_0\right] \frac{\widetilde{E}\,\chi_0}{G_{\mathrm{F}} - \frac{1}{2}\,\widetilde{E}\,\chi_0^2} \right) \tag{5.62}$$

is assumed as proposed in [78, 149], where G_{F}, χ and χ_0 are the fracture energy, a displacement jump-type internal variable and the critical interface opening, respectively. In (5.62), χ_0 is interpreted as the critical interface opening, which is related to the initial fracture strength, namely

$$Q_0 = \widetilde{E}\,\chi_0\,. \tag{5.63}$$

Moreover, variable χ at time t^* is defined as

$$\chi = \max\left\{ \max_{0<t\leq t^*} \left\{ \operatorname{sgn}\left([\![\boldsymbol{u}]\!] \cdot \widetilde{\boldsymbol{n}} \right) \, \| [\![\boldsymbol{u}]\!] \| \right\} \, , \, \chi_0 \right\} . \tag{5.64}$$

For the electrical subproblem, a linear relation between the electric field vector and the electric current density vector in the bulk is adopted in accordance with the restrictions posed by the dissipation inequality (5.19), i.e.

$$\boldsymbol{j} = \boldsymbol{\mathcal{S}} \cdot \boldsymbol{e}\,. \tag{5.65}$$

For the sake of simplicity, an isotropic electrical conductivity tensor is assumed

$$\boldsymbol{\mathcal{S}} = \kappa\,\boldsymbol{I}\,, \tag{5.66}$$

where κ denotes a scalar-valued electrical conductivity parameter. Similar to the bulk, a linear relation between the jump of the electric potential and the mean value of the electric current is considered at the interface. The electrical conductivity is assumed to be influenced by damage evolution at the interface. To this end, a $\left[1 - \widetilde{d}\right]$ formulation is employed as

$$\{\!\{\widetilde{i}\}\!\} = \begin{cases} -\left[1 - \widetilde{d}\right] \widetilde{\kappa}\, [\![\phi]\!] & \text{if } [\![\boldsymbol{u}]\!] \cdot \widetilde{\boldsymbol{n}} > 0 \\ -\widetilde{\kappa}\, [\![\phi]\!] & \text{if } [\![\boldsymbol{u}]\!] \cdot \widetilde{\boldsymbol{n}} \leq 0 \end{cases} , \tag{5.67}$$

where $\widetilde{\kappa}$ denotes the idealised conductivity of the interface.$\}^{\text{qtd.}}_{[76]}$

5.4.2 Analytical solution

$^{\text{qtd.}}_{[76]}\{$This section deals with the derivation of a (quasi-)one-dimensional analytical solution for the calculation of the effective conductivity of a representative volume element with a material interface, see Figure 5.3. For the electrical problem under periodic

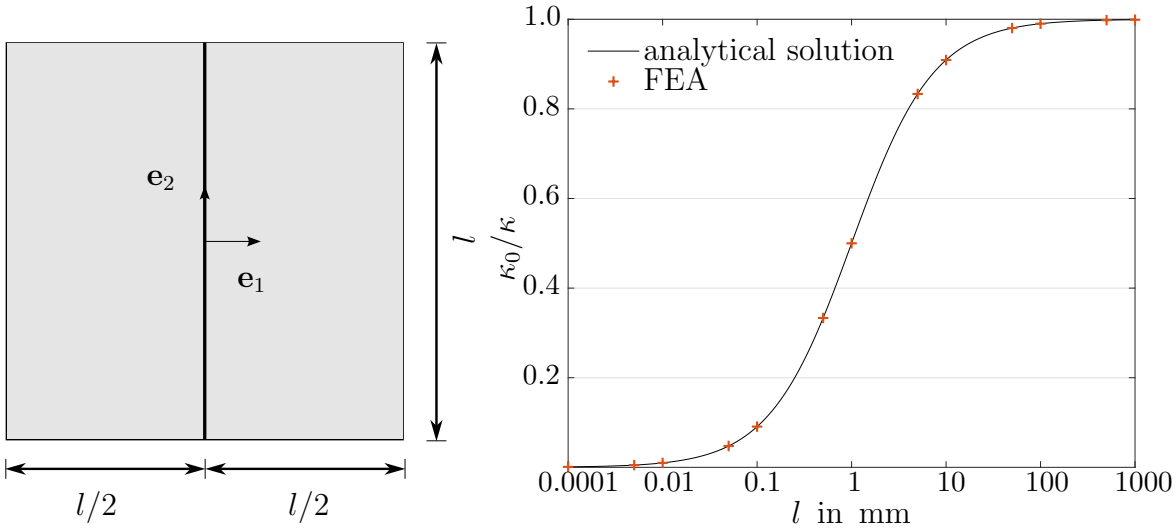

Figure 5.3: RVE of length l and cross-sectional area $A = l \times 1.0\text{mm}$, subjected to periodic electrical boundary conditions. A material interface crossing the boundary is placed at the middle of the unit cell. The boundary conditions are applied in macroscopic problem such that $\Delta\phi$ is parallel to $\mathbf{e}_1$ for RVE. Dimensions are given in mm. Reproduced from [76] under the terms of the Creative Commons Attribution License (CC BY).

boundary conditions with a prescribed electric potential difference $\overline{\Delta\phi}$, electric current density $j = \|\boldsymbol{j}\|$ can be calculated as

$$j = \left[\frac{l/2}{\kappa} + \frac{1}{\widetilde{\kappa}} + \frac{l/2}{\kappa}\right]^{-1} \overline{\Delta\phi} \tag{5.68}$$

using elementary calculation rules for serially connected resistors in electrical circuits. Accordingly, the effective conductivity of the (quasi-)one-dimensional RVE in the direction of $\mathbf{e}_1$, i.e. $\kappa^* = \mathbf{e}_1 \cdot \boldsymbol{\mathcal{S}}^* \cdot \mathbf{e}_1$, reads

$$\kappa_0 = \left[\frac{l}{\kappa} + \frac{1}{\widetilde{\kappa}}\right]^{-1} l\,. \tag{5.69}$$

Comparing the analytical (5.69) and finite element simulation (5.57) results verifies the proposed finite element framework. Moreover, the simulation results shown in Figure 5.3 clearly indicate a size-dependent macroscale material response due to the presence of material interfaces at the microscale. This size effect will be studied in detail in Section 5.4.4.}$^{\text{qtd.}}_{[76]}$

5.4.3 Effective macropscopic conductivity tensor

$^{\text{qtd.}}_{[76]}${The objective of this section is to demonstrate the use of the proposed electro-mechanical multiscale formulation within a two-dimensional setting. Therefore, effective macroscopic conductivity tensors are calculated for the different periodic microstructures

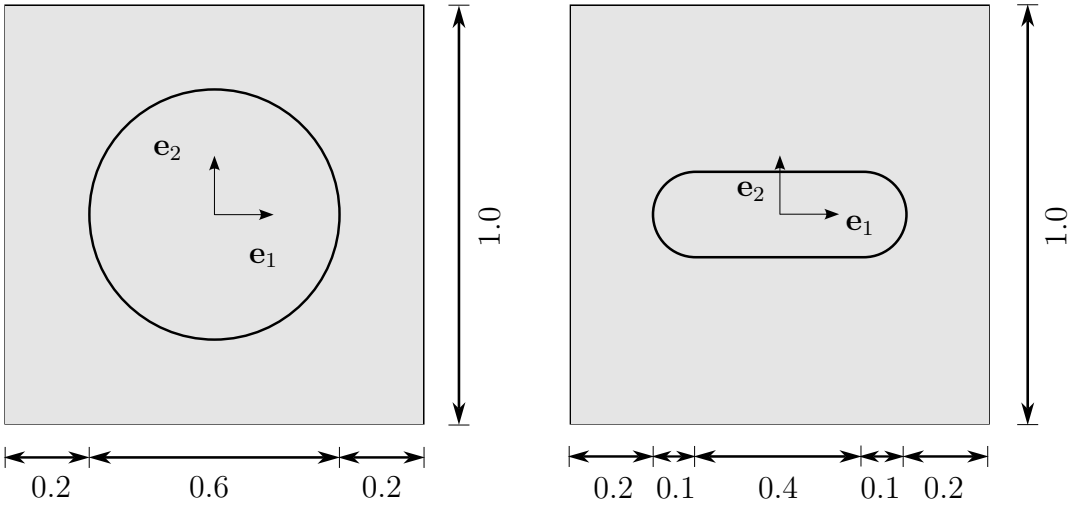

Figure 5.4: Sketch of different two-dimensional RVEs that are analysed with the electro-mechanical multiscale finite element formulation. The microstructures were chosen in accordance with [100]. Dimensions are given in mm. Reprinted from [76] under the terms of the Creative Commons Attribution License (CC BY).

depicted in Figure 5.4. The results are normalised with respect to the idealised material parameters given in Table 5.1, i.e.

$$[\boldsymbol{\mathcal{S}}^*]^{\text{mat}}_{\mathbf{e}_{1,2}} = \begin{bmatrix} 1.0000 & 0 \\ 0 & 1.0000 \end{bmatrix} \kappa \tag{5.70a}$$

$$[\boldsymbol{\mathcal{S}}^*]^{\text{cir}}_{\mathbf{e}_{1,2}} = \begin{bmatrix} 0.7000 & 0 \\ 0 & 0.7000 \end{bmatrix} \kappa \tag{5.70b}$$

$$[\boldsymbol{\mathcal{S}}^*]^{\text{gro}}_{\mathbf{e}_{1,2}} = \begin{bmatrix} 0.9096 & 0 \\ 0 & 0.7322 \end{bmatrix} \kappa \tag{5.70c}$$

The effective macroscopic conductivity tensors corresponding to microstructures with circular (5.70b) and groove-shaped interfaces (5.70c) are compared with the conductivity tensor of an idealised material (5.70a). The presence of the circular cohesive interface causes a reduction in conductivity of approximately 30%. In accordance with theoretical predictions, the constitutive response remains isotropic. In comparison, the reduction in the 22-coefficient of the conductivity tensor caused by the the presence of a groove-shaped interface is significantly higher than the reduction in the 11-coefficient such that the effective macroscopic material response is anisotropic.$\}^{\text{qtd.}}_{[76]}$

5.4.4 Internal length scale

$^{\text{qtd.}}_{[76]}\{$Classic first-order multiscale formulations do not account for size-dependent material behaviour. In other words, the macroscopic response does not change with respect to the

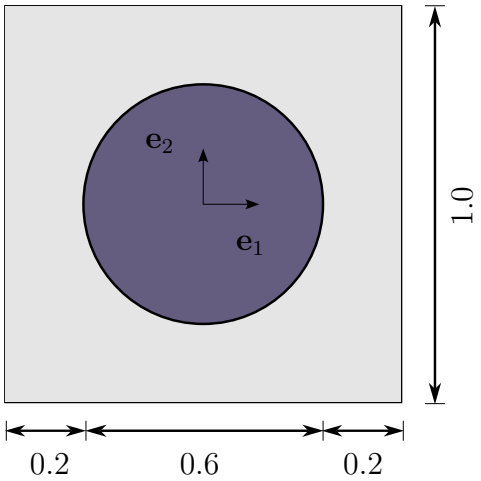

Figure 5.5: Sketch of two-dimensional multi-phase microstructure analysed with the electro-mechanical multiscale finite element formulation. The conductivity of the matrix (indicated by grey colour) and the interface between inclusion and matrix are given in Table 5.1. The conductivity of the inclusion (indicated by green colour) is chosen as $\kappa_{\text{inc}} = 0.1\kappa$. Dimensions are given in mm. Reproduced from [76] under the terms of the Creative Commons Attribution License (CC BY).

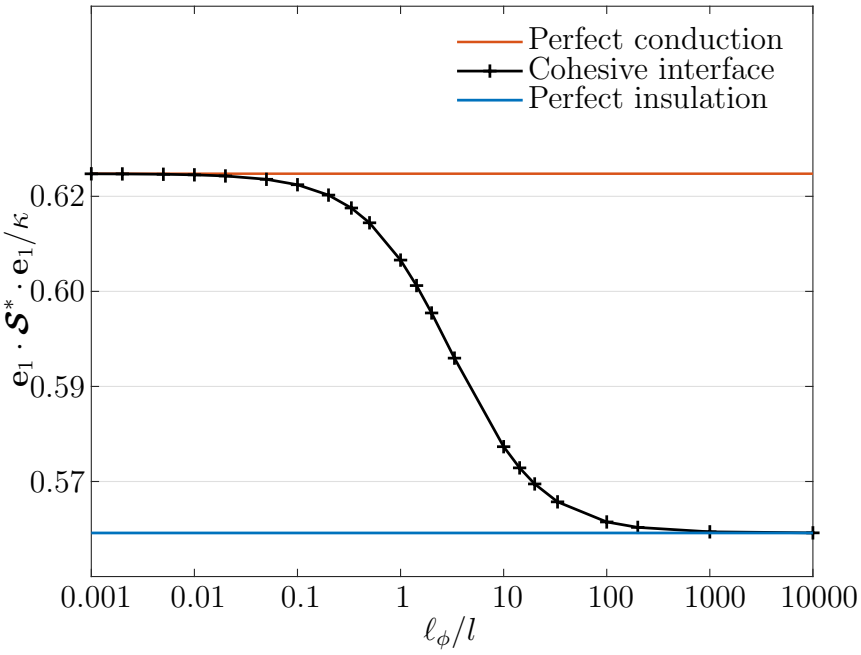

Figure 5.6: Effective macroscopic conductivity of the multi-phase RVE depicted in Figure 5.5. A size-dependent behaviour is observed with limit cases corresponding to a perfect conduction interface and a perfect insulation. Reproduced from [76] under the terms of the Creative Commons Attribution License (CC BY).

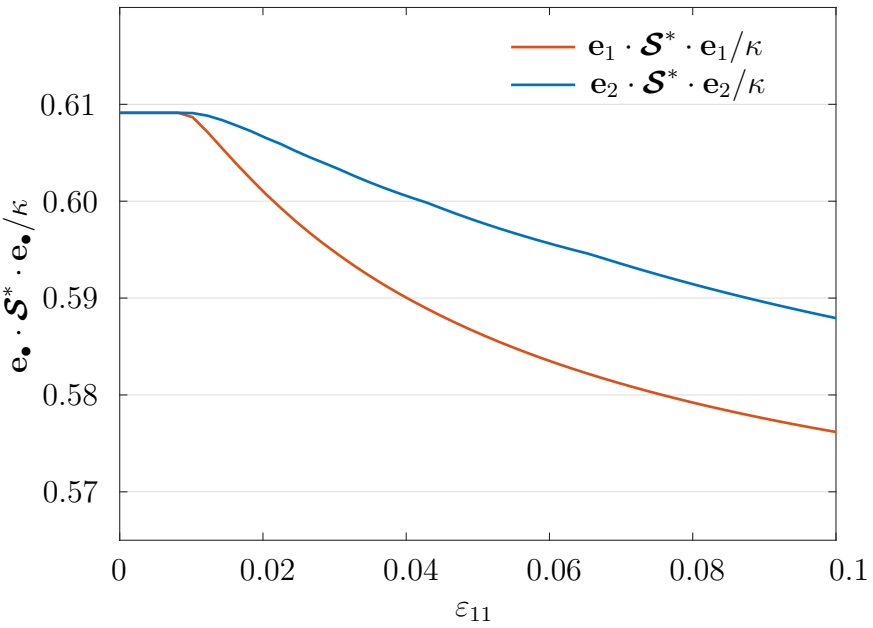

Figure 5.7: Effective conductivity as a function of prescribed mechanical boundary conditions. Reproduced from [76] under the terms of the Creative Commons Attribution License (CC BY).

RVE size. To solve this problem, second-order homogenisation methods that incorporate higher-order gradients are developed, see for instance [107]. On the other hand, it was observed in Section 5.4.2 that by accounting for material interfaces at the microscale, the continuum under consideration is endowed with an internal length scale such that size-effects can naturally be accounted for. In accordance with [98], the internal length scale of the electrical subproblem is introduced as

$$\ell_\phi = \frac{\kappa}{\approx \kappa}\,. \tag{5.71}$$

The ratio of the internal length scale to the RVE size l is the length scale ratio ℓ_ϕ/l. By changing the length scale ratio (e.g. fixing the RVE size, $l = 1.0\,\mathrm{mm}$, while varying the internal length scale) the size-effect induced by the presence of material interfaces can be studied. The matrix-inclusion problem with a cohesive interface shown in Figure 5.5 is exemplarily analysed, and the material response for various length scale ratios is depicted in Figure 5.6. The upper limit corresponds to the perfectly conducting RVE, with the effect of the interface being negligible. The lower limit, on the other hand, corresponds to the case of a pore, i.e. the material interface electrically insulates the inclusion.$\}^{\text{qtd.}}_{[76]}$

5.4.5 Electro-mechanical coupling

$^{\text{qtd.}}_{[76]}\{$This section focuses on the change in the effective macroscopic conductivity tensor due to mechanically-induced damage processes at the microscale. An inclusion with low conduction embedded in high conductor matrix is selected for this example. The material parameters $E_{\text{inc}} = 210\,000\,\mathrm{N/mm^2}$, $\nu_{\text{inc}} = 0.3$ and $\kappa_{\text{inc}} = 145\,\mathrm{A/[Vmm]}$ govern the constitutive response of the inclusion and the material parameters of the matrix

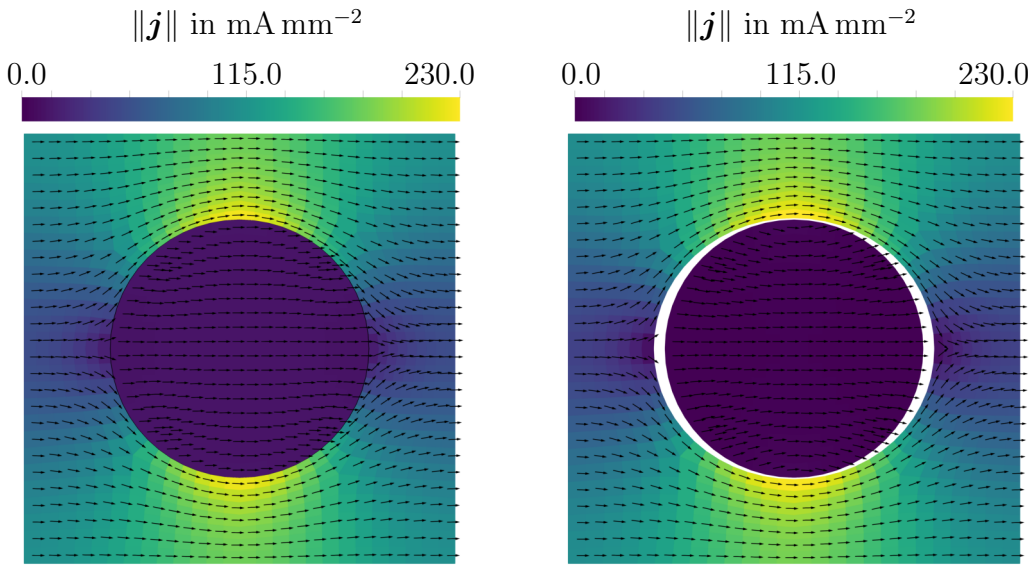

Figure 5.8: Electric current density field $\|\boldsymbol{j}\|$ of the microstructure depicted in Figure 5.5 under given loading conditions for $\beta = 0.1\,\mathrm{mV}$. Left: Damage evolution is not initiated ($\alpha = 0.002$). Right: Deformation-induced damage evolution at the interface leads to a decrease in the effective conductivity ($\alpha = 0.05$). Electric current density vectors are indicated by black arrows. Reproduced from [76] under the terms of the Creative Commons Attribution License (CC BY).

and the interface parameters being chosen according to Table 5.1. In view (5.67), the electrical and mechanical subproblems are coupled at the interface by means of damage variable $\widetilde{d}$. The RVE is loaded mechanically by

$$\boldsymbol{\varepsilon}_0 = \alpha(t)\,\mathbf{e}_1 \otimes \mathbf{e}_1 \tag{5.72a}$$

and electrically via

$$\boldsymbol{e}_0 = \beta\,(t)\;\mathbf{e}_1 \tag{5.72b}$$

with parameters $\alpha\,(t)$ and $\beta\,(t)$ controlling the monotonic load history as a function of time t.

The decrease in the $\boldsymbol{\mathcal{S}}^*_{11}$ and $\boldsymbol{\mathcal{S}}^*_{22}$ coefficients of the effective macroscopic conductivity tensor as a function of deformation in terms of the prescribed macroscale strain $\boldsymbol{\varepsilon}_0$ is shown in Figure 5.7. The obtained values are normalised with respect to the conductivity of the matrix. A constant conductivity in $\mathbf{e}_1-$ and $\mathbf{e}_2-$ direction is observed up to the onset of damage evolution, i.e. for $\alpha \lesssim 0.01$. The initial conductivity is reduced due to the inclusion with comparatively low conduction as well as the resistance of the cohesive interface. After damage evolution starts, a significantly different decrease of the electrical conductivity in the two spatial directions is observed. The norm of electric current density field $\|\boldsymbol{j}\| = \sqrt{\boldsymbol{j}\cdot\boldsymbol{j}}$ for different load cases is additionally illustrated in Figure 5.8 on the deformed configuration. With the displacement jump at the interface being closely related to the damage evolution at the interface and, accordingly, to the degradation of electrical properties, Figure 5.7 clearly reveals the cause of the deformation-induced anisotropy.$\}^{\text{qtd.}}_{[76]}$

6 Computational homogenisation with interfaces: Electrical problem

---

$^{\text{qtd.}}_{[71]}\{$Grain boundaries are one of the major resistive defects in fine-grained crystalline materials [13, 24, 57]. The quantification of grain boundary resistivity in metals has been extensively discussed for decades mainly employing the Andrews method [6] and the Mayadas-Shatkez model [128]. Despite the capabilities of the two models of predicting the electrical resistivities of materials, their validity has been questioned on several occasions [10, 125, 136]. In the light of the partial disagreement in the grain boundary resistivity values obtained by the Andrews method and direct (local) measurements as exemplified in Table 6.1, the objective of this chapter is to revisit the applicability of the Andrews method from a multiscale perspective, i.e. by employing a novel computational homogenisation approach that explicitly accounts for grain boundaries at the microscale, as discussed in Chapter 5.$\}^{\text{qtd.}}_{[71]}$

In view of the limitations of classical models and the potential of multiscale approaches, the scope of the present chapter is twofold:

- *We revisit the classical Andrews method for grain boundary resistivity and reinterpret it through the lens of computational homogenisation, highlighting its assumptions and systematically comparing it to analytical and numerical benchmarks.*

- *We develop and apply a multiscale finite element framework to resolve grain boundary effects in both synthetic and statistically representative polycrystalline microstructures, enabling the derivation of scaling laws and validation against experimental observations.*

The computational multiscale approach towards microstructures featuring cohesive-type material interfaces is briefly summarised in Section 6.1. With the fundamental set of balance equations at hand, a weak form of the problem is derived and a finite element implementation is summarised in Section 6.2. Based on these developments, one-dimensional analytical expressions are derived and compared to the Andrews method in Section 6.3.1. The comparison is extended to two-dimensional structures with particular focus lying on material anisotropies (Section 6.3.2) and primitive isotropic structures (Section 6.3.3). Scaling laws are derived in Section 6.4 before the analysis is eventually extended to a polycrystalline setting in Section 6.5. Finally, Section 6.6 discusses the Mosaic code developed to obtain periodic polycrystal unit cells.

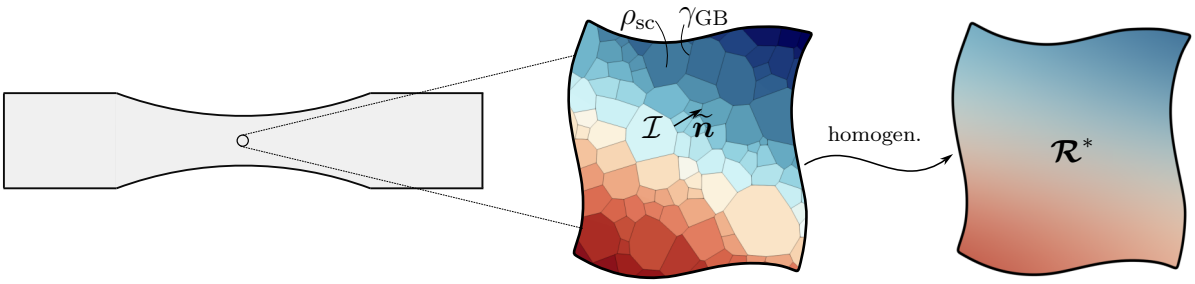

Figure 6.1: Effective (macroscale) material response as calculated from the underlying material microstructure and lower-scale physics in computational multiscale methods. At each macroscale material point, a representative volume element (RVE) is considered which characterises the material microstructure. Reprinted from [71] under the terms of the Creative Commons Attribution License (CC BY).

qtd. [71] {In the Andrews method, the effective resistivity of metals

$$\rho^* = \rho_{sc} + \rho_{GB} \tag{6.1}$$

is approximated as the sum of the single crystal resistivity ρ_{sc} and the accumulated grain boundary resistivity

$$\rho_{GB} = \gamma_{GB} \frac{S_{GB}}{V} = \gamma_{GB}\, k_{GB} \frac{1}{d} = \frac{A}{d}\,, \tag{6.2}$$

with three different representations being established. The first representation is based on the specific grain boundary resistivity γ_{GB} and the grain boundary area S_{GB} per volume V. The second representation results from introducing the geometric proportionality coefficient k_{GB} that relates the grain boundary surface area fraction to the (inverse of the) average grain diameter d. Thirdly, by combining the proportionality coefficient k_{GB} and the specific grain boundary resistivity γ_{GB} one arrives at the representation in terms of the Andrews parameter A, [10]. Relation (6.2) is based on two main factors that determine the grain boundary contribution to the effective resistivity: the specific grain boundary resistivity and the microscale morphology (grain boundary density and alignment). In view of the global nature of (6.2), it is first noted that the contributions of multiple, possibly different types of grain boundaries are accounted for in ρ_{GB} in a cumulative way. This is crucial since it can be deduced from direct grain boundary resistivity measurements that γ_{GB} may take significantly different values in the same material depending on the particular structure of the considered grain boundary, as exemplified for pure Cu in Table 6.1 and studied in detail in [6, 10, 23, 104, 119, 125]. Thus, the particular value for γ_{GB} calculated via (6.2) is to be interpreted as a mean value in case several GB contribute to the measurement. Secondly, γ_{GB} is calculated based on ρ_{GB} under a specific geometric assumption that enters the formulation in the form of k_{GB}. An in-depth study on the validity of this assumption by making use of computational multiscale techniques is the main objective of the present chapter.} qtd. [71]

Table 6.1: Experimentally determined grain boundary resistivity γ_{GB} in pure Cu determined by means of direct local measurements [23, 104] (for [111] tilt boundaries) and global measurements [6, 7, 119, 125].

Global measurements	Local measurements
$3.12\,\mathrm{p\Omega cm^2}$	$19.0\,\mathrm{p\Omega cm^2}$ for $50.72°$
$3.58\,\mathrm{p\Omega cm^2}$	$23.3\,\mathrm{p\Omega cm^2}$ for $45.89°$
$3.60\,\mathrm{p\Omega cm^2}$	$25.9\,\mathrm{p\Omega cm^2}$ for $48.67°$
$4.18\,\mathrm{p\Omega cm^2}$	$39.0\,\mathrm{p\Omega cm^2}$ for $48.68°$
	$39.0\,\mathrm{p\Omega cm^2}$ for $46.45°$
	$9.9\,\mathrm{p\Omega cm^2}$ for $45.5°$
	$10.2\,\mathrm{p\Omega cm^2}$ for $44.4°$
	$10.4\,\mathrm{p\Omega cm^2}$ for $43.7°$
	$12.8\,\mathrm{p\Omega cm^2}$ for $45.6°$
	$14.5\,\mathrm{p\Omega cm^2}$ for $47.5°$

6.1 Computational multiscale formulation

qtd. [71]{To calculate homogenised material properties for microstructures with resistive material interfaces, a computational multiscale formulation was proposed in [76]. In this formulation, the constitutive relations at the microscale are assumed to be known and the objective is to compute the macroscopic response through homogenising the response of the underlying microstructure. In doing so, the proposed multiscale formulation relates the description of physical processes at different length scales as schematically shown in Figure 6.1, while ensuring energy consistency. Material models developed for the individual microscale constituents together with appropriate representations of the microstructure make it possible to obtain the effective (macroscale) response, e.g., in the form of effective resistivity tensors $\boldsymbol{\mathcal{R}}^* : \Omega \to \mathrm{Lin}\left(\mathbb{R}^d, \mathbb{R}^d\right)$

$$\{\rho_{\mathrm{sc}}, \gamma_{\mathrm{GB}}, \mathrm{morphology}\} \quad \overset{\text{homogenisation}}{\longrightarrow} \quad \boldsymbol{\mathcal{R}}^* \,. \tag{6.3}$$

For a macroscopically (quasi-)isotropic setting the effective resistivity tensor takes the form $\boldsymbol{\mathcal{R}}^* = \rho^* \boldsymbol{I}$, with $\boldsymbol{I}$ denoting the second-order identity tensor, and accordingly reduces to the scalar-valued resistivity measure $\rho^* : \Omega \to \mathbb{R}$ that occurs in (6.1).

To obtain the effective response for quasi-stationary electrical processes, the microscale field problem

$$\nabla_y \cdot \boldsymbol{j}\,(\boldsymbol{y}) = 0 \quad (\text{in the bulk})\,, \tag{6.4a}$$

$$[\![\widetilde{i}]\!]\,(\tilde{\boldsymbol{y}}) = 0 \quad (\text{at the interface})\,, \tag{6.4b}$$

is solved. In the continuity equation (6.4), $\boldsymbol{j} : Y \to \mathbb{R}^d$ and $\widetilde{i} : \mathcal{I} \to \mathbb{R}$ represent the electric current density vector in the bulk and the electric current density across the interface, $\mathcal{I} \subset Y$, respectively. Equation (6.4b) arises due to the presence of resistive grain boundaries that are modelled as zero-thickness cohesive-type interfaces at the

microscale. More specifically speaking, this equation implies that the normal jump of the current density vector at the interface vanishes, namely

$$[\![\widetilde{i}]\!]\,(\tilde{\boldsymbol{y}}) = \widetilde{i}^{+}\left(\boldsymbol{y}^{+}\right) - \widetilde{i}^{-}(\tilde{\boldsymbol{y}})\ ,\ \widetilde{i}^{+}(\tilde{\boldsymbol{y}}) = \boldsymbol{j}^{+}\left(\boldsymbol{y}^{+}\right)\cdot\widetilde{\boldsymbol{n}}\left(\boldsymbol{y}^{-}\right) \text{ and } \widetilde{i}^{-}(\tilde{\boldsymbol{y}}) = \boldsymbol{j}^{-}\left(\boldsymbol{y}^{+}\right)\cdot\widetilde{\boldsymbol{n}}\,(\tilde{\boldsymbol{y}})\ . \tag{6.5}$$

In this problem setting, $+$ and $-$ indicate the two opposing sides of interface $\mathcal{I} : \mathbb{R}^{(d-1)} \subset Y$ with the interface unit normal $\widetilde{\boldsymbol{n}} : \mathcal{I} \to \mathbb{R}^{d}$ pointing from the $-$ side to the $+$ side.

In view of (general) solutions of the set of balance equations (6.4) constitutive relations for the individual phases at the microscale are specified. The linear relation

$$\boldsymbol{j}\,(\boldsymbol{y}) = \boldsymbol{\mathcal{R}}_{\mathrm{sc}}^{-1}\,(\boldsymbol{y})\cdot\boldsymbol{e}\,(\boldsymbol{y}) \quad , \quad \boldsymbol{\mathcal{R}}_{\mathrm{sc}}\,(\boldsymbol{y}) = \rho_{\mathrm{sc}}\,(\boldsymbol{y})\ \boldsymbol{I} \tag{6.6}$$

between the electric current density vector and electric field vector $\boldsymbol{e}$ is adopted in the bulk. For the sake of simplicity and without loss of generality, the resistivity tensor of the single crystal $\boldsymbol{\mathcal{R}}_{\mathrm{sc}}$ is assumed to be isotropic and constant. Furthermore, the cohesive-type interface is assumed to act like a resistor, resulting in the definition of the interface current density

$$\widetilde{i}\,(\tilde{\boldsymbol{y}}) = -\,\gamma_{\mathrm{GB}}^{-1}\,(\tilde{\boldsymbol{y}})\ [\![\phi]\!]\,(\tilde{\boldsymbol{y}}) \quad \text{with} \quad [\![\phi]\!]\,(\tilde{\boldsymbol{y}}) = \phi^{+}\left(\boldsymbol{y}^{+}\right) - \phi^{-}\left(\boldsymbol{y}^{-}\right) \tag{6.7}$$

based on the (inverse of the) specific grain boundary resistivity and the jump in electric potential across the interfaces.}$^{\text{qtd.}}_{[71]}$

6.2 Finite element implementation

Since this study focuses exclusively on the electrical subproblem, the finite-element implementation introduced in Section 4.5 reduces to the uncoupled electrical formulation given below.

6.2.1 Weak form of the electrical problem

To derive the weak form of the microscale electrical problem, (6.4a) is multiplied by a test function $\varphi^{\phi} \in H^{1}\,(Y)$ and integrated over domain $Y = Y^{+} \cup Y^{-}$

$$\int_{Y^{+}} \nabla_{y}\cdot\boldsymbol{j}\,(\boldsymbol{y})\,\varphi^{\phi}\,(\boldsymbol{y})\,\mathrm{d}y + \int_{Y^{-}} \nabla_{y}\cdot\boldsymbol{j}\,(\boldsymbol{y})\,\varphi^{\phi}\,(\boldsymbol{y})\,\mathrm{d}y = 0\,, \tag{6.8}$$

and application of the divergence theorem with the identity $[\![\bullet *]\!] = [\![\bullet]\!]\,\{\!\{*\}\!\} + \{\!\{\bullet\}\!\}\,[\![*]\!]$

$$\begin{aligned} -\int_{Y^{+}\cup Y^{-}} \nabla_{y}\varphi^{\phi}\,(\boldsymbol{y})\cdot\boldsymbol{j}\,(\boldsymbol{y})\,\mathrm{d}y + \int_{\partial Y} \varphi^{\phi}\,(\boldsymbol{y})\,\boldsymbol{j}\,(\boldsymbol{y})\cdot\boldsymbol{n}\,(\boldsymbol{y})\,\mathrm{d}y \\ - \int_{\mathcal{I}} [\![\varphi^{\phi}]\!]\,(\tilde{\boldsymbol{y}})\,\{\!\{\widetilde{i}\}\!\}\,(\tilde{\boldsymbol{y}}) + \{\!\{\varphi^{\phi}\}\!\}\,(\tilde{\boldsymbol{y}})\,[\![\widetilde{i}]\!]\,(\tilde{\boldsymbol{y}})\,\mathrm{d}y = 0 \end{aligned} \tag{6.9}$$

specifies, in virtue of (6.4b), the weak form reads

Find $\phi \in H^1(Y^+) \times H^1(Y^-)$ such that

$$-\int_Y \nabla_y \varphi^\phi(\boldsymbol{y}) \cdot \boldsymbol{j}(\boldsymbol{y}) \,\mathrm{d}y = -\int_{\partial Y} \varphi^\phi(\boldsymbol{y})\, \boldsymbol{j}(\boldsymbol{y}) \cdot \boldsymbol{n}(\boldsymbol{y}) \,\mathrm{d}y + \int_{\mathcal{I}} [\![\varphi^\phi]\!](\tilde{\boldsymbol{y}}) \, \{\!\{\widetilde{i}\}\!\}(\tilde{\boldsymbol{y}}) \,\mathrm{d}y \tag{6.10}$$

for all $\varphi^\phi \in \Phi = \{\varphi^\phi \in H^1(Y^+) \times H^1(Y^-) : \varphi^\phi = 0 \text{ on } \partial Y^\phi\}$.

6.2.2 Calculation of macroscopic electric current density vector

Macroscopic quantities are obtained via volume averaging after solving the microscale boundary value problems. The discrete version of the macroscopic electric current density vector is given by

$$\boldsymbol{j}_0(\boldsymbol{x}) = \frac{1}{v}\int_{\partial Y} \boldsymbol{y}\, i(\boldsymbol{y}) \,\mathrm{d}y \approx \frac{1}{v}\sum_{i=1}^{\mathrm{n_{pn}}} {}^{(i)}f^{\phi}\, {}^{(i)}\boldsymbol{y}\,, \tag{6.11}$$

with the definition of $v = \mathrm{vol}(Y)$ in hand.

6.2.3 Calculation of the macroscopic tangent contribution

For periodic boundary conditions, the kinematic relations are given as

$$\Delta^{(j)}\phi_{\mathrm{d}} = -\Delta \boldsymbol{e}_0 \cdot {}^{(j)}\boldsymbol{y} \tag{6.12}$$

and the discrete representation of generalised reaction force vector

$$\Delta^{(i)}f^{\phi} = -\sum_{j=1}^{\mathrm{n_{pn}}} {}^{(ij)}\widehat{\mathbf{K}}^{\phi\phi} \otimes \Delta \boldsymbol{e}_0 \cdot {}^{(j)}\boldsymbol{y} \tag{6.13}$$

is derived. Furthermore, the discrete representation of the change in the electric current density vector yields the following equation

$$\Delta \boldsymbol{j}_0 \approx \underbrace{\left[-\frac{1}{v}\sum_{i=1}^{\mathrm{n_{pn}}}\sum_{j=1}^{\mathrm{n_{pn}}} {}^{(ij)}\widehat{\mathbf{K}}^{\phi\phi} \otimes {}^{(i)}\boldsymbol{y} \otimes {}^{(j)}\boldsymbol{y}\right]}_{=\dfrac{\mathrm{d}\boldsymbol{j}_0}{\mathrm{d}\boldsymbol{e}_0}} : \Delta \boldsymbol{e}_0\,. \tag{6.14}$$

6.3 Revisiting the Andrews method

qtd. [71]{A systematic study of the Andrews method is conducted in this section illustrating both, its capabilities and limitations by comparing the results with those obtained by

Table 6.2: Material parameters used in the analytical solution and finite element-based simulations in accordance with experiments on Cu thin films [23], with ρ_{sc} denoting the single crystal resistivity and γ_{GB} denoting the average grain boundary resistivity for high angle grain boundaries. Note that by assuming ρ_{sc} to be constant, size effects at small grain diameters that would occur due to scattering events are neglected in the proposed formulation.

ρ_{sc}	$1.69\,\mu\Omega\,\mathrm{cm}$
γ_{GB}	$10.00\,\mathrm{p}\Omega\mathrm{cm}^2$

computational homogenisation. To this end, the representative volume elements that characterise a particular microstructure are generated and discretised by means of four-node quadrilateral elements (bulk material) and four-node linear elements (interfaces). Periodic boundary conditions are assumed and material parameters are chosen in accordance with experimental findings, Table 6.2.}$^{\mathrm{qtd.}}_{[71]}$

6.3.1 Elementary one-dimensional analytical example

$^{\mathrm{qtd.}}_{[71]}${This section focuses on the derivation of an analytical solution for the one-dimensional boundary value problem depicted in Figure 6.2. The wire-like structure is subjected to electrical loading in the form of electric potential difference $\Delta\phi$. The total resistance of the wire featuring a single grain boundary is

$$\mathrm{R} = \mathrm{R}_{\mathrm{sc}} + \mathrm{R}_{\mathrm{GB}}\,, \tag{6.15}$$

with individual contributions for the single crystal

$$\mathrm{R}_{\mathrm{sc}} = \rho_{\mathrm{sc}}\,\frac{d}{S_{\mathrm{GB}}}\,, \tag{6.16a}$$

and the grain boundary

$$\mathrm{R}_{\mathrm{GB}} = \widetilde{\gamma}_{\mathrm{GB}}\,\frac{\widetilde{l}}{S_{\mathrm{GB}}} = \gamma_{\mathrm{GB}}\,\frac{1}{S_{\mathrm{GB}}}\,, \tag{6.16b}$$

respectively. The grain boundary (interface) is resolved as a finite, though infinitesimally thin, interphase ($\widetilde{l} \ll d$) in (6.16b) with specific interphase resistivity $\widetilde{\gamma}_{\mathrm{GB}}$. The effective electric current density in the wire is related to the effective electric field via the linear map

$$j = \kappa\, e = \frac{1}{\rho}\, e\,, \tag{6.17}$$

where κ and ρ are the effective conductivity and resistivity, respectively. With the definition of effective electric field $e = -\,\Delta\,\phi/d$, and by making use of classic relations for electrical resistors, one arrives at

$$j = -\,\mathrm{R}^{-1}\,S_{\mathrm{GB}}^{-1}\,\Delta\,\phi \;=\; \left[\mathrm{R}\,\frac{S_{\mathrm{GB}}}{d}\right]^{-1}\,e\,. \tag{6.18}$$

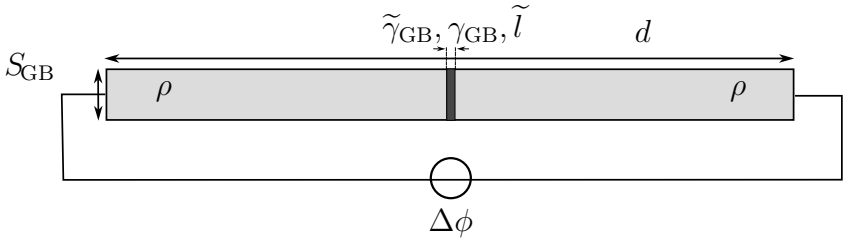

Figure 6.2: Wire-like structure of length d and cross-sectional area S_{GB}, featuring a zero-thickness material interface and being subjected to electrical loading. Reprinted from [71] under the terms of the Creative Commons Attribution License (CC BY).

Inserting the definition of the total resistance (6.15) into (6.18) yields the closed-form relation

$$j = \left[\rho_{\mathrm{sc}} + \mathrm{R}_{\mathrm{GB}} \frac{S_{\mathrm{GB}}}{d}\right]^{-1} e \tag{6.19}$$

between electric current density and electric field. The first term inside the parenthesis is the single crystal resistivity, whereas the second term is related to the material interface with the different representations

$$j = \left[\rho_{\mathrm{sc}} + \widetilde{\gamma}_{\mathrm{GB}} \frac{\widetilde{l}}{d}\right]^{-1} e \tag{6.20a}$$

$$= \left[\rho_{\mathrm{sc}} + \gamma_{\mathrm{GB}} \frac{1}{d}\right]^{-1} e \tag{6.20b}$$

$$= \left[\rho_{\mathrm{sc}} + \gamma_{\mathrm{GB}} \frac{S_{\mathrm{GB}}}{V}\right]^{-1} e\,, \tag{6.20c}$$

revealing the underlying physics in terms of intrinsic length scales $\widetilde{l}$ or the Andrews method (6.2).

The effective (macroscale) constitutive relation between the electric field and the electric current density can equivalently be expressed in terms of conductivities. While the resistivity-based representation (6.20) is commonly used in the material science community, the conductivity-based one

$$j = \left[\frac{1}{\kappa_{\mathrm{sc}}} + \frac{1}{\widetilde{\kappa}_{\mathrm{GB}}} \frac{\widetilde{l}}{d}\right]^{-1} e \tag{6.21a}$$

$$= \left[\frac{1}{\kappa_{\mathrm{sc}}} + \frac{1}{\kappa_{\mathrm{GB}}} \frac{1}{d}\right]^{-1} e \tag{6.21b}$$

$$= \left[\frac{1}{\kappa_{\mathrm{sc}}} + \frac{1}{\kappa_{\mathrm{GB}}} \frac{S_{\mathrm{GB}}}{V}\right]^{-1} e\,, \tag{6.21c}$$

is typically adopted in the computational mechanics community.

Comparing (6.1) and (6.2) with (6.20c) shows that the Andrews method is consistent with classic homogenisation in a one-dimensional setting. In particular, it is observed that:

1. In a uniaxial problem, a S_{GB}/V-scaling is recovered.

2. The S_{GB}/V-scaling in the uniaxial problem is equivalent to a proportionality coefficient $k_{\mathrm{GB}} = d\, S_{\mathrm{GB}}/V = 1.0$.

3. Andrews parameter A and specific grain boundary resistivity γ_{GB} coincide in a one-dimensional setting.$\}^{\mathrm{qtd.}}_{[71]}$

6.3.2 Primitive anisotropic setting

$^{\mathrm{qtd.}}_{[71]}\{$The Andrews method faces a notable limitation as it neglects the influence of grain alignment due to the scalar nature of S_{GB}/V. In order to study this observation, a primitive microstructure as illustrated in Figure 6.3 is examined. The effective resistivity tensors of the microstructure are calculated by means of [76, Equation (56)] and are visualised in Figure 6.4. For the grain sizes $d_{\mathrm{A}} = 0.05\,\mu\mathrm{m}$, $d_{\mathrm{B}} = 0.1\,\mu\mathrm{m}$ and $d_{\mathrm{C}} = 0.5\,\mu\mathrm{m}$, they read

$$[\boldsymbol{\mathcal{R}}^*]^{\mathrm{A}}_{\mathbf{e}_{1,2}} = \begin{bmatrix} 3.69 & 0 \\ 0 & 1.69 \end{bmatrix} \mu\Omega\,\mathrm{cm}\,, \tag{6.22a}$$

$$[\boldsymbol{\mathcal{R}}^*]^{\mathrm{B}}_{\mathbf{e}_{1,2}} = \begin{bmatrix} 2.69 & 0 \\ 0 & 1.69 \end{bmatrix} \mu\Omega\,\mathrm{cm}\,, \tag{6.22b}$$

$$[\boldsymbol{\mathcal{R}}^*]^{\mathrm{C}}_{\mathbf{e}_{1,2}} = \begin{bmatrix} 1.89 & 0 \\ 0 & 1.69 \end{bmatrix} \mu\Omega\,\mathrm{cm}\,. \tag{6.22c}$$

As expected, the set of equations (6.22) shows that the $\mathbf{e}_1$- and $\mathbf{e}_2$-direction are principal axes of the material system, since the related coefficient matrix of resistivity tensor $\boldsymbol{\mathcal{R}}^*$ takes diagonal form.

The set of resistivity tensors (6.22) as a function of grain size d shows that:

1. Care needs to be taken when applying the Andrews method to systems that do not give rise to a quasi-isotropic effective conductivity tensor (e.g. due to deformation-induced texture).

2. Strictly speaking, the Andrews method does not hold for the considered example since the 22-coefficient of the resistivity tensor takes the constant value $\mathbf{e}_2 \cdot \boldsymbol{\mathcal{R}}^* \cdot \mathbf{e}_2 = 1.69\,\mu\Omega\,\mathrm{cm}$ and is, in particular, independent of grain diameter d. This observation is in accordance with recent discussions carried out in the literature, see, e.g. [83].

3. The Andrews method is recovered for the $\mathbf{e}_1$-direction with the problem at hand reducing to the (quasi-)one-dimensional setting discussed in Section 6.3.1.$\}^{\mathrm{qtd.}}_{[71]}$

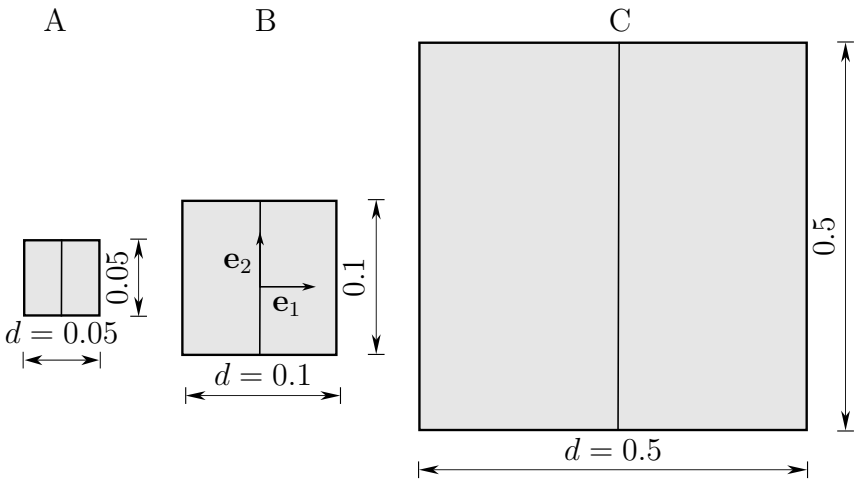

Figure 6.3: Microstructure with different grain sizes d and cross sectional areas $S_{\mathrm{GB}} = d \times 1.0\,\mu\mathrm{m}$ subjected to periodic boundary conditions. A material interface representing the grain boundary is placed in the middle of the microstructure. Dimensions are given in µm. Reprinted from [71] under the terms of the Creative Commons Attribution License (CC BY).

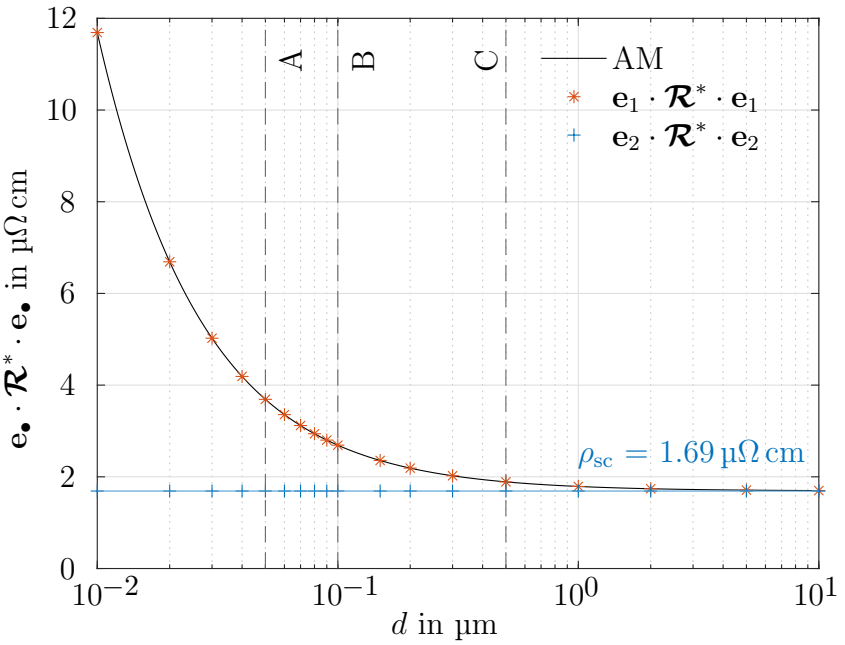

Figure 6.4: Effective resistivity as a function of grain size d. For the Andrews method, a proportionality coefficient $k_{\mathrm{GB}} = 1.0$ is obtained in analogy with Section 6.3.1. The two-dimensional finite element results clearly indicate an anisotropic size-dependent response with principal axes $\mathbf{e}_1$ and $\mathbf{e}_2$. Reprinted from [71] under the terms of the Creative Commons Attribution License (CC BY).

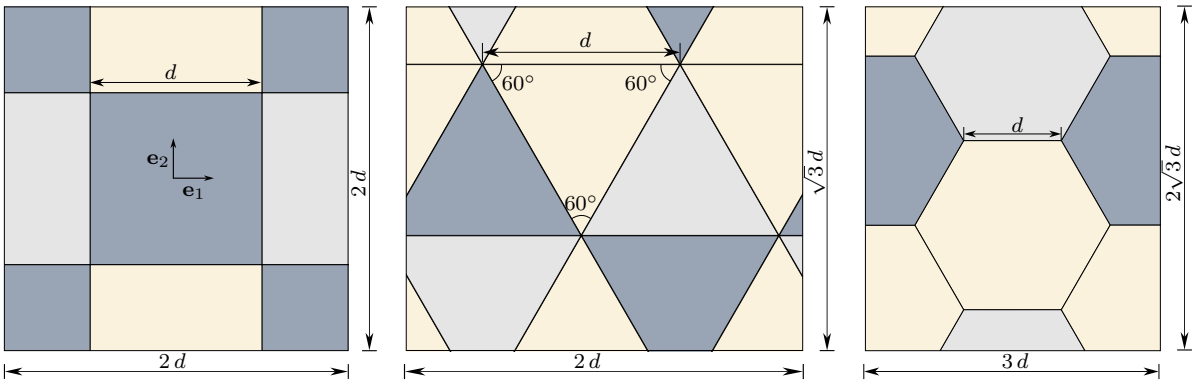

Figure 6.5: Primitive isotropic microstructures based on the dihedral group. Reprinted from [71] under the terms of the Creative Commons Attribution License (CC BY).

6.3.3 Primitive isotropic setting

qtd. [71] {Section 6.3.2 revealed that the Andrews method cannot be applied when the effective response is anisotropic, since it does not properly account for the microscale morphology in terms of grain boundary alignment. Continuing the systematic analysis of (6.2), the focus of this section lies on an isotropic setting. To this end, the synthetic microstructures depicted in Figure 6.5, which represent the first three members of the dihedral group, are analysed.

In particular, it is observed that the application of the homogenisation approach with periodic boundary conditions yields the macroscopic resistivity tensors for hexagonal grain structures with grain sizes $d_\mathrm{A} = 0.05\,\mu\mathrm{m}$, $d_\mathrm{B} = 0.1\,\mu\mathrm{m}$ and $d_\mathrm{C} = 0.5\,\mu\mathrm{m}$, namely

$$[\boldsymbol{\mathcal{R}}^*]^\mathrm{A}_{\mathbf{e}_{1,2}} = \begin{bmatrix} 3.99 & 0 \\ 0 & 3.99 \end{bmatrix} \mu\Omega\,\mathrm{cm}\,, \tag{6.23a}$$

$$[\boldsymbol{\mathcal{R}}^*]^\mathrm{B}_{\mathbf{e}_{1,2}} = \begin{bmatrix} 2.85 & 0 \\ 0 & 2.85 \end{bmatrix} \mu\Omega\,\mathrm{cm}\,, \tag{6.23b}$$

$$[\boldsymbol{\mathcal{R}}^*]^\mathrm{C}_{\mathbf{e}_{1,2}} = \begin{bmatrix} 1.92 & 0 \\ 0 & 1.92 \end{bmatrix} \mu\Omega\,\mathrm{cm}\,. \tag{6.23c}$$

The geometric proportionality coefficients are additionally calculated and the predictions based on (6.2) are shown in Figure 6.6 for the sake of comparison.

To analyse the limits of the Andrews method for quasi-isotropic material responses, a periodic microstructure in which the grain or secondary phase is confined in the matrix is studied in Figure 6.7. For this elementary example, it is observed that the material response is bounded from above in the small diameter range by the response of a porous material and from below in the large diameter range by the single crystal resistivity.

The set of resistivity tensors (6.23) as a function of grain diameter d in conjunction with Figures 6.6 and 6.7 show that:

1. The classic honeycomb-type structures that are typically assumed in the materials science community as idealisations for periodic polycrystals give rise to isotropic resistivity tensors. The same holds for other primitive "grain geometries" of the dihedral group such as the square and equilateral triangle. From a physics point of view this means that the same effective number of grain boundaries per unit length (e.g. $\mathrm{n}_{\mathrm{eff}}^{\mathrm{squ}} = 1$, $\mathrm{n}_{\mathrm{eff}}^{\mathrm{tri}} = 2\cos(\pi/6)$, $\mathrm{n}_{\mathrm{eff}}^{\mathrm{hex}} = 1/\sqrt{3}$) is passed by a charge irrespective of the spatial direction in which it is travelling through the microstructure.

2. In an isotropic setting, resistivity tensor $\boldsymbol{\mathcal{R}}^*$ reduces to a scalar-valued parameter ρ^*.

3. For such an isotropic setting, the predictions of (6.2) with proportionality coefficients $k_{\mathrm{GB}} = d\,S_{\mathrm{GB}}/V$ are consistent with the predictions of computational homogenisation.

4. For a geometry with confined grains, the effective macroscopic resistivity tensor is bounded from above and below. The lower limit corresponds to the perfectly conducting RVE, with the effect of the grain boundary being negligible. The upper limit, on the other hand, corresponds to the case of a pore, i.e. the material interface electrically insulates the confined grain. Even though the response is isotropic, (6.2) cannot predict this behaviour due to its unbounded nature for small grain diameters. In addition to the computational multiscale approach pursued in this contribution, semi-analytical approaches such as generalised self-consistent or Mori-Tanaka schemes [32, 52] may offer alternative means to address this issue.

5. For the first three members of the dihedral group the proportionality coefficients (calculated via $k_{\mathrm{GB}} = d\,S_{\mathrm{GB}}/V$) accordingly take the values

$$k_{\mathrm{GB}}^{\mathrm{squ}} = d\frac{8\,d}{4\,d^2} = 2\,, \tag{6.24a}$$

$$k_{\mathrm{GB}}^{\mathrm{tri}} = d\frac{12\,d}{2\sqrt{3}d^2} = 2\sqrt{3}\,, \tag{6.24b}$$

$$k_{\mathrm{GB}}^{\mathrm{hex}} = d\frac{6\,d}{3\sqrt{3}\,d^2} = \frac{2\sqrt{3}}{3}\,. \tag{6.24c}$$

6. For the particular set of material parameters provided in Table 6.2, (6.1)-(6.2) indicate in view of (6.24) negligible grain boundary contributions to the effective resistivity for grain sizes beyond 10 µm since

$$\mathcal{O}\left(\rho_{\mathrm{sc}}\right) = 1\,\mu\Omega\,\mathrm{cm} \gg 10^{-2}\,\mu\Omega\,\mathrm{cm} = \mathcal{O}\left(\rho_{\mathrm{GB}}\left(d = 10\,\mu\mathrm{m}\right)\right) \tag{6.25}$$

holds.$\}^{\mathrm{qtd.}}_{[71]}$

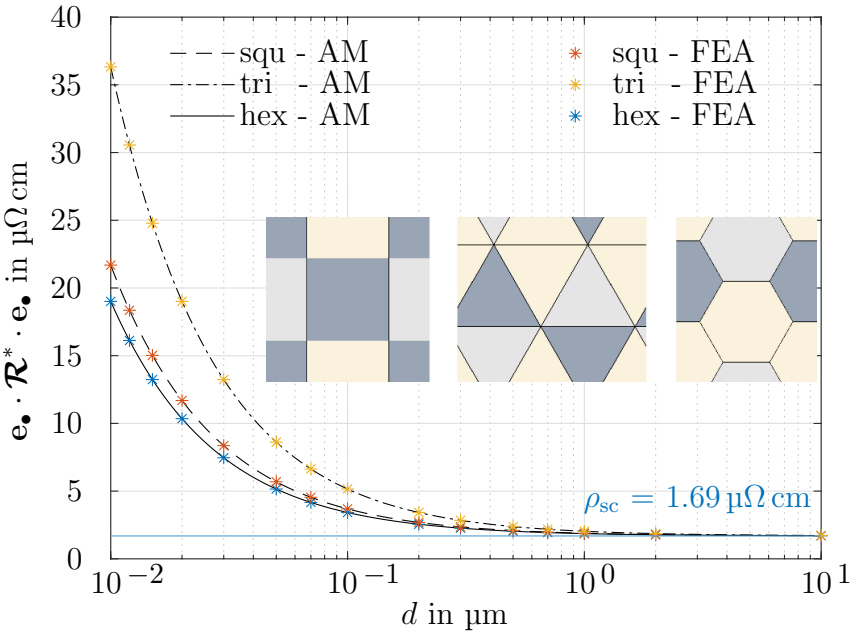

Figure 6.6: Effective resistivity for the synthetic microstructures depicted in Figure 6.5 as a function of grain size d. For the Andrews method, the specific grain boundary resistivity is chosen as $\gamma_{GB} = 10.00\,p\Omega cm^2$ and proportionality coefficients according to (6.24) are used. Reprinted from [71] under the terms of the Creative Commons Attribution License (CC BY).

6.4 Scaling relations

qtd. [71] {The effective isotropic response of the hexagonal microstructure, with material properties according to Table 6.2, is illustrated in Figure 6.6. Based on this investigation, two sets of parameter studies are conducted in this section so as to analyse the influence of the bulk and of the specific grain boundary resistivity. In the first investigation, the ratio of the bulk and specific grain boundary resistivity is kept constant to resemble investigations on different materials, such that

$$\rho_{sc} \leftarrow \alpha\,\rho_{sc}\,, \quad \gamma_{GB} \leftarrow \alpha\,\gamma_{GB}\,, \quad \frac{\alpha\,\gamma_{GB}}{\alpha\,\rho_{sc}} = \widetilde{l} \tag{6.26}$$

with the resistivities being scaled by a factor $\alpha = \{0.5, 1.0, 2.0\}$. In the second investigation, the bulk resistivity ρ_{sc} is kept constant while the specific grain boundary resistivity γ_{GB} is scaled by a factor $\beta = \{0.5, 1.0, 2.0\}$ according to

$$\rho_{sc} \leftarrow \rho_{sc}\,, \quad \gamma_{GB} \leftarrow \beta\,\gamma_{GB}\,, \quad \frac{\beta\,\gamma_{GB}}{\rho_{sc}} = \beta\,\widetilde{l} \tag{6.27}$$

which implies a similar material with different grain boundary types or segregation effects. The corresponding effective resistivity response is plotted against the grain size d in Figure 6.8. As shown in Figure 6.8a, the effective resistivity is proportionally scaled when varying α such that with increasing grain size the value $\alpha\,\rho_{sc}$ is approached. Similarly, Figure 6.8b demonstrates the effect of scaling the specific grain boundary

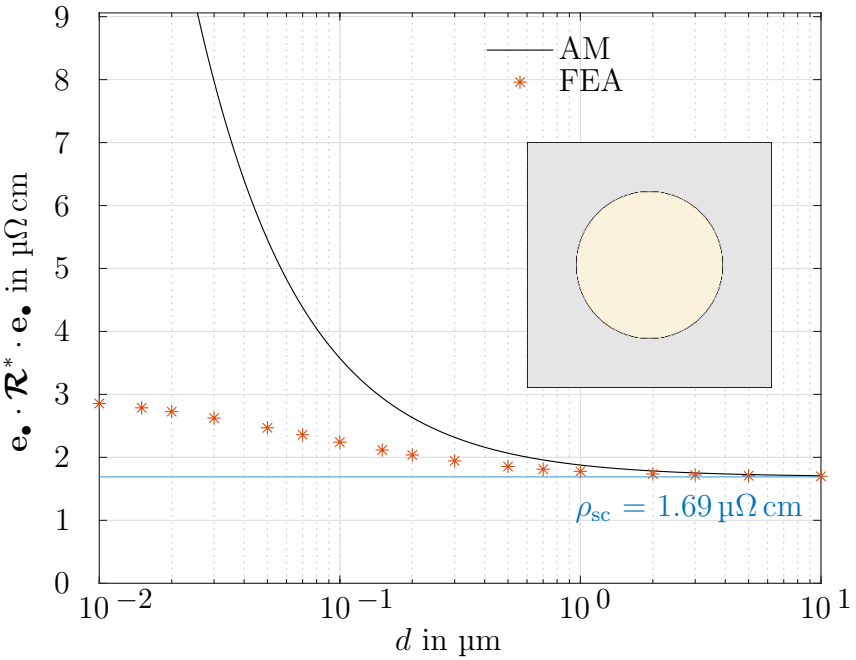

Figure 6.7: Effective resistivity for an inclusion problem with a single circular inclusion of volume fraction $\pi\,(0.3)^2/1.0 \approx 28.3\%$ as a function of grain diameter d. For the Andrews method, the specific grain boundary resistivity is chosen as $\gamma_{GB} = 10.00\,p\Omega cm^2$ and the proportionality coefficient is calculated as $k_{GB} = 2\pi\,0.3 \approx 1.88$. Reprinted from [71] under the terms of the Creative Commons Attribution License (CC BY).

resistivity by factor β while keeping the bulk resistivity constant. In particular, a distinct scaling with factor β along the grain size axis is observed.

The parameter studies on the single crystal and specific grain boundary resistivities, ρ_{sc} and γ_{GB}, show that:

1. Due to the linearity of the governing system of partial differential equations and constitutive relations, scaling both single crystal and specific grain boundary resistivity with factor α results in an α-scaling of the resistivity tensor $\boldsymbol{\mathcal{R}}^*$.

2. Similarly, scaling the ratio of the grain boundary to single crystal resistivity with factor β yields the same results as changing the grain diameter. This is due to the fact that parameter γ_{GB} intrinsically contains an internal length scale $\widetilde{l}$ as highlighted in (6.16b).

3. This has severe implications since it shows that, although the grain diameters of up to $10^{-2}\,\mu m$ considered in the example are unreasonably small, the same curves may be obtained for significantly higher grain diameters when the specific grain boundary resistivity γ_{GB} takes higher values.$\}^{\text{qtd.}}_{[71]}$

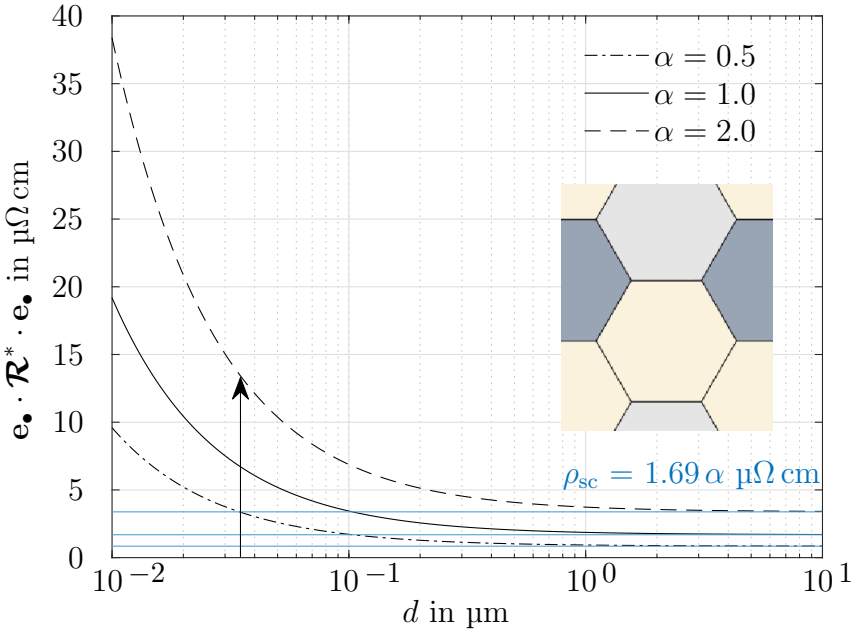

(a) $\alpha-$scaling

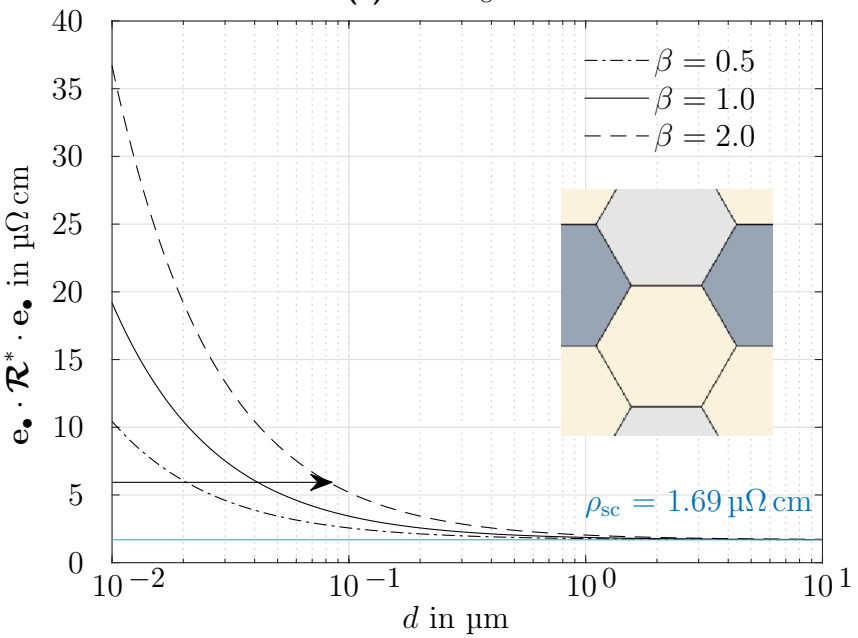

(b) $\beta-$scaling

Figure 6.8: Effective resistivity of an idealised hexagon microstructure for varying resistivity ratios as a function of grain size d. Reprinted from [71] under the terms of the Creative Commons Attribution License (CC BY).

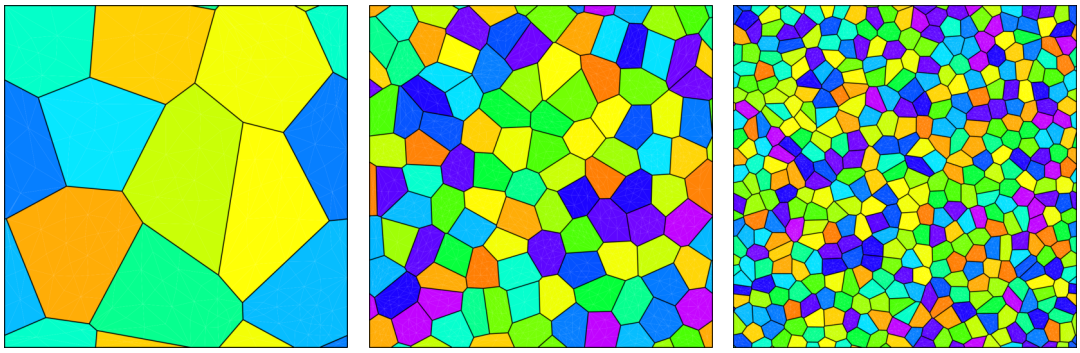

Figure 6.9: Sketch of a two-dimensional representative polycrystalline microstructure analysed with the proposed computational homogenisation scheme. The periodic tessellations are generated by using NEPER [148] and MOSAIC [75]. The cell morphology is specified such that the grain size distribution (log-normal distribution for the mean grain diameter with a standard deviation of 5.0%) matches the experimental data [171]. Reprinted from [71] under the terms of the Creative Commons Attribution License (CC BY).

6.5 Polycrystalline microstructure investigations

qtd. [71]{Extending the studies on primitive microstructures to realistic ones, this section focuses on the investigation of polycrystalline microstructures as exemplarily shown in Figure 6.9. Three different sets of microstructures are generated by using the open-source software NEPER [148], each characterised by a different number of grains ($\mathrm{n}_{\mathrm{Grain}} \in \{10, 100, 400\}$). Despite the variation in number of grains, these sets exhibit statistically identical cell morphologies as specified by the mean grain diameter and the standard deviation of 5.0% of the underlying log-normal distribution. For each set, five different periodic realisations of the microstructure are created to analyse the statistical significance of the simulation results. The macroscopic resistivity tensors indicate an anisotropic behaviour and the $\mathbf{e}_1-$ and $\mathbf{e}_2-$coordinate axes are, in general, not aligned with the principal material axes. The anisotropic properties of the macroscopic resistivity tensors are analysed by resolving them onto their principal axes through eigendecomposition

$$\boldsymbol{\mathcal{R}}^* = \sum_{i=1}^{2} \lambda_i^{\boldsymbol{\mathcal{R}}^*} \boldsymbol{n}_i \otimes \boldsymbol{n}_i \,, \tag{6.28}$$

wherein $\lambda_\bullet^{\boldsymbol{\mathcal{R}}^*}$ and $\boldsymbol{n}_\bullet$ represent the principal resistivity values and corresponding principal axes. The mean value $\overline{\lambda_\bullet^{\boldsymbol{\mathcal{R}}^*}}$ and standard deviation $s(\lambda_\bullet^{\boldsymbol{\mathcal{R}}^*})$ of the determined principal resistivity values of the five different realisations for each set are calculated and plotted against the grain size in Figure 6.10. Specifically speaking, the area between $\left(\overline{\lambda_\bullet^{\boldsymbol{\mathcal{R}}^*}} \pm s(\lambda_\bullet^{\boldsymbol{\mathcal{R}}^*})\right)$ is coloured for each set.

Concluding the analysis of polycrystalline microstructures, the multiscale predictions for realisations with $\mathrm{n}_{\mathrm{Grain}} = 400$ are shown together with the predictions by the Andrews method (for hexagonal grains with $k_{\mathrm{GB}} = 2\sqrt{3}/3$) and experimental data points reproduced from [171] in Figure 6.11.

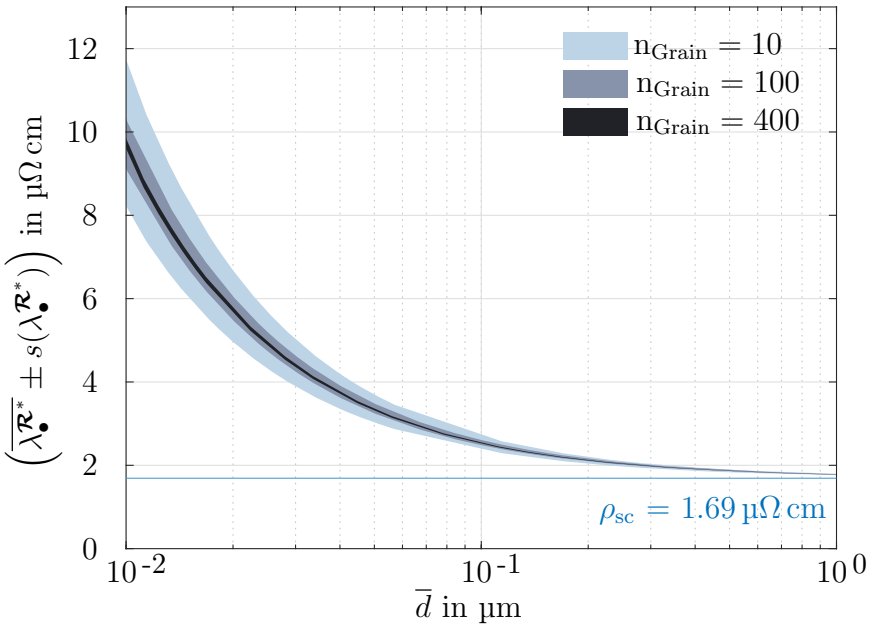

Figure 6.10: Mean value and standard deviation of the effective principal resistivities for three microstructure sets ($n_{Grain} = \{10, 100, 400\}$) as a function of mean grain diameter $\overline{d}$, typically used in the evaluation of experimental micrographs and calculated by means of the intercept method according to ASTM E1382 [9]. Reprinted from [71] under the terms of the Creative Commons Attribution License (CC BY).

The study on polycrystalline specimens with a pre-defined grain size distribution consisting of (mostly) hexagonal grains shows that:

1. The particular realisations of the microstructure approach the quasi-isotropic limit case for an increasing number of grains considered in the simulations.

2. The quasi-isotropic limit response predicted by the computational homogenisation approach is (within numerical tolerances) identical to the predictions for the hexagonal unit cell discussed in Section 6.3.3. Accordingly, the resistivity of quasi-isotropic systems can be predicted by calculating proportionality coefficient k_{GB} and by making use of (6.1)-(6.2).

3. In view of experiments, the predictive capabilities of the computational multiscale approach and of the analytical solution based on geometry factors are clearly revealed for the quasi-isotropic limit case. Whereas the analytical solution is limited to the latter, the multiscale approach intrinsically makes it possible to consider the more general anisotropic case and to predict the corresponding resistivity tensor $\boldsymbol{\mathcal{R}}^*$ based on the underlying microstructure.$\}^{\text{qtd.}}_{[71]}$

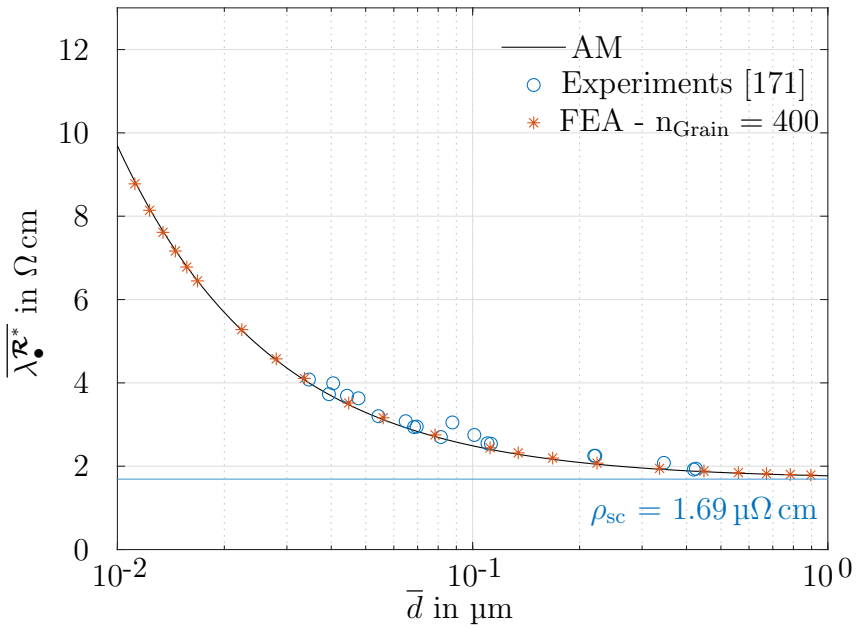

Figure 6.11: Effective mean resistivity $\overline{\lambda_{\bullet}^{\mathcal{R}^*}}$ as a function of mean grain diameter $\overline{d}$, typically used in the evaluation of experimental micrographs and calculated by means of the intercept method according to ASTM E1382 [9]. For Andrews method, the specific grain boundary resistivity is chosen as $\gamma_{\mathrm{GB}} = 3.58\,\mathrm{p\Omega cm}^2$ in accordance to [125] and the corresponding proportionality coefficient is calculated as $k_{\mathrm{GB}} = 2\sqrt{3}/3$. Reprinted from [71] under the terms of the Creative Commons Attribution License (CC BY).

6.6 Neper-Mosaic: Seamless generation of periodic representative volume elements on unit domains

qtd. [75]{To enforce periodic boundary conditions (PBCs) in finite element simulations, the microstructure itself must exhibit periodicity, so that the RVE can be replicated in all directions. Several software packages are available for the generation of polycrystalline microstructures and discretisation, such as Neper [148], DREAM3D [67], VORO++ [155], OptiMic [161] and MCRpy [159]. These tools offer valuable functionalities to create realistic microstructures with specific grain size distributions, aspect ratios, and crystal orientations. For an in-depth discussion on RVE generation, the reader may refer to [12]. In the context of this work, we focus on Neper, a well-established software for generating digital microstructures [43, 111, 112, 117, 126, 152, 184]. Neper enables the generation of non-periodic tessellations and periodic tessellations as depicted in Figure 6.12, with non-periodic tessellations offering more control over the microstructure's arrangement than periodic ones. Neper's ability to generate geometrically periodic microstructures with non-rectilinear boundaries (extending the unit square or cube) creates a challenge for traditional RVE simulations with periodic boundary conditions as described above since typical search algorithms for identifying corresponding nodes on opposite boundaries of the RVE rely on planar surfaces. Mosaic fills this gap by

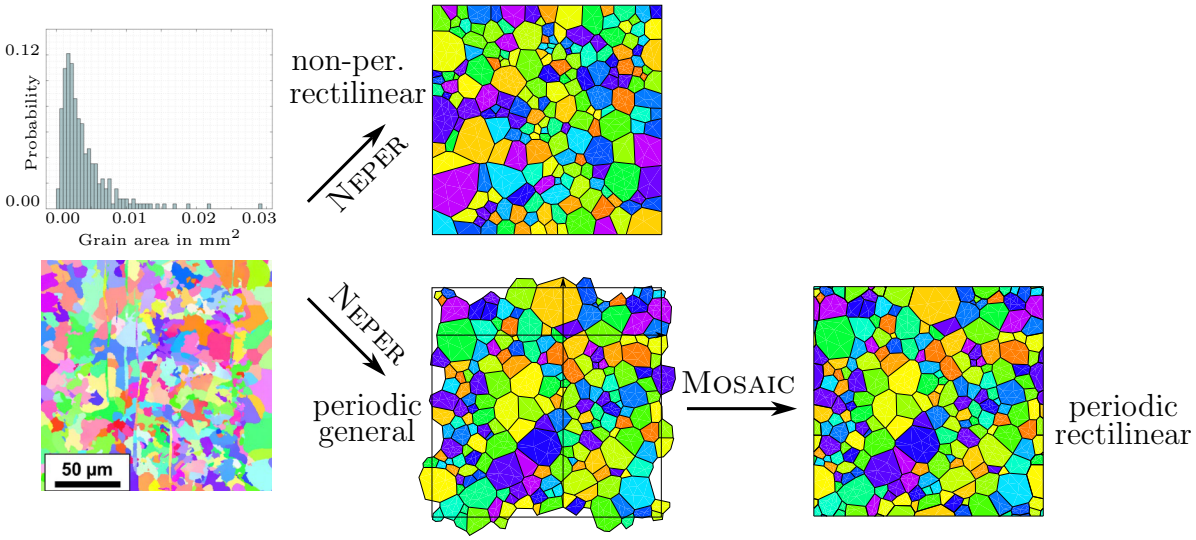

Figure 6.12: Neper creates rectilinear non-periodic or general (non-rectilinear) periodic RVEs with user-defined morphological properties such as the mean grain diameter and the number of grains. Mosaic transforms any periodic RVE to an equivalent rectilinear version while maintaining periodicity. The experimental insert, reproduced from [39] with kind permission, illustrates the inverse pole figure of a 16MnCrS5 case-hardening steel. Reprinted from [75] under the terms of the Creative Commons Attribution License (CC BY).

automatically transforming general periodic RVEs into equivalent rectilinear periodic structures. This enables realistic RVE studies with periodic boundary conditions.}$^{\text{qtd.}}_{[75]}$

6.6.1 Software description

$^{\text{qtd.}}_{[75]}${In this section, a short overview regarding the architecture and functionalities of Mosaic is given.}$^{\text{qtd.}}_{[75]}$

6.6.1.1 Software architecture

$^{\text{qtd.}}_{[75]}${Mosaic is written in Python and makes use of the application programming interface (API) of the open-source mesh generation software Gmsh [62] and the Python library numpy for numerical computing. The source code is available on GitHub (see the link to the repository in the Code metadata Table 6.3), and is designed to be modular, facilitating future extensions and ensuring code maintainability. Mosaic adopts a layered approach where the well-defined modules interact sequentially, as schematically illustrated in Figure 6.13.

The initial layer focuses on preprocessing. It reads the periodic microstructure information from Neper-generated Gmsh files (.geo), which contain the grain geometries (coordinates, lines, surfaces, and volumes). Mosaic automatically extracts essential data from these files, including the problem's dimension, the size of the periodic domain, and the number of grains.

Table 6.3: Code metadata.

Current code version	v1.0.1
Permanent link to code/repository used for this code version	github.com/InstituteOfMechanics/Neper_Mosaic_RVE_Generator
Permanent link to Reproducible Capsule	github.com/ElsevierSoftwareX/SOFTX-D-24-00374
Legal Code License	GPL-3.0 License
Code versioning system used	git
Software code languages, tools, and services used	Python
Compilation requirements, operating environments & dependencies	Neper 4.8.2, Gmsh 4.13, OCC 7.8.1, Python Standard Library (sys, argparse, logging, defaultdict, dataclass, itertools), numpy Python library, gmsh Python library
If available Link to developer documentation/manual	github.com/InstituteOfMechanics/Neper_Mosaic_RVE_Generator.git
Support email for questions	dilek.guezel@tu-dortmund.de (Please use Github issue tracker.)

The subsequent layer handles the core transformation process. The Gmsh API is utilised to convert the geometric definitions into a format compatible with the Gmsh OpenCASCADE (OCC) geometry kernel. This enables the application of OCC's advanced geometric manipulation capabilities, especially Boolean operations, to enforce periodicity by replicating the microstructure at each boundary, and subsequently extracting a rectilinear domain. This process is applied in either two or three dimensions and provides a periodic, rectilinear RVE, equivalent to the original periodic RVE.

The final layer manages the output generation. Users can specify the related format, choosing from options such as:

- Geometry file for further discretisation purposes or visualisation: .geo_unrolled (Gmsh), .brep (OCC BRep), .step (STEP)
- Mesh files compatible with different simulation/visualisation software: .msh (Gmsh), .inp (Abaqus), .vtk (ParaView), .key (LSDYNA) .stl (STL surface)
- The ability to define grain-groups in the output, facilitating material property assignment in subsequent simulations.}$^{\text{qtd.}}_{[75]}$

6.6.1.2 Software functionalities

$^{\text{qtd.}}_{[75]}${Mosaic offers a range of functionalities that address the challenges of converting general periodic microstructures generated by Neper to two- and three-dimensional periodic rectilinear RVEs:

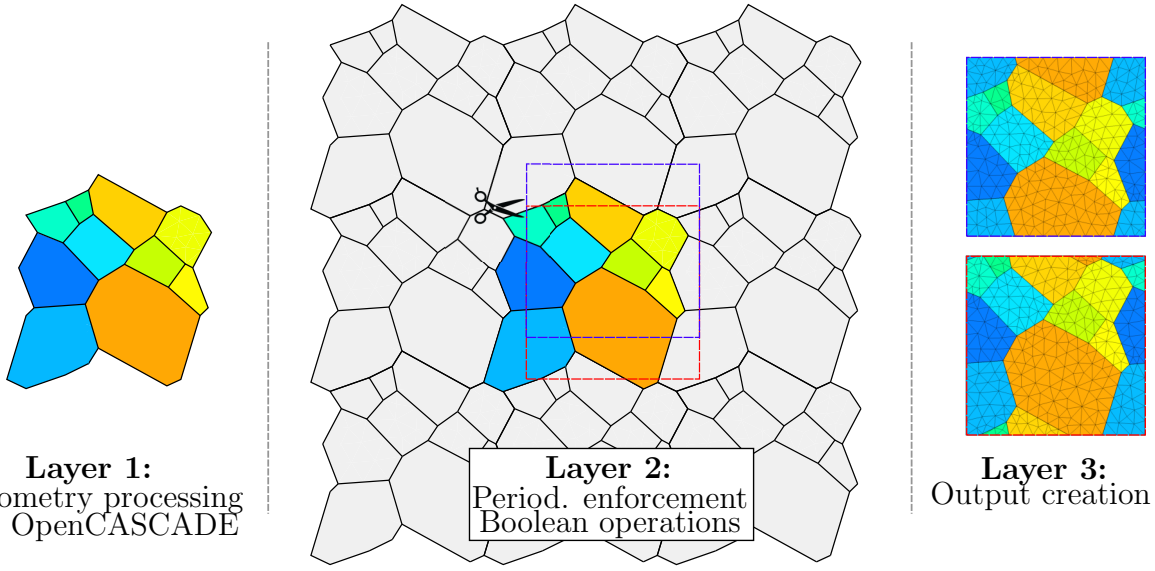

Figure 6.13: Schematic description of MOSAIC's algorithm. In the first layer, the NEPER-generated .geo file is processed such that it is compatible with the Gmsh OCC kernel. The RVE is then replicated at all boundaries, and a rectilinear, periodic subdomain is extracted by a Boolean cut. In the final layer, output is created according to user preferences. The origin of the periodic rectilinear domain can be specified by means of command line parameters as exemplified by the two periodic microstructure representations (red and blue box). This results in alternative but statistically equivalent representations of the microstructure and might be beneficial for meshing purposes. Reprinted from [75] under the terms of the Creative Commons Attribution License (CC BY).

- Periodicity enforcement: MOSAIC ensures geometric compatibility with periodic boundary conditions in simulations.
- Periodic mesh: MOSAIC provides periodic meshes that are necessary for finite-element simulations if periodicity is to be enforced in a strong sense.
- Versatile output options: Users can tailor the output to their specific needs, choosing from various file formats and the option to group grains for material property assignment.
- Compatibility with open-source codes: MOSAIC can be seamlessly integrated into workflows using, for instance, ciGen [140] to study RVEs featuring material interfaces.
- Python-enabled: MOSAIC can be used as a command-line tool or as a Python package within another Python program.}$^{\text{qtd.}}_{[75]}$

6.6.2 Illustrative examples

$^{\text{qtd.}}_{[75]}${This section focuses on various illustrative examples to show the different functionalities of MOSAIC as summarised in Table 6.4.}$^{\text{qtd.}}_{[75]}$

Table 6.4: Command line options for MOSAIC.

Flag/Option	Argument	Description
(Input File)	File path	NEPER-generated '.geo' file
(Output File)	File path	Transformed microstructure file (e.g. '.geo', '.msh', '.inp')
`-h`	None	Show help message and options
`-v`	None	Enable verbose output for detailed progress information
`--show_gui`	None	Open Gmsh GUI to visualise microstructure transformation
`--show_gmsh`	None	Enable Gmsh terminal output
`--ciGen`	None	Create ciGen input file to generate cohesive zone elements
`-x0`, `-y0`, `-z0`	Float	x-, y-, z-translation of the rectilinear domain
`-cl`	Float	Characteristic element length

6.6.2.1 Enforced periodicity: RVE examples

qtd.[75]{To run MOSAIC from the command line, users need to specify the input file (a NEPER-generated .geo file), the desired output file (with the appropriate extension for the format: .geo, .msh, .inp), and optional flags. The `-v` flag enables verbose output, providing detailed information about the software's progress. The `--show_gui` flag opens the Gmsh graphical user interface, allowing users to visualise the microstructure and its transformation. The `--show_gmsh` flag displays the Gmsh output in the terminal. The example shown in Figure 6.12 can be generated using the following command:

```
$ python3 -m neper_mosaic examples/n100-id1.geo testout.msh -v
   ↪ --show_gui --show_gmsh
```

Figure 6.14 shows a three-dimensional RVE with 64 grains, generated with MOSAIC, and demonstrates the flexibility of MOSAIC's output generation by defining the RVE in various formats: Gmsh geometry file (.geo_unrolled), Gmsh mesh file (.msh), ParaView file (.vtk) and Abaqus input file (.inp). The example shown in Figure 6.14 can be generated by the following command:}qtd.[75]

```
$ python3 -m neper_mosaic examples/n64-id1.geo testout.msh
   ↪ testout.vtk testout.geo_unrolled
```

6.6.2.2 Flexible output generation: A study on quasi-stationary electrical processes

qtd.[75]{This section illustrates the potential impact of MOSAIC by showcasing computational homogenisation results for the electrical resistivity of microstructures generated by MOSAIC.

Table 6.5: Material parameters used in the finite element-based simulations.

ρ_{M}	$68.9\,\mu\Omega\,\mathrm{cm}$
ρ_{F}	$86.2\,\mu\Omega\,\mathrm{cm}$
γ_{GB}	$68.9\,\mathrm{p}\Omega\mathrm{cm}^2$

Initially, a periodic NEPER-tessellation with a specified number of grains $\mathrm{n}_{\mathrm{Grain}} = 256$ is generated. Neper employs a grain growth algorithm to define the grain morphology, with user-specified log-normal distributions for the equivalent diameter and circularity. A key strength of MOSAIC lies in its ability to correctly group grains, especially those intersecting the RVE boundaries. This makes the assignment of specific material properties to individual grains within the RVE possible. Additionally, for this study, zero-thickness interface elements representing grain boundaries are generated by the open-source software ciGen [140]. ciGen can directly process the mesh files (.msh) created by MOSAIC.

As an illustrative example for the simulation workflow enabled by MOSAIC, we consider a dual-phase steel with ferritic and martensitic constituents, as well as linear constitutive relations for the bulk and interfaces. MOSAIC is used to create periodic RVEs based on microstructures generated by Neper and to assign each microscale constituent (ferrite, martensite) to a specific group. Based on these groups, resistivity values for the individual constituents according to Table 6.5 are assigned in the finite element simulation.

To determine the effective electrical properties, specifically speaking the macroscopic resistivity tensor denoted by $\boldsymbol{\mathcal{R}}^*$, the computational homogenisation scheme proposed in [100] and extended in [71, 76] is employed

$$\{\rho_{\mathrm{M}}, \rho_{\mathrm{F}}, \gamma_{\mathrm{GB}}, \mathrm{morphology}\} \quad \overset{\text{homogenisation}}{\longrightarrow} \quad \boldsymbol{\mathcal{R}}^* \tag{6.29}$$

where ρ_{M}, ρ_{F}, γ_{GB} are the specific resistivity values of the martensitic phase, the ferritic phase and the grain boundaries, respectively. Periodic boundary conditions for the electric problem are applied as follows

$$\phi^+ - \phi^- = -\boldsymbol{e}_0 \cdot \left[\boldsymbol{y}^+ - \boldsymbol{y}^-\right] \quad \text{and} \quad i^+ = -i^- \quad \text{on} \quad Y\,. \tag{6.30}$$

The obtained effective resistivity tensors exhibit anisotropy due to the underlying microstructure. These tensors are resolved onto their principal axes by spectral decomposition, as given in (6.28).

Figure 6.15b illustrates three distinct scenarios for resistivity. In the first scenario, all grains are assigned the properties of either martensite or ferrite. In the second scenario, a specific martensite volume fraction $\phi_{\mathrm{M}} = 0.78$ is considered by using group definitions to create a more realistic phase distribution. As expected, the effective resistivity calculated for the $\phi_{\mathrm{M}} = 0.78$ case lies between the two previously calculated limits. The third scenario considers the additional resistivity caused by the presence of grain boundaries. Here, a grain-size dependent response is observed. As the grain size decreases, the effective resistivity of the material increases.$\}^{\text{qtd.}}_{[75]}$

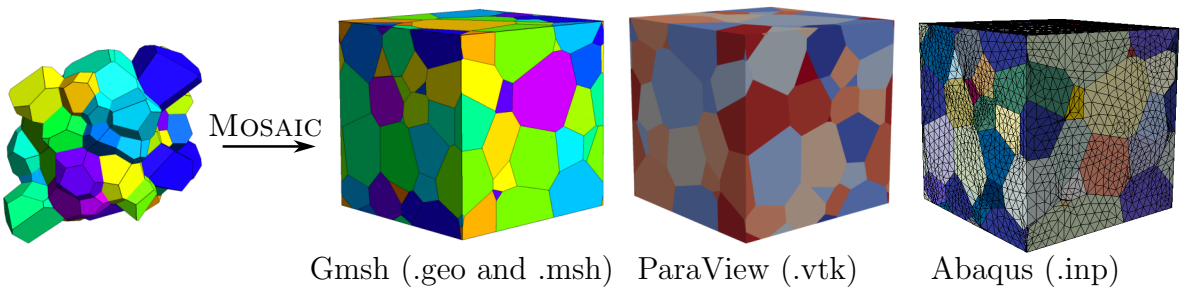

Figure 6.14: Neper-generated periodic microstructure with $n_{Grain} = 64$, transformed into a unit cube RVE using Mosaic. Output options include Gmsh geometry and mesh files, vtk files, or Abaqus input files. Reprinted from [75] under the terms of the Creative Commons Attribution License (CC BY).

6.6.3 Impact

qtd. [75]{Mosaic, a Python-based open-source software tool, has the potential to significantly impact the computational mechanics and materials science community. Its key strength lies in its seamless interaction with the well-established open-source software Neper, which has a large and active user base from both, academia and industry. Neper is employed for microstructure generation in computational materials science and engineering, with applications extending beyond metals to fields such as geology (rock formations), energy storage materials (battery electrodes), and biological materials (bone structures). Neper generates realistic microstructures, being more profound than simple Voronoi tessellations, by offering grain growth algorithms. These realistic microstructures are then used to design new materials with tailored material properties and to predict their performance under different loading conditions. This includes research areas such as crystal plasticity, where the accurate representation of grain structures and periodic boundary conditions is crucial for the understanding of deformation mechanisms at the microscale. Furthermore, a recent publication by Grilli et al. [66] in the context of fracture mechanics makes use of Abaqus to insert interface elements in two-dimensional non-periodic RVEs created by Neper.

While Neper is capable of creating periodic tessellations, these structures extend beyond a confined square or cubic domain. When a square/cubic domain is preferred due to boundary conditions, this requires careful handling. Mosaic addresses this challenge by providing an efficient workflow for Neper's output. It directly processes a Neper generated geometry and transforms it into an equivalent periodic microstructure confined within a square or cubic domain, suitable for creating a periodic mesh for simulations. This enables the straightforward application of periodic boundary conditions and, eventually, RVE studies with realistic microstructures.

Mosaic utilises the functionalities of Gmsh, an open-source mesh generation tool. This integration provides Mosaic users with a broad selection of meshing algorithms (structured, unstructured, adaptive) for creating customised meshes suitable for their specific simulation needs, see Appendix C.1. This extends to integrating with ciGen an

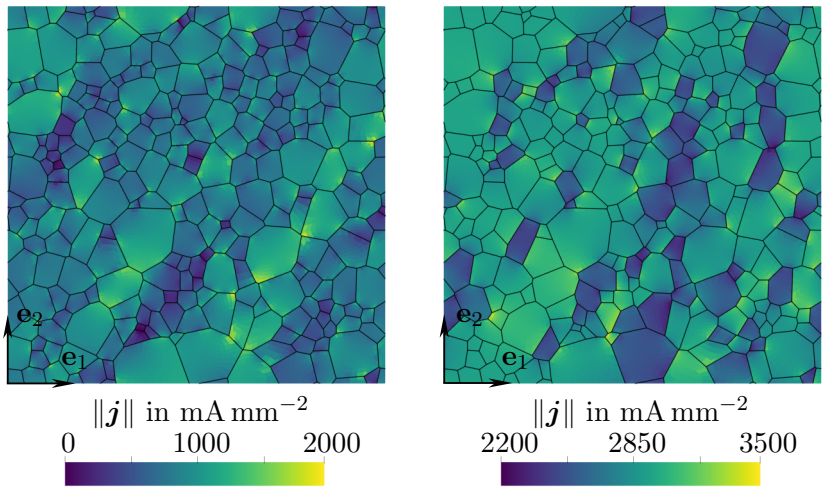

(a) Polycrystalline microstructures ($n_{Grain} = 256$, unit domain) with (left) and without grain boundaries (right). Grains represent randomly assigned ferritic and martensitic constituents. The electric current density distributions, $\boldsymbol{j}$, at the microscale are depicted. The RVE is loaded electrically by effective electric field $\overline{\boldsymbol{e}}_0 = 1.0\,\mathbf{e}_1 + 2.0\,\mathbf{e}_2$ mV.

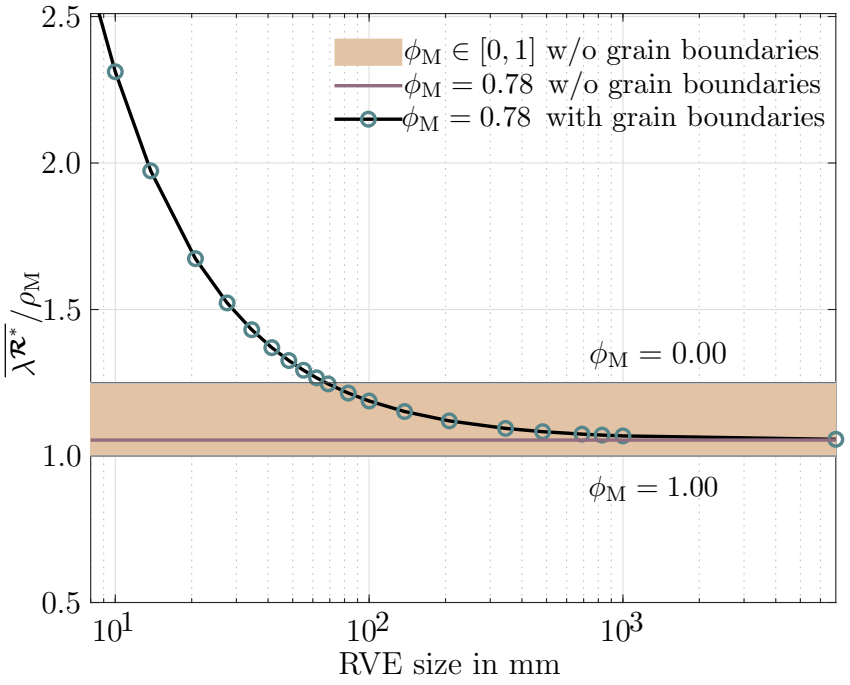

(b) Effective mean resistivity $\overline{\lambda^{\mathcal{R}^*}} = \frac{1}{2}\left[\lambda_1^{\mathcal{R}^*} + \lambda_2^{\mathcal{R}^*}\right]$ as a function of RVE size. To define the limit cases, all grains are assigned either the material properties of ferrite or martensite. For the specific martensite volume fraction $\phi_M = 0.78$, the Neper-Mosaic workflow is used to create a digital microstructure twin. This microstructure is then analysed with and without accounting for the resistivity of grain boundaries.

Figure 6.15: Computational homogenisation results for a ferritic-martensitic dual-phase steel. Reproduced from [75] under the terms of the Creative Commons Attribution License (CC BY).

open-source software which uses the specific mesh format generated by Gmsh/Mosaic to efficiently account for zero-thickness cohesive zone elements.}$^{\text{qtd.}}_{[75]}$

C Appendix

Appendix C.1 contains a comparative analysis of mesh quality generated using Mosaic and Neper.

C.1 Mesh quality investigation

$^{\text{qtd.}}_{[75]}${In this appendix, the quality of meshes created with Mosaic and Neper is exemplarily compared. Both codes utilise Gmsh as the meshing software – the geometries, however, differ significantly. The geometry obtained from Neper is not confined to a rectilinear domain. In contrast, Mosaic generates geometries on box-type domains, resulting in additional surfaces or volumes being cut by the domain boundaries.

For comparison purposes, three-dimensional periodic tessellations with a specified number of grains $n_{Grain} \in \{4, 8, 16, 32, 64\}$ were generated by Neper (grain growth algorithm, unit domain) and processed with Mosaic. These microstructure representations were then meshed in both codes with the same characteristic element length, $cl = 0.08$. Figure 6.16a illustrates the mesh quality in terms of the minimal signed inverted condition number (minSICN, [95]). For both, the original Neper-generated and the confined microstructure generated by Mosaic, Gmsh appears to produce meshes with reasonably good minSICN values, with most of the data lying in the upper half of the box plots. This suggests that most elements have an acceptable shape. However, there are a few outliers visible in Figure 6.16a. These indicate that, in some instances, a few elements with significantly lower quality compared to the mesh-average were generated. Comparing the meshes for the Neper- and Mosaic-generated microstructures, the higher number of outliers in the Mosaic-workflow is likely caused by the newly generated cut surfaces and volumes. Another reason is that the meshes generated by Mosaic are strictly periodic, which incurs additional restrictions during meshing. One potential approach to address this issue is to manually translate the origin of the rectilinear domain (command line option: -x0, -y0, -z0). Figure 6.16b provides the mesh quality statistics for selected translations of the unit cell (edge length 1.0) in the 32-grain example. While the overall mesh quality is very similar for all analysed translations, a reduction in the number of low quality elements can, for instance, be observed for $x = 0.4$. In addition to the translation of the unit cell, standard approaches such as partitioning methods may, of course, be invoked by the user to achieve the desired mesh quality.}$^{\text{qtd.}}_{[75]}$

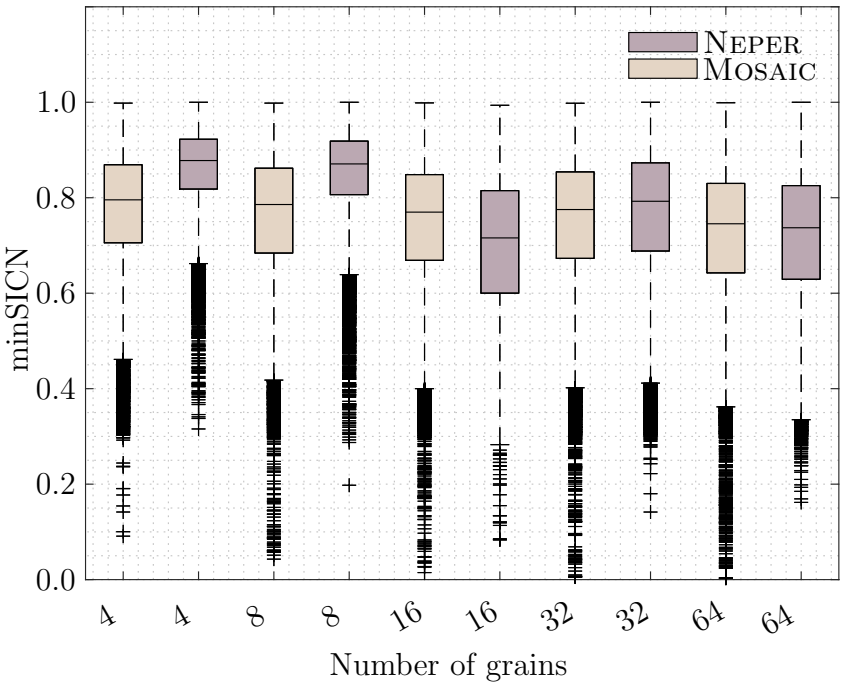

(a) Comparison of mesh quality (minSICN) for three-dimensional periodic tessellations with varying number of grains.

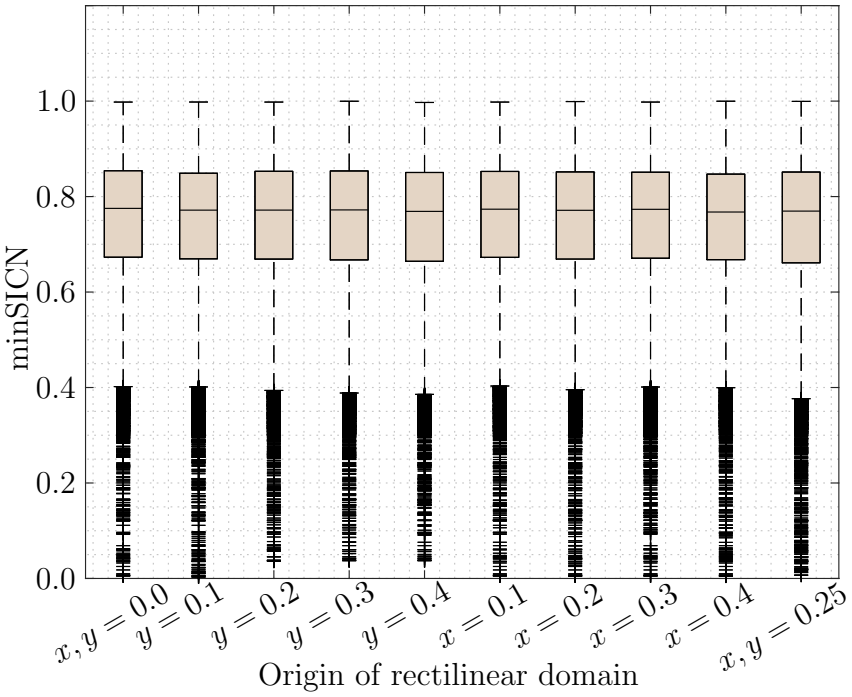

(b) Comparison of mesh quality (minSICN) for the Mosaic-workflow ($n_{Grain} = 32$) and varying translation parameters.

Figure 6.16: Study of mesh quality for different microstructure realisations in terms of the number of grains and the translation of the unit cell. Standard box plots with 1.5 interquartile range are used for visualisation purposes. Reprinted from [75] under the terms of the Creative Commons Attribution License (CC BY).

7 Mathematical homogenisation: Thermo-electrical problem

qtd. [72] {In the context of thermo-electrically coupled problems, understanding the coupled behaviour of thermal and electrical fields is crucial for optimising the performance of devices such as integrated circuits, thermoelectric generators and coolers. Joule heating describes the process where the kinetic energy of electrons flowing through a resistive material is converted into heat. This heat generation can significantly influence the material's electrical and thermal properties such as its thermal and electrical conductivities. These thermo-electrically coupled effects, further complicated by the intricate microstructures of heterogeneous materials, pose significant challenges for accurate modelling and prediction.

To address these challenges, a comprehensive thermo-electrically coupled homogenisation framework for electrical conductors is developed in this chapter. To this end, we resort to analytical homogenisation, formal asymptotic expansion and Hill–Mandel-type multiscale techniques.

In view of the different homogenisation approaches, the scope of the present chapter is twofold:

- *As a model problem for PDE systems with non-trivial couplings, we focus on thermo-electrical phenomena and provide the homogenised set of field equations with particular focus lying on Joule heating and temperature dependent electrical conductivities.*

- *We approach the two-scale problem from a physics point of view by using a Hill–Mandel-type energy-equivalence statement and show the consistency of the homogenised problem with the heuristic method of asymptotic expansions and the mathematically rigorous results of analytical homogenisation.*} qtd. [72]

The chapter is organised as follows: Section 7.1 provides an overview of the thermodynamic principles governing thermo-electrically coupled problems. Section 7.2 focuses on the micro-to-macro transition by using energy-based multiscale techniques, asymptotic expansions and analytical homogenisation. In Section 7.3, representative numerical results are provided so as to showcase the effectiveness of these methods in capturing the behaviour of heterogeneous thermo-electric materials.

7.1 Continuum thermodynamics

This section provides an overview of the underlying thermodynamical principles that govern thermo-electrically coupled problems in electrical conductors. To avoid repetition, only governing equations are presented here. For detailed derivations and background, the reader is referred to Chapter 4. The coupled system of equations in local form is given by

$$\nabla \cdot \boldsymbol{j}(\boldsymbol{x}) = 0 \qquad \forall \boldsymbol{x} \in \Omega\,, \tag{7.1a}$$

$$-\nabla \cdot \boldsymbol{q}(\boldsymbol{x}) + r(\boldsymbol{x}) + \boldsymbol{j}(\boldsymbol{x}) \cdot \boldsymbol{e}(\boldsymbol{x}) = 0 \qquad \forall \boldsymbol{x} \in \Omega\,. \tag{7.1b}$$

In addition, localisation of Maxwell's equations imposes a constraint on the electric potential field, which can be satisfied by defining the electric field as $\boldsymbol{e}(\boldsymbol{x}) = -\nabla_x \phi$. Furthermore, the local form of the dissipation inequality

$$-\frac{1}{\theta(\boldsymbol{x})}\,\boldsymbol{q}(\boldsymbol{x}) \cdot \nabla_x \theta(\boldsymbol{x}) + \boldsymbol{j}(\boldsymbol{x}) \cdot \boldsymbol{e}(\boldsymbol{x}) \geq 0 \qquad \forall \boldsymbol{x} \in \Omega \tag{7.2}$$

is obtained. Equation (7.2) poses restrictions on the constitutive relations for thermo-electrical processes. In general, by choosing a temperature-dependent relation between the electric current density vector and the electric field vector of the form

$$\boldsymbol{j}(\boldsymbol{x}) = \boldsymbol{\mathcal{S}}(\theta, \boldsymbol{x}) \cdot \boldsymbol{e}(\boldsymbol{x}) = -\boldsymbol{\mathcal{S}}(\theta, \boldsymbol{x}) \cdot \nabla_x \phi(\boldsymbol{x}) \tag{7.3}$$

with positive semi-definite, symmetric electrical conductivity tensor $\boldsymbol{\mathcal{S}} : \mathbb{R}^+ \times \Omega \to \mathrm{Lin}\left(\mathbb{R}^d, \mathbb{R}^d\right)$, the electrical part of the dissipation inequality can be *a priori* fulfilled. Similarly, by adopting the linear relation between the heat flux vector and the (negative) temperature gradient

$$\boldsymbol{q}(\boldsymbol{x}) = -\boldsymbol{\mathcal{K}}(\boldsymbol{x}) \cdot \nabla_x \theta(\boldsymbol{x}) \tag{7.4}$$

where $\boldsymbol{\mathcal{K}} : \Omega \to \mathrm{Lin}\left(\mathbb{R}^d, \mathbb{R}^d\right)$ denotes the positive semi-definite, symmetric thermal conductivity tensor, thermodynamic consistency of the thermal part of the dissipation inequality is established.

7.2 Micro-to-macro transition

qtd. [72] {This section focuses on the homogenisation of the thermo-electrically coupled problem introduced in Section 7.1. First, the problem is investigated with the energy-based computational homogenisation approach. Loosely speaking, this amounts to defining an appropriate Hill–Mandel condition which ensures that the energy at the macroscale is equivalent to the average energy at the microscale. Thereafter, the formal method of asymptotic expansions is investigated and effective (macroscopic) equations are derived accordingly. Noteworthy, the temperature dependence of the electrical conductivity tensor complicates the asymptotic analysis. Finally, analytical homogenisation techniques

are applied and two-scale convergence results are presented. The nonlinear nature of the coupled problem makes the two-scale convergence analysis non-trivial with, particularly, the existence proof requiring special care. As a homogenisation result, the mathematically rigorous method of analytical homogenisation, the heuristic method of asymptotic expansions, and the energy-based approach yield the same set of equations. In this regard, the rigorous two-scale convergence proof inherent to analytical homogenisation provides justification for the asymptotic expansion and for the physically motivated assumptions underlying the energy-based approach.}$^{\text{qtd.}}_{[72]}$

7.2.1 Hill–Mandel-type homogenisation

In the absence of mechanical fields, the coupled thermo-electro-mechanical multiscale framework introduced in Chapter 4 reduces to a simplified form. We study conduction in a periodic medium occupying the macroscopic domain $\Omega \subset \mathbb{R}^d$. At the microscale we work with the reference unit cell $Y = (0,1)^d$. A function $g : \mathbb{R}^d \to \mathbb{R}^m$ is denoted Y-periodic if $g(\boldsymbol{y} + \mathbf{e}_i) = g(\boldsymbol{y})$ for a.e. $\boldsymbol{y} \in \mathbb{R}^d$ and for each Euclidean base vector $\mathbf{e}_i$ $(i = 1, \dots, d)$. We use $L^\infty_\#(Y)$ for essentially bounded Y-periodic functions, and $H^1_\#(Y)$ for H^1-functions that are Y-periodic. Let $\boldsymbol{y} \in Y$ be the microscopic coordinate. Throughout this chapter, v corresponds to the Lebesgue measure of Y. $^{\text{qtd.}}_{[72]}$\{Under the assumption of strict scale separation, the coupled governing equations 4.2 simplifies to

$$\nabla_y \cdot \boldsymbol{j}(\boldsymbol{y}) = -\nabla_y \cdot [\boldsymbol{\mathcal{S}}(\theta_0, \boldsymbol{y}) \cdot \nabla_y \phi(\boldsymbol{y})] = 0 \qquad \forall \boldsymbol{y} \in Y\,, \tag{7.5a}$$

$$\nabla_y \cdot \boldsymbol{q}(\boldsymbol{y}) = -\nabla_y \cdot [\boldsymbol{\mathcal{K}}(\boldsymbol{y}) \cdot \nabla_y \theta(\boldsymbol{y})] \quad = 0 \qquad \forall \boldsymbol{y} \in Y\,. \tag{7.5b}$$

All $\boldsymbol{y}$-dependent quantities used in the homogenisation are Y-periodic – in particular $\boldsymbol{\mathcal{S}}(\theta_0, \boldsymbol{y})$, $\boldsymbol{\mathcal{K}}(\boldsymbol{y})$ are Y-periodic and uniformly bounded and elliptic. Moreover, whenever microscopic fluctuations are introduced, these are taken in $H^1_\#(Y)$. As demonstrated in Chapter 4, macroscopic quantities are related to their microscopic counterparts through volume averages over unit cells. To this end, the macroscopic electric field vector

$$\boldsymbol{e}_0 = \frac{1}{v} \int_{\partial Y} -\phi(\boldsymbol{y})\, \boldsymbol{n}(\boldsymbol{y})\, \mathrm{d}y \tag{7.6}$$

in terms of the electric potential field at the boundary is obtained. Analogously, the effective macroscopic temperature gradient is expressed as

$$\nabla_x \theta_0 = \frac{1}{v} \int_{\partial Y} \theta(\boldsymbol{y})\, \boldsymbol{n}(\boldsymbol{y})\, \mathrm{d}y\,. \tag{7.7}$$

Furthermore, the effective macroscopic electric current density tensor is given by

$$\boldsymbol{j}_0 = \frac{1}{v} \int_{\partial Y} \boldsymbol{y}\, i(\boldsymbol{y})\, \mathrm{d}y\,, \tag{7.8}$$

and the macroscopic heat flux takes the form

$$\boldsymbol{q}_0 = \frac{1}{v} \int_{\partial Y} -\boldsymbol{y}\, q(\boldsymbol{y})\, \mathrm{d}y\,. \tag{7.9}$$

The energy equivalence conditions for electrical and thermal problem are given in (4.11) and (4.12), respectively. The use of periodic boundary conditions ensures that the generalised Hill–Mandel relations are satisfied. Having established the energy equivalence between scales, we can define the coupled macroscale problem as

$$\nabla_x \cdot \boldsymbol{j}_0(\boldsymbol{x}) = 0 \qquad \forall \boldsymbol{x} \in \Omega\,, \tag{7.10a}$$

$$\nabla_x \cdot \boldsymbol{q}_0(\boldsymbol{x}) = \boldsymbol{j}_0(\boldsymbol{x}) \cdot \boldsymbol{e}_0(\boldsymbol{x}) + r_0(\boldsymbol{x}) \quad \forall \boldsymbol{x} \in \Omega\,, \tag{7.10b}$$

with its alternative form

$$-\nabla_x \cdot \left[\boldsymbol{\mathcal{S}}^*(\theta_0, \boldsymbol{x}) \cdot \nabla_x \phi_0(\boldsymbol{x})\right] = 0 \qquad \forall \boldsymbol{x} \in \Omega\,, \tag{7.11a}$$

$$-\nabla_x \cdot \left[\boldsymbol{\mathcal{K}}^*(\theta_0, \boldsymbol{x}) \cdot \nabla_x \theta_0(\boldsymbol{x})\right] = \nabla_x \phi_0(\boldsymbol{x}) \cdot \boldsymbol{\mathcal{S}}^*(\theta_0, \boldsymbol{x}) \cdot \nabla_x \phi_0(\boldsymbol{x}) + r_0(\boldsymbol{x}) \quad \forall \boldsymbol{x} \in \Omega\,, \tag{7.11b}$$

where $\boldsymbol{\mathcal{S}}^* : \mathbb{R}^+ \times \Omega \to \mathrm{Lin}\left(\mathbb{R}^d, \mathbb{R}^d\right)$ and $\boldsymbol{\mathcal{K}}^* : \Omega \to \mathrm{Lin}\left(\mathbb{R}^d, \mathbb{R}^d\right)$ denote the effective electrical and thermal conductivity tensor, respectively. In (7.10b), the macroscopic heat source $r_0 : \Omega \to \mathbb{R}$ is calculated through volume averages. Once the local problem (7.5) is solved, the effective fluxes can be calculated using (7.8) and (7.9). Moreover, the effective electrical conductivity tensor can be determined through the relation

$$\begin{aligned}
\boldsymbol{\mathcal{S}}^*(\theta_0, \boldsymbol{x}) \cdot \boldsymbol{e}_0(\boldsymbol{x}) = \boldsymbol{j}_0(\boldsymbol{x}) &= \frac{1}{v}\int_Y \boldsymbol{j}(\boldsymbol{y})\,\mathrm{d}y \\
&= \frac{1}{v}\int_Y \boldsymbol{\mathcal{S}}(\theta_0, \boldsymbol{y}) \cdot \left[\boldsymbol{e}_0(\boldsymbol{x}) - \nabla_y \widetilde{\phi}(\boldsymbol{x}, \boldsymbol{y})\right] \mathrm{d}y \\
&= \underbrace{\frac{1}{v}\int_Y \boldsymbol{\mathcal{S}}(\theta_0, \boldsymbol{y}) \cdot \left[\boldsymbol{I} - \boldsymbol{\mathcal{M}}^\phi(\boldsymbol{x}, \boldsymbol{y})\right] \mathrm{d}y}_{\boldsymbol{\mathcal{S}}^*(\theta_0,\, \boldsymbol{x})} \cdot \boldsymbol{e}_0(\boldsymbol{x})\,,
\end{aligned} \tag{7.12a}$$

where $\boldsymbol{\mathcal{M}}^\phi : \Omega \times Y \to \mathrm{Lin}\left(\mathbb{R}^d, \mathbb{R}^d\right)$ denotes the structure tensor that defines the relation between the (gradient of the) fluctuation field and the applied macroscopic field, namely $\nabla_y \widetilde{\phi} = \boldsymbol{\mathcal{M}}^\phi \cdot \boldsymbol{e}_0$. Similarly, the effective thermal conductivity tensor is derived as

$$\begin{aligned}
\boldsymbol{\mathcal{K}}^*(\boldsymbol{x}) \cdot \nabla_x \theta_0(\boldsymbol{x}) = \boldsymbol{q}_0(\boldsymbol{x}) &= \frac{1}{v}\int_Y \boldsymbol{q}(\boldsymbol{y})\,\mathrm{d}y \\
&= -\frac{1}{v}\int_Y \boldsymbol{\mathcal{K}}(\boldsymbol{y}) \cdot \left[\nabla_x \theta_0(\boldsymbol{x}) + \nabla_y \widetilde{\theta}(\boldsymbol{x}, \boldsymbol{y})\right] \mathrm{d}y \\
&= \underbrace{-\frac{1}{v}\int_Y \boldsymbol{\mathcal{K}}(\boldsymbol{y}) \cdot \left[\boldsymbol{I} + \boldsymbol{\mathcal{M}}^\theta(\boldsymbol{y})\right] \mathrm{d}y}_{\boldsymbol{\mathcal{K}}^*(\boldsymbol{x})} \cdot \nabla_x \theta_0(\boldsymbol{x})\,.
\end{aligned} \tag{7.12b}$$

The corresponding relation between the (gradient of the) temperature fluctuation field and the macroscopic gradient of temperature is defined through the structure tensor $\boldsymbol{\mathcal{M}}^\theta : Y \to \mathrm{Lin}\left(\mathbb{R}^d, \mathbb{R}^d\right)$, namely $\nabla_y \widetilde{\theta} = \boldsymbol{\mathcal{M}}^\theta \cdot \nabla_x \theta_0$.}$^{\text{qtd.}}_{[72]}$

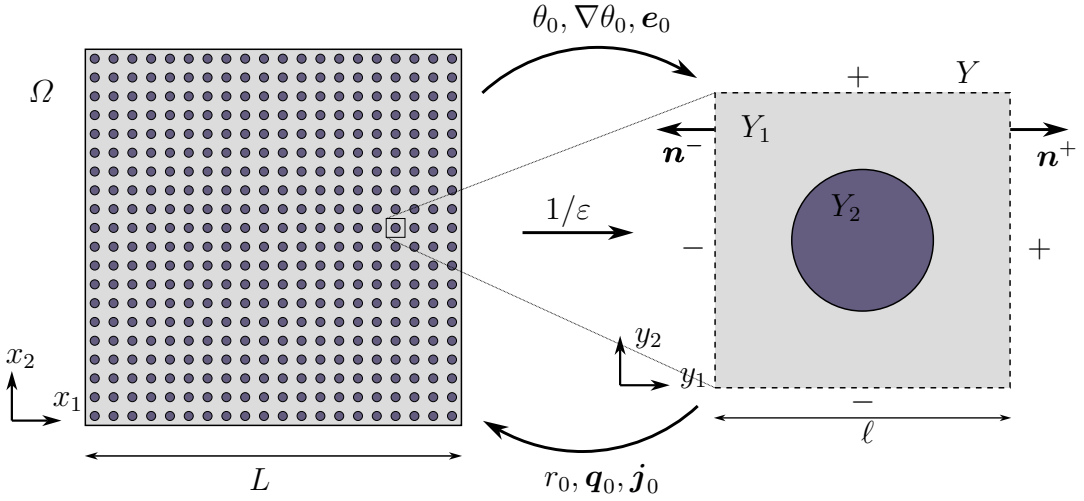

Figure 7.1: Macroscopic Ω and microscopic domains Y with a distinct separation of the corresponding length scales L and ℓ. The periodic representative cell Y is composed of two constituent domains Y_1 and Y_2, representing different materials. Scale separation occurs for $\ell \ll L$. Reprinted from [72] under the terms of the Creative Commons Attribution License (CC BY).

7.2.2 Two-scale asymptotic expansion

qtd. [72] {The following section explores the method of two-scale asymptotic expansions. This approach involves representing the solution fields as power series in a parameter, ε, and systematically separating the governing equations into distinct problems at each scale. The leading-order term in the expansion captures the homogenised solution, whereas higher-order terms account for microstructural fluctuations. By employing two-scale asymptotic expansions, explicit expressions for the effective coefficients of the homogenised equation can be derived, providing insights into the macroscopic behaviour of the material. It is further assumed that the material properties exhibit periodic or quasi-periodic variations on the microscale, characterised by a well-defined microstructure. Additionally, the material coefficients and the solution to the governing partial differential equation are required to possess sufficient regularity to guarantee the validity of the asymptotic expansion procedure. For more information regarding asymptotic analysis, readers may refer to [18].

The method of two-scale asymptotic expansions assumes that the solution of the governing equation for the electrical problem (7.1a) is given by

$$\phi_\varepsilon(\boldsymbol{x}) = \sum_{i=0}^{+\infty} \varepsilon^i \phi_i\left(\boldsymbol{x}, \frac{\boldsymbol{x}}{\varepsilon}\right) = \phi_0\left(\boldsymbol{x}, \frac{\boldsymbol{x}}{\varepsilon}\right) + \varepsilon\,\phi_1\left(\boldsymbol{x}, \frac{\boldsymbol{x}}{\varepsilon}\right) + \varepsilon^2\,\phi_2\left(\boldsymbol{x}, \frac{\boldsymbol{x}}{\varepsilon}\right) + \mathcal{O}\left(\varepsilon^3\right) \tag{7.13a}$$

where each term $\phi_i(\boldsymbol{x}, \boldsymbol{y})$ depends on the macroscopic variable $\boldsymbol{x} \in \Omega$ and the microscopic variable $\boldsymbol{y} = \boldsymbol{x}/\varepsilon \in Y$. Assuming a distinct separation of scales, $\boldsymbol{x}$ and $\boldsymbol{y}$ are treated as independent variables. Similarly, the solution to (7.1b) can be expanded as

$$\theta_\varepsilon(\boldsymbol{x}) = \sum_{i=0}^{+\infty} \varepsilon^i \theta_i\left(\boldsymbol{x}, \frac{\boldsymbol{x}}{\varepsilon}\right) = \theta_0\left(\boldsymbol{x}, \frac{\boldsymbol{x}}{\varepsilon}\right) + \varepsilon\,\theta_1\left(\boldsymbol{x}, \frac{\boldsymbol{x}}{\varepsilon}\right) + \varepsilon^2\,\theta_2\left(\boldsymbol{x}, \frac{\boldsymbol{x}}{\varepsilon}\right) + \mathcal{O}\left(\varepsilon^3\right) . \tag{7.13b}$$

Moreover, ϕ_i and θ_i are periodic in $\boldsymbol{y}$ with period $Y = (0,1)^d$. For a sufficiently smooth field f, the calculation rule

$$\nabla f\left(\boldsymbol{x}, \boldsymbol{y} = \frac{\boldsymbol{x}}{\varepsilon}\right) = \nabla_x f(\boldsymbol{x}, \boldsymbol{y}) + \frac{1}{\varepsilon}\nabla_y f(\boldsymbol{x}, \boldsymbol{y})\Big|_{\boldsymbol{y}=\boldsymbol{x}/\varepsilon}, \tag{7.14}$$

holds. Applying (7.14) to the asymptotic expansions of the electric potential and temperature fields, (7.13), we obtain the following expressions for their gradients

$$\begin{aligned}\nabla\phi_\varepsilon(\boldsymbol{x}) = {} & \nabla_x\phi_0\left(\boldsymbol{x}, \frac{\boldsymbol{x}}{\varepsilon}\right) + \frac{1}{\varepsilon}\nabla_y\phi_0\left(\boldsymbol{x}, \frac{\boldsymbol{x}}{\varepsilon}\right) + \varepsilon\left[\nabla_x\phi_1\left(\boldsymbol{x}, \frac{\boldsymbol{x}}{\varepsilon}\right) + \frac{1}{\varepsilon}\nabla_y\phi_1\left(\boldsymbol{x}, \frac{\boldsymbol{x}}{\varepsilon}\right)\right] \\ & + \varepsilon^2\left[\nabla_x\phi_2\left(\boldsymbol{x}, \frac{\boldsymbol{x}}{\varepsilon}\right) + \frac{1}{\varepsilon}\nabla_y\phi_2\left(\boldsymbol{x}, \frac{\boldsymbol{x}}{\varepsilon}\right)\right] + \mathcal{O}(\varepsilon^2)\,,\end{aligned} \tag{7.15a}$$

$$\begin{aligned}\nabla\theta_\varepsilon(\boldsymbol{x}) = {} & \nabla_x\theta_0\left(\boldsymbol{x}, \frac{\boldsymbol{x}}{\varepsilon}\right) + \frac{1}{\varepsilon}\nabla_y\theta_0\left(\boldsymbol{x}, \frac{\boldsymbol{x}}{\varepsilon}\right) + \varepsilon\left[\nabla_x\theta_1\left(\boldsymbol{x}, \frac{\boldsymbol{x}}{\varepsilon}\right) + \frac{1}{\varepsilon}\nabla_y\theta_1\left(\boldsymbol{x}, \frac{\boldsymbol{x}}{\varepsilon}\right)\right] \\ & + \varepsilon^2\left[\nabla_x\theta_2\left(\boldsymbol{x}, \frac{\boldsymbol{x}}{\varepsilon}\right) + \frac{1}{\varepsilon}\nabla_y\theta_2\left(\boldsymbol{x}, \frac{\boldsymbol{x}}{\varepsilon}\right)\right] + \mathcal{O}(\varepsilon^2)\,.\end{aligned} \tag{7.15b}$$

The next step in the analysis is a detailed examination of the electrical problem. We begin by expanding conductivity tensor $\boldsymbol{\mathcal{S}}\left(\theta_\varepsilon, \frac{\boldsymbol{x}}{\varepsilon}\right)$ into a Taylor series around the macroscopic temperature θ_0

$$\begin{aligned}\boldsymbol{\mathcal{S}}\left(\theta_\varepsilon, \frac{\boldsymbol{x}}{\varepsilon}\right) = {} & \boldsymbol{\mathcal{S}}\left(\theta_0, \frac{\boldsymbol{x}}{\varepsilon}\right) + \varepsilon\,\theta_1\left(\boldsymbol{x}, \frac{\boldsymbol{x}}{\varepsilon}\right)\frac{\partial}{\partial\theta_0}\boldsymbol{\mathcal{S}}\left(\theta_0, \frac{\boldsymbol{x}}{\varepsilon}\right) \\ & + \varepsilon^2\left[\theta_2\left(\boldsymbol{x}, \frac{\boldsymbol{x}}{\varepsilon}\right)\frac{\partial}{\partial\theta_0}\boldsymbol{\mathcal{S}}\left(\theta_0, \frac{\boldsymbol{x}}{\varepsilon}\right) + \theta_1^2\left(\boldsymbol{x}, \frac{\boldsymbol{x}}{\varepsilon}\right)\frac{1}{2}\frac{\partial^2}{\partial\theta_0^2}\boldsymbol{\mathcal{S}}\left(\theta_0, \frac{\boldsymbol{x}}{\varepsilon}\right)\right] + \mathcal{O}\left(\varepsilon^3\right) .\end{aligned} \tag{7.16}$$

It is tacitly assumed that all derivatives employed in the method of asymptotic expansions are sufficiently regular. Substituting (7.3), (7.15a) and (7.16) into the continuity equation for the electric charge (7.1a), and collecting terms of the same order in ε, yields

$$\begin{aligned}-\nabla_x\cdot\left[\boldsymbol{\mathcal{S}}\cdot\left[\nabla_x\phi_0 + \frac{1}{\varepsilon}\nabla_y\phi_0 + \varepsilon\left[\nabla_x\phi_1 + \frac{1}{\varepsilon}\nabla_y\phi_1\right] + \varepsilon^2\left[\nabla_x\phi_2 + \frac{1}{\varepsilon}\nabla_y\phi_2\right] + \mathcal{O}\left(\varepsilon^2\right)\right]\right] \\ -\frac{1}{\varepsilon}\nabla_y\cdot\left[\boldsymbol{\mathcal{S}}\cdot\left[\nabla_x\phi_0 + \frac{1}{\varepsilon}\nabla_y\phi_0 + \varepsilon\left[\nabla_x\phi_1 + \frac{1}{\varepsilon}\nabla_y\phi_1\right] + \varepsilon^2\left[\nabla_x\phi_2 + \frac{1}{\varepsilon}\nabla_y\phi_2\right] + \mathcal{O}\left(\varepsilon^2\right)\right]\right] \\ = 0\end{aligned}$$

(7.17)

Identifying the coefficients for the powers of ε yields a hierarchical set of field equations. By analysing the ε^{-2} equation, we arrive at

$$-\nabla_y \cdot [\boldsymbol{\mathcal{S}}(\theta_0, \boldsymbol{y}) \cdot \nabla_y \phi_0(\boldsymbol{x}, \boldsymbol{y})] = 0\,. \tag{7.18a}$$

For each fixed $\boldsymbol{x} \in \Omega$ we treat $\boldsymbol{y}$ as the variable and interpret (7.18a) in the weak $Y-$periodic sense: Find $\phi_0(\boldsymbol{x}, \cdot) \in H^1_{\#}(Y)/\mathbb{R}$ such that

$$\int_Y \nabla_y \varphi(\boldsymbol{y}) \cdot \boldsymbol{\mathcal{S}}(\theta_0, \boldsymbol{y}) \cdot \nabla_y \phi_0(\boldsymbol{x}, \boldsymbol{y})\, \mathrm{d}y = 0 \qquad \forall \varphi \in H^1_{\#}(Y)/\mathbb{R}\,, \tag{7.18b}$$

where $H^1_{\#}(Y)/\mathbb{R}$ denotes the quotient by additive constants in the microscopic variable $\boldsymbol{y}$. Assuming $\boldsymbol{\mathcal{S}}(\theta_0, \cdot) \in L^\infty_{\#}(Y)^{d\times d}$ to be symmetric, uniformly elliptic and bounded, the associated bilinear form is coercive on $H^1_{\#}(Y)/\mathbb{R}$ and (7.18b) implies $\nabla_y \phi_0(\boldsymbol{x}, \cdot) = \boldsymbol{0}$. Hence, ϕ_0 is independent of $\boldsymbol{y}$ and only depends on the macroscopic variable $\boldsymbol{x}$ so that

$$\phi_0 \equiv \phi_0(\boldsymbol{x})\,. \tag{7.18c}$$

An alternative proof of (7.18c) is provided in Appendix D.1.

The ε^{-1} equation takes the form

$$\begin{aligned} -\nabla_x \cdot [\boldsymbol{\mathcal{S}}(\theta_0, \boldsymbol{y}) \cdot \nabla_y \phi_0] - \nabla_y \cdot [\boldsymbol{\mathcal{S}}(\theta_0, \boldsymbol{y}) \cdot \nabla_x \phi_0] - \nabla_y \cdot [\boldsymbol{\mathcal{S}}(\theta_0, \boldsymbol{y}) \cdot \nabla_y \phi_1] \\ -\nabla_y \cdot \left[\theta_1 \frac{\partial \boldsymbol{\mathcal{S}}(\theta_0, \boldsymbol{y})}{\partial \theta_0} \cdot \nabla_y \phi_0\right] = 0\,. \end{aligned} \tag{7.19a}$$

and by using (7.18c) simplifies to

$$-\nabla_y \cdot [\boldsymbol{\mathcal{S}}(\theta_0, \boldsymbol{y}) \cdot \nabla_y \phi_1] = \nabla_y \cdot [\boldsymbol{\mathcal{S}}(\theta_0, \boldsymbol{y}) \cdot \nabla_x \phi_0]\,. \tag{7.19b}$$

The unknown ϕ_1 within the periodic unit cell Y can be expressed explicitly in terms of ϕ_0. In particular, the linear relation

$$\phi_1(\boldsymbol{x}, \boldsymbol{y}) = \sum_{i=1}^{d} \frac{\partial \phi_0(\boldsymbol{x})}{\partial x_i} \zeta_i(\boldsymbol{x}, \boldsymbol{y}) \tag{7.19c}$$

is obtained, where $\zeta_i \in H^1_{\#} : \Omega \times Y \to \mathbb{R}^d$ for $i \in \{1, \ldots, d\}$ are the solutions to the so-called cell or corrector problem for the electrical field

$$\begin{cases} -\nabla_y \cdot [\boldsymbol{\mathcal{S}}(\theta_0, \boldsymbol{y}) \cdot [\mathbf{e}_i + \nabla_y \zeta_i(\boldsymbol{x}, \boldsymbol{y})]] = 0 & \forall \boldsymbol{y} \in Y\,, \\ \qquad\qquad \boldsymbol{y} \mapsto \zeta_i(\boldsymbol{x}, \boldsymbol{y}) & Y\text{-periodic}\,. \end{cases} \tag{7.19d}$$

The subscript # is used throughout to denote periodic boundary conditions, i.e., $H^1_{\#}(Y)$ refers to the space of functions in H^1 that are Y-periodic. This formulation enables the computation of the corrector field. Here, $\mathbf{e}_i$ represents the canonical basis of $\mathbb{R}^d$. Solving

the cell problem elucidates how microscopic material property fluctuations influence local fields (e.g. temperature or electric potential) and their gradients. This information is integral for deriving the effective (homogenised) material response at the macroscopic scale. The presence of $\mathbf{e}_i$ on the left-hand side represents a unit load applied in the i-th direction, and solving the cell problem (7.19d) for each $\mathbf{e}_i$ yields the corresponding corrector fields ζ_i, which encapsulate the material's microscopic response to directional loading.

Remark 10. The electrical conductivity tensor in the cell problem explicitly incorporates only the spatial variable $\boldsymbol{y}$ and the macroscopic temperature, as demonstrated through the Taylor expansion. This finding aligns with the studies in [114, 174, 175], which address multiscale problems featuring similar temperature-dependent conductivity and stiffness coefficients.}$^{\text{qtd.}}_{[72]}$

Remark 11. As observed by Telega et al. in [174], the weak (variational) formulation of the cell problem treats the macroscopic field as a fixed parameter. This key observation enables the interpretation of the variational problem as a convex minimisation problem. Formulating the local problem in this way allows variational bounding techniques – originally developed for linear problems – to be extended to certain classes of nonlinear problems.

$^{\text{qtd.}}_{[72]}$Proceeding to the ε^0 equation in the asymptotic expansion

$$
\begin{aligned}
&-\nabla_x\cdot\left[\boldsymbol{\mathcal{S}}\left(\theta_0,\boldsymbol{y}\right)\cdot\nabla_x\phi_0\right]-\nabla_x\cdot\left[\boldsymbol{\mathcal{S}}\left(\theta_0,\boldsymbol{y}\right)\cdot\nabla_y\phi_1\right]-\nabla_x\cdot\left[\theta_1\frac{\partial\boldsymbol{\mathcal{S}}\left(\theta_0,\boldsymbol{y}\right)}{\partial\theta_0}\cdot\nabla_y\phi_0\right]\\
&-\nabla_y\cdot\left[\boldsymbol{\mathcal{S}}\left(\theta_0,\boldsymbol{y}\right)\cdot\nabla_x\phi_1\right]-\nabla_y\cdot\left[\boldsymbol{\mathcal{S}}\left(\theta_0,\boldsymbol{y}\right)\cdot\nabla_y\phi_2\right]-\nabla_y\cdot\left[\theta_1\frac{\partial\boldsymbol{\mathcal{S}}\left(\theta_0,\boldsymbol{y}\right)}{\partial\theta_0}\cdot\nabla_x\phi_0\right]\\
&-\nabla_y\cdot\left[\theta_1\frac{\partial\boldsymbol{\mathcal{S}}\left(\theta_0,\boldsymbol{y}\right)}{\partial\theta_0}\cdot\nabla_y\phi_1\right]-\nabla_y\cdot\left[\theta_2\frac{\partial\boldsymbol{\mathcal{S}}\left(\theta_0,\boldsymbol{y}\right)}{\partial\theta_0}\cdot\nabla_y\phi_0\right]\\
&-\nabla_y\cdot\left[\frac{1}{2}\,\theta_1^2\,\frac{\partial^2\boldsymbol{\mathcal{S}}\left(\theta_0,\boldsymbol{y}\right)}{\partial\theta_0^2}\cdot\nabla_y\phi_0\right]=0
\end{aligned}
\tag{7.20a}
$$

and with (7.18c) at hand, we arrive at

$$
\begin{aligned}
&-\nabla_x\cdot\left[\boldsymbol{\mathcal{S}}\left(\theta_0,\boldsymbol{y}\right)\cdot\left[\nabla_x\phi_0+\nabla_y\phi_1\right]\right]-\nabla_y\cdot\left[\boldsymbol{\mathcal{S}}\left(\theta_0,\boldsymbol{y}\right)\cdot\nabla_x\phi_1\right]\\
&\quad-\nabla_y\cdot\left[\theta_1\frac{\partial\boldsymbol{\mathcal{S}}\left(\theta_0,\boldsymbol{y}\right)}{\partial\theta_0}\cdot\left[\nabla_x\phi_0+\nabla_y\phi_1\right]\right]=\nabla_y\cdot\left[\boldsymbol{\mathcal{S}}\left(\theta_0,\boldsymbol{y}\right)\cdot\nabla_y\phi_2\right]\,.
\end{aligned}
\tag{7.20b}
$$

Equation (7.20b) admits a periodic solution for the unknown ϕ_2 if and only if the following compatibility condition is satisfied

$$
\begin{aligned}
\int_Y &-\nabla_x\cdot\left[\boldsymbol{\mathcal{S}}\left(\theta_0,\boldsymbol{y}\right)\cdot\left[\nabla_x\phi_0+\nabla_y\phi_1\right]\right]-\nabla_y\cdot\left[\boldsymbol{\mathcal{S}}\left(\theta_0,\boldsymbol{y}\right)\cdot\nabla_x\phi_1\right]\\
&-\nabla_y\cdot\left[\theta_1\frac{\partial\boldsymbol{\mathcal{S}}\left(\theta_0,\boldsymbol{y}\right)}{\partial\theta_0}\cdot\left[\nabla_x\phi_0+\nabla_y\phi_1\right]\right]\,\mathrm{d}y=0\,.
\end{aligned}
\tag{7.20c}
$$

Constraint (7.20c) can be expressed as equation for ϕ_0 by making use of (7.19c), and since the integral of a periodic function's divergence vanishes, the homogenised equation for the electrical problem further simplifies to

$$-\nabla_x \cdot [\boldsymbol{\mathcal{S}}^* \cdot \nabla_x \phi_0 (\boldsymbol{x})] = 0 \quad \forall \boldsymbol{x} \in \Omega, \tag{7.21a}$$

with the closed-form relation for the homogenised electrical conductivity tensor

$$\mathcal{S}^*_{ij} = \int_Y \mathbf{e}_i \cdot \boldsymbol{\mathcal{S}} (\theta_0, \boldsymbol{y}) \cdot \nabla_y \zeta_j (\boldsymbol{y}) + \mathcal{S}_{ij} (\theta_0, \boldsymbol{y}) \, \mathrm{d}y = \int_Y \mathbf{e}_i \cdot \boldsymbol{\mathcal{S}} (\theta_0, \boldsymbol{y}) \cdot [\nabla_y \zeta_j (\boldsymbol{x}, \boldsymbol{y}) + \mathbf{e}_j] \, \mathrm{d}y \tag{7.21b}$$

A more detailed derivation of the homogenised equation and conductivity tensor is provided in Appendix D.2. The set of equations (7.21) concludes the asymptotic analysis for the electrical problem setting.

Next, the thermal problem is examined. Given the inherent similarities between the electrical and the thermal problem (with the exception of the source terms and conductivity tensor $\boldsymbol{\mathcal{K}}$ assumed to be temperature-independent), the presentation is condensed to avoid redundancy. As in the electrical problem, a cascade of equations is obtained by inserting the constitutive relation for the heat flux vector (7.4) and the asymptotic expansions (7.15) into the energy equation (7.1b)

$$\begin{aligned}
&-\nabla_x \cdot \left[\boldsymbol{\mathcal{K}} (\boldsymbol{y}) \cdot \left[\nabla_x \theta_0 + \frac{1}{\varepsilon} \nabla_y \theta_0 + \varepsilon \left[\nabla_x \theta_1 + \frac{1}{\varepsilon} \nabla_y \theta_1 \right] + \varepsilon^2 \left[\nabla_x \theta_2 + \frac{1}{\varepsilon} \nabla_y \theta_2 \right] + \mathcal{O} \left(\varepsilon^2 \right) \right] \right] \\
&-\frac{1}{\varepsilon} \nabla_y \cdot \left[\boldsymbol{\mathcal{K}} (\boldsymbol{y}) \cdot \left[\nabla_x \theta_0 + \frac{1}{\varepsilon} \nabla_y \theta_0 + \varepsilon \left[\nabla_x \theta_1 + \frac{1}{\varepsilon} \nabla_y \theta_1 \right] + \varepsilon^2 \left[\nabla_x \theta_2 + \frac{1}{\varepsilon} \nabla_y \theta_2 \right] + \mathcal{O} \left(\varepsilon^2 \right) \right] \right] \\
&\quad - \left[\nabla_x \phi_0 + \frac{1}{\varepsilon} \nabla_y \phi_0 + \varepsilon \left[\nabla_x \phi_1 + \frac{1}{\varepsilon} \nabla_y \phi_1 \right] + \varepsilon^2 \left[\nabla_x \phi_2 + \frac{1}{\varepsilon} \nabla_y \phi_2 \right] + \mathcal{O} \left(\varepsilon^2 \right) \right] \\
&\quad \cdot [\boldsymbol{\mathcal{S}} (\theta_0, \boldsymbol{y}) + \dots] \cdot \left[\nabla_x \phi_0 + \frac{1}{\varepsilon} \nabla_y \phi_0 + \varepsilon \left[\nabla_x \phi_1 + \frac{1}{\varepsilon} \nabla_y \phi_1 \right] + \varepsilon^2 \left[\nabla_x \phi_2 + \frac{1}{\varepsilon} \nabla_y \phi_2 \right] \right] \\
&\quad = r_0 (\boldsymbol{x}, \boldsymbol{y}) \, .
\end{aligned} \tag{7.22}$$

Moreover, to simplify the presentation and without loss of generality, the particular form of thermal heat source $r_\varepsilon (\boldsymbol{x}) = \varepsilon^0 r_0 (\boldsymbol{x}, \boldsymbol{y})$ is adopted.

The corresponding ε^{-2} equation is given by

$$-\nabla_y \cdot [\boldsymbol{\mathcal{K}} (\boldsymbol{y}) \cdot \nabla_y \theta_0] = \nabla_y \phi_0 \cdot \boldsymbol{\mathcal{S}} (\theta_0, \boldsymbol{y}) \cdot \nabla_y \phi_0 \, . \tag{7.23a}$$

Due to (7.18c), the right-hand side of (7.23a) vanishes and it is concluded that θ_0 is a function that depends only on the macroscopic variable $\boldsymbol{x}$, namely

$$\theta_0 \equiv \theta_0 (\boldsymbol{x}) \, . \tag{7.23b}$$

With (7.18c) and (7.23b) at hand, the ε^{-1} equation reads,

$$-\nabla_y \cdot [\boldsymbol{\mathcal{K}} (\boldsymbol{y}) \cdot \nabla_y \theta_1] = \nabla_y \cdot [\boldsymbol{\mathcal{K}} (\boldsymbol{y}) \cdot \nabla_x \theta_0] \, . \tag{7.24a}$$

Similarly, (7.24a) is solved by using the linearity of $\theta_1(\boldsymbol{x},\boldsymbol{y})$ with respect to the first derivative of $\theta_0(\boldsymbol{x})$

$$\theta_1(\boldsymbol{x},\boldsymbol{y}) = \sum_{i=1}^{d} \frac{\partial\theta_0(\boldsymbol{x})}{\partial x_i}\,\xi_i(\boldsymbol{y})\;, \tag{7.24b}$$

and by introducing the cell problem for the thermal problem setting

$$\begin{cases} -\nabla_y\cdot[\boldsymbol{\mathcal{K}}(\boldsymbol{y})\cdot[\mathbf{e}_i+\nabla_y\xi_i(\boldsymbol{y})]] = 0 \qquad \forall \boldsymbol{y}\in Y\,, \\ \qquad\qquad\qquad\qquad \boldsymbol{y}\mapsto\xi_i(\boldsymbol{y}) \quad Y\text{-periodic}\,, \end{cases} \tag{7.24c}$$

where $\xi_i \in H^1_{\#} : Y \to \mathbb{R}^d$ for $i\in\{1,\dots,d\}$ are the corresponding solution fields. It is noteworthy that despite the strong coupling of the thermal problem to the electrical problem via the dissipative heat source in (7.1b), the coupling term does not appear at the microscopic level (cell problem). However, the effect of the underlying microstructure clearly manifests itself in the effective form of the macroscale coupling term. Vice versa, the constitutive relations in the electrical problem are evaluated at macroscale temperature θ_0 which is constant in each unit cell. Consequently, this leads to distinct, purely electrical and purely thermal cell problems.

Remark 12. The solution fields to the electrical and thermal cell problem in (7.19c) and (7.24b) are related to the structural tensors defined earlier in Section 7.2.1, i.e.

$$\mathcal{M}^{\phi}_{jk}(\boldsymbol{x},\boldsymbol{y}) = -\frac{\partial\,\zeta_j(\boldsymbol{x},\boldsymbol{y})}{\partial\,y_k} \tag{7.25a}$$

$$\mathcal{M}^{\theta}_{jk}(\boldsymbol{y}) = -\frac{\partial\,\xi_j(\boldsymbol{y})}{\partial\,y_k} \tag{7.25b}$$

To obtain the homogenised macroscale boundary value problem, the ε^0 equation is expressed as

$$\begin{aligned} -\nabla_y\cdot[\boldsymbol{\mathcal{K}}(\boldsymbol{y})\cdot\nabla_y\theta_2] = {}& \nabla_x\cdot[\boldsymbol{\mathcal{K}}(\boldsymbol{y})\cdot\nabla_x\theta_0] + \nabla_x\cdot[\boldsymbol{\mathcal{K}}(\boldsymbol{y})\cdot\nabla_y\theta_1] + \nabla_y\cdot[\boldsymbol{\mathcal{K}}(\boldsymbol{y})\cdot\nabla_x\theta_1] \\ & + \nabla_x\phi_0\cdot\boldsymbol{\mathcal{S}}(\theta_0,\boldsymbol{y})\cdot\nabla_x\phi_0 + 2\,\nabla_x\phi_0\cdot\boldsymbol{\mathcal{S}}(\theta_0,\boldsymbol{y})\cdot\nabla_y\phi_1 \\ & + 2\,\nabla_x\phi_1\cdot\boldsymbol{\mathcal{S}}(\theta_0,\boldsymbol{y})\cdot\nabla_y\phi_0 + \nabla_y\phi_1\cdot\boldsymbol{\mathcal{S}}(\theta_0,\boldsymbol{y})\cdot\nabla_y\phi_1 + r_0(\boldsymbol{x},\boldsymbol{y}) \end{aligned} \tag{7.26a}$$

where use has been made of (7.18c) and (7.23b). Integrating the right-hand side of (7.26a) over Y yields

$$\begin{aligned} \int_Y \nabla_x\cdot[\boldsymbol{\mathcal{K}}(\boldsymbol{y})\cdot[\nabla_x\theta_0+\nabla_y\theta_1]] + \nabla_y\cdot[\boldsymbol{\mathcal{K}}(\boldsymbol{y})\cdot\nabla_x\theta_1] \\ + [\nabla_x\phi_0+\nabla_y\phi_1]\cdot\boldsymbol{\mathcal{S}}(\theta_0,\boldsymbol{y})\cdot[\nabla_x\phi_0+\nabla_y\phi_1] + r_0(\boldsymbol{x},\boldsymbol{y})\;\mathrm{d}y = 0\,. \end{aligned} \tag{7.26b}$$

By inserting (7.19c) and (7.24b) into (7.26b), the homogenised equation for the thermal problem takes the form

$$-\nabla_x\cdot[\boldsymbol{\mathcal{K}}^*\cdot\nabla_x\theta_0(\boldsymbol{x})] - \nabla_x\phi_0(\boldsymbol{x})\cdot\boldsymbol{\mathcal{A}}^*\cdot\nabla_x\phi_0(\boldsymbol{x}) = \int_\Omega r_0(\boldsymbol{x},\boldsymbol{y})\,\mathrm{d}y \quad \forall\boldsymbol{x}\in\Omega\,, \tag{7.27a}$$

where the homogenised thermal conductivity tensor $\boldsymbol{\mathcal{K}}^*$ and coupling tensor $\boldsymbol{\mathcal{A}}^*$ are given by

$$\mathcal{K}^*_{ij} = \int_Y \mathbf{e}_i \cdot \boldsymbol{\mathcal{K}}(\boldsymbol{y}) \cdot [\nabla_y \xi_j(\boldsymbol{y}) + \mathbf{e}_j] \, \mathrm{d}y = \mathbf{e}_i \cdot \int_Y \boldsymbol{\mathcal{K}}(\boldsymbol{y}) \cdot [\mathbf{e}_j \otimes \mathbf{e}_j + \nabla_y \xi_j(\boldsymbol{x}, \boldsymbol{y}) \otimes \mathbf{e}_j] \, \mathrm{d}y \cdot \mathbf{e}_j \,, \tag{7.27b}$$

$$\begin{aligned} \mathcal{A}^*_{ij} &= \int_Y [\nabla_y \zeta_i(\boldsymbol{x}, \boldsymbol{y}) + \mathbf{e}_i] \cdot \boldsymbol{\mathcal{S}}(\theta_0, \boldsymbol{y}) \cdot [\nabla_y \zeta_j(\boldsymbol{x}, \boldsymbol{y}) + \mathbf{e}_j] \, \mathrm{d}y \\ &= \mathbf{e}_i \cdot \int_Y [\mathbf{e}_i \otimes \mathbf{e}_i + \mathbf{e}_i \otimes \nabla_y \xi_i(\boldsymbol{x}, \boldsymbol{y})] \cdot \boldsymbol{\mathcal{S}}(\theta_0, \boldsymbol{y}) \cdot [\mathbf{e}_j \otimes \mathbf{e}_j + \nabla_y \xi_j(\boldsymbol{x}, \boldsymbol{y}) \otimes \mathbf{e}_j] \, \mathrm{d}y \cdot \mathbf{e}_j \,. \end{aligned} \tag{7.27c}$$

The tensors $\boldsymbol{\mathcal{S}}^*, \boldsymbol{\mathcal{K}}^*, \boldsymbol{\mathcal{A}}^*$ describe the effective (homogenised) properties of the heterogeneous material. To solve the thermo-electrically coupled system of equations (7.1a) and (7.1b), correctors ζ_i and ξ_i are determined by solving the cell problems (7.21a) and (7.27a), respectively. These computations involve solving $2 \times d$ boundary value problems, which yield the homogenised effective electrical conductivity tensor $\boldsymbol{\mathcal{S}}^*$, thermal conductivity tensor $\boldsymbol{\mathcal{K}}^*$, and coupling tensor $\boldsymbol{\mathcal{A}}^*$. With the homogenised tensors at hand, the homogenised (macroscale) problem can be solved for ϕ_0 and θ_0. If the first-order terms are required, ϕ_1 and θ_1 can be calculated using (7.19c) and (7.24b). Notably, the final homogenised problem and the homogenised tensors are identical to the solution obtained from the analytical approach discussed in Section 7.2.3, validating the accuracy and effectiveness of the asymptotic homogenisation method for the problem at hand. Finally observe the identity $\mathcal{A}^*_{ij} = \mathcal{S}^*_{ij}$, since

$$\begin{aligned} 0 &= \int_Y \nabla_y \zeta_i(\boldsymbol{x}, \boldsymbol{y}) \cdot \boldsymbol{\mathcal{S}}(\theta_0, \boldsymbol{y}) \cdot [\nabla_y \zeta_j(\boldsymbol{x}, \boldsymbol{y}) + \mathbf{e}_j] \, \mathrm{d}y \\ &= \int_{\partial Y} \boldsymbol{n}(\boldsymbol{y}) \cdot \boldsymbol{\mathcal{S}}(\theta_0, \boldsymbol{y}) \cdot [\nabla_y \zeta_j(\boldsymbol{y}) + \mathbf{e}_j] \, \zeta_i(\boldsymbol{y}) \, \mathrm{d}y \\ &\quad - \int_Y \nabla_y \cdot [\boldsymbol{\mathcal{S}}(\theta_0, \boldsymbol{y}) \cdot [\nabla_y \zeta_j(\boldsymbol{y}) + \mathbf{e}_j]] \, \zeta_i(\boldsymbol{y}) \, \mathrm{d}y \end{aligned} \tag{7.28}$$

holds, by virtue of (7.19d).

Remark 13. Comparing the effective conductivity tensors derived from Hill–Mandel type homogenisation (7.12) and asymptotic expansions (7.21b)-(7.27b), we observe that Hill–Mandel homogenisation yields volume-averaged quantities, whereas asymptotic and subsequent analytical homogenisation do not explicitly account for the factor $1/\mathrm{vol}(Y)$. The underlying reason is that asymptotic and analytic homogenisation are typically carried out after a dimensional analysis such that the unit cell is rescaled to $Y = (0,1)^d$ and the $1/\mathrm{vol}(Y)$-factor is implicitly accounted for.}$^{\text{qtd.}}_{[72]}$

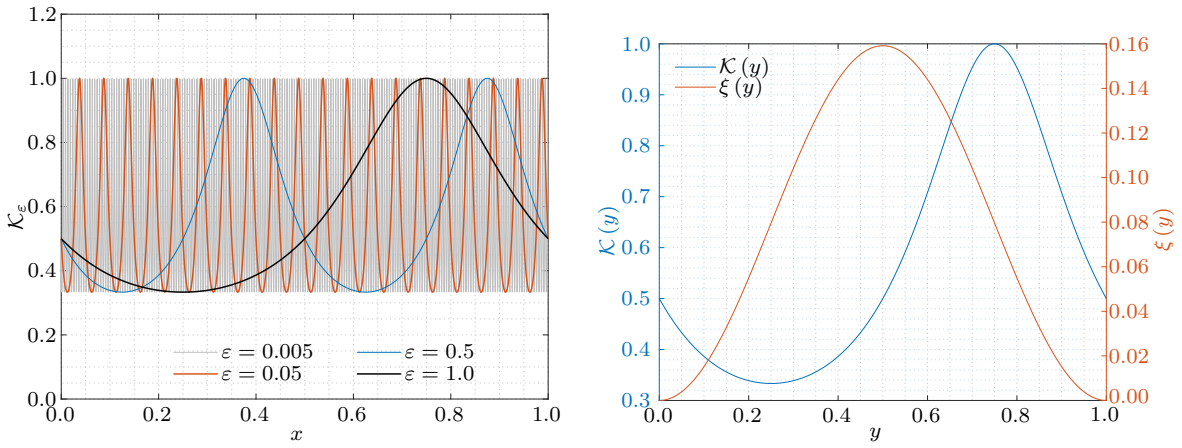

(a) Conductivity as a function of x, with various ε values

(b) Characteristic and conductivity function over Y

Figure 7.2: Illustration of model problem

Remark 14. To demonstrate the principles of homogenisation in a simplified setting, we consider the one-dimensional stationary heat conduction problem governed by the Poisson equation on a domain $\Omega = (0, 1)$. The temperature field θ_ε satisfies

$$-\nabla \cdot \left[\mathcal{K}\left(\frac{x}{\varepsilon}\right) \cdot \nabla\theta_\varepsilon(x)\right] = r(x) \quad \text{in} \quad \Omega\,, \tag{7.29a}$$

$$\theta_\varepsilon(x) = 0 \quad \text{on} \quad \partial\Omega\,. \tag{7.29b}$$

Under the assumption of strict scale separation, $\ell \ll L$, the thermal conductivity $\mathcal{K}\left(\frac{x}{\varepsilon}\right)$

$$\mathcal{K}\left(\frac{x}{\varepsilon}\right) = \frac{1}{2 + \sin\left(2\,\pi\,\frac{x}{\varepsilon}\right)} \tag{7.30}$$

exhibits rapid oscillations $\varepsilon \to 0$, see Figure 7.2. The homogenised limit problem reads

$$-\nabla \cdot [\mathcal{K}^* \cdot \nabla\theta_0(x)] = r(x) \quad \text{in} \quad \Omega\,, \tag{7.31a}$$

$$\theta_0(x) = 0 \quad \text{on} \quad \partial\Omega\,, \tag{7.31b}$$

where $\mathcal{K}^*$ denotes the effective thermal conductivity. To derive the homogenised model, we employ a two-scale asymptotic expansion of the form

$$\theta_\varepsilon(x) \approx \theta_0(x) + \varepsilon\,\theta_1\left(x, \frac{x}{\varepsilon}\right)\,. \tag{7.32}$$

In one-dimensional periodic homogenisation, the effective thermal conductivity is given by the harmonic mean of a unit period $Y = (0, 1)$. For the specific form of $\mathcal{K}(y) = 1/[2 + \sin(2\,\pi\,y)]$, the resulting homogenised conductivity is

$$\mathcal{K}^* = \frac{1}{2}\,. \tag{7.33}$$

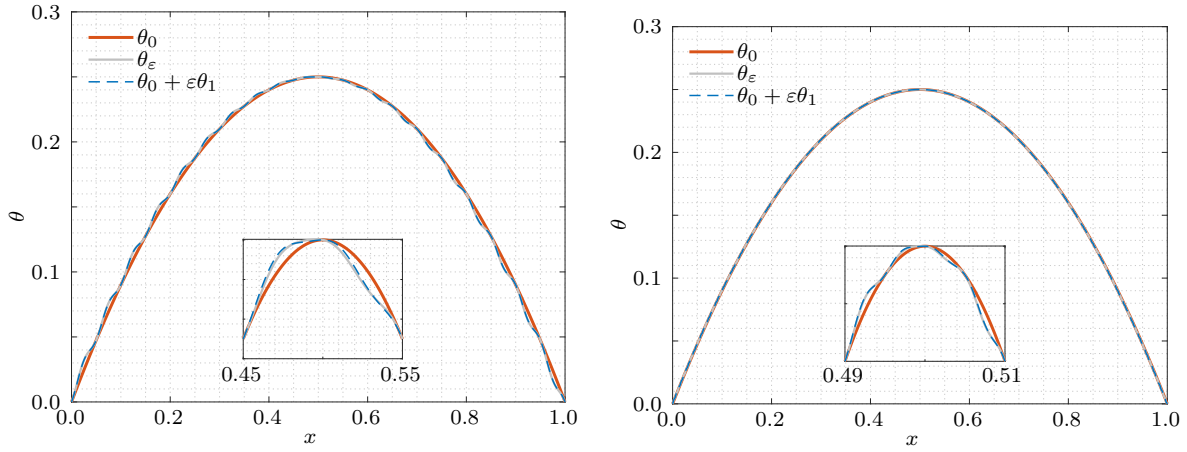

(a) $\varepsilon = 0.05$ **(b)** $\varepsilon = 0.005$

Figure 7.3: The macroscopic solution θ_0 to the limit problem (7.31) and approximated solution with corrector field $\theta_\varepsilon \approx \theta_0 + \varepsilon\,\theta_1$ and exact solution θ_ε for different ε values.

The detailed derivation of this result, along with the corresponding cell problem and first-order corrector function, is provided in Appendix D.3. With the effective conductivity result at hand, the macroscale temperature is expressed as

$$\theta_0\,(x) = -x^2 + x = x\,[1 - x] \tag{7.34}$$

with the applied boundary conditions, $\theta_0(0) = \theta_0(1) = 0$. A two-scale expansion yields the first-order corrector

$$\theta_\varepsilon\,(x) \approx \theta_0\,(x) + \varepsilon\,\xi\left(\frac{x}{\varepsilon}\right)\frac{\mathrm{d}\theta_0\,(x)}{\mathrm{d}x} = x\,[1 - x] + \frac{\varepsilon}{4\,\pi}\left[1 - \cos\left(2\,\pi\,\frac{x}{\varepsilon}\right)\right][1 - 2\,x] \tag{7.35}$$

compared to the exact solution

$$\theta_\varepsilon\,(x) = -x^2 + 2\,C_1\,x + \frac{\varepsilon}{2\,\pi}\,x\,\cos\left(2\,\pi\frac{x}{\varepsilon}\right) - \left[\frac{\varepsilon}{2\,\pi}\right]^2\sin\left(2\,\pi\frac{x}{\varepsilon}\right) - C_1\frac{\varepsilon}{2\,\pi}\cos\left(2\,\pi\frac{x}{\varepsilon}\right) + C_2 \tag{7.36a}$$

with constants

$$C_1 = C_2\left[\frac{2\,\pi}{\varepsilon}\right], \tag{7.36b}$$

$$C_2 = \frac{\varepsilon}{4\,\pi} - \frac{\varepsilon^2}{8\,\pi^2}\,. \tag{7.36c}$$

Figure 7.3 compares the homogenised solution (7.34), the first-order corrector (7.35), and the exact solution (7.36a) for different ε values. As expected, the first-order corrector significantly improves the approximation of θ_ε by capturing the oscillatory behaviour, especially for moderately small ε.

7.2.3 Two-scale convergence

$\overset{\text{qtd.}}{\underset{[72]}{}}\{$The aim of analytical homogenisation is to derive the effective properties and governing equations for heterogeneous materials in a mathematically rigorous manner. In the following thesis, the method of *two-scale convergence*, which was introduced by Nguetseng [139] and Allaire [3], is employed to perform the homogenisation of the coupled system of second-order elliptic equations. Before proceeding with a rigorous analysis of the problem, we introduce the concept of two-scale convergence and related definitions:

Definition 24. **(Weak two-scale convergence)** Let $1 \leq p < \infty$. A sequence of function u_ε in $L^p(\Omega)$ is said to two-scale converge weakly to a limit $u_0 \in L^p(\Omega \times Y)$ if, for any function $\varphi(\boldsymbol{x}, \boldsymbol{y})$ in $L^q(\Omega; C_\#(Y))$, it satisfies

$$\lim_{\varepsilon \to 0} \int_\Omega u_\varepsilon(\boldsymbol{x})\, \varphi\left(\boldsymbol{x}, \frac{\boldsymbol{x}}{\varepsilon}\right) \mathrm{d}x = \int_\Omega \int_Y u_0(\boldsymbol{x}, \boldsymbol{y})\, \varphi(\boldsymbol{x}, \boldsymbol{y})\, \mathrm{d}y\, \mathrm{d}x\,, \tag{7.37}$$

where $C_\#$ denotes the space of differentiable functions in $\mathbb{R}^d$ that are periodic of period Y, and q is such that $\frac{1}{p} + \frac{1}{q} = 1$. We adopt the notation $u_\varepsilon \overset{p}{\rightharpoonup} u_0$, and if we want to emphasise the dependence on the variables, we write $u_\varepsilon(\boldsymbol{x}) \overset{p}{\rightharpoonup} u_0(\boldsymbol{x}, \boldsymbol{y})$.

Definition 25. **(Strong two-scale convergence)** Let $1 \leq p < \infty$. A sequence of function u_ε in $L^p(\Omega)$, is said to two-scale converge strongly to a limit $u_0 \in L^p(\Omega \times Y)$ if $u_\varepsilon \overset{p}{\rightharpoonup} u_0$ and

$$\lim_{\varepsilon \to 0} \|u_\varepsilon\|_{L^p(\Omega)} \to \|u_0\|_{L^p(\Omega \times Y)}\,. \tag{7.38}$$

We write $u_\varepsilon \overset{p}{\twoheadrightarrow} u_0$ or $u_\varepsilon(\boldsymbol{x}) \overset{p}{\twoheadrightarrow} u_0(\boldsymbol{x}, \boldsymbol{y})$. $\}^{\text{qtd.}}_{[72]}$

Remark 15. The two-scale limit contains more information than the standard L^p limit. This is due to the fact that the microscopic oscillations are retained in the two-scale limit, whereas they are averaged out in classical weak convergence. In this work, we adopt the intuitive interpretation of two-scale convergence introduced in [143] and further employed in [53, 96].

To illustrate this concept, we revisit the approximate function introduced in Remark 14. Let $\Omega = (0, 1)$, and consider the two sequences

$$u_\varepsilon\left(x, \frac{x}{\varepsilon}\right) = x\,[1 - x] + \frac{1}{4\,\pi}\left[1 - \cos\left(2\,\pi\,\frac{x}{\varepsilon}\right)\right][1 - 2\,x]\,, \tag{7.39a}$$

$$\widetilde{u}_\varepsilon\left(x, \frac{x}{\varepsilon}\right) = x\,[1 - x] + \frac{1}{4\,\pi}\left[1 - \cos\left(2\,\pi\,\frac{x}{\varepsilon}\right)\right][1 - 2\,x] + \sin\left(4\,\pi\,\frac{x}{\varepsilon}\right)\,, \tag{7.39b}$$

which both share the same weak $L^2(\Omega)$ limit, namely

$$u(x) = x\,[1 - x]\,. \tag{7.39c}$$

However, for fixed ε, they possess different two-scale limits

$$u_0(x, y) = x\,[1 - x] + \frac{1}{4\,\pi}\,[1 - \cos(2\,\pi\,y)]\,[1 - 2\,x] \tag{7.40a}$$

and

$$\widetilde{u}_0(x,y) = x\,[1-x] + \frac{1}{4\,\pi}\,[1-\cos(2\,\pi\,y)]\,[1-2\,x] + \sin(4\,\pi\,y) \tag{7.40b}$$

as illustrated in Figure 7.4.

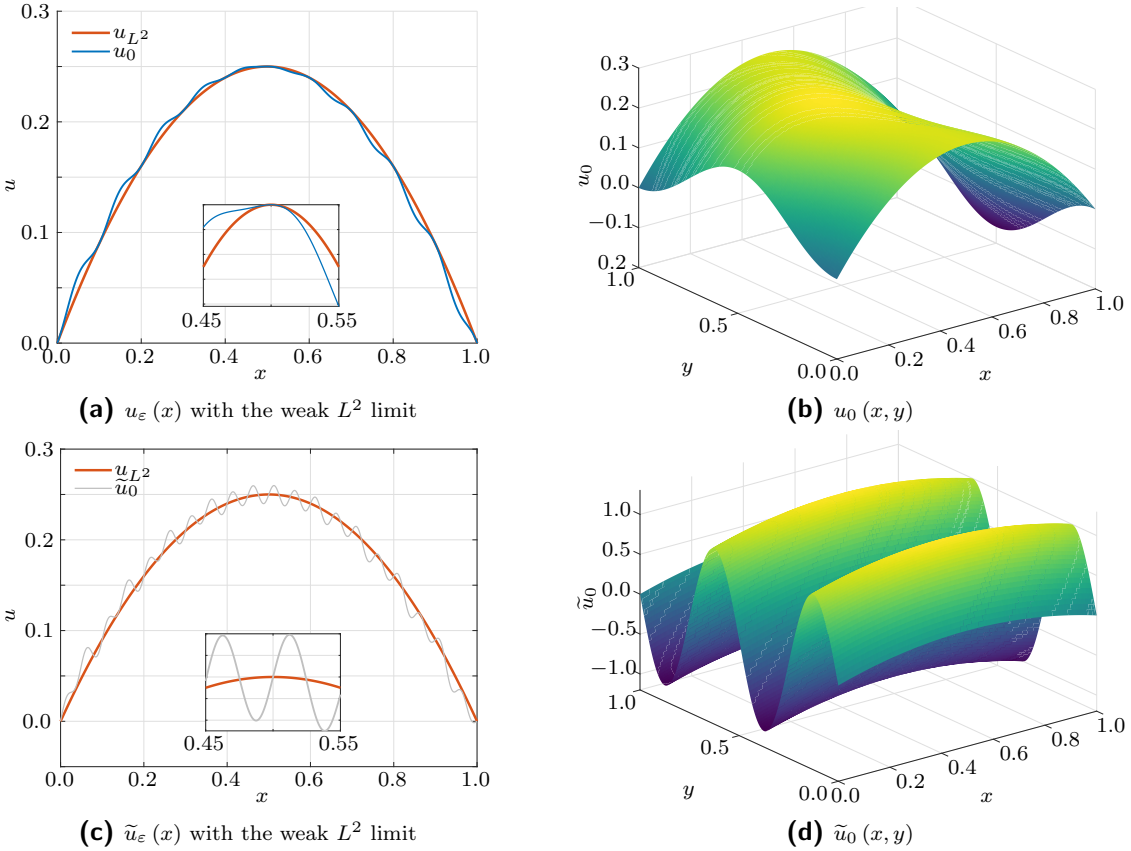

(a) $u_\varepsilon(x)$ with the weak L^2 limit **(b)** $u_0(x,y)$

(c) $\widetilde{u}_\varepsilon(x)$ with the weak L^2 limit **(d)** $\widetilde{u}_0(x,y)$

Figure 7.4: Comparison of the sequences u_ε and $\widetilde{u}_\varepsilon$.

Lemma 1. [qtd. [72]]{**(Admissible test functions)** Let $1 \leq p < \infty$, and $B_p(\Omega;Y)$ denote one of the following Banach spaces $L^p(\Omega;C_\#(Y))$, $L^p\left(Y;C\left(\bar{\Omega}\right)\right)$ or $C\left(\bar{\Omega};C_\#(Y)\right)$. For every function $u \in B_p(\Omega;Y)$, $u\left(\boldsymbol{x},\frac{\boldsymbol{x}}{\varepsilon}\right) \in L^p(\Omega)$ and

$$\lim_{\varepsilon\to 0}\left\|u\left(\boldsymbol{x},\frac{\boldsymbol{x}}{\varepsilon}\right)\right\|_{L^p(\Omega)} \to \|u\|_{L^p(\Omega)}\,, \tag{7.41}$$

hold. Moreover, for $1 < p < \infty$, the relation $u\left(\boldsymbol{x},\frac{\boldsymbol{x}}{\varepsilon}\right) \twoheadrightarrow u$ holds.

The convergence of $\left\|u\left(\boldsymbol{x},\frac{\boldsymbol{x}}{\varepsilon}\right)\right\|_{L^p(\Omega)}$ is shown in [122, Theorem 4] and the two-scale convergence can be deduced as in [181, Lemma 1.7].

We have to formulate compactness results, guaranteeing the existence of convergent subsequences within a bounded set, in order to give sense to weak and strong two-scale convergence theorems:

Theorem 1. **(Two-scale compactness result)** If u_ε is a bounded sequence in $L^p(\Omega)$, where $1 < p < \infty$, then there exists a subsequence u_ε and an $u_0 \in L^p(\Omega \times Y)$, such that

$$u_\varepsilon \xrightarrow{p} u_0 \,. \tag{7.42}$$

Theorem 2. **(Two-scale compactness result for weakly differentiable functions)** Let u_ε be a bounded sequence in $W^{1,p}(\Omega)$, where $p \in (1, \infty)$, which converges weakly to $u_0 \in W^{1,p}(\Omega)$. Then, there exist $u_0 \in W^{1,p}(\Omega)$, $u_1 \in L^p\left(\Omega; W^{1,p}_{\#}(Y)/\mathbb{R}\right)$ and a subsequence u_ε such that

$$u_\varepsilon \xrightarrow{p} u_0 \,, \tag{7.43}$$

$$\nabla u_\varepsilon \xrightarrow{p} \nabla_x u_0 + \nabla_y u_1 \,, \tag{7.44}$$

where $W^{1,p}_{\#}(Y)$ denotes the space of Y-periodic $W^{1,p}$-functions.

For a.e. $\boldsymbol{x} \in \Omega$ we consider the equivalence class $[u_1(\boldsymbol{x}, \boldsymbol{y})] \in W^{1,p}_{\#}(Y)/\mathbb{R}$ and set

$$\left\| [u_1(\boldsymbol{x}, \boldsymbol{y})] \right\|_{W^{1,p}_{\#}(Y)/\mathbb{R}} := \left\| \nabla_y u_1(\boldsymbol{x}, \boldsymbol{y}) \right\|_{L^p(Y)} . \tag{7.45}$$

This is well defined since $\nabla_y(u_1(\boldsymbol{x}, \boldsymbol{y}) + c) = \nabla_y u_1(\boldsymbol{x}, \boldsymbol{y})$ for any $c \in \mathbb{R}$ and, by the periodic Poincaré–Wirtinger inequality, it is equivalent to $\inf_{c \in \mathbb{R}} \| u_1(\boldsymbol{x}, \boldsymbol{y}) - c \|_{W^{1,p}(Y)}$. With this choice, the space $L^p\left(\Omega; W^{1,p}_{\#}(Y)/\mathbb{R}\right)$ is well defined. This outcome is natural because the underlying fields contribute to the cell problem in form of their gradients only. The proofs for Theorem 1 an Theorem 2 for $p = 2$ are found in [3] and for the general case $1 < p < \infty$ in [122, Theorem 13].

Lemma 2. **(Products of two-scale-converging functions)** Let $1 < p, p_1, p_2 < \infty$ such that $\frac{1}{p_1} + \frac{1}{p_2} = \frac{1}{p}$. Let u_ε be a sequence in $L^{p_1}(\Omega)$, v_ε a sequence in $L^{p_2}(\Omega)$ and $u_0 \in L^{p_1}(\Omega \times Y)$, $v_0 \in L^{p_2}(\Omega \times Y)$ such that $u_\varepsilon \xrightarrow{p_1} u_0$ and $v_\varepsilon \xrightarrow{p_2} v_0$ (respectively $v_\varepsilon \xrightarrow{p_2} v_0$). Then, $u_\varepsilon v_\varepsilon \xrightarrow{p} u_0 v_0$ (respectively $u_\varepsilon v_\varepsilon \xrightarrow{p} u_0 v_0$).

Lemma 2 is shown for instance in [181, Lemma 1.14 (respectively Lemma 1.15)].

To model the thermo-electrical response of materials as introduced in Section 7.1, we consider the following coupled system of partial differential equations

$$-\nabla \cdot \left[\boldsymbol{\mathcal{S}}_\varepsilon(\theta_\varepsilon(\boldsymbol{x}), \boldsymbol{x}) \cdot \nabla \phi_\varepsilon(\boldsymbol{x}) \right] = 0 \quad \forall \boldsymbol{x} \in \Omega \,, \tag{7.46a}$$

$$-\nabla \cdot \left[\boldsymbol{\mathcal{K}}_\varepsilon(\boldsymbol{x}) \cdot \nabla \theta_\varepsilon(\boldsymbol{x}) \right] - \nabla \phi_\varepsilon(\boldsymbol{x}) \cdot \boldsymbol{\mathcal{S}}_\varepsilon(\theta_\varepsilon(\boldsymbol{x}), \boldsymbol{x}) \cdot \nabla \phi_\varepsilon(\boldsymbol{x}) = r_\varepsilon(\boldsymbol{x}) \quad \forall \boldsymbol{x} \in \Omega \,, \tag{7.46b}$$

with the boundary conditions

$$\phi_\varepsilon = \phi_p \text{ on } \partial\Omega \tag{7.46c}$$

$$\theta_\varepsilon = \theta_p \text{ on } \partial\Omega \,. \tag{7.46d}$$

On domain Ω the medium consists of a fine mixture of different materials or phases leading to space dependent coefficients $\boldsymbol{\mathcal{S}}_\varepsilon$ and $\boldsymbol{\mathcal{K}}_\varepsilon$. We assume that the typical length

scale for the mixture is of order $0 < \varepsilon \ll 1$. In order to rigorously prove results, we focus on a Dirichlet-type problem with boundary values $\{\bullet\}_p$. Additionally, to state a well-posed weak form of (7.46), we pose the following assumptions on the electrical and thermal conductivity tensors and boundary conditions:

Assumption 1. We assume that

- $\boldsymbol{\mathcal{S}}_\varepsilon(\theta, \boldsymbol{x}) = \mathcal{S}_1(\theta)\, \boldsymbol{\mathcal{S}}_2(\boldsymbol{x}/\varepsilon)$ for $\mathcal{S}_1 \in C^0(\mathbb{R}, [s_{\min}, s_{\max}])$ for constants $0 < s_{\min} < s_{\max} < \infty$, $\boldsymbol{\mathcal{S}}_2 \in L^\infty_\#(Y)^{d\times d}$ with $\boldsymbol{\gamma}\cdot\boldsymbol{\mathcal{S}}_2\cdot\boldsymbol{\gamma} \geq \alpha|\boldsymbol{\gamma}|^2$ for a constant $\alpha > 0$ and all $\boldsymbol{\gamma} \in \mathbb{R}^d$,
- $\boldsymbol{\mathcal{K}}_\varepsilon(\boldsymbol{x}) = \boldsymbol{\mathcal{K}}(\boldsymbol{x}/\varepsilon)$ for $\boldsymbol{\mathcal{K}} \in L^\infty_\#(Y)^{d\times d}$ with $\boldsymbol{\gamma}\cdot\boldsymbol{\mathcal{K}}\cdot\boldsymbol{\gamma} \geq \alpha|\boldsymbol{\gamma}|^2$ for a constant $\alpha > 0$ and all $\boldsymbol{\gamma} \in \mathbb{R}^d$,
- $\theta_p \in H^1(\Omega)$, $\phi_p \in H^1(\Omega)$ with $\max\{\phi_p - \phi_m, 0\}, \max\{-\phi_p - \phi_m, 0\} \in H^1_0(\Omega)$ for some $\phi_m < \infty$.

Remark 16. The homogenisation results to be established in this section can be generalised to coefficients $\boldsymbol{\mathcal{S}}_\varepsilon$ of the form $\boldsymbol{\mathcal{S}}_\varepsilon(\theta, \boldsymbol{x}) = \boldsymbol{\mathcal{S}}(\theta, \boldsymbol{x}, \boldsymbol{x}/\varepsilon)$ for $\boldsymbol{\mathcal{S}} \in C^0\left(\mathbb{R}, C^0\left(\overline{\Omega}, L^\infty_\#(Y)\right)\right)^{d\times d}$, such that $\boldsymbol{\mathcal{S}}$ is uniformly coercive and bounded, i.e. there exist constants $\alpha, C > 0$ such that

$$\boldsymbol{\gamma}\cdot\boldsymbol{\mathcal{S}}(\theta, \boldsymbol{x}, \boldsymbol{y})\cdot\boldsymbol{\gamma} \geq \alpha|\boldsymbol{\gamma}|^2 \quad \text{for all } \theta, \boldsymbol{x} \in \mathbb{R}\times\overline{\Omega} \text{ and a.e. } \boldsymbol{y} \in Y, \quad \|\mathcal{S}\|_{L^\infty(\mathbb{R}\times\Omega\times Y)} \leq C. \tag{7.47}$$

The corresponding weak formulations are obtained as follows. We substitute $u_\varepsilon \coloneqq \phi_\varepsilon - \phi_p$ and $v_\varepsilon \coloneqq \theta_\varepsilon - \theta_p$, multiply (7.46a) and (7.46b) with test functions $\varphi^\phi, \varphi^\theta$, integrate over the domain Ω and use the divergence theorem to arrive at:

Find $(u_\varepsilon, v_\varepsilon) \in H^1_0(\Omega)\times H^1_0(\Omega)$ such that

$$\begin{aligned}
&\int_\Omega \nabla\varphi^\phi(\boldsymbol{x})\cdot\boldsymbol{\mathcal{S}}_\varepsilon([\theta_p + v_\varepsilon](\boldsymbol{x}), \boldsymbol{x})\cdot\nabla u_\varepsilon(\boldsymbol{x})\ \mathrm{d}x \\
&\quad = -\int_\Omega \nabla\varphi^\phi(\boldsymbol{x})\cdot\boldsymbol{\mathcal{S}}_\varepsilon([\theta_p + v_\varepsilon](\boldsymbol{x}), \boldsymbol{x})\cdot\nabla\phi_p(\boldsymbol{x})\ \mathrm{d}x, \qquad (7.48a) \\
&\int_\Omega \nabla\varphi^\theta(\boldsymbol{x})\cdot\boldsymbol{\mathcal{K}}_\varepsilon(\boldsymbol{x})\cdot\nabla v_\varepsilon(\boldsymbol{x})\ \mathrm{d}x = -\int_\Omega \nabla\varphi^\theta(\boldsymbol{x})\cdot\boldsymbol{\mathcal{K}}_\varepsilon(\boldsymbol{x})\cdot\nabla\theta_p(\boldsymbol{x})\ \mathrm{d}x \\
&\quad -\int_\Omega \nabla[\phi_p + u_\varepsilon](\boldsymbol{x})\cdot\boldsymbol{\mathcal{S}}_\varepsilon([\theta_p + v_\varepsilon](\boldsymbol{x}), \boldsymbol{x})\cdot\nabla[\phi_p + u_\varepsilon](\boldsymbol{x})\ \varphi^\theta(\boldsymbol{x})\ \mathrm{d}x \\
&\quad -\int_\Omega r_\varepsilon(\boldsymbol{x})\,\varphi^\theta(\boldsymbol{x})\ \mathrm{d}x \qquad (7.48b)
\end{aligned}$$

for all $\varphi^\phi \in H^1_0(\Omega)$ and $\varphi^\theta \in H^1_0(\Omega)$

Proposition 1. Let $\boldsymbol{\mathcal{S}}_\varepsilon$, $\boldsymbol{\mathcal{K}}_\varepsilon$, ϕ_p and θ_p satisfy Assumption 1. Then, there exists a solution $(u_\varepsilon, v_\varepsilon) \in H_0^1(\Omega) \times H_0^1(\Omega)$ of (7.48). Moreover, there exists a constant C such that for all solutions $(u_\varepsilon, v_\varepsilon) \in H_0^1(\Omega) \times H_0^1(\Omega)$ of (7.48)

$$\|u_\varepsilon\|_{L^2(\Omega)} + \|\nabla u_\varepsilon\|_{L^2(\Omega)} + \|v_\varepsilon\|_{L^2(\Omega)} + \|\nabla v_\varepsilon\|_{L^2(\Omega)} \leq C\,, \tag{7.49}$$

and for $\phi_\varepsilon = \phi_p + u_\varepsilon$,

$$\|\phi_\varepsilon\|_{L^\infty(\Omega)} \leq C\,, \tag{7.50}$$

holds.

Proof. We show the existence of a solution $(u_\varepsilon, v_\varepsilon) \in H_0^1(\Omega) \times H_0^1(\Omega)$ of (7.48) by means of a fixed point argument.

The fixed point operator $L_\varepsilon \colon L^2(\Omega) \to H_0^1(\Omega)$ maps a given $\widetilde{v}_\varepsilon \in L^2(\Omega)$ on $v_\varepsilon \in H_0^1(\Omega)$, which is the first part of the solution $(v_\varepsilon, u_\varepsilon)$ of

$$\begin{aligned}
&\int_\Omega \nabla\varphi^\phi(\boldsymbol{x}) \cdot \boldsymbol{\mathcal{S}}_\varepsilon\left([\theta_p + v_\varepsilon](\boldsymbol{x}), \boldsymbol{x}\right) \cdot \nabla u_\varepsilon(\boldsymbol{x})\ \mathrm{d}x = \\
&\qquad -\int_\Omega \nabla\varphi^\phi(\boldsymbol{x}) \cdot \boldsymbol{\mathcal{S}}_\varepsilon\left([\theta_p + v_\varepsilon](\boldsymbol{x}), \boldsymbol{x}\right) \cdot \nabla \phi_p(\boldsymbol{x})\ \mathrm{d}x \qquad \forall \varphi^\phi \in H_0^1(\Omega)\,,
\end{aligned} \tag{7.51a}$$

$$\begin{aligned}
&\int_\Omega \nabla\varphi^\theta(\boldsymbol{x}) \cdot \boldsymbol{\mathcal{K}}_\varepsilon(\boldsymbol{x}) \cdot \nabla v_\varepsilon(\boldsymbol{x})\ \mathrm{d}x = -\int_\Omega \nabla\varphi^\theta(\boldsymbol{x}) \cdot \boldsymbol{\mathcal{K}}_\varepsilon(\boldsymbol{x}) \cdot \nabla \theta_p(\boldsymbol{x})\ \mathrm{d}x \\
&-\int_\Omega \nabla\left[\phi_p + u_\varepsilon\right](\boldsymbol{x}) \cdot \boldsymbol{\mathcal{S}}_\varepsilon\left([\theta_p + \widetilde{v}_\varepsilon](\boldsymbol{x}), \boldsymbol{x}\right) \cdot \nabla\left[\phi_p + u_\varepsilon\right](\boldsymbol{x})\, \varphi^\theta(\boldsymbol{x})\ \mathrm{d}x \\
&-\int_\Omega r_\varepsilon(\boldsymbol{x})\, \varphi^\theta(\boldsymbol{x})\ \mathrm{d}x \qquad\qquad \forall \varphi^\theta \in H_0^1(\Omega)\,.
\end{aligned} \tag{7.51b}$$

Note that (7.48) differs from (7.51) in that $\boldsymbol{\mathcal{S}}_\varepsilon\left([\theta_p + v_\varepsilon](\boldsymbol{x}), \boldsymbol{x}\right)$ is replaced by $\boldsymbol{\mathcal{S}}_\varepsilon\left([\theta_p + \widetilde{v}_\varepsilon](\boldsymbol{x}), \boldsymbol{x}\right)$. This changes the bi-directional coupling of the equations to a one-directional coupling. Thus, one can solve (7.51a) for u_ε without considering (7.48b), and in a second step solve (7.48b) for v_ε.

A natural definition of L_ε would be a composition of the solution operator $U_\varepsilon \colon L^2(\Omega) \to H_0^1(\Omega)$ of (7.51a) and a solution operator for (7.48b) that maps a given $u_\varepsilon \in H_0^1(\Omega)$ on the solution v_ε. However, such a solution operator would not be well-defined, since the second integral on the right-hand side of (7.48b) is not well-defined for arbitrary $u_\varepsilon \in H^1(\Omega)$ and $\varphi^\theta \in H_0^1(\Omega)$ due to a lack of integrability. However, we show below that: if u_ε is additionally a solution to (7.51a) for given $\widetilde{v}_\varepsilon$, this integral can be identified with $\langle R_\varepsilon(\widetilde{v}_\varepsilon), \varphi^\theta\rangle_{H^{-1}(\Omega), H_0^1(\Omega)}$ for an element $R_\varepsilon(\widetilde{v}_\varepsilon) = R_\varepsilon(\widetilde{v}_\varepsilon) \in H^{-1}(\Omega)$ and, thus, is well-defined. Note that R_ε itself is a mapping from $L^2(\Omega)$ to $H^{-1}(\Omega)$ with

$$\begin{aligned}
&\langle R_\varepsilon(\widetilde{v}_\varepsilon), \varphi^\theta\rangle_{H^{-1}(\Omega),\, H_0^1(\Omega)} = \\
&\qquad -\int_\Omega \nabla\left[\phi_p + U_\varepsilon(\widetilde{v}_\varepsilon)\right](\boldsymbol{x}) \cdot \boldsymbol{\mathcal{S}}_\varepsilon\left([\theta_p + \widetilde{v}_\varepsilon](\boldsymbol{x}), \boldsymbol{x}\right) \cdot \nabla\left[\phi_p + U_\varepsilon(\widetilde{v}_\varepsilon)\right](\boldsymbol{x})\ \varphi^\theta(\boldsymbol{x})\ \mathrm{d}x\,.
\end{aligned} \tag{7.52}$$

Consequently, instead of (7.51b), we consider the equation

$$\int_\Omega \nabla\varphi^\theta(\boldsymbol{x})\cdot\boldsymbol{\mathcal{K}}_\varepsilon(\boldsymbol{x})\cdot\nabla v_\varepsilon(\boldsymbol{x})\ \mathrm{d}x = -\int_\Omega \nabla\varphi^\theta(\boldsymbol{x})\cdot\boldsymbol{\mathcal{K}}_\varepsilon(\boldsymbol{x})\cdot\nabla\theta_p(\boldsymbol{x})\ \mathrm{d}x$$
$$+\langle \text{h.s.},\varphi\rangle_{H^{-1}(\Omega),H_0^1(\Omega)} - \int_\Omega r_\varepsilon(\boldsymbol{x})\,\varphi^\theta(\boldsymbol{x})\ \mathrm{d}x \qquad \forall\varphi^\theta\in H_0^1(\Omega) \tag{7.53}$$

for some h.s. $\in H^{-1}(\Omega)$ and denote the solution operator of (7.53) by $V_\varepsilon\colon H^{-1}(\Omega)\to L^2(\Omega)$, i.e. h.s. $\mapsto V_\varepsilon(\text{h.s.}) := v_\varepsilon$, where $v_\varepsilon\in H_0^1(\Omega)$ is the solution of (7.53).

We define L_ε by $v_\varepsilon\mapsto L_\varepsilon(v_\varepsilon) := (V_\varepsilon\circ R_\varepsilon)(\widetilde{v}_\varepsilon)$ and obtain for well-defined U_ε, R_ε and V_ε from (7.51a), (7.53) and (7.52) that $(v_\varepsilon,u_\varepsilon)$ is a solution to (7.48) if and only if v_ε is a fixed point of L_ε and $u_\varepsilon = U_\varepsilon(v_\varepsilon)$, i.e. $(v_\varepsilon,u_\varepsilon) = (L_\varepsilon(v_\varepsilon), U_\varepsilon(v_\varepsilon))$. To apply Schauder's fixed point theorem, we have to verify that L_ε is continuous and has a bounded range in $H^1(\Omega)$. Then, Rellich's theorem yields the compactness of L_ε as mapping from $L^2(\Omega)$ to $L^2(\Omega)$.

Solution operator U_ε for (7.51a) with given $\widetilde{v}_\varepsilon$:

Let $\widetilde{v}_\varepsilon\in L^2(\Omega)$ be given. To show that U_ε is well-defined, we have to show that (7.51a) has a unique solution $u_\varepsilon\in H_0^1(\Omega)$ for given $\widetilde{v}_\varepsilon\in L^2(\Omega)$.

By Assumption 1, the coefficient field $\boldsymbol{\mathcal{S}}_\varepsilon((\theta_p+\widetilde{v}_\varepsilon)(\boldsymbol{x}),\boldsymbol{x}) = \mathcal{S}_1([\theta_p+\widetilde{v}_\varepsilon](\boldsymbol{x}))\,\boldsymbol{\mathcal{S}}_2(\boldsymbol{x}/\varepsilon)$ satisfies the uniform bounds $\alpha\, s_{\min}|\boldsymbol{\xi}|^2 \le \boldsymbol{\xi}\cdot\boldsymbol{\mathcal{S}}_\varepsilon([\theta_p+\widetilde{v}_\varepsilon](\boldsymbol{x}),\boldsymbol{x})\cdot\boldsymbol{\xi}$ and $\boldsymbol{\xi}\cdot\boldsymbol{\mathcal{S}}_\varepsilon([\theta_p+\widetilde{v}_\varepsilon](\boldsymbol{x}),\boldsymbol{x})\cdot\boldsymbol{\gamma} \le s_{\max}\|\boldsymbol{\mathcal{S}}_2\|_{L^\infty(Y)}|\boldsymbol{\xi}||\boldsymbol{\gamma}|$ for a.e. $\boldsymbol{x}$ and all $\boldsymbol{\xi},\boldsymbol{\gamma}\in\mathbb{R}^d$. Consequently, the bilinear form $a_{\varepsilon,v}(u,\varphi) = \int_\Omega \nabla\varphi\cdot\boldsymbol{\mathcal{S}}_\varepsilon([\theta_p+\widetilde{v}_\varepsilon](\boldsymbol{x}),\boldsymbol{x})\cdot\nabla u\ \mathrm{d}x$ is uniformly coercive and bounded on $H_0^1(\Omega)$ with constants independent of $\widetilde{v}_\varepsilon$. Thus, we can apply the Lemma of Lax-Milgram, which shows the existence and uniqueness of a solution $u_\varepsilon\in H_0^1(\Omega)$ to (7.51a) for all $\varphi^\phi\in H_0^1(\Omega)$ and given $\widetilde{v}_\varepsilon\in L^2(\Omega)$. In order to obtain ε-independent *a priori* estimates, we choose $\varphi^\phi = u_\varepsilon$ as a test function in (7.51a), and use the uniform coercivity condition and essential boundedness of the coefficient matrix $\boldsymbol{\mathcal{S}}_\varepsilon$ introduced in Assumption 1,

$$\begin{aligned}\alpha\, s_{\min}\|\nabla u_\varepsilon\|_{L^2(\Omega)}^2 &\le \int_\Omega \nabla u_\varepsilon(\boldsymbol{x})\cdot\boldsymbol{\mathcal{S}}_\varepsilon([\theta_p+\widetilde{v}_\varepsilon](\boldsymbol{x}),\boldsymbol{x})\cdot\nabla u_\varepsilon(\boldsymbol{x})\ \mathrm{d}x\\ &= -\int_\Omega \nabla u_\varepsilon(\boldsymbol{x})\cdot\boldsymbol{\mathcal{S}}_\varepsilon([\theta_p+\widetilde{v}_\varepsilon](\boldsymbol{x}),\boldsymbol{x})\cdot\nabla\phi_p(\boldsymbol{x})\ \mathrm{d}x\\ &\le s_{\max}\|\boldsymbol{\mathcal{S}}_2\|_{L^\infty(\Omega)}\|\nabla\phi_p\|_{L^2(\Omega)}\|\nabla u_\varepsilon\|_{L^2(\Omega)} \le C\|\nabla u_\varepsilon\|_{L^2(\Omega)}.\end{aligned} \tag{7.54}$$

Using the Poincaré inequality, we can also estimate $\|u_\varepsilon\|_{L^2(\Omega)}$ and obtain

$$\|u_\varepsilon\|_{L^2(\Omega)} + \|\nabla u_\varepsilon\|_{L^2(\Omega)} \le C \tag{7.55}$$

for a constant C, which is independent of ε.

Continuity of U_ε:

For fixed $\varepsilon > 0$, let $(\widetilde{v}_{\varepsilon,i})_{i\in\mathbb{N}}$ be a sequence in $L^2(\Omega)$ that converges to $\widetilde{v}_\varepsilon \in L^2(\Omega)$ and let $u_\varepsilon = U_\varepsilon(\widetilde{v}_\varepsilon)$, $u_{\varepsilon,i} = U_\varepsilon(\widetilde{v}_{\varepsilon,i})$ for $i \in \mathbb{N}$. Thus, $\widetilde{v}_\varepsilon, u_\varepsilon$ satisfy (7.51a) and $\widetilde{v}_{\varepsilon,i}, u_{\varepsilon,i}$ satisfy

$$\begin{aligned}\int_\Omega \nabla\varphi^\phi(\boldsymbol{x}) \cdot \boldsymbol{\mathcal{S}}_\varepsilon([\theta_p + \widetilde{v}_{\varepsilon,i}](\boldsymbol{x}), \boldsymbol{x}) \cdot \nabla u_{\varepsilon,i}(\boldsymbol{x})\,\mathrm{d}x = \\ -\int_\Omega \nabla\varphi^\phi(\boldsymbol{x}) \cdot \boldsymbol{\mathcal{S}}_\varepsilon([\theta_p + \widetilde{v}_{\varepsilon,i}](\boldsymbol{x}), \boldsymbol{x}) \cdot \nabla\phi_p(\boldsymbol{x})\,\mathrm{d}x \quad \forall\varphi^\phi \in H_0^1(\Omega).\end{aligned} \tag{7.56}$$

We subtract (7.51a) from (7.56) and choose $\varphi^\phi = u_{\varepsilon,i} - u_\varepsilon$. After rearranging, we obtain

$$\begin{aligned}&\int_\Omega \nabla[u_{\varepsilon,i} - u_\varepsilon](\boldsymbol{x}) \cdot \boldsymbol{\mathcal{S}}_\varepsilon([\theta_p + \widetilde{v}_{\varepsilon,i}](\boldsymbol{x}), \boldsymbol{x}) \cdot \nabla[u_{\varepsilon,i} - u_\varepsilon](\boldsymbol{x})\,\mathrm{d}x = \\ &-\int_\Omega \nabla[u_{\varepsilon,i} - u_\varepsilon](\boldsymbol{x}) \cdot [\boldsymbol{\mathcal{S}}_\varepsilon([\theta_p + \widetilde{v}_{\varepsilon,i}](\boldsymbol{x}), \boldsymbol{x}) - \boldsymbol{\mathcal{S}}_\varepsilon([\theta_p + \widetilde{v}_\varepsilon](\boldsymbol{x}), \boldsymbol{x})] \cdot \nabla[\phi_p + u_\varepsilon](\boldsymbol{x})\,\mathrm{d}x.\end{aligned} \tag{7.57}$$

We estimate the left-hand side using the uniform coercivity of $\boldsymbol{\mathcal{S}}_\varepsilon([\theta_p + \widetilde{v}_{\varepsilon,i}](\boldsymbol{x}), \boldsymbol{x})$ and the right-hand side using the Hölder inequality to arrive at

$$\begin{aligned}&\alpha s_{\min} \|\nabla[u_{\varepsilon,i} - u_\varepsilon]\|_{L^2(\Omega)}^2 \leq \\ &\quad \|[\boldsymbol{\mathcal{S}}_\varepsilon(\theta_p + \widetilde{v}_{\varepsilon,i}, \boldsymbol{x}) - \boldsymbol{\mathcal{S}}_\varepsilon(\theta_p + \widetilde{v}_\varepsilon, \boldsymbol{x})]\ \nabla[\phi_p + u_\varepsilon]\|_{L^2(\Omega)} \|\nabla[u_{\varepsilon,i} - u_\varepsilon]\|_{L^2(\Omega)}.\end{aligned} \tag{7.58}$$

We divide (7.58) by $\|\nabla[u_{\varepsilon,i} - u_\varepsilon]\|_{L^2(\Omega)}$, if it is different from zero, to deduce

$$\|\nabla[u_{\varepsilon,i} - u_\varepsilon]\|_{L^2(\Omega)} \leq C \|[\boldsymbol{\mathcal{S}}_\varepsilon(\theta_p + \widetilde{v}_{\varepsilon,i}, \boldsymbol{x}) - \boldsymbol{\mathcal{S}}_\varepsilon(\theta_p + \widetilde{v}_\varepsilon, \boldsymbol{x})]\ \nabla[\phi_p + u_\varepsilon]\|_{L^2(\Omega)}. \tag{7.59}$$

We note that the convergence of $\widetilde{v}_{\varepsilon,i} \to \widetilde{v}_\varepsilon$ in $L^2(\Omega)$ implies $\|\boldsymbol{\mathcal{S}}_\varepsilon(\theta_p + \widetilde{v}_{\varepsilon,i}, \cdot) - \boldsymbol{\mathcal{S}}_\varepsilon(\theta_p + \widetilde{v}_\varepsilon, \cdot)\|_{L^2(\Omega)} \to 0$ since $\boldsymbol{\mathcal{S}}_\varepsilon$ is continuous with respect to its first argument and essentially bounded. Application of Lemma 3 to the sequence $\boldsymbol{\mathcal{S}}_\varepsilon(\theta_p + \widetilde{v}_{\varepsilon,i}, \cdot) - \boldsymbol{\mathcal{S}}_\varepsilon(\theta_p + \widetilde{v}_\varepsilon, \cdot)$ and to the constant sequence $\nabla[\phi_p + u_\varepsilon]$ shows the convergence of the right-hand side of (7.59) to zero for $i \to \infty$. Thus, $\|\nabla[u_{\varepsilon,i} - u_\varepsilon]\|_{L^2(\Omega)} \to 0$, which shows that $U_\varepsilon \colon L^2(\Omega) \to H_0^1(\Omega)$ is continuous.

Right-hand side of (7.53) (R_ε):

We note that for arbitrary $u_\varepsilon, \widetilde{v}_\varepsilon \in H_0^1(\Omega)$ the second integral on the right-hand side of (7.51b) is not well-posed due to a lack of integrability. A priori, we can only use test functions $\varphi^\theta \in W_0^{1,\infty}(\Omega)$. Thus, we cannot use the fixed-point argument to determine a solution v_ε to (7.51b) for arbitrary given $u_\varepsilon \in H_0^1(\Omega)$. Instead, we show that the mapping of φ^θ to the second integral on the right-hand side of (7.51b) can be identified by an element in $H^{-1}(\Omega)$ if $u_\varepsilon, \widetilde{v}_\varepsilon \in H_0^1(\Omega)$ satisfy (7.51a), i.e. $u_\varepsilon = U_\varepsilon(\widetilde{v}_\varepsilon)$.

Let $\widetilde{v}_\varepsilon \in L^2(\Omega)$ be given and $u_\varepsilon = U_\varepsilon(\widetilde{v}_\varepsilon) \in H_0^1(\Omega)$ be the solution to (7.51a) as defined above. We apply the weak maximum principle [63, Theorem 8.1] on $-\nabla \cdot [\boldsymbol{\mathcal{S}}_\varepsilon([\theta_p + \widetilde{v}_\varepsilon](\boldsymbol{x}), \boldsymbol{x}) \cdot \nabla [\phi_p + u_\varepsilon](\boldsymbol{x})] = 0$ so as to estimate $\|u_\varepsilon + \phi_p\|_{L^\infty(\Omega)}$ by the boundary values

$$\|u_\varepsilon + \phi_p\|_{L^\infty(\Omega)} \leq \sup_{\partial\Omega} |u_\varepsilon + \phi_p| = \sup_{\partial\Omega} |\phi_p| \leq \phi_m \,. \tag{7.60}$$

Let $\varphi \in C_0^1(\Omega)$ be arbitrary. We choose $\varphi^\phi = [\phi_p + u_\varepsilon]\,\varphi \in H_0^1(\Omega)$ in (7.51a) and use the product rule

$$\begin{aligned} 0 &= \int_\Omega \nabla \left[[\phi_p + u_\varepsilon](\boldsymbol{x})\ \varphi(\boldsymbol{x})\right] \cdot \boldsymbol{\mathcal{S}}_\varepsilon([\theta_p + \widetilde{v}_\varepsilon](\boldsymbol{x}), \boldsymbol{x}) \cdot \nabla [\phi_p + u_\varepsilon](\boldsymbol{x})\ \mathrm{d}x \\ &= \int_\Omega \nabla [\phi_p + u_\varepsilon](\boldsymbol{x}) \cdot \boldsymbol{\mathcal{S}}_\varepsilon([\theta_p + \widetilde{v}_\varepsilon](\boldsymbol{x}), \boldsymbol{x}) \cdot \nabla [\phi_p + u_\varepsilon](\boldsymbol{x})\ \varphi(\boldsymbol{x})\ \mathrm{d}x \\ &\quad + \int_\Omega \nabla\varphi(\boldsymbol{x}) \cdot \boldsymbol{\mathcal{S}}_\varepsilon([\theta_p + \widetilde{v}_\varepsilon](\boldsymbol{x}), \boldsymbol{x}) \cdot \nabla [\phi_p + u_\varepsilon](\boldsymbol{x})\ [\phi_p + u_\varepsilon](\boldsymbol{x})\ \mathrm{d}x \\ &=: R_\varepsilon(\widetilde{v}_\varepsilon, \varphi) + \widetilde{R}_\varepsilon(\widetilde{v}_\varepsilon, \varphi)\ . \end{aligned} \tag{7.61}$$

Using the Hölder inequality and the uniform estimates (7.55) and (7.60), we obtain

$$|\widetilde{R}_\varepsilon(\widetilde{v}_\varepsilon, \varphi)| \leq C\, \|\nabla [\phi_p + u_\varepsilon]\|_{L^2(\Omega)}\, \|\phi_p + u_\varepsilon\|_{L^\infty(\Omega)}\, \|\nabla\varphi\|_{L^2(\Omega)} \leq C\, \|\nabla\varphi\|_{L^2(\Omega)} \tag{7.62}$$

for all $\varphi \in C_0^1(\Omega)$, with a constant C independent of ε. Hence, for fixed $\widetilde{v}_\varepsilon$, the map $\varphi \mapsto \widetilde{R}_\varepsilon(\widetilde{v}_\varepsilon, \varphi)$ is a bounded linear functional on $C_0^1(\Omega)$ with respect to the H_0^1-norm. Since $C_0^1(\Omega)$ is dense in $H_0^1(\Omega)$, this functional extends uniquely by continuity to an element of $H^{-1}(\Omega)$. We denote this extension by $\widetilde{R}_\varepsilon(\widetilde{v}_\varepsilon)$ and obtain the uniform bound

$$\|\widetilde{R}_\varepsilon(\widetilde{v}_\varepsilon)\|_{H^{-1}(\Omega)} \leq C\,. \tag{7.63}$$

Thus, we get $\widetilde{R}_\varepsilon(\widetilde{v}_\varepsilon, \cdot) = \widetilde{R}_\varepsilon(\widetilde{v}_\varepsilon) \in H^{-1}(\Omega)$ and by (7.61) arrive at $R_\varepsilon(\widetilde{v}_\varepsilon) = R_\varepsilon(\widetilde{v}_\varepsilon, \cdot) = -\widetilde{R}_\varepsilon(\widetilde{v}_\varepsilon, \cdot) = -\widetilde{R}_\varepsilon(\widetilde{v}_\varepsilon) \in H^{-1}(\Omega)$. Additionally, with the uniform estimate of (7.62) at hand, we obtain

$$\|R_\varepsilon(\widetilde{v}_\varepsilon)\|_{H^{-1}(\Omega)} = \|\widetilde{R}_\varepsilon(\widetilde{v}_\varepsilon)\|_{H^{-1}(\Omega)} \leq C\,. \tag{7.64}$$

Continuity of R_ε:

Let $\widetilde{v}_\varepsilon, \widetilde{v}_{\varepsilon,i} \in L^2(\Omega)$ and $u_\varepsilon = U_\varepsilon(\widetilde{v}_\varepsilon)$, $u_{\varepsilon,i} = U_\varepsilon(\widetilde{v}_{\varepsilon,i})$ for $i \in \mathbb{N}$ such that $\widetilde{v}_{\varepsilon,i} \to \widetilde{v}_\varepsilon$ in $L^2(\Omega)$, which implies the convergence $u_{\varepsilon,i} \to u_\varepsilon$ in $H^1(\Omega)$ by the continuity of U_ε and the uniform essential boundedness of $u_{\varepsilon,i} + \phi_p$. With the Hölder inequality, we get

$$\begin{aligned} \|R_\varepsilon(\widetilde{v}_\varepsilon) - R_\varepsilon(\widetilde{v}_{\varepsilon,i})\|_{H^{-1}(\Omega)} &= \sup_{\varphi \in H_0^1(\Omega),\, \varphi \neq 0} \frac{|R_\varepsilon(\widetilde{v}_\varepsilon, \varphi) - R_\varepsilon(\widetilde{v}_{\varepsilon,i}, \varphi)|}{\|\varphi\|_{H_0^1(\Omega)}} \\ &= \sup_{\varphi \in H_0^1(\Omega),\, \varphi \neq 0} \frac{|\widetilde{R}_\varepsilon(\widetilde{v}_\varepsilon, \varphi) - \widetilde{R}_\varepsilon(\widetilde{v}_{\varepsilon,i}, \varphi)|}{\|\nabla\varphi\|_{L^2(\Omega)}} \\ \leq \|\boldsymbol{\mathcal{S}}_\varepsilon(\theta_p + \widetilde{v}_\varepsilon) \cdot \nabla [\phi_p + u_\varepsilon]\ [\phi_p + u_\varepsilon] &- \boldsymbol{\mathcal{S}}_\varepsilon(\theta_p + \widetilde{v}_{\varepsilon,i}) \cdot \nabla [\phi_p + u_{\varepsilon,i}]\ [\phi_p + u_{\varepsilon,i}]\, \|_{L^2(\Omega)}\,. \end{aligned} \tag{7.65}$$

Arguing as above, the strong convergence of $\widetilde{v}_{\varepsilon,i}$ to $\widetilde{v}_\varepsilon$ implies the strong convergence of $\boldsymbol{\mathcal{S}}_\varepsilon\left(\left[\theta_p+\widetilde{v}_{\varepsilon,i}\right](\boldsymbol{x}),\boldsymbol{x}\right)$ to $\boldsymbol{\mathcal{S}}_\varepsilon\left(\left[\theta_p+\widetilde{v}_\varepsilon\right](\boldsymbol{x}),\boldsymbol{x}\right)$. Then, we apply Lemma 3 twice to deduce the convergence of the right-hand side of (7.65) to zero and, thus, the continuity of $R_\varepsilon\colon L^2(\Omega)\to H^{-1}(\Omega)$.

Solution operator V_ε for (7.53) with given heat source (h.s.) in $H^{-1}(\Omega)$:

The lemma of Lax-Milgram ensures the existence and uniqueness of a solution $v_\varepsilon\in H_0^1(\Omega)$ of (7.53) and, thus, V_ε is well-defined. Moreover, choosing $\varphi^\theta=v_\varepsilon$ and using the uniform coercivity and boundedness of $\boldsymbol{\mathcal{K}}_\varepsilon$, standard energy estimates and the Poincaré inequality lead to

$$\|v_\varepsilon\|_{L^2(\Omega)}+\|\nabla v_\varepsilon\|_{L^2(\Omega)}\leq C\left[\|\nabla\theta_p\|_{L^2(\Omega)}+\|\text{h.s.}\|_{H^{-1}(\Omega)}\right]. \tag{7.66}$$

Compactness of the fixed point operator and a priori estimates:

Combining the estimates (7.64) and (7.66) yields

$$\|L_\varepsilon\left(\widetilde{v}_\varepsilon v_\varepsilon\right)\|_{L^2(\Omega)}+\|\nabla L_\varepsilon\left(\widetilde{v}_\varepsilon v_\varepsilon\right)\|_{L^2(\Omega)}\leq C\qquad\text{for all }\widetilde{v}_\varepsilon v_\varepsilon\in H_0^1(\Omega). \tag{7.67}$$

Using the compact embedding of $j\colon H_0^1(\Omega)\to L^2(\Omega)$ and the continuity of V_ε and R_ε, we obtain that $j\circ L_\varepsilon$ is a compact operator from $\{v\in L^2(\Omega)\mid\|v\|_{L^2(\Omega)}\leq C\}$ to $\{v\in L^2(\Omega)\mid\|v\|_{L^2(\Omega)}\leq C\}$ for a sufficiently large constant C.

Schauder's fixed point theorem establishes the existence of a fixed point $v_\varepsilon\in L^2(\Omega)$ such that (7.48) has a solution. A priori bounds in (7.49) then follow by combining: (i) the energy estimate for the electrical problem, cf. (7.55), which gives $\|u_\varepsilon\|_{L^2(\Omega)}+\|\nabla u_\varepsilon\|_{L^2(\Omega)}\leq C$; (ii) the energy estimate for the thermal problem with h.s. $=R_\varepsilon(v_\varepsilon)$, cf. (7.66), which gives $\|v_\varepsilon\|_{L^2(\Omega)}+\|\nabla v_\varepsilon\|_{L^2(\Omega)}\leq C$; and (iii) the weak maximum principle for $\phi_\varepsilon=\phi_p+u_\varepsilon$, cf. (7.60), which yields $\|\phi_\varepsilon\|_{L^\infty(\Omega)}\leq C$.}$^{\text{qtd.}}_{[72]}$ □

Remark 17. In the case of linear second-order elliptic equations of the form

$$-\nabla\cdot\left[\boldsymbol{\mathcal{K}}_\varepsilon(\boldsymbol{x})\cdot\nabla\theta_\varepsilon(\boldsymbol{x})\right]=r_\varepsilon(\boldsymbol{x})\quad\forall\boldsymbol{x}\in\Omega, \tag{7.68a}$$

with the boundary condition

$$\theta_\varepsilon=\theta_p\ \text{ on }\partial\Omega. \tag{7.68b}$$

and r_ε denoting a given function in $L^2(\Omega)$, it admits a unique solution θ_ε in H_0^1. Owing to the well-posedness and linearity of the problem, one may directly rely on classical existence and uniqueness results from elliptic PDE theory. As a consequence, the intermediate regularity steps discussed earlier can be avoided in this case.

Theorem 3. qtd. [72]{ Let $(u_\varepsilon, v_\varepsilon) \in H_0^1(\Omega) \times H_0^1(\Omega)$ be a sequence of solutions of (7.48), with the following definitions $u_\varepsilon \coloneqq \phi_\varepsilon - \phi_p$ and $v_\varepsilon \coloneqq \theta_\varepsilon - \theta_p$. Then, there exists a subsequence $(\phi_\varepsilon, \theta_\varepsilon)$ such that

$$\phi_\varepsilon \to \phi_0 \qquad \text{in } L^2(\Omega)\,, \tag{7.69a}$$
$$\theta_\varepsilon \to \theta_0 \qquad \text{in } L^2(\Omega)\,, \tag{7.69b}$$

where $(\phi_0, \theta_0) \in H^1(\Omega) \times H^1(\Omega)$ is a solution of

$$\int_\Omega \nabla_x \varphi_0^\phi(\boldsymbol{x}) \cdot \boldsymbol{\mathcal{S}}^*(\theta_0(\boldsymbol{x}), \boldsymbol{x}) \cdot \nabla_x \phi_0(\boldsymbol{x})\, \mathrm{d}x = 0\,, \tag{7.70a}$$

$$\begin{aligned}&\int_\Omega \nabla_x \varphi_0^\theta(\boldsymbol{x}) \cdot \boldsymbol{\mathcal{K}}^*(\boldsymbol{x}) \cdot \nabla_x \theta_0(\boldsymbol{x})\, \mathrm{d}x = \\ &-\int_\Omega \varphi_0^\theta(\boldsymbol{x})\, \nabla_x \phi_0(\boldsymbol{x}) \cdot \boldsymbol{\mathcal{A}}^*(\theta_0(\boldsymbol{x}), \boldsymbol{x}) \cdot \nabla_x \phi_0(\boldsymbol{x})\, \mathrm{d}x - \int_\Omega r_0(\boldsymbol{x})\, \varphi_0^\theta(\boldsymbol{x})\, \mathrm{d}x\end{aligned} \tag{7.70b}$$

for all $\varphi_0^\phi \in H^1(\Omega)$ and $\varphi_0^\theta \in H^1(\Omega)$.
The effective conductivity and coupling tensors for a parameter $\theta_0 \in \mathbb{R}$ are given by

$$\mathcal{S}_{ij}^*(\theta_0) = \int_Y \mathbf{e}_i \cdot \boldsymbol{\mathcal{S}}(\theta_0, \boldsymbol{y}) \cdot [\mathbf{e}_j + \nabla_y \zeta_j]\, \mathrm{d}y\,, \tag{7.71a}$$

$$\mathcal{K}_{ij}^* = \int_Y \mathbf{e}_i \cdot \boldsymbol{\mathcal{K}}(\boldsymbol{y}) \cdot [\mathbf{e}_j + \nabla_y \xi_j]\, \mathrm{d}y\,, \tag{7.71b}$$

$$\mathcal{A}_{ij}^*(\theta_0) = \int_Y [\mathbf{e}_i + \nabla_y \zeta_i] \cdot \boldsymbol{\mathcal{S}}(\theta_0, \boldsymbol{y}) \cdot [\mathbf{e}_j + \nabla_y \zeta_j]\, \mathrm{d}y\,, \tag{7.71c}$$

where use has been made of the solutions $\zeta_i(\theta_0, \boldsymbol{y}) \in H_\#^1(Y)$ to the decoupled electrical cell problem

$$\int_Y \nabla_y \varphi_1^\phi(\boldsymbol{y}) \cdot \boldsymbol{\mathcal{S}}(\theta_0, \boldsymbol{y}) \cdot [\mathbf{e}_i + \nabla_y \zeta_i(\theta_0, \boldsymbol{y})]\, \mathrm{d}y = 0 \text{ for all } \varphi_1^\phi \in H_\#^1(Y) \tag{7.72a}$$

and the solutions $\xi_i(\boldsymbol{y}) \in H_\#^1(Y)$ to the thermal cell problem

$$\int_Y \nabla_y \varphi_1^\theta(\boldsymbol{y}) \cdot \boldsymbol{\mathcal{K}}(\boldsymbol{y}) \cdot [\mathbf{e}_i + \nabla_y \xi_i(\boldsymbol{y})]\, \mathrm{d}y = 0 \text{ for all } \varphi_1^\theta \in H_\#^1(Y)\,. \tag{7.72b}$$

Remark 18. In Theorem 3, the convergence result holds only up to subsequences since the uniqueness of the solution to the limit equation is not clear. The convergence result for $(\phi_\varepsilon, \theta_\varepsilon)$ could be extended to the entire sequence, if one could show that the limit system (7.70) has a unique solution.

Proof. Before we can identify the limit equations, we deduce the precise form of the two-scale limit of the sequences ϕ_ε and θ_ε. By Proposition 1, the sequences u_ε and v_ε are bounded in $H_0^1(\Omega)$. Thus, there exist $u_0, v_0 \in H_0^1(\Omega)$ and subsequences u_ε and v_ε such that u_ε and v_ε converge weakly in $H_0^1(\Omega)$ to u_0 and v_0, respectively. By the compact embedding of $H_0^1(\Omega)$ in $L^2(\Omega)$ and after passing to a further subsequence, the strong convergence results $u_\varepsilon \to u_0$ and $v_\varepsilon \to v_0$ are obtained. Moreover, by the two-scale compactness result for gradients, Theorem 2, we obtain u_1, $v_1 \in L^2\left(\Omega, H^1_\#(Y)\right)$ such that after passing to a further subsequence we arrive at

$$\nabla u_\varepsilon \rightharpoonup \nabla_x u_0 + \nabla_y u_1\,, \qquad \nabla v_\varepsilon \rightharpoonup \nabla_x v_0 + \nabla_y v_1\,. \tag{7.73}$$

To shorten the notation in the limit process, we work in terms of $\phi_\varepsilon := u_\varepsilon + \phi_p$ and $\theta_\varepsilon := v_\varepsilon + \theta_p$ instead of u_ε and v_ε. We get the convergence results

$$\phi_\varepsilon \to \phi_0\,, \qquad \theta_\varepsilon \to \theta_0 \qquad \text{in } L^2(\Omega)\,, \tag{7.74}$$

$$\nabla\phi_\varepsilon \overset{2}{\rightharpoonup} \nabla_x\phi_0 + \nabla_y\phi_1\,, \qquad \nabla\theta_\varepsilon \overset{2}{\rightharpoonup} \nabla_x\theta_0 + \nabla_y\theta_1 \tag{7.75}$$

for $\phi_0 := u_0 + \phi_p$, $\theta_0 := v_0 + \theta_p$, $\phi_1 = u_1$ and $\theta_1 = v_1$.

Moreover, due to the uniform essential boundedness of ϕ_ε given by (7.50) in Proposition 1, we can improve the convergence result to

$$\phi_\varepsilon \to \phi_0 \qquad \text{in } L^p(\Omega) \tag{7.76}$$

for every $p \in [1, \infty)$.

Passage to the limit for the electrical problem:

We test (7.48a) with test function

$$\varphi^\phi(\boldsymbol{x}) = \varphi_0^\phi(\boldsymbol{x}) + \varepsilon\,\varphi_1^\phi\left(\boldsymbol{x}, \frac{\boldsymbol{x}}{\varepsilon}\right) \tag{7.77}$$

where $\varphi_0^\phi(\boldsymbol{x}) \in C_0^\infty(\Omega)$ and $\varphi_1^\phi \in C_0^\infty\left(\Omega; C^\infty_\#(Y)\right)$. The high frequency oscillations are of period ε and in resonance with the oscillations of ϕ_ε of the same frequency. Hence, these oscillations are not hidden by averaging while passing to the limit in

$$\int_\Omega \left[\nabla_x\varphi_0^\phi(\boldsymbol{x}) + \varepsilon\,\nabla_x\varphi_1^\phi\left(\boldsymbol{x}, \frac{\boldsymbol{x}}{\varepsilon}\right) + \nabla_y\varphi_1^\phi\left(\boldsymbol{x}, \frac{\boldsymbol{x}}{\varepsilon}\right)\right]\cdot\boldsymbol{\mathcal{S}}_\varepsilon\left(\theta_\varepsilon(\boldsymbol{x}), \boldsymbol{x}\right)\cdot\nabla\phi_\varepsilon(\boldsymbol{x})\;\mathrm{d}x = 0\,. \tag{7.78}$$

In order to pass to the limit, we have to show the strong two-scale convergence of $\boldsymbol{\mathcal{S}}_\varepsilon\left(\theta_\varepsilon(\boldsymbol{x}), \boldsymbol{x}\right)$. We rewrite $\boldsymbol{\mathcal{S}}_\varepsilon\left(\theta_\varepsilon(\boldsymbol{x}), \boldsymbol{x}\right) = \mathcal{S}_1\left(\theta_\varepsilon(\boldsymbol{x})\right)\boldsymbol{\mathcal{S}}_2\left(\boldsymbol{x}/\varepsilon\right)$. Due to the boundedness and continuity of $\mathcal{S}_1$, we can transfer the strong $L^2(\Omega)$-convergence of θ_ε to θ_0, to the

strong $L^p(\Omega)$-convergence of $\mathcal{S}_1(\theta_\varepsilon(\boldsymbol{x}))$ to $\mathcal{S}_1(\theta_0(\boldsymbol{x}))$ for every $p \in [1,\infty)$. Moreover, the strong two-scale convergence of $\boldsymbol{\mathcal{S}}_2(\boldsymbol{x}/\varepsilon) \overset{p}{\twoheadrightarrow} \boldsymbol{\mathcal{S}}_2(\boldsymbol{y})$ for every $p \in (1,\infty)$ is given by Lemma 1. Thus, by Lemma 2 the product $\boldsymbol{\mathcal{S}}_\varepsilon(\theta_\varepsilon(\boldsymbol{x}),\boldsymbol{x}) = \mathcal{S}_1(\theta_\varepsilon(\boldsymbol{x}))\,\boldsymbol{\mathcal{S}}_2(\boldsymbol{x}/\varepsilon) \overset{p}{\twoheadrightarrow} \boldsymbol{\mathcal{S}}(\theta_0(\boldsymbol{x}),\boldsymbol{y}) \coloneqq \mathcal{S}_1(\theta_0(\boldsymbol{x}))\,\boldsymbol{\mathcal{S}}_2(\boldsymbol{y})$ for every $p \in (1,\infty)$. Together with the weak convergence of ∇u_ε and the strong two-scale convergence of $\nabla_x\phi_0(\boldsymbol{x},\boldsymbol{x}/\varepsilon)$, $\varepsilon\nabla_x\varphi_1(\boldsymbol{x},\boldsymbol{x}/\varepsilon)$ and $\nabla_y\phi_1(\boldsymbol{x},\boldsymbol{x}/\varepsilon)$, which is given by Lemma 1, we can pass to the limit $\varepsilon \to 0$ and obtain

$$\int_\Omega \int_Y \left[\nabla_x\varphi_0^\phi(\boldsymbol{x}) + \nabla_y\varphi_1^\phi(\boldsymbol{x},\boldsymbol{y})\right] \cdot \boldsymbol{\mathcal{S}}(\theta_0(\boldsymbol{x}),\boldsymbol{y}) \cdot [\nabla_x\phi_0(\boldsymbol{x}) + \nabla_y\phi_1(\boldsymbol{x},\boldsymbol{y})]\,\mathrm{d}y\,\mathrm{d}x = 0\,. \tag{7.79}$$

By a density argument, (7.79) holds for all $\varphi_0^\phi \in H_0^1(\Omega)$ and $\varphi_1^\phi \in L^2\left(\Omega, H^1_\#(Y)/\mathbb{R}\right)$.

With (7.79) at hand, we obtain the weak formulation of the two-scale limit problem

Find $(\phi_0,\phi_1) \in H^1(\Omega) \times L^2\left(\Omega, H^1_\#(Y)\right)$ such that $\phi_0 - \phi_p \in H_0^1(\Omega)$ and

$$\int_\Omega \int_Y \left[\nabla_x\varphi_0^\phi(\boldsymbol{x}) + \nabla_y\varphi_1^\phi(\boldsymbol{x},\boldsymbol{y})\right] \cdot \boldsymbol{\mathcal{S}}(\theta_0(\boldsymbol{x}),\boldsymbol{y}) \cdot [\nabla_x\phi_0(\boldsymbol{x}) + \nabla_y\phi_1(\boldsymbol{x},\boldsymbol{y})]\,\mathrm{d}y\,\mathrm{d}x = 0 \tag{7.80}$$

hold for all $\varphi_0^\phi \in H_0^1(\Omega)$ and $\varphi_1^\phi \in L^2\left(\Omega, H^1_\#(Y)/\mathbb{R}\right)$.

The existence of a solution to (7.79) is ensured by the homogenisation process. Choosing $\varphi_0^\phi = 0$ and using the linearity of (7.72a) leads to

$$\phi_1(\boldsymbol{x},\boldsymbol{y}) = \sum_{i=1}^{d} \frac{\partial\phi_0(\boldsymbol{x})}{\partial x_i}\,\zeta_i(\theta_0(\boldsymbol{x}),\boldsymbol{y})\,, \tag{7.81}$$

where $\zeta_i(\theta_0,\boldsymbol{x}) \in H^1_\#(Y)$ is the unique solution (up to an additive constant) of the cell problem (7.72a). Choosing $\varphi_1^\phi = 0$ gives rise to the homogenised problem (7.70a) with $\boldsymbol{\mathcal{S}}^*$ given by (7.71a).

Passage to the limit for the thermal problem:

By choosing the test function in (7.48b) as

$$\varphi^\theta(\boldsymbol{x}) = \varphi_0^\theta(\boldsymbol{x}) + \varepsilon\,\varphi_1^\theta\left(\boldsymbol{x},\frac{\boldsymbol{x}}{\varepsilon}\right)\,, \tag{7.82}$$

with $\varphi_0^\theta(\boldsymbol{x}) \in C_0^\infty(\Omega)$ and $\varphi_1^\theta \in C_0^\infty\left(\Omega; C^\infty_\#(Y)\right)$, we obtain

$$\begin{aligned}
&\int_\Omega \left[\nabla_x\varphi_0^\theta(\boldsymbol{x}) + \varepsilon\,\nabla_x\varphi_1^\theta\left(\boldsymbol{x},\frac{\boldsymbol{x}}{\varepsilon}\right) + \nabla_y\varphi_1^\theta\left(\boldsymbol{x},\frac{\boldsymbol{x}}{\varepsilon}\right)\right] \cdot \boldsymbol{\mathcal{K}}_\varepsilon(\boldsymbol{x}) \cdot \nabla\theta_\varepsilon\,\mathrm{d}x \\
&\quad + \int_\Omega r_\varepsilon\left(\boldsymbol{x},\frac{\boldsymbol{x}}{\varepsilon}\right)\left[\varphi_0^\theta(\boldsymbol{x}) + \varepsilon\,\varphi_1^\theta\left(\boldsymbol{x},\frac{\boldsymbol{x}}{\varepsilon}\right)\right]\mathrm{d}x \\
&= -\int_\Omega \nabla\phi_\varepsilon(\boldsymbol{x}) \cdot \boldsymbol{\mathcal{S}}_\varepsilon(\theta_\varepsilon(\boldsymbol{x}),\boldsymbol{x}) \cdot \nabla\phi_\varepsilon(\boldsymbol{x})\left[\varphi_0^\theta(\boldsymbol{x}) + \varepsilon\,\varphi_1^\theta\left(\boldsymbol{x},\frac{\boldsymbol{x}}{\varepsilon}\right)\right]\mathrm{d}x
\end{aligned} \tag{7.83}$$

For the left-hand side of (7.83), one can pass to the limit by standard arguments and obtains

$$\begin{aligned}
&\int_\Omega \left[\nabla_x \varphi_0^\theta(\boldsymbol{x}) + \varepsilon\, \nabla_x \varphi_1^\theta\left(\boldsymbol{x}, \frac{\boldsymbol{x}}{\varepsilon}\right) + \nabla_y \varphi_1^\theta\left(\boldsymbol{x}, \frac{\boldsymbol{x}}{\varepsilon}\right)\right] \cdot \boldsymbol{\mathcal{K}}_\varepsilon(\boldsymbol{x}) \cdot \nabla\theta_\varepsilon(\boldsymbol{x})\ \mathrm{d}x \\
&\quad + \int_\Omega r_\varepsilon\left(\boldsymbol{x}, \frac{\boldsymbol{x}}{\varepsilon}\right)\left[\varphi_0^\theta(\boldsymbol{x}) + \varepsilon\, \varphi_1^\theta\left(\boldsymbol{x}, \frac{\boldsymbol{x}}{\varepsilon}\right)\right] \mathrm{d}x \\
&\to \int_\Omega \int_Y \left[\nabla_x \varphi_0^\theta(\boldsymbol{x}) + \nabla_y \varphi_1^\theta(\boldsymbol{x}, \boldsymbol{y})\right] \cdot \boldsymbol{\mathcal{K}}(\boldsymbol{y}) \cdot \left[\nabla_x \theta_0(\boldsymbol{x}) + \nabla_y \theta_1(\boldsymbol{x}, \boldsymbol{y})\right] \mathrm{d}y\ \mathrm{d}x \\
&\quad + \int_\Omega \int_Y r_0(\boldsymbol{x}, \boldsymbol{y})\ \varphi_0^\theta(\boldsymbol{x})\ \mathrm{d}y\, \mathrm{d}x\,.
\end{aligned} \tag{7.84}$$

However, the nonlinearity of the right-hand side requires some detailed discussion. Since $\nabla\phi_\varepsilon$, a priori, only two-scale converges weakly, we can not pass to the limit because it does not appear linearly. We address this issue by rewriting the right-hand side of (7.48b) as in the existence proof of the microscopic problem using (7.48a). Testing (7.48a) with the ε-dependent test function $\varphi^\phi(\cdot) = \phi_\varepsilon(\cdot)\left[\varphi_0^\theta(\cdot) + \varepsilon\, \varphi_1^\theta\left(\cdot, \frac{\cdot}{\varepsilon}\right)\right]$ and using $\nabla\varphi^\phi(\cdot) = \nabla\phi_\varepsilon(\cdot)\left[\varphi_0^\theta(\cdot) + \varepsilon\, \varphi_1^\theta\left(\cdot, \frac{\cdot}{\varepsilon}\right)\right] + \phi_\varepsilon(\cdot)\, \nabla\left[\varphi_0^\theta(\cdot) + \varepsilon\, \varphi_1^\theta\left(\cdot, \frac{\cdot}{\varepsilon}\right)\right]$ yields

$$\begin{aligned}
&\int_\Omega \nabla\phi_\varepsilon(\boldsymbol{x}) \cdot \boldsymbol{\mathcal{S}}_\varepsilon\left(\theta_\varepsilon(\boldsymbol{x}), \boldsymbol{x}\right) \cdot \nabla\phi_\varepsilon(\boldsymbol{x}) \left[\varphi_0^\theta(\boldsymbol{x}) + \varepsilon\, \varphi_1^\theta\left(\boldsymbol{x}, \frac{\boldsymbol{x}}{\varepsilon}\right)\right] \mathrm{d}x \\
&= -\int_\Omega \nabla\phi_\varepsilon(\boldsymbol{x}) \cdot \boldsymbol{\mathcal{S}}_\varepsilon\left(\theta_\varepsilon(\boldsymbol{x}), \boldsymbol{x}\right) \cdot \nabla \left[\varphi_0^\theta(\boldsymbol{x}) + \varepsilon\, \varphi_1^\theta\left(\boldsymbol{x}, \frac{\boldsymbol{x}}{\varepsilon}\right)\right] \phi_\varepsilon(\boldsymbol{x})\ \mathrm{d}x \\
&= -\int_\Omega \nabla\phi_\varepsilon(\boldsymbol{x}) \cdot \boldsymbol{\mathcal{S}}_\varepsilon\left(\theta_\varepsilon(\boldsymbol{x}), \boldsymbol{x}\right) \cdot \left[\nabla_x \varphi_0^\theta(\boldsymbol{x}) + \varepsilon \nabla_x \varphi_1^\theta\left(\boldsymbol{x}, \frac{\boldsymbol{x}}{\varepsilon}\right) + \nabla_y \varphi_1^\theta\left(\boldsymbol{x}, \frac{\boldsymbol{x}}{\varepsilon}\right)\right] \phi_\varepsilon(\boldsymbol{x})\ \mathrm{d}x\,.
\end{aligned} \tag{7.85}$$

With the weak two-scale convergence of $\nabla\phi_\varepsilon$, the strong two-scale convergence of the coefficient matrix $\boldsymbol{\mathcal{S}}_\varepsilon(\theta_\varepsilon(\boldsymbol{x}))$, the strong two-scale convergence of the gradients of the test functions and the strong two-scale convergence of $\phi_\varepsilon(x)$ at hand, we eventually obtain the limit equation

$$\begin{aligned}
&\int_\Omega \nabla\phi_\varepsilon(\boldsymbol{x}) \cdot \boldsymbol{\mathcal{S}}_\varepsilon\left(\theta_\varepsilon(\boldsymbol{x}), \boldsymbol{x}\right) \cdot \nabla\phi_\varepsilon(\boldsymbol{x}) \left[\varphi_0^\theta(\boldsymbol{x}) + \varepsilon\, \varphi_1^\theta\left(\boldsymbol{x}, \frac{\boldsymbol{x}}{\varepsilon}\right)\right] \mathrm{d}x \\
&\to -\int_\Omega \int_Y \left[\nabla_x \phi_0(\boldsymbol{x}) + \nabla_y \phi_1(\boldsymbol{x}, \boldsymbol{y})\right] \cdot \boldsymbol{\mathcal{S}}\left(\theta_0(\boldsymbol{x}), \boldsymbol{y}\right) \cdot \left[\nabla_x \varphi_0^\theta(\boldsymbol{x}) + \nabla_y \varphi_1^\theta(\boldsymbol{x}, \boldsymbol{y})\right] \phi_0(\boldsymbol{x}) \mathrm{d}y\, \mathrm{d}x\,.
\end{aligned} \tag{7.86}$$

We simplify the right-hand side of (7.86) by eliminating the term $\nabla_y \varphi_1^\theta$. Choosing $\varphi_0^\phi = 0$ and $\varphi_1^\phi = \phi_0\, \varphi_1^\theta$ in the two-scale limit equation of the electrical problem (7.79) results in

$$\int_\Omega \int_Y \left[\nabla_x \phi_0(\boldsymbol{x}) + \nabla_y \phi_1(\boldsymbol{x}, \boldsymbol{y})\right] \cdot \boldsymbol{\mathcal{S}}\left(\theta_0(\boldsymbol{x}), \boldsymbol{y}\right) \cdot \left[\phi_0(\boldsymbol{x})\, \nabla_y \varphi_1^\theta(\boldsymbol{x}, \boldsymbol{y})\right] \mathrm{d}y\ \mathrm{d}x = 0\,. \tag{7.87}$$

Inserting (7.87) in the right-hand side of of (7.86), we obtain

$$\begin{aligned}&\int_{\Omega} \nabla\phi_\varepsilon(\boldsymbol{x}) \cdot \boldsymbol{\mathcal{S}}_\varepsilon(\theta_\varepsilon(\boldsymbol{x}), \boldsymbol{x}) \cdot \nabla\phi_\varepsilon(\boldsymbol{x}) \left[\varphi_0^\theta(\boldsymbol{x}) + \varepsilon\, \varphi_1^\theta\left(\boldsymbol{x}, \frac{\boldsymbol{x}}{\varepsilon}\right)\right] \mathrm{d}x \\ \to &-\int_\Omega \int_Y \left[\nabla_x\phi_0(\boldsymbol{x}) + \nabla_y\phi_1(\boldsymbol{x}, \boldsymbol{y})\right] \cdot \boldsymbol{\mathcal{S}}(\theta_0(\boldsymbol{x}), \boldsymbol{y}) \cdot \left[\phi_0(\boldsymbol{x})\ \nabla_x\varphi_0^\theta(\boldsymbol{x})\right] \mathrm{d}y\ \mathrm{d}x\,.\end{aligned} \tag{7.88}$$

By using (7.84) and (7.88), we finally pass to the limit in (7.83)

$$\begin{aligned}&\int_\Omega \int_Y \left[\nabla_x\varphi_0^\theta(\boldsymbol{x}) + \nabla_y\varphi_1^\theta(\boldsymbol{x}, \boldsymbol{y})\right] \cdot \boldsymbol{\mathcal{K}}(\boldsymbol{y}) \cdot \left[\nabla_x\theta_0(\boldsymbol{x}) + \nabla_y\theta_1(\boldsymbol{x}, \boldsymbol{y})\right] \mathrm{d}y\ \mathrm{d}x \\ &\qquad + \int_\Omega \int_Y r_0(\boldsymbol{x}, \boldsymbol{y})\ \varphi_0^\theta(\boldsymbol{x})\ \mathrm{d}y\,\mathrm{d}x \\ = &\int_\Omega \int_Y \left[\nabla_x\phi_0(\boldsymbol{x}) + \nabla_y\phi_1(\boldsymbol{x}, \boldsymbol{y})\right] \cdot \boldsymbol{\mathcal{S}}(\theta_0(\boldsymbol{x}), \boldsymbol{y}) \cdot \left[\phi_0(\boldsymbol{x})\ \nabla_x\varphi_0^\theta(\boldsymbol{x})\right] \mathrm{d}y\ \mathrm{d}x\,.\end{aligned} \tag{7.89}$$

Indeed, (7.89) could be used as the two-scale limit system. However, it is in a different form than the system obtained from a formal asymptotic expansion or Hill–Mandel-type energy-based homogenisation. The reason is that we rewrote the right-hand side of (7.48b) by using (7.48a) when rigorously passing to the limit. To retrieve the limit system for the thermal problem obtained in Section 7.2.1 and Section 7.2.2, we rewrite the right-hand side of (7.88) by using the two-scale limit system for the electrical problem (7.79). Choosing $\varphi_0^\phi = \phi_0\,\varphi_0^\theta$ and $\varphi_1^\phi = \phi_1\,\varphi_0^\theta$ in (7.79), we obtain

$$\int_\Omega \int_Y \left[\nabla_x\left[\phi_0\,\varphi_0^\theta\right](\boldsymbol{x}) + \nabla_y\left[\phi_1\,\varphi_0^\theta\right](\boldsymbol{x}, \boldsymbol{y})\right] \cdot \boldsymbol{\mathcal{S}}(\theta_0(\boldsymbol{x}), \boldsymbol{y}) \cdot \left[\nabla_x\phi_0(\boldsymbol{x}) + \nabla_y\phi_1(\boldsymbol{x}, \boldsymbol{y})\right] \mathrm{d}y\,\mathrm{d}x = 0\,. \tag{7.90}$$

Using the product rule and observing that φ_0^θ does not depend on $\boldsymbol{y}$, we can rewrite (7.90) as

$$\begin{aligned}&\int_\Omega \int_Y \left[\phi_0(\boldsymbol{x})\ \nabla_x\varphi_0^\theta(\boldsymbol{x})\right] \cdot \boldsymbol{\mathcal{S}}(\theta_0(\boldsymbol{x}), \boldsymbol{y}) \cdot \left[\nabla_x\phi_0(\boldsymbol{x}) + \nabla_y\phi_1(\boldsymbol{x}, \boldsymbol{y})\right] \mathrm{d}y\,\mathrm{d}x \\ = &-\int_\Omega \int_Y \varphi_0^\theta(\boldsymbol{x}) \left[\nabla_x\phi_0(\boldsymbol{x}) + \nabla_y\phi_1(\boldsymbol{x}, \boldsymbol{y})\right] \cdot \boldsymbol{\mathcal{S}}(\theta_0(\boldsymbol{x}), \boldsymbol{y}) \cdot \left[\nabla_x\phi_0(\boldsymbol{x}) + \nabla_y\phi_1(\boldsymbol{x}, \boldsymbol{y})\right] \mathrm{d}y\,\mathrm{d}x\,.\end{aligned} \tag{7.91}$$

Replacing the right-hand side of (7.89) by (7.91) gives the alternative version of the two-scale limit equation for the thermal problem

$$\begin{aligned}&\int_\Omega \int_Y \left[\nabla_x\varphi_0^\theta(\boldsymbol{x}) + \nabla_y\varphi_1^\theta(\boldsymbol{x}, \boldsymbol{y})\right] \cdot \boldsymbol{\mathcal{K}}(\boldsymbol{y}) \cdot \left[\nabla_x\theta_0(\boldsymbol{x}) + \nabla_y\theta_1(\boldsymbol{x}, \boldsymbol{y})\right] \mathrm{d}y\ \mathrm{d}x \\ &+ \int_\Omega \int_Y r_0(\boldsymbol{x}, \boldsymbol{y})\ \varphi_0^\theta(\boldsymbol{x})\ \mathrm{d}y\,\mathrm{d}x \\ = &-\int_\Omega \int_Y \varphi_0^\theta(\boldsymbol{x}) \left[\nabla_x\phi_0(\boldsymbol{x}) + \nabla_y\phi_1(\boldsymbol{x}, \boldsymbol{y})\right] \cdot \boldsymbol{\mathcal{S}}(\theta_0(\boldsymbol{x}), \boldsymbol{y}) \cdot \left[\nabla_x\phi_0(\boldsymbol{x}) + \nabla_y\phi_1(\boldsymbol{x}, \boldsymbol{y})\right] \mathrm{d}y\,\mathrm{d}x\,.\end{aligned} \tag{7.92}$$

By a density argument (7.92) holds for all $\varphi_0^\theta \in H_0^1(\Omega)$ and $\varphi_1^\theta \in L^2\left(\Omega, H_\#^1(Y)/\mathbb{R}\right)$ so that we eventually obtain the final version of the weak form of the thermal two-scale limit problem

Find $(\theta_0, \theta_1) \in H^1(\Omega) \times L^2\left(\Omega, H_\#^1(Y)\right)$ such that $\theta_0 - \theta_p \in H_0^1(\Omega)$ and

$$\begin{aligned}
&-\int_\Omega \int_Y \left[\nabla_x \varphi_0^\theta(\boldsymbol{x}) + \nabla_y \varphi_1^\theta(\boldsymbol{x}, \boldsymbol{y})\right] \cdot \boldsymbol{\mathcal{K}}(\boldsymbol{y}) \cdot \left[\nabla_x \theta_0(\boldsymbol{x}) + \nabla_y \theta_1(\boldsymbol{x}, \boldsymbol{y})\right] \mathrm{d}y \, \mathrm{d}x \\
&-\int_\Omega \int_Y r_0(\boldsymbol{x}, \boldsymbol{y}) \; \varphi_0^\theta(\boldsymbol{x}) \; \mathrm{d}y \, \mathrm{d}x \\
&= \int_\Omega \int_Y \varphi_0^\theta(\boldsymbol{x}) [\nabla_x \phi_0(\boldsymbol{x}) + \nabla_y \phi_1(\boldsymbol{x}, \boldsymbol{y})] \cdot \boldsymbol{\mathcal{S}}(\theta_0(\boldsymbol{x}), \boldsymbol{y}) \cdot [\nabla_x \phi_0(\boldsymbol{x}) + \nabla_y \phi_1(\boldsymbol{x}, \boldsymbol{y})] \, \mathrm{d}y \, \mathrm{d}x
\end{aligned} \tag{7.93}$$

hold for all $\varphi_0^\theta \in H_0^1(\Omega)$ and $\varphi_1^\theta \in L^2\left(\Omega, H_\#^1(Y)/\mathbb{R}\right)$.

To derive the homogenised system, we separate the macro- and microscopic variables. In line with the derivations for the electrical problem, we choose $\varphi_0^\theta = 0$ and use the linearity of (7.72b) to obtain

$$\theta_1(\boldsymbol{x}, \boldsymbol{y}) = \sum_{i=1}^{d} \frac{\partial \theta_0(\boldsymbol{x})}{\partial x_i} \xi_i(\boldsymbol{y}), \tag{7.94}$$

for $\xi_i \in H_\#^1(Y)$ given by (7.72b).

Analogously, by choosing $\varphi_1^\theta = 0$ and by inserting (7.81) and (7.94) into the ensuing equation we arrive at

$$\begin{aligned}
\int_\Omega \nabla_x \varphi_0^\theta(\boldsymbol{x}) \cdot \boldsymbol{\mathcal{K}}^*(\boldsymbol{x}) \cdot \nabla_x \theta_0(\boldsymbol{x}) \; \mathrm{d}x = &-\int_\Omega \varphi_0^\theta(\boldsymbol{x}) \; \nabla_x \phi_0(\boldsymbol{x}) \cdot \boldsymbol{\mathcal{A}}^*(\theta_0, \boldsymbol{x}) \cdot \nabla_x \phi_0(\boldsymbol{x}) \; \mathrm{d}x \\
&-\int_\Omega r_0(\boldsymbol{x}) \; \varphi_0^\theta(\boldsymbol{x}) \; \mathrm{d}x
\end{aligned} \tag{7.95}$$

with $\boldsymbol{\mathcal{K}}^*$ and $\boldsymbol{\mathcal{A}}^*$ given by (7.71b) and (7.71c). □

Remark 19. By choosing $\varphi_0^\phi = \phi_0 \, \varphi_0^\theta$ and $\varphi_1^\phi = 0$ in (7.79), we arrive at

$$\begin{aligned}
&\int_\Omega \int_Y \left[\phi_0(\boldsymbol{x}) \; \nabla_x \varphi_0^\theta(\boldsymbol{x})\right] \cdot \boldsymbol{\mathcal{S}}(\theta_0(\boldsymbol{x}), \boldsymbol{y}) \cdot \left[\nabla_x \phi_0(\boldsymbol{x}) + \nabla_y \phi_1(\boldsymbol{x}, \boldsymbol{y})\right] \mathrm{d}y \, \mathrm{d}x \\
&= -\int_\Omega \int_Y \left[\nabla_x \phi_0(\boldsymbol{x}) \; \varphi_0^\theta(\boldsymbol{x})\right] \cdot \boldsymbol{\mathcal{S}}(\theta_0(\boldsymbol{x}), \boldsymbol{y}) \cdot \left[\nabla_x \phi_0(\boldsymbol{x}) + \nabla_y \phi_1(\boldsymbol{x}, \boldsymbol{y})\right] \mathrm{d}y \, \mathrm{d}x \, .
\end{aligned} \tag{7.96}$$

Using this result in the right-hand side of (7.89), the thermal two-scale limit problem simplifies further to

$$\begin{aligned}
&\int_\Omega \int_Y \left[\nabla_x \varphi_0^\theta(\boldsymbol{x}) + \nabla_y \varphi_1^\theta(\boldsymbol{x},\boldsymbol{y})\right] \cdot \boldsymbol{\mathcal{K}}(\boldsymbol{y}) \cdot \left[\nabla_x \theta_0(\boldsymbol{x}) + \nabla_y \theta_1(\boldsymbol{x},\boldsymbol{y})\right] \mathrm{d}y \; \mathrm{d}x \\
&+ \int_\Omega \int_Y r_0(\boldsymbol{x},\boldsymbol{y}) \; \varphi_0^\theta(\boldsymbol{x}) \; \mathrm{d}x \\
= &- \int_\Omega \int_Y \left[\nabla_x \phi_0(\boldsymbol{x}) \; \varphi_0^\theta(\boldsymbol{x})\right] \cdot \boldsymbol{\mathcal{S}}(\theta_0(\boldsymbol{x}),\boldsymbol{y}) \cdot \left[\nabla_x \phi_0(\boldsymbol{x}) + \nabla_y \phi_1(\boldsymbol{x},\boldsymbol{y})\right] \mathrm{d}y \; \mathrm{d}x \; .
\end{aligned} \tag{7.97}$$

Additionally, by following the same steps as in the derivation of (7.95), we conclude that (7.71c) simplifies to (7.71a). From a physical perspective, this result implies that the effective electrical conductivity tensor and the effective coupling tensor are equivalent, i.e. $\}^{\text{qtd.}}_{[72]}$

$$\boldsymbol{\mathcal{S}}^*(\theta_0(\boldsymbol{x}),\boldsymbol{x}) \equiv \boldsymbol{\mathcal{A}}^*(\theta_0(\boldsymbol{x}),\boldsymbol{x}) \; . \tag{7.98}$$

7.3 Representative simulation results

$^{\text{qtd.}}_{[72]}\{$Concluding the study of thermo-electrically coupled multiscale-problems, we focus on representative boundary values problems in one, two- and three-dimensional settings. In Section 7.3.1, we discuss the classic ordered checkerboard problem, for which an analytical solution is available. Remaining in a two-dimensional setting, we extend the study in Section 7.3.2 to more realistic two-phase microstructures with particular focus lying on the microscale corrector fields. Approaching the three-dimensional setting, we eventually analyse dissipative coupling effects for random three-dimensional microstructures in Section 7.3.3.

In accordance with (2.51)–(7.3) and by using that the microscale constitutive relations are to be evaluated at (fixed) macroscale temperature θ_0, we drop the explicit temperature dependence and take the conductivity tensors to be of the form

$$\boldsymbol{\mathcal{S}}(\boldsymbol{y}) = \kappa_\phi(\boldsymbol{y}) \; \boldsymbol{I} \tag{7.99}$$

and

$$\boldsymbol{\mathcal{K}}(\boldsymbol{y}) = \kappa_\theta(\boldsymbol{y}) \; \boldsymbol{I} \tag{7.100}$$

with scalar-valued conductivity coefficients $\kappa_\phi > 0$ and $\kappa_\theta > 0$.

We base our studies on isoparametric finite element discretisations (4-noded quadrilateral elements and 8-noded hexahedral elements) and use Gaussian-type quadrature rules (4-point and 8-point) to evaluate integrals in the two- and three-dimensional settings, respectively.$\}^{\text{qtd.}}_{[72]}$

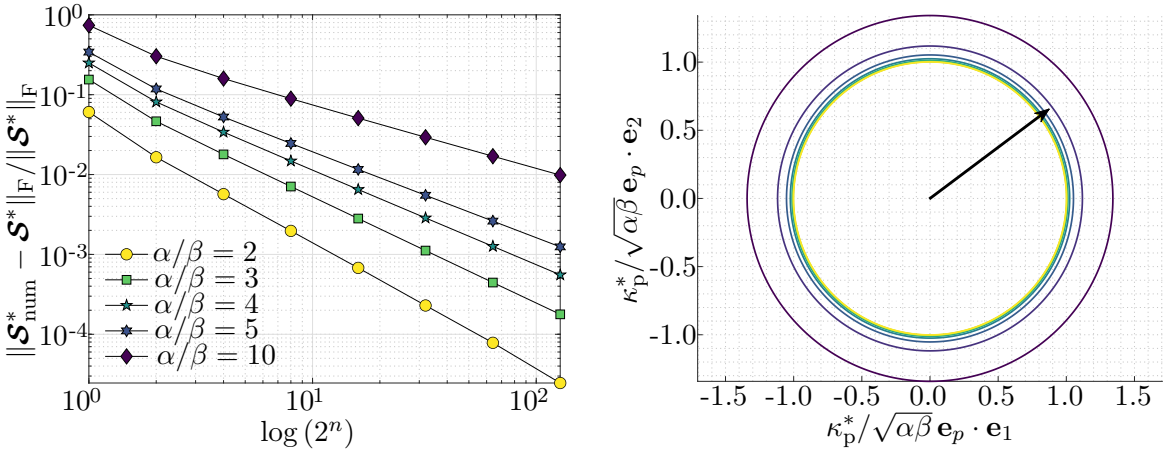

(a) Relative error with respect to analytical solution

(b) (Normalised) Directional conductivity for $\alpha/\beta = 5$

Figure 7.5: Mesh refinement study for the ordered checkerboard problem. (a) Relative error with respect to the analytical solution as a function of phase contrast and mesh density. (b) (Normalised) Directional conductivities for $\alpha/\beta = 5$ and mesh densities according to (a). Mesh density decreases in direction of arrow in (b). Reprinted from [72] under the terms of the Creative Commons Attribution License (CC BY).

7.3.1 Periodic checkerboard-type microstructures

qtd. [72]{The effective properties of periodic checkerboard-type microstructures with two different constituents have been extensively studied in [20, 25, 42, 121, 180]. In particular, Dykhne demonstrated in the seminal work [42] that the effective conductivity of two-dimensional periodic checkerboard-type microstructures with statistically equivalent phase distributions is equal to the geometric mean.

For the study at hand, we choose the particular function for the scalar-valued conductivity coefficients

$$\kappa_\bullet(\boldsymbol{y}) = \begin{cases} \alpha & (\boldsymbol{y}\cdot\mathbf{e}_1, \boldsymbol{y}\cdot\mathbf{e}_2) \in \left]0, 0.5\right[^2 \cup \left]0.5, 1\right[^2 , \\ \beta & \text{otherwise} \end{cases} \tag{7.101}$$

and expect the effective conductivity tensors to be of the form

$$\boldsymbol{\mathcal{S}}^* = \boldsymbol{\mathcal{K}}^* = \sqrt{\alpha\,\beta}\,\boldsymbol{I}\,. \tag{7.102}$$

To validate the finite element implementation, we evaluate (7.70) for different finite element discretisations and study the convergence behaviour upon mesh refinement as well as the isotropy of the effective constitutive response. To this end, we make use of the projected effective conductivities

$$\kappa^*_{\mathrm{p}} = \left[\mathbf{e}_{\mathrm{p}} \cdot \left[\boldsymbol{\mathcal{S}}^*\right]^{-1} \cdot \mathbf{e}_{\mathrm{p}}\right]^{-1} . \tag{7.103}$$

The respective findings for $2^n \times 2^n$ discretisations are provided in Figure 7.5. Additionally, we depict the corrector field and its gradient in Figure 7.6, with the localised

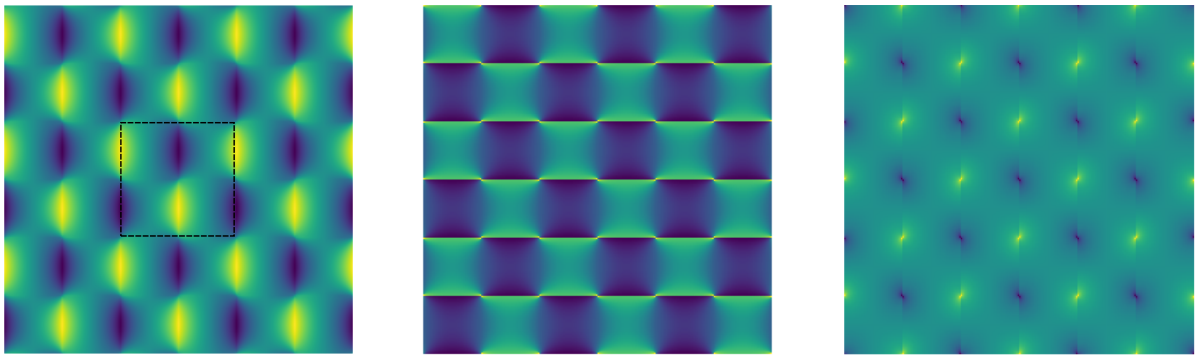

Figure 7.6: Corrector field $\zeta_1(\boldsymbol{y})$ (left) and its gradient $\nabla_y \zeta_1(\boldsymbol{y})$ (middle and right). The central square marks the representative unit cell corresponding to the $2^n \times 2^n$ discretisation. Reprinted from [72] under the terms of the Creative Commons Attribution License (CC BY).

nature of the solution near the phase boundaries being clearly visible. These singularities are the underlying cause for the seemingly high errors observed in Figure 7.5 for rather moderate mesh sizes. For this reason, special numerical techniques to handle the checkerboard problem have been proposed [20, 65, 79] which are, however, not in the scope of this work.$\}^{\text{qtd.}}_{[72]}$

7.3.2 Two-dimensional multi-inclusion problem

$^{\text{qtd.}}_{[72]}\{$Extending the study on regular periodic microstructures we focus on general (periodic) multi-inclusion problems in a two-dimensional setting. We adopt a phase contrast $\kappa_\bullet^{\text{inclusion}}/\kappa_\bullet^{\text{matrix}} = 5$ and provide the corresponding corrector fields and their gradients in Figure 7.7. Based on these, we calculate the effective conductivity tensors

$$[\boldsymbol{\mathcal{S}}^*]_{\mathbf{e}_{1,2}} = [\boldsymbol{\mathcal{K}}^*]_{\mathbf{e}_{1,2}} = \begin{bmatrix} 1.433 & -0.006 \\ -0.006 & 1.437 \end{bmatrix} \kappa_\bullet^{\text{matrix}}, \tag{7.104}$$

which are found to be (almost) quasi-isotropic.

Remark 20. To compute effective conductivity tensors, the unit load method, derived from the method of asymptotic expansions, can be utilised. Alternatively, the method of condensation or the perturbation method can be employed to achieve similar results. Details of the finite element implementation are omitted, as they are not central to this chapter. Discrete closed-form solutions for the homogenised fields and the associated tangent contributions are based on [100]. While the current investigation includes an additional temperature field, the underlying framework, based on [100], can be readily extended to thermo-electrical case due to the analogous nature of the temperature field to the electric potential field.$\}^{\text{qtd.}}_{[72]}$

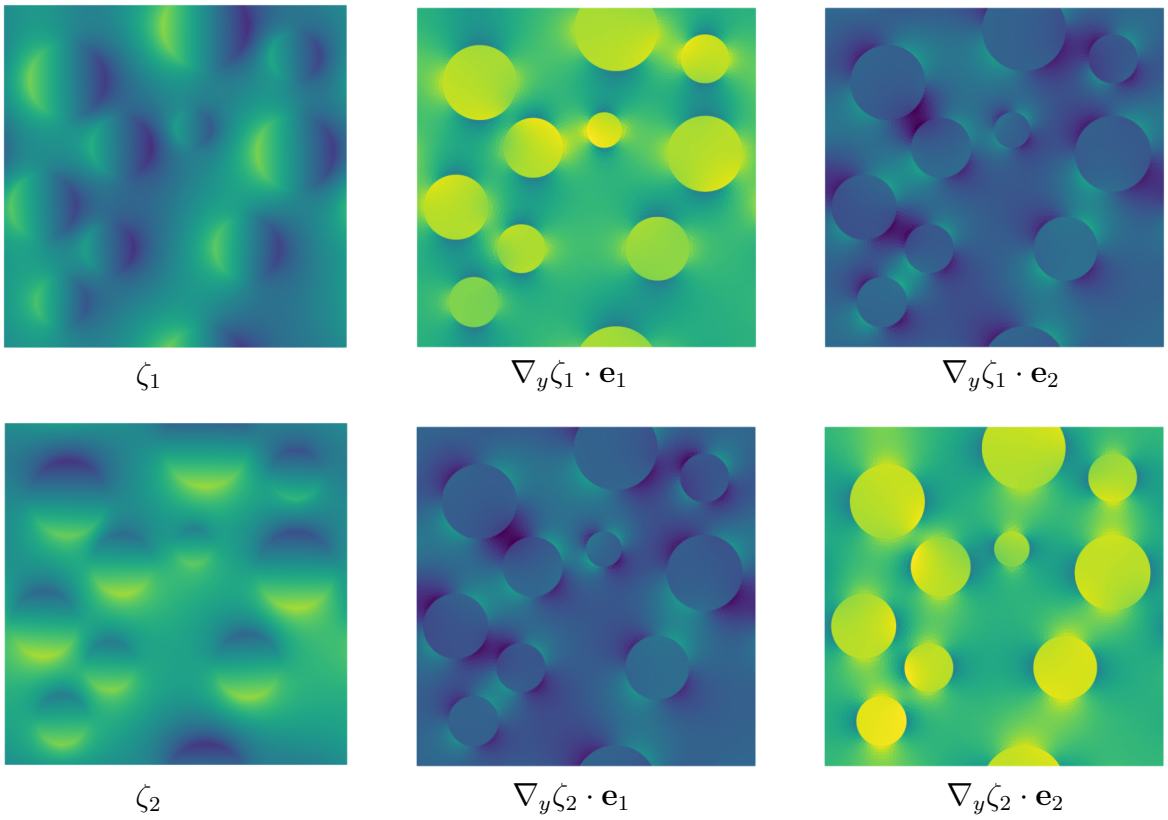

Figure 7.7: Corrector fields $\zeta_i(\boldsymbol{y})$ (left) and their gradients $\nabla_y \zeta_i(\boldsymbol{y})$ (middle and right) for unit loads in $\mathbf{e}_1$- and $\mathbf{e}_2$-direction, respectively. Reprinted from [72] under the terms of the Creative Commons Attribution License (CC BY).

7.3.3 Three-dimensional multi-inclusion problem

$^{\text{qtd.}}_{[72]}\{$Focusing on the influence of the microstructure on the thermo-electrical coupling, we study the three-dimensional multi-inclusion problem depicted in Figure 7.8a. The effective macroscopic coupling tensor for this particular microstructure and a phase contrast $\kappa_\bullet^{\text{inclusion}}/\kappa_\bullet^{\text{matrix}} = 5$, namely

$$[\boldsymbol{\mathcal{A}}^*]_{\mathbf{e}_{1,2,3}} = \begin{bmatrix} 1.183 & 0.000 & 0.000 \\ 0.000 & 1.272 & 0.000 \\ 0.000 & 0.000 & 1.183 \end{bmatrix} \kappa_\bullet^{\text{matrix}} \tag{7.105}$$

is anisotropic. In view of (7.105), we evaluate the dissipative macroscale heat source $\mathcal{D}^* = \nabla\phi_0 \cdot \boldsymbol{\mathcal{A}}^* \cdot \nabla\phi_0$ for loading directions $\mathbf{e}_\text{p}$ on the sphere. The corresponding visualisation in Figure 7.8b clearly shows the influence of the underlying microstructure on the coupling term.$\}^{\text{qtd.}}_{[72]}$

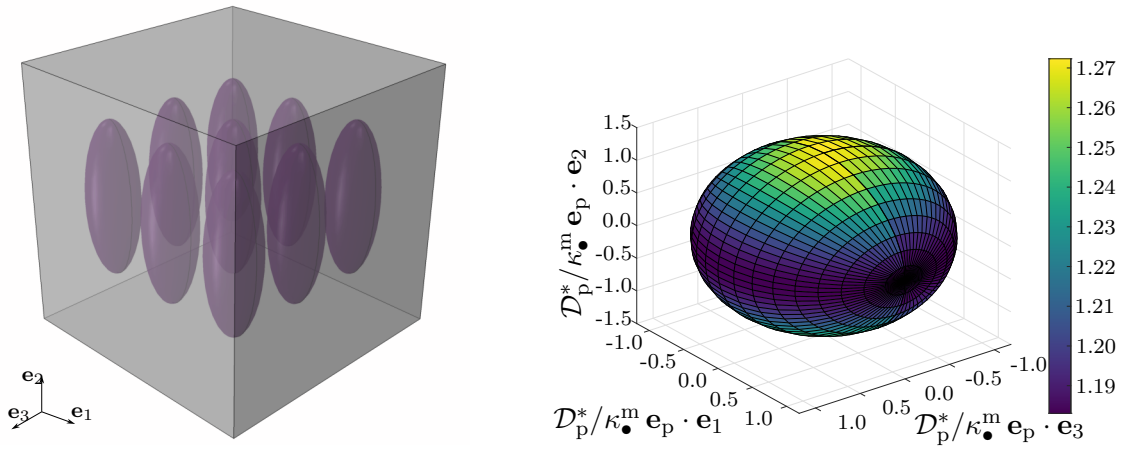

(a) Three-dimensional multi-inclusion problem

(b) Directional dissipation contribution

Figure 7.8: Dissipative macroscale heat source for a three-dimensional multi-inclusion problem with phase contrast $\kappa_{\bullet}^{\mathrm{inclusion}}/\kappa_{\bullet}^{\mathrm{matrix}} = 5$. Reprinted from [72] under the terms of the Creative Commons Attribution License (CC BY).

D Appendix

In Appendix D.1, the zeroth-order equation in the asymptotic analysis is derived as an alternative to the argument given for (7.18a). Appendix D.2 presents the derivation of the effective conductivity tensor in tensor notation. Appendix D.3 details the relevant steps of the asymptotic analysis for the one-dimensional bar example. Finally, Appendix D.4 provides a supplementary argument for the existence proof in the two-scale convergence analysis.

D.1 Zeroth-order equation in asymptotic analysis

qtd. [72] {Alternatively to the argument given in Section 7.2.2, (7.18c) can be obtained by multiplying (7.18a) with ϕ_0 and by integrating the ensuing equation over the periodic unit cell Y.

Proof. For any uniformly bounded and positive definite second order tensor $\boldsymbol{\mathcal{S}}$ there exist two positive constants $0 < \alpha \leq \beta < \infty$ such that for any vector $\boldsymbol{\gamma} \in \mathbb{R}^d$

$$\alpha \left|\boldsymbol{\gamma}\right|^2 \leq \boldsymbol{\gamma} \cdot \boldsymbol{\mathcal{S}}\left(\theta_\varepsilon, \boldsymbol{y}\right) \cdot \boldsymbol{\gamma} \leq \beta \left|\boldsymbol{\gamma}\right|^2, \tag{7.106a}$$

holds. The positive-definiteness of $\boldsymbol{\mathcal{S}}$ guarantees that the material conducts electricity/heat in all directions. The inequality ensures that the dissipation associated with the electric field (represented by the gradient of the potential $-\nabla_y \phi_0$) is bounded. This prevents the energy norm from becoming negative, arbitrarily small or infinite, which is

crucial for the stability of the system. Based on (7.106a), choosing $\boldsymbol{\gamma} = -\nabla_y \phi_0$ results in

$$\begin{aligned} \alpha \int_Y |\nabla_y \phi_0|^2 \, \mathrm{d}y &\leq \int_Y [\boldsymbol{\mathcal{S}}(\theta_0, \boldsymbol{y}) \cdot \nabla_y \phi_0] \cdot \nabla_y \phi_0 \, \mathrm{d}y \\ &= -\int_Y \nabla_y \cdot [\boldsymbol{\mathcal{S}}(\theta_0, \boldsymbol{y}) \cdot \nabla_y \phi_0] \, \phi_0 \, \mathrm{d}y + \int_{\partial Y} [\boldsymbol{\mathcal{S}}(\theta_0, \boldsymbol{y}) \cdot \nabla_y \phi_0] \cdot \boldsymbol{n} \, \phi_0 \, \mathrm{d}y \end{aligned} \tag{7.106b}$$

The first term on the right-hand side vanishes due to (7.18a). The second term vanishes due to periodicity. As a result,

$$\nabla_y \phi_0(\boldsymbol{x}, \boldsymbol{y}) = 0 \quad \Longrightarrow \quad \phi_0 \equiv \phi_0(\boldsymbol{x}) \, . \tag{7.106c}$$

is obtained.$\}^{\text{qtd.}}_{[72]}$ □

D.2 Effective conductivity tensor

Proof. $^{\text{qtd.}}_{[72]}\{$The effective conductivity tensor $\boldsymbol{\mathcal{S}}^*$ can be obtained by inserting (7.19c) into (7.20c)

$$-\nabla_x \cdot \left[\int_Y \boldsymbol{\mathcal{S}}(\theta_0, \boldsymbol{y}) \cdot \sum_{i=1}^{d} \frac{\partial \phi_0(\boldsymbol{x})}{\partial x_i} \left[\nabla_y \zeta_i(\boldsymbol{y}) + \mathbf{e}_i \right] \mathrm{d}y \right] = 0 \tag{7.107a}$$

and by rearranging the term on the left-hand side$\}^{\text{qtd.}}_{[72]}$

$$\begin{aligned} \int_Y \boldsymbol{\mathcal{S}}(\theta_0, \boldsymbol{y}) \cdot \sum_{i=1}^{d} \frac{\partial \phi_0(\boldsymbol{x})}{\partial x_i} \left[\nabla_y \zeta_i(\boldsymbol{y}) + \mathbf{e}_i \right] \mathrm{d}y &= \sum_{i=1}^{d} \left[\int_Y \boldsymbol{\mathcal{S}}(\theta_0, \boldsymbol{y}) \cdot \left[\nabla_y \zeta_i(\boldsymbol{y}) + \mathbf{e}_i \right] \mathrm{d}y \right] \frac{\partial \phi_0(\boldsymbol{x})}{\partial x_i} \\ &= \sum_{k=1}^{d} \left[\sum_{i=1}^{d} \sum_{j=1}^{d} \left[\int_Y \mathcal{S}_{kj}(\theta_0, \boldsymbol{y}) \cdot \left[\nabla_y \zeta_i(\boldsymbol{y}) + \mathbf{e}_i \right]_j \mathrm{d}y \right] \frac{\partial \phi_0(\boldsymbol{x})}{\partial x_i} \right] \mathbf{e}_k \\ &= \sum_{k=1}^{d} \left[\sum_{i=1}^{d} \mathcal{S}^*_{ki} \frac{\partial \phi_0(\boldsymbol{x})}{\partial x_i} \right] \mathbf{e}_k = \boldsymbol{\mathcal{S}}^* \cdot \nabla_x \phi_0(\boldsymbol{x}) \, . \end{aligned} \tag{7.107b}$$

□

D.3 Derivation of one-dimensional problem

In one-dimensional periodic homogenisation, the effective conductivity is given by the harmonic mean over a single period $Y = (0, 1)$, i.e.

$$\frac{1}{\mathcal{K}^*} = \int_Y \frac{1}{\mathcal{K}(y)} \, \mathrm{d}y \, . \tag{7.108}$$

Evaluating the effective conductivity for our specific $\mathcal{K}(y)$, as provide in (7.30), results in

$$\frac{1}{\mathcal{K}^*} = \int_0^1 2 + \sin(2\,\pi\,y)\,\mathrm{d}y = 2 \quad \rightarrow \quad \mathcal{K}^* = \frac{1}{2}\,. \tag{7.109}$$

Additionally inserting the calculated effective conductivity into the homogenised equation with a source term $r(x) = 1$ yields

$$\theta_0(x) = -x^2 + C_1\,x + C_2\,. \tag{7.110}$$

To capture first-order effects of the microscale, we solve the cell problem

$$-\frac{\mathrm{d}}{\mathrm{d}y}\left[\mathcal{K}(y)\left[1+\frac{\mathrm{d}\xi}{\mathrm{d}y}\right]\right] = 0 \quad \rightarrow \quad \mathcal{K}(y)\left[1+\frac{\mathrm{d}\xi}{\mathrm{d}y}\right] = C \tag{7.111a}$$

for some constant C, with periodic boundary conditions on Y. Further arranging the equation leads to the following condition

$$1+\frac{\mathrm{d}\xi}{\mathrm{d}y} = \frac{C}{\mathcal{K}(y)} \quad \rightarrow \quad \frac{\mathrm{d}\xi}{\mathrm{d}y} = \frac{C}{\mathcal{K}(y)} - 1\,. \tag{7.111b}$$

In order to determine constant C, we need to integrate over Y and impose periodic boundary conditions, i.e.

$$\int_0^1 \frac{\mathrm{d}\xi}{\mathrm{d}y}\,\mathrm{d}y = 0 \rightarrow \int_0^1 \left[\frac{C}{\mathcal{K}(y)} - 1\right]\mathrm{d}y = 0 \quad \rightarrow \quad C = \frac{1}{\int_0^1 \frac{1}{\mathcal{K}(y)}\,\mathrm{d}y} \tag{7.111c}$$

Finally, we obtain $C = \mathcal{K}^*$, and inserting constant C back into (7.111b) results in the general form of the characteristic equation, namely

$$\frac{\mathrm{d}\xi}{\mathrm{d}y} = \frac{\mathcal{K}^*}{\mathcal{K}(y)} - 1 \quad \rightarrow \quad \xi(y) = \int_0^y \left[\frac{\mathcal{K}^*}{\mathcal{K}(s)} - 1\right]\mathrm{d}s\,. \tag{7.111d}$$

For the problem at hand

$$\xi(y) = \int_0^y \frac{1}{2}\sin(2\,\pi\,s)\;\mathrm{d}s = -\frac{1}{4\,\pi}\left[\cos(2\,\pi\,y) - 1\right] \tag{7.112}$$

is obtained, see Figure 7.2b.

D.4 Analysis tools

Lemma 3. [qtd. [72]]{Let $\Omega \subset \mathbb{R}^d$ be open and u_n, v_n be sequences in $L^2(\Omega)$ that strongly converge to $v \in L^2(\Omega)$ and $u \in L^2(\Omega)$, respectively. Moreover, assume that v_n is uniformly essentially bounded, i.e. $\|v_n\|_{L^\infty(\Omega)} \leq C$. Then, the product $u_n\,v_n$ strongly converges in $L^2(\Omega)$ to $u\,v$.

Proof. We note that the uniform essential boundedness of v_n implies the essential boundedness of v. Thus, $u\,v \in L^2(\Omega)$. By the convergence of u_n and v_n, we can pass to subsequences u_{n_k} and v_{n_k} that converge pointwise to u and v, respectively. Moreover, the subsequence can be chosen such that there exists a function $g \in L^2(\Omega)$, which dominates $|u_{n_k}|$ almost everywhere, i.e. $|u_{n_k}(x)| \leq g(x)$ for a.e. $x \in \Omega$. Consequently, the product $u_{n_k}\,v_{n_k}$ converges pointwise almost everywhere to $u\,v$ and $u_{n_k}\,v_{n_k}$ is dominated by $C\,g$. The dominated convergence theorem provides the convergence of $u_{n_k}\,v_{n_k}$ to $u\,v$. Since this argument holds also after passing to an arbitrary subsequence, the convergence holds for the entire sequence.}$^{\text{qtd.}}_{[72]}$ □

8 Concluding remarks

This thesis presents a thermo-electro-mechanically coupled computational multiscale framework for electrical conductors containing microstructural features such as inclusions, pores, grain and phase boundaries. The central motivation lies in quantifying how microstructural features and interfacial degradation influence macroscopic (effective) electrical response.**Chapter 2** establishes the theoretical foundation by deriving thermodynamically consistent field equations and validating their finite element implementation. Building on this, **Chapter 3** introduces a cohesive zone formulation that captures interfacial failure and explicitly accounts for interface temperature, thereby enabling coupled degradation modelling. **Chapter 4** develops a multiscale homogenisation scheme for conductive materials under combined loading, extending existing electro-mechanical approaches to include thermal subproblem. **Chapter 5** integrates cohesive-type interfaces into the multiscale framework, demonstrating the emergence of size effects within a first-order setting. In **Chapter 6**, the proposed multiscale framework is applied to polycrystalline materials, demonstrating predictive capability against analytical benchmarks and highlighting the limitations of classical grain boundary resistivity models. Finally, **Chapter 7** provides mathematical justification for the adopted multiscale framework by deriving the same macroscopic equations via asymptotic expansion and two-scale convergence. Together, these contributions provide a multiscale modelling framework for coupled thermo-electro-mechanical behaviour in electrical conductors, with particular emphasis on understanding the role of microstructure and material interfaces in macroscopic material response.

8.1 Summary and conclusion

qtd. [74]{In **Chapter 3**, a fully coupled thermo-electro-mechanical cohesive zone formulation is proposed. To this end, the fundamentals of continuum thermodynamics for a continuum with material interfaces are summarised. In particular, the governing equations for quasi-static, quasi-stationary processes are derived, and the second law of thermodynamics is investigated. The particular form of the dissipation inequality for the bulk and the interface is obtained, and the restrictions on the constitutive functions are studied in detail. With the governing sets of balance and constitutive relations at hand, a weak formulation and the associated finite element formulation for the proposed electro-thermo-mechanically coupled cohesive zone framework are discussed. Following the ap-

proach in [98], specific constitutive forms motivated by the influence of mechanically-induced interfacial damage on the electrical conductivity are adopted and extended to thermal coupling. Next, a (quasi-)one-dimensional boundary value problem is analysed, and the proposed finite element implementation is validated against analytical solutions. The focus is eventually set on more general two-dimensional boundary value problems as motivated by experimentally observed failure processes in wire bonds. It was shown that the framework presented in this chapter can capture thermo-electro-mechanically-induced interface failure processes. Furthermore, the fundamental formulation provides a basis for simulating different damage mechanisms. These can be incorporated by taking into account well-established evolution equations for the damage variable under consideration that may include coupling to different micromechanical processes such a plasticity. The proposed formulation thus serves as basis for future developments by establishing a general framework that may be applied to different materials and experimental findings. In view of recent developments on generalised imperfect interfaces the proposed framework shall further be extended in future contributions so as to account for interface-elastic effects and tangential currents to the interface. Moreover, certain applications may require a geometrically exact description of the interface such that the small deformation assumption is not valid anymore and the formulation needs to be extended accordingly.}$^{\text{qtd.}}_{[74]}$

The scope of **Chapter 4** is to present a first-order computational multiscale framework for electrical conductors subjected to thermo-electro-mechanical loading. This chapter builds directly upon the governing equations introduced in **Chapter 2**, and extends the electro-mechanical formulations of [100] by incorporating thermal effects into the multiscale setting. Particular attention is paid to the coupling terms arising from Joule heating and thermal expansion, which are consistently upscaled within the Hill–Mandel energy equivalence framework. Scale-bridging relations for thermo-electro-mechanical problem are proposed. In addition, energetically consistent boundary conditions are discussed in detail, and the computational procedure is derived from a variational principle. Importantly, **Chapter 4** establishes the general multiscale formulation for coupled thermo-electro-mechanical problems and serves as the theoretical and numerical foundation for subsequent chapters.

$^{\text{qtd.}}_{[76]}${In **Chapter 5**, a computational multiscale formulation for electrical conductors that features material interfaces at the microscale is proposed and a finite element implementation is discussed. Several numerical examples are studied in two-dimensional settings to show the applicability of the proposed formulation. The finite element results are compared against analytical solutions in order to validate the proposed formulation. Different microstructures are analysed to show the influence of the material interfaces on the effective macroscale conductivity tensor. The characteristic size effect that is associated with the presence of material interfaces is revealed, and it is observed that (as opposed to classic first-order homogenisation approaches) the macroscale response is not independent of the geometric dimensions of the RVE. The influence of mechanically induced interfacial degradation processes on the effective electrical conductivity is exemplarily studied to demonstrate the capabilities of the proposed formulation for coupled problems. In this regard, it is important to note that the constitutive relations used are

purely academic at this stage and not based on experimental data. They were selected to show the fully coupled behaviour and the applicability of the proposed framework. The application to experiments will, accordingly, be the focus of future work.}[qtd. 76]

[qtd. 71]{In **Chapter 6**, it is shown that the Andrews method, a well-established approach for quantifying grain boundary resistivity in fine-grained crystalline materials, is consistent with the predictions of computational multiscale methods for non-degenerated quasi-isotropic microstructures but that it exhibits notable limitations. The Andrews method fails for (quasi-)isotropic polycrystalline and multiphase microstructures when the secondary phase is strictly confined within the microstructure. The inability of the Andrews method to consider the alignment of grains, attributed to the scalar nature of S_{GB}/V, becomes evident when scrutinising primitive anisotropic microstructures. The Andrews method intrinsically assumes the same value for all grain boundaries of a particular microstructure. This significant simplification is in contrast to experimental findings that are based on local experimental approaches. As suggested in this work, integrating computational multiscale formulations promises an accurate capturing of microstructure details and alignment effects. In particular, computational multiscale methods naturally allow for different grain boundary resistivities to be assigned to each grain boundary of a particular microstructure and make it possible to calculate resistivity tensors that intrinsically account for morphologically-induced anisotropies. In this regard, multiscale techniques both provide a solid theoretical foundation for the Andrews method and address its intrinsic drawbacks. Put into perspective, the present chapter contributes to a comprehensive understanding of accumulated grain boundary resistivity, ensuring that the refined models align closely with experimental observations and thereby enabling a detailed understanding of the experimentally recorded data.}[qtd. 71][qtd. 75]{Additionally, this chapter presents Mosaic, a Python-based open-source software tool developed to address the challenge of using non-rectilinear, periodic microstructures generated by Mosaic in simulations requiring periodic boundary conditions. Mosaic efficiently transforms these complex microstructures into rectilinear, periodic representations suitable for finite element analysis. Cohesive zone elements can optionally be added by an interface to the open-source software ciGen. In summary, Mosaic offers a streamlined workflow for the creation of periodic, rectilinear RVEs with flexible output options for researchers and engineers working with polycrystalline materials.}[qtd. 75]

[qtd. 72]{Motivated by the non-trivial homogenisation of dissipative terms in thermo-electrically coupled systems, **Chapter 7** conducted a comprehensive analysis of the governing multiscale multiphysics problem using Hill–Mandel-type homogenisation, asymptotic expansions, and two-scale convergence results. We derived homogenised field equations that explicitly consider Joule heating and temperature-dependent electrical conductivities. Through these analyses, we showcased the merits and limitations of the different approaches in capturing the coupled thermo-electric response of heterogeneous conductors. In the periodic, stationary, uniformly elliptic regime analysed here and when considering a distinct separation of length scales, the approaches are consistent but take different roles: Hill–Mandel averaging appeals to physical intuition, yields energetically consistent macroscale relations and integrates naturally into FE^2 implemen-

tations. Asymptotic expansions expose the underlying corrector problems and provide closed-form representations of effective tensors but rely on regularity and can be delicate beyond leading order terms or near boundary layers. Two-scale convergence provides rigorous compactness results and limit identification under minimal assumptions, albeit being less constructive for computations. The effectiveness of the different methods in predicting the homogenised material response was demonstrated through numerical examples in two- and three-dimensional settings. The key findings of this chapter are as follows. The nonlinear nature of the coupled problem poses a challenge for the rigorous mathematical analysis with regularity issues complicating the associated existence proof. Addressing these, we resorted to a fixed point argument and provided a rigorous mathematical foundation to the coupled multiscale system by means of two-scale convergence results. We showed that the asymptotic ansatz, that is often favoured in engineering applications due to its formal nature, finds rigorous justification in the two-scale convergence framework. We demonstrated that the physics-based assumptions commonly made in Hill–Mandel-type homogenisation approaches – such as evaluating microscale constitutive relations at a fixed macroscale temperature and neglecting heat sources in microscale boundary value problems – are consistent with the mathematically rigorous results derived from two-scale convergence analysis.In the regime considered in the scope of this work (periodic coefficients, stationary problems, bounded and uniformly elliptic operators, monotone coupling, distinct scale separation) the three frameworks were shown to be compatible: (i) the Hill–Mandel-type homogenisation approach is precisely the energy form of the cell problems that arise in the formal asymptotic ansatz and (ii) the two-scale limits stipulate the same correctors and effective tensors as the asymptotic method. These observations are consistent with standard results in computational homogenisation: methods derived from asymptotic expansions and those based on Hill–Mandel averaging produce the same homogenised constitutive tensors and identical macroscopic equations for linear periodic media. Our nonlinear thermo-electric system still belongs to this compatible class since it is stationary, periodic, uniformly elliptic and monotone. Hence, the three routes coincide. Put into perspective, the theoretical developments provide a solid foundation for the study of thermo-electrically coupled processes in heterogeneous materials across scales.}$^{\text{qtd.}}_{[72]}$

8.2 Outlook

The computational multiscale framework developed in this thesis provides a foundation for modelling thermo-electro-mechanical behaviour in electrical conductors. While the emphasis has been placed on fundamental developments and academic case studies, the methodologies presented here offer several promising directions for future research.

- A natural extension of this work lies in the experimental calibration and validation of the cohesive zone formulations. In particular, the generalised traction-separation law must be adapted to specific material systems to quantify the influence of material interfaces – most notably, grain boundaries. Experimental evidence indicates that each grain boundary exhibits a distinct electrical resistivity, governed by its

crystallographic characteristics, such as the relative orientation of neighbouring grains and the geometry of the grain boundary plane [23]. These interfaces give rise to discontinuities in the electric potential field and contribute to an overall increase in the bulk resistivity. The proposed formulation can capture such effects by modelling grain boundaries as cohesive, (lowly-conducting) interfaces. Future work involves dedicated experimental investigations to characterise these interface properties. Specifically, sub-microscale four-point probe measurements is to be employed to measure grain boundary resistivities directly. These data can then be used to calibrate the constitutive models and validate their predictive capabilities against actual grain boundary structures, thereby deepening the understanding of their contribution to the macroscopic electrical response.

- Another direction is the extension of the multiscale framework to incorporate generalised imperfect interfaces at the microscale. While the current formulation captures cohesive-type behaviour with degradation-driven resistivity changes, generalised interface models offer the flexibility to represent a broader range of physical phenomena. Incorporating such models would enable the simulation of more complex microstructural features, including phase boundaries with graded properties, elastic interfaces, and mechanically active interfaces. This generalisation would also facilitate the coupling of additional physical processes at interfaces. When embedded into a computational homogenisation setting, these enriched models could provide new insight into how interface-level physics affects the macroscopic response.

- While the consistency between Hill–Mandel-type computational homogenisation, asymptotic expansions, and two-scale convergence has been demonstrated for bulk materials with moderate material contrast, several open questions remain. In particular, the current mathematical framework assumes that all constituents possess finite and sufficiently regular material properties. This assumption excludes important limiting cases such as pores or inclusions with vanishing conductivity (i.e., infinite contrast scenarios), which are highly relevant in porous metals and damage-induced microstructures.

- The rigorous mathematical treatment of microscale problem featuring material interfaces – especially in the context of coupled thermo-electrical problems – remains unexplored. Future work should focus on extending two-scale convergence theory to incorporate cohesive or imperfect interfaces, where the definition of temperature-dependent interfacial conductivity presents an open and compelling challenge.

Bibliography

[1] E. C. Aifantis. The physics of plastic deformation. *International Journal of Plasticity*, 3(3):211–247, 1987. doi:10.1016/0749-6419(87)90021-0.

[2] A. A. Akay, S. Göktepe, and E. Gürses. Formulation of a bilinear traction-separation interface law in boundary elements with homogenization. *Procedia Structural Integrity*, 61:138–147, 2024. doi:10.1016/j.prostr.2024.06.019.

[3] G. Allaire. Homogenization and two-scale convergence. *SIAM Journal on Mathematical Analysis*, 23(6):1482–1518, 1992. doi:10.1137/0523084.

[4] H. W. Alt. *Lineare Funktionalanalysis*. Springer-Lehrbuch. Springer Berlin, Heidelberg, 2012. doi:10.1007/978-3-662-22101-3.

[5] M. M. Ameen, R. H. J. Peerlings, and M. G. D. Geers. A quantitative assessment of the scale separation limits of classical and higher-order asymptotic homogenization. *European Journal of Mechanics – A/Solids*, 71:89–100, 2018. doi:10.1016/j.euromechsol.2018.02.011.

[6] P. V. Andrews. Resistivity due to grain boundaries in pure copper. *Physics Letters*, 19(7):558–560, 1965. doi:10.1016/0031-9163(65)90776-6.

[7] P. V. Andrews, M. B. West, and C. R. Robeson. The effect of grain boundaries on the electrical resistivity of polycrystalline copper and aluminium. *The Philosophical Magazine: A Journal of Theoretical Experimental and Applied Physics*, 19(161):887–898, 1969. doi:10.1080/14786436908225855.

[8] I. Arias, S. Serebrinsky, and M. Ortiz. A phenomenological cohesive model of ferroelectric fatigue. *Acta Materialia*, 54(4):975–984, 2006. doi:10.1016/j.actamat.2005.10.035.

[9] ASTM E1382-97. Standard Test Methods for Determining Average Grain Size Using Semiautomatic and Automatic Image Analysis. Standard, ASTM International, West Conshohocken, PA, 2015.

[10] I. Bakonyi. Accounting for the resistivity contribution of grain boundaries in metals: Critical analysis of reported experimental and theoretical data for Ni and Cu. *European Physical Journal Plus*, 136:410, 2021. doi:10.1140/epjp/s13360-021-01303-4.

[11] G. I. Barenblatt. The formation of equilibrium cracks during brittle fracture. General ideas and hypotheses. Axially-symmetric cracks. *Journal of Applied Mathematics and Mechanics*, 23(3):622–636, 1959. doi:10.1016/0021-8928(59)90157-1.

[12] S. Bargmann, B. Klusemann, J. Markmann, J. E. Schnabel, K. Schneider, C. Soyarslan, and J. Wilmers. Generation of 3D representative volume elements for heterogeneous materials: A review. *Progress in Materials Science*, 96:322–384, 2018. doi:10.1016/j.pmatsci.2018.02.003.

[13] K. Barmak, A. Darbal, K. J. Ganesh, P. J. Ferreira, J. M. Rickman, T. Sun, B. Yao, A. P. Warren, and K. R. Coffey. Surface and grain boundary scattering in nanometric Cu thin films: A quantitative analysis including twin boundaries. *Journal of Vacuum Science and Technology A: Vacuum, Surfaces, and Films*, 32 (6):061503, 2014. doi:10.1116/1.4894453.

[14] Z. P. Bažant and G. Pijaudier-Cabot. Nonlocal continuum damage, localization instability and convergence. *Journal of Applied Mechanics*, 55:287–293, 1988. doi:10.1115/1.3173674.

[15] L. Benabou, Z. Sun, and P. R. Dahoo. A thermo-mechanical cohesive zone model for solder joint lifetime prediction. *International Journal of Fatigue*, 49:18–30, 2013. doi:10.1016/j.ijfatigue.2012.12.008.

[16] I. Benedetti. An integral framework for computational thermo-elastic homogenization of polycrystalline materials. *Computer Methods in Applied Mechanics and Engineering*, 407:115927, 2023. doi:10.1016/j.cma.2023.115927.

[17] I. Benedetti, V. Gulizzi, and A. Milazzo. A microstructural model for homogenisation and cracking of piezoelectric polycrystals. *Computer Methods in Applied Mechanics and Engineering*, 357:112595, 2019. doi:10.1016/j.cma.2019.112595.

[18] A. Bensoussan, J.-L. Lions, and G. Papanicolaou. Asymptotic analysis for periodic structures. In *Studies in Mathematics and Its Applications*, volume 5, pages 1–231. Elsevier, 1978. doi:10.1016/S0168-2024(08)70195-4.

[19] H. Berger, S. Kari, U. Gabbert, R. Rodriguez-Ramos, R. Guinovart, J. A. Otero, and J. Bravo-Castillero. An analytical and numerical approach for calculating effective material coefficients of piezoelectric fiber composites. *International Journal of Solids and Structures*, 42(21–22):5692–5714, 2005. doi:10.1016/j.ijsolstr.2005.03.016.

[20] S. A. Berggren, D. Lukkassen, A. Meidell, and L. Simula. A new method for numerical solution of checkerboard fields. *Journal of Applied Mathematics*, 1(4): 157–173, 2001. doi:10.1155/S1110757X01000316.

[21] R. Berthelsen and A. Menzel. Computational homogenisation of thermo-viscoplastic composites: Large strain formulation and weak micro-periodicity. *Computer Methods in Applied Mechanics and Engineering*, 348:575–603, 2019. doi:10.1016/j.cma.2018.12.032.

[22] R. Bharali, F. Larsson, and R. Jänicke. Computational homogenisation of phase-field fracture. *European Journal of Mechanics – A/Solids*, 88:104247, 2021. doi:10.1016/j.euromechsol.2021.104247.

[23] H. Bishara, S. Lee, T. Brink, M. Ghidelli, and G. Dehm. Understanding grain boundary electrical resistivity in Cu: The effect of boundary structure. *ACS*

Nano, 15(10):16607–16615, 2021. doi:10.1021/acsnano.1c06367.

[24] H. Bishara, L. Langenohl, X. Zhou, B. Gault, J. P. Best, and G. Dehm. Decoupling the electrical resistivity contribution of grain boundaries in dilute fe-alloyed Cu thin films. *Scripta Materialia*, 230:115393, 2023. doi:10.1016/j.scriptamat.2023.115393.

[25] X. Blanc and C. Le Bris. *Dimension > 2: The "Simple" Cases: Abstract or Periodic Settings*, pages 99–170. Springer Nature Switzerland, Cham, 2023. doi:10.1007/978-3-031-21833-0_3.

[26] M. J. Borden, C. V. Verhoosel, M. A. Scott, T. J. R. Hughes, and C. M. Landis. A phase-field description of dynamic brittle fracture. *Computer Methods in Applied Mechanics and Engineering*, 217-220:77–95, 2012. doi:10.1016/j.cma.2012.01.008.

[27] E. Bosco, R. H. J. Peerlings, and M. G. D. Geers. Asymptotic homogenization of hygro-thermo-mechanical properties of fibrous networks. *International Journal of Solids and Structures*, 115-116:180–189, 2017. doi:10.1016/j.ijsolstr.2017.03.015.

[28] B. Bourdin, G. A. Francfort, and J.-J. Marigo. Numerical experiments in revisited brittle fracture. *Journal of the Mechanics and Physics of Solids*, 48(4):797–826, 2000. doi:10.1016/S0022-5096(99)00028-9.

[29] J. R. Bowler and N. Bowler. Theory of four-point alternating current potential drop measurements on conductive plates. *Proceedings of the Royal Society of London Series A*, 463:817–836, 2007. doi:10.1098/rspa.2006.1791.

[30] L. Brassart, H. M. Inglis, L. Delannay, I. Doghri, and P. H. Geubelle. An extended Mori–Tanaka homogenization scheme for finite strain modeling of debonding in particle-reinforced elastomers. *Computational Materials Science*, 45(3):611–616, 2009. doi:10.1016/j.commatsci.2008.06.021.

[31] F. X. Che, L. C. Wai, and T. C. Chai. Failure mode and mechanism analysis for Cu wire bond on Cu/low-k chip by wire pull test and finite-element analysis. *IEEE Transactions on Device and Materials Reliability*, 18(2):163–172, 2018. doi:10.1109/TDMR.2018.2808348.

[32] Q. Chen, G. Chatzigeorgiou, F. Meraghni, and A. Javili. Homogenization of size-dependent multiphysics behavior of nanostructured piezoelectric composites with energetic surfaces. *European Journal of Mechanics – A/Solids*, 96:104731, 2022. doi:10.1016/j.euromechsol.2022.104731.

[33] J. Crespo-Miguel, S. Lucarini, A. Arias, and D. Garcia-Gonzalez. Thermo-electro-mechanical microstructural interdependences in conductive thermoplastics. *npj Computational Materials*, 9:134, 2023. doi:10.1038/s41524-023-01091-8.

[34] J. Crespo-Miguel, S. Lucarini, S. Garzon-Hernandez, A. Arias, E. Martínez Pañeda, and D. Garcia-Gonzalez. In-silico platform for the multi-functional design of 3d printed conductive components. *Nature Communications*, 16:1359, 2025. doi:10.1038/s41467-025-56707-y.

[35] E. De Giorgi and S. Spagnolo. Sulla convergenza degli integrali dell'energia per operatori ellitici del secondo ordine. *Bollettino dell'Unione Matematica Italiana*, 8:391–411, 1973.

[36] E. De Giorgi. Sulla convergenza di alcune successioni d'integrali del tipo dell'area. *Rendiconti di Matematica*, 8:277–294, 1975.

[37] R. Del Toro, M. L. De Bellis, M. Vasta, and A. Bacigalupo. Multifield asymptotic homogenization for periodic materials in non-standard thermoelasticity. *International Journal of Mechanical Sciences*, 265:108835, 2024. doi:10.1016/j.ijmecsci.2023.108835.

[38] D. S. Dugdale. Yielding of steel sheets containing slits. *Journal of the Mechanics and Physics of Solids*, 8(2):100–104, 1960. doi:10.1016/0022-5096(60)90013-2.

[39] A. Dunlap. *Elektronenmikroskopische Untersuchung der schädigungsrelevanten physikalischen Mechanismen in umgeformten Einsatzstahl 16MnCrS5*. PhD thesis, Rheinisch-Westfälische Technische Hochschule Aachen.

[40] T. A. Dutra, R. T. L. Ferreira, H. B. Resende, A. Guimarães, and J. M. Guedes. A complete implementation methodology for Asymptotic Homogenization using a finite element commercial software: preprocessing and postprocessing. *Composite Structures*, 245:112305, 2020. doi:10.1016/j.compstruct.2020.112305.

[41] G. Duvant, C. John, and J. Lions. *Inequalities in Mechanics and Physics*. Grundlehren der mathematischen Wissenschaften. Springer Berlin Heidelberg, 2012.

[42] A. M. Dykhne. Conductivity of a two-dimensional two-phase system. *Journal of Experimental and Theoretical Physics*, 32(1):63–65, 1971.

[43] M. Ekh, N. Larijani, E. Dartfeldt, M. Kapp, and R. Pippan. Prediction of the mechanical behaviour of pearlitic steel based on microcompression tests, micromechanical models and homogenization approaches. *European Journal of Mechanics – A/Solids*, 67:272–279, 2018. doi:10.1016/j.euromechsol.2017.09.013.

[44] K. Enakoutsa, J. B. Leblond, and G. Perrin. Numerical implementation and assessment of a phenomenological nonlocal model of ductile rupture. *Computer Methods in Applied Mechanics and Engineering*, 196(13–16):1946–1957, 2007. doi:10.1016/j.cma.2006.10.003.

[45] A. C. Eringen. *Nonlinear Theory of Continuous Media*. McGraw-Hill Series in Engineering Siences. McGraw-Hill, 1962.

[46] A. C. Eringen and G. A. Maugin. *Electrodynamics of Continua I: Foundations and Solid Media*. Springer New York, 2012.

[47] M. Fagerström and R. Larsson. A thermo-mechanical cohesive zone formulation for ductile fracture. *Journal of the Mechanics and Physics of Solids*, 56(10):3037–3058, 2008. doi:10.1016/j.jmps.2008.06.002.

[48] F. Fantoni, A. Bacigalupo, and M. Paggi. Multi-field asymptotic homogenization of thermo-piezoelectric materials with periodic microstructure. *International Journal*

of Solids and Structures, 120:31–56, 2017. doi:10.1016/j.ijsolstr.2017.04.009.

[49] M. Fergoug, A. Parret-Fréaud, N. Feld, B. Marchand, and S. Forest. A general boundary layer corrector for the asymptotic homogenization of elastic linear composite structures. *Composite Structures*, 285:115091, 2022. doi:10.1016/j.compstruct.2021.115091.

[50] S. Firooz, P. Steinmann, and A. Javili. Homogenization of composites with extended general interfaces: Comprehensive review and unified modeling. *Applied Mechanics Reviews*, 73(4):040802, 2021. doi:10.1115/1.4051481.

[51] S. Firooz and A. Javili. Understanding the role of general interfaces in the overall behavior of composites and size effects. *Computational Materials Science*, 162: 245–254, 2019. doi:10.1016/j.commatsci.2019.02.042.

[52] S. Firooz, G. Chatzigeorgiou, P. Steinmann, and A. Javili. Extended general interfaces: Mori–tanaka homogenization and average fields. *International Journal of Solids and Structures*, 254-255:111933, 2022. doi:10.1016/j.ijsolstr.2022.111933.

[53] L. Flodén, A. Holmbom, M. Olsson Lindberg, and J. Persson. Two-scale convergence: Some remarks and extensions. *Pure and Applied Mathematics Quarterly*, 9 (3):461–486, 2013. doi:10.4310/PAMQ.2013.v9.n3.a4.

[54] S. Forest. Micromorphic approach for gradient elasticity, viscoplasticity, and damage. *Journal of Engineering Mechanics*, 135(3):117–131, 2009. doi:10.1061/(ASCE)0733-9399(2009)135:3(117).

[55] G. A. Francfort and J.-J. Marigo. Revisiting brittle fracture as an energy minimization problem. *Journal of the Mechanics and Physics of Solids*, 46(8):1319–1342, 1998. doi:10.1016/S0022-5096(98)00034-9.

[56] F. Fritzen, S. Forest, T. Böhlke, D. Kondo, and T. Kanit. Computational homogenization of elasto-plastic porous metals. *International Journal of Plasticity*, 29: 102–119, 2012. doi:10.1016/j.ijplas.2011.08.005.

[57] D. Gall. The search for the most conductive metal for narrow interconnect lines. *Journal of Applied Physics*, 127(5):050901, 2020. doi:10.1063/1.5133671.

[58] C. L. Gan, C. Francis, B. L. Chan, and U. Hashim. Extended reliability of gold and copper ball bonds in microelectronic packaging. *Gold Bulletin*, 46(2):103–115, 2013. doi:10.1007/s13404-013-0087-8.

[59] A. M. Gebauer, M. R. Pfaller, F. A. Braeu, C. J. Cyron, and W. A. Wall. A homogenized constrained mixture model of cardiac growth and remodeling: analyzing mechanobiological stability and reversal. *Biomechanics and Modeling in Mechanobiology*, 22:1983–2002, 2023. doi:10.1007/s10237-023-01747-w.

[60] M. G. D. Geers, V. G. Kouznetsova, K. Matouš, and J. Yvonnet. Homogenization methods and multiscale modeling: Nonlinear problems. In E. Stein, R. de Borst, and T. Hughes, editors, *Encyclopedia of Computational Mechanics Second Edition*, pages 1–34. John Wiley & Sons, Ltd, 2017. doi:10.1002/9781119176817.ecm2107.

[61] T. Gentieu, A. Catapano, J. Jumel, and J. Broughton. A mean-field homogenisation scheme with CZM-based interfaces describing progressive inclusions debonding. *Composite Structures*, 229:111398, 2019. doi:10.1016/j.compstruct.2019.111398.

[62] C. Geuzaine and J.-F. Remacle. Gmsh: A 3-D finite element mesh generator with built-in pre- and post-processing facilities. *International Journal for Numerical Methods in Engineering*, 79(11):1309–1331, 2009. doi:10.1002/nme.2579.

[63] D. Gilbarg and N. S. Trudinger. *Elliptic partial differential equations of second order*, volume 224 of *Grundlehren der mathematischen Wissenschaften [Fundamental Principles of Mathematical Sciences]*. Springer-Verlag, Berlin, second edition, 1983. doi:10.1007/978-3-642-61798-0.

[64] M. Graham and S. Klinge. Multiscale homogenisation of diffusion in enzymatically-calcified hydrogels. *Journal of the Mechanical Behavior of Biomedical Materials*, 149:106244, 2024. doi:10.1016/j.jmbbm.2023.106244.

[65] L. Greengard and J.-Y. Lee. Electrostatics and heat conduction in high contrast composite materials. *Journal of Computational Physics*, 211(1):64–76, 2006. doi:10.1016/j.jcp.2005.05.004.

[66] N. Grilli, E. Tarleton, and A. C. F. Cocks. Neper2CAE and PyCiGen: Scripts to generate polycrystals and interface elements in Abaqus. *SoftwareX*, 13:100651, 2021. doi:10.1016/j.softx.2020.100651.

[67] M. A. Groeber and M. A. Jackson. DREAM.3D: a digital representation environment for the analysis of microstructure in 3D. *Integrating Materials and Manufacturing Innovation*, 3:56–72, 2014. doi:10.1186/2193-9772-3-5.

[68] N. M. P. Guillaume, M. W. Cresswell, R. A. Allen, S. Everist, and L. W. Linholm. Comparison of sheet-resistance measurements obtained by standard and small-area four-point probing. In *ICMTS 1999. Proceedings of 1999 International Conference on Microelectronic Test Structures*, pages 62–.66, 1999. doi:10.1109/ICMTS.1999.766217.

[69] M. E. Gurtin and I. A. Murdoch. A continuum theory of elastic material surfaces. *Archive for Rational Mechanics and Analysis*, 57:291–323, 1975. doi:10.1007/BF00261375.

[70] S. Göktepe, O. J. Abilez, K. K. Parker, and E. Kuhl. A multiscale model for eccentric and concentric cardiac growth through sarcomerogenesis. *Journal of Theoretical Biology*, 265(3):433–442, 2010. doi:10.1016/j.jtbi.2010.04.023.

[71] D. Güzel, T. Kaiser, H. Bishara, G. Dehm, and A. Menzel. Revisiting andrews method and grain boundary resistivity from a computational multiscale perspective. *Mechanics of Materials*, 198:105115, 2024. doi:10.1016/j.mechmat.2024.105115.

[72] D. Güzel, D. Wiedemann, T. Kaiser, and A. Menzel. On dissipative effects in thermo-electrically coupled systems: Hill–Mandel-type homogenisation, asymptotic expansions and two-scale convergence. *Journal of the Mechanics and Physics*

of Solids, 208:106427, 2026. doi:10.1016/j.jmps.2025.106427.

[73] D. Güzel, T. Kaiser, L. Lücker, N. Baak, F. Walther, and A. Menzel. Characterisation of damage by means of electrical measurements: Numerical predictions. *Proceedings in Applied Mathematics and Mechanics*, 23(2):e202300013, 2023. doi:10.1002/pamm.202300013.

[74] D. Güzel, T. Kaiser, and A. Menzel. A thermo-electro-mechanically coupled cohesive zone formulation for predicting interfacial damage. *European Journal of Mechanics – A/Solids*, 99:104935, 2023. doi:10.1016/j.euromechsol.2023.104935.

[75] D. Güzel, T. Furlan, T. Kaiser, and A. Menzel. Neper-Mosaic: Seamless generation of periodic representative volume elements on unit domains. *SoftwareX*, 28:101912, 2024. doi:10.1016/j.softx.2024.101912.

[76] D. Güzel, T. Kaiser, and A. Menzel. A computational multiscale approach towards the modelling of microstructures with material interfaces in electrical conductors. *Mathematics and Mechanics of Solids*, 30(2):247–266, 2025. doi:10.1177/10812865231202721.

[77] A. Hattiangadi and T. Siegmund. An analysis of the delamination of an environmental protection coating under cyclic heat loads. *European Journal of Mechanics – A/Solids*, 24(3):361–370, 2005. doi:10.1016/j.euromechsol.2005.01.003.

[78] T. Heitbreder, N. S. Ottosen, M. Ristinmaa, and J. Mosler. Consistent elastoplastic cohesive zone model at finite deformations – Variational formulation. *International Journal of Solids and Structures*, 106–107:284–293, 2017. doi:10.1016/j.ijsolstr.2016.10.027.

[79] J. Helsing and R. Ojala. Corner singularities for elliptic problems: Integral equations, graded meshes, quadrature, and compressed inverse preconditioning. *Journal of Computational Physics*, 227(20):8820–8840, 2008. doi:10.1016/j.jcp.2008.06.022.

[80] R. Hill. Elastic properties of reinforced solids: Some theoretical principles. *Journal of the Mechanics and Physics of Solids*, 11(5):357–372, 1963. doi:10.1016/0022-5096(63)90036-X.

[81] A. Hillerborg, M. Modéer, and P.-E. Petersson. Analysis of crack formation and crack growth in concrete by means of fracture mechanics and finite elements. *Cement and Concrete Research*, 6(6):773–781, 1976. doi:10.1016/0008-8846(76)90007-7.

[82] C. B. Hirschberger, N. Sukumar, and P. Steinmann. Computational homogenization of material layers with micromorphic mesostructure. *Philosophical Magazine*, 88(30–32):3603–3631, 2008. doi:10.1080/14786430802502567.

[83] J. P. Hou, R. Li, Q. Wang, H. Y. Yu, Z. J. Zhang, Q. Y. Chen, H. Ma, X. M. Wu, X. W. Li, and Z. F. Zhang. Breaking the trade-off relation of strength and electrical conductivity in pure Al wire by controlling texture and grain boundary. *Journal of Alloys and Compounds*, 769:96–109, 2018. doi:10.1016/j.jallcom.2018.07.358.

[84] J. M. Hu, M. Pecht, and A. Dasgupta. A probabilistic approach for predicting thermal fatigue life of wire bonding in microelectronics. *Journal of Electronic Packaging*, 113(3):275–285, 1991. doi:10.1115/1.2905407.

[85] K. Hutter, A. Ursescu, and A. A. F. van de Ven. *Electromagnetic Field Matter Interactions in Thermoelastic Solids and Viscous Fluids*, volume 710. 2006. doi:10.1007/3-540-37240-7.

[86] H. M. Inglis, P. H. Geubelle, K. Matouš, H. Tan, and Y. Huang. Cohesive modeling of dewetting in particulate composites: micromechanics vs. multiscale finite element analysis. *Mechanics of Materials*, 39(6):580–595, 2007. doi:10.1016/j.mechmat.2006.08.008.

[87] J. Isenberg, D. Biro, and W. Warta. Fast, contactless and spatially resolved measurement of sheet resistance by an infrared method. *Progress in Photovoltaics: Research and Applications*, 12(7):539–552, 2004. doi:10.1002/pip.548.

[88] M. Itskov. *Tensor Algebra and Tensor Analysis for Engineers—With Applications to Continuum Mechanics*. Springer Cham, 2012.

[89] A. Javili, G. Chatzigeorgiou, and P. Steinmann. Computational homogenization in magneto-mechanics. *International Journal of Solids and Structures*, 50(25–26): 4197–4216, 2013. doi:10.1016/j.ijsolstr.2013.08.024.

[90] A. Javili, A. McBride, and P. Steinmann. Numerical modelling of thermomechanical solids with highly conductive energetic interfaces. *International Journal for Numerical Methods in Engineering*, 93(5):551–574, 2013. doi:10.1002/nme.4402.

[91] A. Javili, A. McBride, and P. Steinmann. Thermomechanics of solids with lower-dimensional energetics: On the importance of surface, interface, and curve structures at the nanoscale. A unifying review. *Applied Mechanics Reviews*, 65(1): 010802, 2013. doi:10.1115/1.4023012.

[92] A. Javili, S. Kaessmair, and P. Steinmann. General imperfect interfaces. *Computer Methods in Applied Mechanics and Engineering*, 275:76–97, 2014. doi:10.1016/j.cma.2014.02.022.

[93] A. Javili, P. Steinmann, and J. Mosler. Micro-to-macro transition accounting for general imperfect interfaces. *Computer Methods in Applied Mechanics and Engineering*, 317:274–317, 2017. doi:10.1016/j.cma.2016.12.025.

[94] A. Javili, F. Larsson, K. Runesson, and P. Steinmann. On a canonical interface model with application to micro-heterogeneous elastic solids. *Computer Methods in Applied Mechanics and Engineering*, 440:117925, 2025. doi:10.1016/j.cma.2025.117925.

[95] A. Johnen, C. Geuzaine, T. Toulorge, and J.-F. Remacle. Efficient computation of the minimum of shape quality measures on curvilinear finite elements. *Computer-Aided Design*, 103:24–33, 2018. doi:10.1016/j.cad.2018.03.001.

[96] P. Johnsen. *Homogenization of Partial Differential Equations using Multiscale Methods*. PhD thesis, Mittuniversitetet, 2021.

[97] B.-F. Ju, Y. Ju, and M. Saka. Quantitative measurement of submicrometre electrical conductivity. *Journal of Physics D: Applied Physics*, 40(23):7467, 2007. doi:10.1088/0022-3727/40/23/031.

[98] T. Kaiser and A. Menzel. Fundamentals of electro-mechanically coupled cohesive zone formulations for electrical conductors. *Computational Mechanics*, 68:51–67, 2021. doi:10.1007/s00466-021-02019-z.

[99] T. Kaiser, M. Cordill, C. Kirchlechner, and A. Menzel. Electrical and mechanical behaviour of metal thin films with deformation-induced cracks predicted by computational homogenisation. *International Journal of Fracture*, 231(2):223–242, 2021. doi:10.1007/s10704-021-00582-3.

[100] T. Kaiser and A. Menzel. An electro-mechanically coupled computational multiscale formulation for electrical conductors. *Archive of Applied Mechanics*, 91: 1509–1526, 2021. doi:10.1007/s00419-020-01837-6.

[101] M.-A. Keip and M. Rambausek. A multiscale approach to the computational characterization of magnetorheological elastomers. *International Journal for Numerical Methods in Engineering*, 107(4):338–360, 2016. doi:10.1002/nme.5178.

[102] M.-A. Keip, P. Steinmann, and J. Schröder. Two-scale computational homogenization of electro-elasticity at finite strains. *Computer Methods in Applied Mechanics and Engineering*, 278:62–79, 2014. doi:10.1016/j.cma.2014.04.020.

[103] D. Kim, J. Lee, T. Nomura, E. M. Dede, J. Yoo, and S. Min. Topology optimization of functionally graded anisotropic composite structures using homogenization design method. *Computer Methods in Applied Mechanics and Engineering*, 369: 113220, 2020. doi:10.1016/j.cma.2020.113220.

[104] T.-H. Kim, X.-G. Zhang, D. M. Nicholson, B. M. Evans, N. S. Kulkarni, B. Radhakrishnan, E. A. Kenik, and A.-P. Li. Large discrete resistance jump at grain boundary in copper nanowire. *Nano Letters*, 10:3096–3100, 2010. doi:10.1021/nl101734h.

[105] R. Kinder, M. Mikolášek, D. Donoval, J. Kováč, and M. Tlaczala. Measurement system with hall and a four point probes for characterization of semiconductors. *Journal of Electrical Engineering*, 64(2):106–111, 2013. doi:10.2478/jeec-2012-0015.

[106] D. M. Kochmann, J. B. Hopkins, and L. Valdevit. Multiscale modeling and optimization of the mechanics of hierarchical metamaterials. *MRS Bulletin*, 44:773–781, 2019. doi:10.1557/mrs.2019.228.

[107] V. G. Kouznetsova, M. G. D. Geers, and W. A. M. Brekelmans. Multi-scale constitutive modelling of heterogeneous materials with a gradient-enhanced computational homogenization scheme. *International Journal for Numerical Methods in Engineering*, 54(8):1235–1260, 2002. doi:10.1002/nme.541.

[108] V. G. Kouznetsova, W. A. M. Brekelmans, and F. P. T. Baaijens. Approach to micro-macro modeling of heterogeneous materials. *Computational Mechanics*, 27: 37–48, 2001. doi:10.1007/s004660000212.

[109] S. Kozinov and M. Kuna. Simulation of damage in ferroelectric actuators by means of cohesive zone model. *Sensors and Actuators A: Physical*, 233:176–183, 2015. doi:10.1016/j.sna.2015.06.030.

[110] O. Krol. *Thermo-Mechanical Modelling of Solids and Interfaces -Theory, Numerics and Applications*. PhD thesis, Technische Universität Kaiserslautern, 2007.

[111] L. Kuna, J. Mangeri, E. P. Gorzkowski, J. A. Wollmershauser, and S. Nakhmanson. Mesoscale modeling of polycrystalline light transmission. *Acta Materialia*, 175:82–89, 2019. doi:10.1016/j.actamat.2019.06.001.

[112] V. Lacaille, C. Morel, E. Feulvarch, G. Kermouche, and J.-M. Bergheau. Finite element analysis of the grain size effect on diffusion in polycrystalline materials. *Computational Materials Science*, 95:187–191, 2014. doi:10.1016/j.commatsci.2014.07.026.

[113] K. Langenfeld, P. Junker, and J. Mosler. Quasi-brittle damage modeling based on incremental energy relaxation combined with a viscous-type regularization. *Continuum Mechanics and Thermodynamics*, 30(5):1125–1144, 2018. doi:10.1007/s00161-018-0669-z.

[114] G. Laschet. Homogenization of the thermal properties of transpiration cooled multi-layer plates. *Computer Methods in Applied Mechanics and Engineering*, 191 (41–42):4535–4554, 2002. doi:10.1016/S0045-7825(02)00319-5.

[115] V. Lefèvre and O. Lopez-Pamies. Homogenization of elastic dielectric composites with rapidly oscillating passive and active source terms. *SIAM Journal on Applied Mathematics*, 77(6):1962–1988, 2017. doi:10.1137/17M1110432.

[116] P. Lennemann, Y. P. Korkolis, and A. E. Tekkaya. Influence of changing loading directions on damage in sheet metal forming. *Advances in Industrial and Manufacturing Engineering*, 8:100139, 2024. doi:10.1016/j.aime.2024.100139.

[117] J. Liu, J. Li, G. Dirras, K. Ameyama, F. Cazes, and M. Ota. A three-dimensional multi-scale polycrystalline plasticity model coupled with damage for pure Ti with harmonic structure design. *International Journal of Plasticity*, 100:192–207, 2018. doi:10.1016/j.ijplas.2017.10.006.

[118] S. Liu, S. Hao, and Y. Shen. Asymptotic homogenization for phase field fracture of heterogeneous materials and application to toughening. *Composite Structures*, 339:118134, 2024. doi:10.1016/j.compstruct.2024.118134.

[119] L. Lu, Y. Shen, X. Chen, L. Qian, and K. Lu. Ultrahigh strength and high electrical conductivity in Copper. *Science*, 304(5669):422–426, 2004. doi:10.1126/science.1092905.

[120] Y. Lu, Y. Feng, W. Huang, Z. Su, Y. E. Ma, and S. Wang. A multiscale modeling for progressive failure behavior of unidirectional fiber-reinforced composites based on phase-field method. *Engineering Fracture Mechanics*, 310:110517, 2024. doi:10.1016/j.engfracmech.2024.110517.

[121] D. Lukkassen and A. Meidell. Generalized chessboard structures whose effective conductivities are integer valued. *Journal of Applied Mathematics*, 2012:1–7, 2012. doi:10.1155/2012/874239.

[122] D. Lukkassen, G. Nguetseng, and P. Wall. Two-scale convergence. *International Journal of Pure and Applied Mathematics*, 2(1):35–86, 2002.

[123] T. Luo, F. Serrano-Sánchez, H. Bishara, S. Zhang, R. Bueno Villoro, J. J. Kuo, C. Felser, C. Scheu, G. J. Snyder, J. P. Best, G. Dehm, Y. Yu, D. Raabe, C. Fu, and B. Gault. Dopant-segregation to grain boundaries controls electrical conductivity of n-type NbCo(Pt)Sn half-Heusler alloy mediating thermoelectric performance. *Acta Materialia*, 217:117147, 2021. doi:10.1016/j.actamat.2021.117147.

[124] M. A. Machado. Eddy currents probe design for NDT applications: A review. *Sensors*, 24(17), 2024. doi:10.3390/s24175819.

[125] K. M. Mannan and K. R. Karim. Grain boundary contribution to the electrical conductivity of polycrystalline Cu films. *Journal of Physics F: Metal Physics*, 5 (9):1687, 1975. doi:10.1088/0305-4608/5/9/009.

[126] M. Marino, B. Hudobivnik, and P. Wriggers. Computational homogenization of polycrystalline materials with the Virtual Element Method. *Computer Methods in Applied Mechanics and Engineering*, 355:349–372, 2019. doi:10.1016/j.cma.2019.06.004.

[127] K. Matouš, M. G. Kulkarni, and P. H. Geubelle. Multiscale cohesive failure modeling of heterogeneous adhesives. *Journal of the Mechanics and Physics of Solids*, 56(4):1511–1533, 2008. doi:10.1016/j.jmps.2007.08.005.

[128] A. F. Mayadas and M. Shatzkes. Electrical-resistivity model for polycrystalline films: The case of arbitrary reflection at external surfaces. *Physical Review B*, 1: 1382–1389, 1970. doi:10.1103/PhysRevB.1.1382.

[129] I. Miccoli, F. Edler, H. Pfnür, and C. Tegenkamp. The 100th anniversary of the four-point probe technique: The role of probe geometries in isotropic and anisotropic systems. *Journal of Physics: Condensed Matter*, 27(22):223201, 2015. doi:10.1088/0953-8984/27/22/223201.

[130] J. C. Michel, H. Moulinec, and P. Suquet. Effective properties of composite materials with periodic microstructure: a computational approach. *Computer Methods in Applied Mechanics and Engineering*, 172(1–4):109–143, 1999. doi:10.1016/S0045-7825(98)00227-8.

[131] C. Miehe. Numerical computation of algorithmic (consistent) tangent moduli in large-strain computational inelasticity. *Computer Methods in Applied Mechanics and Engineering*, 134(3–4):223–240, 1996. doi:10.1016/0045-7825(96)01019-5.

[132] C. Miehe. Computational micro-to-macro transitions for discretized microstructures of heterogeneous materials at finite strains based on the minimization of averaged incremental energy. *Computer Methods in Applied Mechanics and Engineering*, 192(5–6):559–591, 2003. doi:10.1016/S0045-7825(02)00564-9.

[133] C. Miehe, J. Schotte, and J. Schröder. Computational micro–macro transitions and overall moduli in the analysis of polycrystals at large strains. *Computational Materials Science*, 16(1–4):372–382, 1999. doi:10.1016/S0927-0256(99)00080-4.

[134] C. Miehe, M. Hofacker, and F. Welschinger. A phase field model for rate-independent crack propagation: Robust algorithmic implementation based on operator splits. *Computer Methods in Applied Mechanics and Engineering*, 199 (45–48):2765–2778, 2010. doi:10.1016/j.cma.2010.04.011.

[135] J. Mosler and I. Scheider. A thermodynamically and variationally consistent class of damage-type cohesive models. *Journal of the Mechanics and Physics of Solids*, 59(8):1647–1668, 2011. doi:10.1016/j.jmps.2011.04.012.

[136] R. C. Munoz and C. Arenas. Size effects and charge transport in metals: Quantum theory of the resistivity of nanometric metallic structures arising from electron scattering by grain boundaries and by rough surfaces. *Applied Physics Reviews*, 4 (1):011102, 2017. doi:10.1063/1.4974032.

[137] F. Murat and L. Tartar. H-convergence. In A. Cherkaev and R. Kohn, editors, *Topics in the Mathematical Modelling of Composite Materials*, pages 21–43. Birkhäuser Boston, Boston, MA, 1997. doi:10.1007/978-1-4612-2032-9_3.

[138] A. Needleman. A continuum model for void nucleation by inclusion debonding. *Journal of Applied Mathematics*, 54(3):525–531, 1987. doi:10.1115/1.3173064.

[139] G. Nguetseng. A general convergence result for a functional related to the theory of homogenization. *SIAM Journal on Mathematical Analysis*, 20(3):608–623, 1989. doi:10.1137/0520043.

[140] V. P. Nguyen. An open source program to generate zero-thickness cohesive interface elements. *Advances in Engineering Software*, 74:27–39, 2014. doi:10.1016/j.advengsoft.2014.04.002.

[141] V. P. Nguyen, O. Lloberas-Valls, M. Stroeven, and L. J. Sluys. Computational homogenization for multiscale crack modeling: Implementational and computational aspects. *International Journal for Numerical Methods in Engineering*, 89 (2):192–226, 2012. doi:10.1002/nme.3237.

[142] F. S. Oliveira, R. B. Cipriano, F. T. da Silva, E. C. Romão, and C. A. M. dos Santos. Simple analytical method for determining electrical resistivity and sheet resistance using the van der Pauw procedure. *Scientific Reports*, 10:16379, 2020. doi:10.1038/s41598-020-72097-1.

[143] M. Olsson. *G-Convergence and Homogenization of Some Monotone Operators*. PhD thesis, Mittuniversitetet, 2008.

[144] M. Ortiz and A. Pandolfi. Finite-deformation irreversible cohesive elements for three-dimensional crack-propagation analysis. *International Journal for Numerical Methods in Engineering*, 44(9):1267–1282, 1999. doi:10.1002/(SICI)1097-0207(19990330)44:9<1267::AID-NME486>3.0.CO;2-7.

[145] J.-H. Park, Y.-S. Choi, H.-J. Lee, H.-C. Shim, J.-P. Ahn, and J.-C. Lee. Direct-contact microelectrical measurement of the electrical resistivity of a solid electrolyte interface. *Nano Letters*, 19(6):3692–3698, 2019. doi:10.1021/acs.nanolett.9b00765.

[146] R. H. J. Peerlings, R. D. Borst, W. A. M. Brekelmans, J. H. P. D. Vree, and I. Spee. Some observations on localisation in non-local and gradient damage models. *European Journal of Mechanics – A/Solids*, 15:937–953, 1996.

[147] J. Pinho-da-Cruz, J. A. Oliveira, and F. Teixeira-Dias. Asymptotic homogenisation in linear elasticity. Part I: Mathematical formulation and finite element modelling. *Computational Materials Science*, 45(4):1073–1080, 2009. doi:10.1016/j.commatsci.2009.02.025.

[148] R. Quey, P. R. Dawson, and F. Barbe. Large-scale 3D random polycrystals for the finite element method: Generation, meshing and remeshing. *Computer Methods in Applied Mechanics and Engineering*, 200(17):1729–1745, 2011. doi:10.1016/j.cma.2011.01.002.

[149] R. Radulovic, O. T. Bruhns, and J. Mosler. Effective 3D failure simulations by combining the advantages of embedded Strong Discontinuity Approaches and classical interface elements. *Engineering Fracture Mechanics*, 78(12):2470–2485, 2011. doi:10.1016/j.engfracmech.2011.06.007.

[150] A. Ramírez-Torres, S. Di Stefano, A. Grillo, R. Rodríguez-Ramos, J. Merodio, and R. Penta. An asymptotic homogenization approach to the microstructural evolution of heterogeneous media. *International Journal of Non-Linear Mechanics*, 106:245–257, 2018. doi:10.1016/j.ijnonlinmec.2018.06.012.

[151] M. Reed and B. Simon. In *Methods of Modern Mathematical Physics: Functional Analysis*. Academic Press, 1972. doi:10.1016/B978-0-12-585001-8.50005-2.

[152] I. A. Rodrigues Lopes, M. Vieira de Carvalho, J. A. Marques da Silva, R. P. Cardoso Coelho, and F. M. Andrade Pires. Second-order homogenisation of crystal plasticity and martensitic transformation. *European Journal of Mechanics – A/Solids*, 102:105104, 2023. doi:10.1016/j.euromechsol.2023.105104.

[153] S. Rothe, J. H. Schmidt, and S. Hartmann. Analytical and numerical treatment of electro-thermo-mechanical coupling. *Archive of Applied Mechanics*, 85:1245–1264, 2014. doi:10.1007/s00419-014-0948-5.

[154] S. Roychowdhury, Y. D. Arun Roy, and R. H. Dodds. Ductile tearing in thin aluminum panels: Experiments and analyses using large-displacement, 3D surface cohesive elements. *Engineering Fracture Mechanics*, 69(8):983–1002, 2002. doi:10.1016/S0013-7944(01)00113-8.

[155] C. Rycroft. Voro++: a three-dimensional Voronoi cell library in C++. 2009. doi:10.2172/946741.

[156] S. Saeb, P. Steinmann, and A. Javili. Designing tunable composites with general interfaces. *International Journal of Solids and Structures*, 171:181–188, 2019. doi:10.1016/j.ijsolstr.2019.04.006.

[157] S. Saeb, P. Steinmann, and A. Javili. On effective behavior of microstructures embedding general interfaces with damage. *Computational Mechanics*, 64:1473–1494, 2019. doi:10.1007/s00466-019-01727-x.

[158] M. Schneider. A review of nonlinear FFT-based computational homogenization methods. *Acta Mechanica*, 232:2051–2100, 2021. doi:10.1007/s00707-021-02962-1.

[159] P. Seibert, A. Raßloff, K. A. Kalina, M. Ambati, and M. Kästner. Microstructure characterization and reconstruction in python: MCRpy. *Integrating Materials and Manufacturing Innovation*, 11:1–17, 2022. doi:10.1007/s40192-022-00273-4.

[160] A. Sengupta, P. Papadopoulos, and R. L. Taylor. A multiscale finite element method for modeling fully coupled thermomechanical problems in solids. *International Journal for Numerical Methods in Engineering*, 91(13):1386–1405, 2012. doi:10.1002/nme.4320.

[161] P. H. Serrao, S. Sandfeld, and A. Prakash. OptiMic: A tool to generate optimized polycrystalline microstructures for materials simulations. *SoftwareX*, 15:100708, 2021. doi:10.1016/j.softx.2021.100708.

[162] S. Sharba, J. Herb, and F. Fritzen. Reduced order homogenization of thermoelastic materials with strong temperature dependence and comparison to a machine-learned model. *Archive of Applied Mechanics*, 93:2855–2876, 2023. doi:10.1007/s00419-023-02411-6.

[163] C. Soyarslan, J. Havinga, L. Abelmann, and T. van den Boogaard. Asymptotic homogenization in the determination of effective intrinsic magnetic properties of composites. *Results in Physics*, 44:106188, 2023. doi:10.1016/j.rinp.2022.106188.

[164] S. Spagnolo. Sulla convergenza di soluzioni di equazioni paraboliche ed ellittiche. *Annali della Scuola Normale Superiore di Pisa, Classe di Scienze*, 22(4):571–597, 1968.

[165] D. W. Spring and G. H. Paulino. Computational homogenization of the debonding of particle reinforced composites: The role of interphases in interfaces. *Computational Materials Science*, 109:209–224, 2015. doi:10.1016/j.commatsci.2015.07.012.

[166] D. J. Steigmann and R. W. Ogden. Plane deformations of elastic solids with intrinsic boundary elasticity. *Proceedings of the Royal Society A: Mathematical, Physical and Engineering Sciences*, 453(1959):853–877, 1997.

[167] D. J. Steigmann and R. W. Ogden. Elastic surface-substrate interactions. *Proceedings of the Royal Society A: Mathematical, Physical and Engineering Sciences*, 455(1982):437–474, 1999.

[168] P. Steinmann. Formulation and computation of geometrically non-linear gradient damage. *International Journal for Numerical Methods in Engineering*, 46(5):757–779, 1999. doi:10.1002/(SICI)1097-0207(19991020)46:5<757::AID-NME731>3.0.CO;2-N.

[169] P. Steinmann and O. Häsner. On material interfaces in thermomechanical solids. *Archive of Applied Mechanics*, 75:31–41, 2005. doi:10.1007/s00419-005-0383-8.

[170] P. E. Stelzig. *On Problems in Homogenization and Two-scale Convergence*. PhD thesis, Università degli Studi di Trento, 2012.

[171] T. Sun, B. Yao, A. P. Warren, K. Barmak, M. F. Toney, R. E. Peale, and K. R. Coffey. Surface and grain-boundary scattering in nanometric Cu films. *Physical Review B*, 81:155454, 2010. doi:10.1103/PhysRevB.81.155454.

[172] H. Tan, Y. Huang, C. Liu, and P. H. Geubelle. The Mori–Tanaka method for composite materials with nonlinear interface debonding. *International Journal of Plasticity*, 21(10):1890–1918, 2005. doi:10.1016/j.ijplas.2004.10.001.

[173] A. A. O. Tay, K. S. Yeo, J. H. Wu, and T. B. Lim. Wirebond deformation during molding of ic packages. *Journal of Electronic Packaging*, 117(1):14–19, 1995. doi:10.1115/1.2792061.

[174] J. Telega, S. Tokarzewski, and A. Gałka. Effective conductivity of nonlinear two-phase media: Homogenization and two-point Padé approximants. *Acta Applicandae Mathematicae*, 61:295–315, 2000. doi:10.1023/A:1006487103815.

[175] I. Temizer. On the asymptotic expansion treatment of two-scale finite thermoelasticity. *International Journal of Engineering Science*, 53:74–84, 2012. doi:10.1016/j.ijengsci.2012.01.003.

[176] J. Utzinger, P. Steinmann, and A. Menzel. On the simulation of cohesive fatigue effects in grain boundaries of a piezoelectric mesostructure. *International Journal of Solids and Structures*, 45(17):4687–4708, 2008. doi:10.1016/j.ijsolstr.2008.04.017.

[177] M. J. Van den Bosch, P. J. G. Schreurs, and M. G. D. Geers. A cohesive zone model with a large displacement formulation accounting for interfacial fibrilation. *European Journal of Mechanics – A/Solids*, 26:1–19, 2007. doi:10.1016/j.euromechsol.2006.09.003.

[178] B. Vazic, B. E. Abali, and P. Newell. Generalized thermo-mechanical framework for heterogeneous materials through asymptotic homogenization. *Continuum Mechanics and Thermodynamics*, 35(1):159–181, 2023. doi:10.1007/s00161-022-01171-y.

[179] C. V. Verhoosel, J. J. C. Remmers, and M. A. Gutierrez. A partition of unity-based multiscale approach for modeling fracture in piezoelectric ceramics. *International Journal for Numerical Methods in Engineering*, 82:966–994, 2009. doi:10.1002/nme.2792.

[180] A. Wautier and B. B. Guzina. On the second-order homogenization of wave motion in periodic media and the sound of a chessboard. *Journal of the Mechanics and Physics of Solids*, 78:382–414, 2015. doi:10.1016/j.jmps.2015.03.001.

[181] D. Wiedemann. *Analytical Homogenisation of Transport Processes in Evolving Porous Media*. PhD thesis, Universität Augsburg, 2023.

[182] K. Willam, I. Rhee, and B. Shing. Interface damage model for thermomechanical degradation of heterogeneous materials. *Computer Methods in Applied Mechanics and Engineering*, 193(30–32):3327–3350, 2004. doi:10.1016/j.cma.2003.09.020.

[183] Z. Wu, Q. Lin, and Y. Chen. Application of fast multipole boundary element method for two-dimensional nonlinear interface debonding of particulate composites. *Engineering Analysis with Boundary Elements*, 113:72–81, 2020. doi:10.1016/j.enganabound.2019.12.017.

[184] T. Yalçinkaya, S. O. Çakmak, and C. Tekoğlu. A crystal plasticity based finite element framework for RVE calculations of two-phase materials: Void nucleation in dual-phase steels. *Finite Elements in Analysis and Design*, 187:103510, 2021. doi:10.1016/j.finel.2020.103510.

[185] H. Yang, B. E. Abali, W. H. Müller, S. Barboura, and J. Li. Verification of asymptotic homogenization method developed for periodic architected materials in strain gradient continuum. *International Journal of Solids and Structures*, 238: 111386, 2022. doi:10.1016/j.ijsolstr.2021.111386.

[186] Y. Yang, C. Lei, C.-F. Gao, and J. Li. Asymptotic homogenization of three-dimensional thermoelectric composites. *Journal of the Mechanics and Physics of Solids*, 76:98–126, 2015. doi:10.1016/j.jmps.2014.12.006.

[187] C.-F. Yu, C.-M. Chan, L.-C. Chan, and K.-C. Hsieh. Cu wire bond microstructure analysis and failure mechanism. *Microelectronics Reliability*, 51(1):119–124, 2011. doi:10.1016/j.microrel.2010.04.022.

[188] J. Yvonnet, N. Auffray, and V. Monchiet. Computational second-order homogenization of materials with effective anisotropic strain-gradient behavior. *International Journal of Solids and Structures*, 191-192:434–448, 2020. doi:10.1016/j.ijsolstr.2020.01.006.

[189] I. Özdemir, W. A. M. Brekelmans, and M. G. D. Geers. FE^2 computational homogenization for the thermo-mechanical analysis of heterogeneous solids. *Computer Methods in Applied Mechanics and Engineering*, 198(3–4):602–613, 2008. doi:10.1016/j.cma.2008.09.008.

[190] I. Özdemir, W. A. M. Brekelmans, and M. G. D. Geers. A thermo-mechanical cohesive zone model. *Computational Mechanics*, 46:735–745, 2010. doi:10.1007/s00466-010-0507-z.

Publication series of the Institute of Mechanics

published to date:

2010/01 Palnau, V.: Implementierung eines netzfreien Diskretisierungsverfahrens und seine Anwendung auf die Scherbandanalyse.
ISBN 978-3-921823-51-4

2010/02 Klusemann, B.: Application of homogenization methods and crystal plasticity to the modeling of heterogeneous materials of technological interest.
ISBN 978-3-921823-53-8

2011/01 Hortig, C.: Local and non-local thermomechanical modeling and finite-element simulation of high-speed cutting.
ISBN 978-3-921823-54-5

2011/02 Parvizian, F.: Modeling of microstructure evolution in aluminum alloys during hot extrusion.
ISBN 978-3-921823-56-9

2011/03 Noman, M.: Characterization and model identification for the simulation of the forming behavior of ferritic steels.
ISBN 978-3-921823-55-2

2011/04 Kayser, T.: Characterization of microstructure in aluminum alloys based on electron backscatter diffraction.
ISBN 978-3-921823-57-6

2011/05 Bargmann, S.: Computational modeling of material behavior on different scales based on continuum mechanics.
ISBN 978-3-921823-58-3

2013/01 Waffenschmidt, T.: Modelling and simulation of adaptation and degradation in anisotropic biological tissues.
ISBN 978-3-921823-61-3

2015/01 Ostwald, R.: Modelling and simulation of phase-transformations in elastoplastic polycrystals.
ISBN 978-3-921823-66-8

2016/01 Subramanian, M.: Phenomenological modelling and simulation of ferroelectric ceramics.
ISBN 978-3-921823-74-3

2016/02 Clausmeyer, T.: Evolution of plastic anisotropy in metals.
ISBN 978-3-921823-76-7

2017/01 Holtermann, R.: Computational multiscale modelling of grinding processes.
ISBN 978-3-921823-86-6

2017/02 Bartels, A.: Modelling of evolving microstructures at different scales.
ISBN 978-3-921823-93-4

2017/03 Dusthakar Kumar Rao, D. K.: Computational modelling of single and polycrystalline ferroelectric materials.
ISBN 978-3-921823-94-1

2019/01 Buckmann, K.: Microstructure evolution in functional magnetic materials.
ISBN 978-3-947323-09-8

2019/02 Kaiser, T.: Computational modelling of non-simple and anisotropic materials.
ISBN 978-3-947323-14-2

2019/03 Heitbreder, T.: Modelling of material interfaces at different length scales.
ISBN 978-3-947323-18-0

2020/01 Berthelsen, R.: Computational homogenisation of thermomechanical problems.
ISBN 978-3-947323-19-7

2020/02 Sievers, C.: Describing the macroscopic behavior of surfaces based on atomistic models.
ISBN 978-3-947323-24-1

2022/01 Rose, L.: Optimisation based parameter identification using optical field measurements.
ISBN 978-3-947323-31-9

2023/01 Langenfeld, K.: Continuum modeling of brittle and ductile damage: theory and computational frameworks.
ISBN 978-3-947323-41-8

2023/02 Schulte, R.: Parameter identification approaches with application to different classes of materials.
ISBN 978-3-947323-45-6

2023/03 Kaiser, T.: Multiscale multiphysics material modelling.
ISBN 978-3-947323-46-3

2024/01 Noll, I.: Thermomechanical modelling and simulation of laser powder bed fusion processes.
ISBN 978-3-947323-49-4

2024/02 Witt, C.: Isogeometric analysis of anisotropic mechanical and electromechanical higher-gradient continua.
ISBN 978-3-947323-50-0

2025/01 Kurzeja, P.: Modeling, control and opportunities of mechanical interfaces across the scales.
ISBN 978-3-947323-51-7

2025/02 Lammen, H.: Modeling and simulation of general imperfect interfaces using phase-field-theory.
ISBN 978-3-947323-52-4

2025/03 Sprave, L.: Computational modelling and simulation of ductile damage in metals.
ISBN 978-3-947323-54-8

2025/04 Schewe, M.: Computational modelling of surface interactions – wear, material separation and deposition.
ISBN 978-3-947323-55-5

2025/05 Wiegold, T.: On the numerical modeling of interfaces in engineering applications.
ISBN 978-3-947323-53-1

2025/06 Güzel, D.: Multiscale modelling of thermo-electro-mechanically coupled material behaviour.
ISBN XXX-X-XXXXXX-XX-X